國立臺灣大學工學院工程科學及海洋工程學系
碩士論文

Department of Engineering Science and Ocean Engineering
College of Engineering
National Taiwan University
Master Thesis

使用半潛式臺大浮台之 15 MW 浮式風機系統於新竹外海場址正常運轉性能研究

Normal Operating Performance Study of a 15 MW Floating Wind Turbine System Using Semi-Submersible TaidaFloat Platform in the Hsinchu Offshore Area

湯凱沂

Hoi-Yi Tong

指導教授：趙修武 博士

Advisor: Dr.-Ing. Shiu-Wu Chau

中華民國 111 年 9 月

September, 2022

doi:10.6342/NTU202204241

doi:10.6342/NTU202204241

Abstract

This study predicts the normal operating performance of a 15 MW floating wind turbine system equipped with a semi-submersible TaidaFloat platform, an IEA 15-MW offshore wind turbine and a 3×2 mooring design under the metocean conditions of the Hsinchu offshore area in the Taiwan Strait. The potential component of hydrodynamic properties is calculated by Ansys Aqwa, and the viscous component of hydrodynamic properties is obtained with the help of STAR-CCM+. The motion equations are solved by OrcaFlex to obtain the motion response and generator power, as well as the dynamic response of the mooring system and the aerodynamic loading of the wind turbine. Assuming that the wave has the same direction as the wind, this study compares the mean value and standard deviation of the motion response, generator power and mooring line tension between potential and viscous flow approaches by considering the combinations of seven wind directions and four current directions under the common wave and high wave condition in the Hsinchu offshore area. The numerical prediction shows that the viscous effect has a large impact on the hydrodynamic properties in the heave, roll and pitch motions. The angle between the leading mooring line of the system and the dominant wind direction in the Taiwan Strait, which is coming from the northeast, is recommended to be 0°, with the largest mean generator power of around 14 MW and 15 MW, and the maximum mean mooring line tension of 1.643 MN and 1.254 MN under the CW and HW condition, respectively, in order to deliver a relatively favorable performance of the system.

Keywords: Floating Wind Turbine, Semi-Submersible, Hydrodynamic Properties, Motion Response, Generator Power, Mooring Line Tension, Normal Operating, Hsinchu Offshore Area, Taiwan Strait

doi:10.6342/NTU202204241

doi:10.6342/NTU202204241

摘要

本研究預測在新竹外海海氣象條件下，使用半潛式臺大浮台、IEA 15-MW 離岸風機以及 3×2 型式繫纜系統的浮式風機系統之正常運轉性能。本研究以 Ansys Aqwa 及 STAR-CCM+預測水動力特性，以 OrcaFlex 預測浮式風機系統的繫纜受力及風機氣動力並求解運動方程式以獲得運動響應及風機功率。假設波向與風向相同，本研究考慮七個風向及四個流向的組合，預測在新竹外海一般及高波兩種波況下，浮式風機系統運動響應、風機功率和繫纜受力的平均值及標準差，並討論非黏性流和黏性流模擬方法對預測浮式風機系統性能的影響。模擬結果顯示，在起伏、橫搖及縱搖運動中，黏性對於水動力特性的影響較大。本研究結果顯示，當風機系統主纜繩與臺灣海峽最常見的東北風向夾角為 0°時，在一般及高波波況下平均功率約為 14 MW 及 15 MW，最大平均纜繩受力為 1.643 MN 及 1.254 MN，此時風機系統之正常運轉性能相對較佳。

關鍵字：浮式風機、半潛式浮台、水動力特性、運動響應、風機功率、纜繩受力、正常運轉、新竹外海、臺灣海峽

doi:10.6342/NTU202204241

doi:10.6342/NTU202204241

Content

doi:10.6342/NTU202204241

doi:10.6342/NTU202204241

Nomenclature

Latin Symbols

A	Disk area	[m^2]
A_{ij}	Added mass in translation/rotation	[kg]/[kg·m^2/rad]
$A_{ij,p}$	Potential component of added mass in translation/rotation	[kg]/[kg·m^2/rad]
$A_{ij,v}$	Viscous component of added mass in translation/rotation	[kg]/[kg·m^2/rad]
A_k	Predicted added mass in translation/rotation	[kg]/[kg·m^2/rad]
A_w	Amplitude of incident wave	[m]
a	Axial induction factor	[-]
a	Area vector	[m^2]
a'	Angular velocity induction factor	[-]
a_{ex}	External cross-sectional stress area	[m^2]
a_{in}	Internal cross-sectional stress area	[m^2]
B_{ij}	Damping in translation/rotation	[N·s/m]/[N·m·s/rad]
$B_{ij,p}$	Potential component of damping in translation/rotation	[N·s/m]/[N·m·s/rad]
$B_{ij,v}$	Viscous component of damping in translation/rotation	[N·s/m]/[N·m·s/rad]
B_k	Predicted damping in translation/rotation	[N·s/m]/[N·m·s/rad]
B_w	Wave direction	[rad]
C_d	Drag coefficient	[-]
C_{ij}	Stiffness of floating body in translation/rotation	[N/m]/[N·m/rad]
C_k	Stiffness of floating body in translation/rotation	[N/m] /[N·m/rad]
C_l	Lift coefficient	[-]
C_α	Sharpening factor	[-]
C_θ	Angle factor	[-]
C_φ	Actual damping	[N·s/m]
$CD_{k\omega}$	Cross-diffusion coefficient	[-]
CG	Center of gravity of wind turbine system	[m]
Co	Courant number	[-]
c	Chord length of blade section	[m]
c_c	Critical damping value for segment	[s]
c_d	Damping for mooring line	[s]
D_k	Amplitude of force	[N/m^2]
d	Distance to wall	[m]
EA	Axial stiffness of line	[N]
F	Correction term	[-]

doi:10.6342/NTU202204241

F_a	Axial force	[N]
$F_{e,i}$	Wave exciting force/moment	[N]/[N·m]
$F_{o,i}$	Force/Moment other than fluid force	[N]/[N·m]
F_r	Radiation force	[N]
F_t	Tangential force	[N]
G	Green's function	[1/m]
GK	Dimensionless gain correction factor	[-]
g	Gravitational acceleration	[m/s^2]
g_i	Gravity component in i-direction	[m/s^2]
H_h	Hub height	[m]
H_s	Significant wave height	[m]
h	Water depth	[m]
I	Moment of inertia	[kg·m^2]
I_d	Drivetrain inertia	[kg·m^2]
I_g	Generator inertia	[kg·m^2]
I_r	Rotor inertia	[kg·m^2]
J_o	Bessel function of the first kind	[m^2]
K_d	Blade-pitch controller derivative gain	[m^2]
K_i	Blade-pitch controller integral gain	[-]
K_p	Blade-pitch controller proportional gain	[s]
K_φ	Stiffness	[N/m]
k	Turbulent kinetic energy	[J]
k_0	Wave number of incident wave	[1/m]
k_{tt}	Coefficient for torque coupling tension	[N·m/°]
k_w	Wave number	[1/m]
L	Characteristic length	[m]
l	Segment length	[m]
l_0	Initial segment length	[m]
M_{ij}	Floating body mass	[kg]
M_φ	Mass	[kg]
m	Segment mass	[kg]
N_g	High-speed to low-speed gearbox ratio	[-]
n	Discrete-time-step counter	[-]
n	Normal vector	[-]
n_B	Number of blades	[-]
P	Mechanical power	[W]
P_0	Rated mechanical power	[W]
P_1	Pressure before actuator disk	[Pa]
P_2	Pressure behind actuator disk	[Pa]
P_d	Dynamic pressure	[Pa]

doi:10.6342/NTU202204241

P_g	Generator power	[W]
P_{in}	Fluid pressure before system	[Pa]
P_{out}	Fluid pressure behind system	[Pa]
$\bar{p}$	Mean fluid pressure in viscous flow	[Pa]
p_d	Diffraction pressure	[Pa]
p_{ex}	External pressure	[Pa]
p_i	Inflow pressure	[Pa]
p_{in}	Internal pressure	[Pa]
p_r	Radiation pressure	[Pa]
Q	Moment	[N·m]
Q_d	Wave drift QTF in translation/rotation	[N/m^2]/[N/m]
R	Blade length	[m]
R_r	Rotor radius	[m]
R_w	Flow field radius	[m]
r	Cross section radius	[m]
r_h	Hub radius	[m]
RAO_i	Response amplitude operator in translation/rotation	[m/m]/[°/m]
S	Immersed area of floating body	[m^2]
$\mathbf{S}$	Mean strain rate tensor	[1/s]
T	Wave period	[s]
T_a	Low-speed shaft aerodynamic torque	[N·m]
T_e	Effective tension	[N]
T_g	High-speed shaft generator torque	[N·m]
T_r	Thrust force	[N]
T_s	Discrete time step	[s]
T_w	Wall tension	[N]
T_z	Zero-crossing period	[s]
t	Time	[s]
U	Relative inflow velocity	[m/s]
U_1	Flow velocity before system	[m/s]
U_2	Flow velocity behind system	[m/s]
U_B	Wind speed obtained from the Beaufort scale	[m/s]
U_c	Current speed at free surface	[m/s]
U_{in}	Inflow velocity	[m/s]
U_{in}^c	Inflow velocity of current	[m/s]
U_{in}^w	Inflow velocity of wind	[m/s]
U_{out}	Outflow velocity	[m/s]
U_w	Wind speed at hub height	[m/s]
$u_{f,n}$	Unfiltered generator speed	[rad/s]
$\bar{u}_i$	Mean velocity component in i-direction	[m/s]

doi:10.6342/NTU202204241

u_i'	Turbulent velocity component in i-direction	[m/s]
V	Cell Volume	[m^3]
V_f	Forced motion velocity in translation/rotation	[m/s]/[°/s]
V_i	Volume of the i-th fluid in a cell	[m^3]
V_{P_c}	Characteristic velocity	[m/s]
$\mathbf{v}$	Flow field velocity	[m/s]
$\bar{\mathbf{v}}$	Mean velocity	[m/s]
$\mathbf{v}_{c,i}$	Boundary sharpening velocity of the i-th fluid	[m/s]
$\mathbf{v}_{d,i}$	Diffusion velocity of the i-th fluid	[m/s]
(x, y, z)	Coordinate system	[m]
x_i	Displacement in i-direction	[m]/[°]
$\dot{x}_i$	Velocity in i-direction	[m/s]/[°/s]
$\ddot{x}_i$	Acceleration in i-direction	[m/s^2]/[°/s^2]
x_k	Generalized displacement in translation/rotation	[m]/[°]
$y_{f,n}$	Filtered generator speed	[rad/s]
z_i	Coordinate	[m]

doi:10.6342/NTU202204241

Greek Symbols

α	Angle of attack	[°]
α_i	Volume fraction of the i-th fluid	[-]
α_c	Volume fraction of central cell	[-]
α_d	Volume fraction of downwind cell	[-]
α_f	Low-pass filter coefficient	[-]
α_f^{HRIC}	Modified volume fraction at cell interface	[-]
α_u	Volume fraction of upwind cell	[-]
α_w	Angle of incident wave	[°]
β_b	Blade pitch angle	[°]
$\beta_{b,k}$	Blade pitch angle when pitch sensitivity has doubled from its value at rated operating point	[°]
$\Delta\beta_b$	Small perturbation of blade pitch angle	[°]
γ	Parameter of the JONSWAP spectrum	[-]
ε	Total mean axial strain	[-]
ζ	Amplitude of forced motion in translation/rotation	[m]/[°]
ζ_φ	Damping ratio	[-]
η_i	Linear/angular displacement	[m]/[°]
θ	Relative inflow angle	[°]
θ_c	Current direction	[°]
θ_p	Angle between fluid interface and cell interface	[°]
θ_w	Wind/wave direction	[°]
λ	Wave length	[m]
λ_a	Target tension damping	[-]
λ_s	Expansion factor of segment	[-]
μ	Viscosity	[kg/(m·s)]
μ_0	Integral constant	[-]
μ_i	Fluid viscosity of the i-th fluid	[kg/(m·s)]
μ_t	Eddy viscosity	[kg/(m·s)]
ν	Kinematic viscosity	[m^2/s]
ν_P	Poisson ratio	[-]
ξ_c	Normalized volume fraction of central cell	[-]
ξ_f	Normalized volume fraction at cell interface	[-]
ξ_f^*	Normalized volume fraction modified by Courant number	[-]
ξ_f^{**}	Normalized volume fraction modified by angle	[-]
ρ	Fluid density	[kg/m^3]
ρ_i	Fluid density of the i-th fluid	[kg/m^3]
σ	Local solidity	[m]
σ_d	Diffraction strength of source point	[m/s]

doi:10.6342/NTU202204241

σ_j	Radiation strength of source point	[m/s]
τ	Segment twist angle	[°]
τ_{ij}	Shear stress	[Pa]
Φ	Amplitude of velocity potential	[m^2/s]
$\mathbf{\Phi}$	Velocity potential	[m^2/s]
Φ_d	Diffraction wave velocity potential	[m^2/s]
Φ_i	Incident wave velocity potential	[m^2/s]
Φ_j	Radiation velocity potential	[m^2/s]
φ_k	Phase difference	[s]
Ω	Low-speed shaft rotational speed	[rad/s]
Ω_0	Low-speed shaft rated rotational speed	[rad/s]
Ω_r	Rotor speed	[rad/s]
$\Delta\dot{\Omega}$	Low-speed shaft rotational acceleration	[rad/s^2]
ω	Specific turbulence dissipation rate	[1/s]
ω'	Induced angular frequency	[rad/s]
ω_0	Incident wave frequency	[rad/s]
ω_a	Angular frequency	[rad/s]
ω_s	Corner frequency	[rad/s]
ω_n	Natural frequency	[rad/s]

doi:10.6342/NTU202204241

List of Figures

doi:10.6342/NTU202204241

doi:10.6342/NTU202204241

doi:10.6342/NTU202204241

doi:10.6342/NTU202204241

doi:10.6342/NTU202204241

doi:10.6342/NTU202204241

doi:10.6342/NTU202204241

List of Tables

doi:10.6342/NTU202204241

doi:10.6342/NTU202204241

doi:10.6342/NTU202204241

doi:10.6342/NTU202204241

1 Introduction

1.1 Literature Review

Heronemus [1] first introduced the idea of an electricity-generation-purpose floating wind turbine platform in 1972 and the first offshore wind turbine with a rated power of 220 kW was constructed and installed in Swedish offshore area by World Wind in 1990 [2]. The capacity of offshore wind energy annually in Europe increased from 1991 to 2008, where the major installed capacity was contributed by bottom-fixed offshore wind turbines [1]. The research on floating offshore wind energy started in 1990 [3]~[5] while the installation and operation of floating offshore wind turbines were beginning from 2008 [6].

Some previous studies researched on the offshore wind resources and environment conditions of the Taiwan Strait are first summarized. The seismic and geological data of Zhangbin offshore area was analyzed in [7] and the influence of climate change on wind resources in the Taiwan Strait was predicted in [8]. Performance of different types of floating platform were also discussed in related researches. There are three general categories of floating platform for offshore wind turbine, i.e., semi-submersible, spar type, and tension leg platforms. The motion response of spar type platform was studied in [9]~[11]. [12] and [13] investigated on the motion response of semi-submersible platform. [14] compared the hydrodynamic and global motion behavior in the South China Sea among semi-submersible, spar type, and tension leg platforms. According to [14], the spar type platform has a better performance in general, but it requires a deep water depth. In contrast, the performance of the semi-submersible platform is promising because it only requires a relatively shallow water depth, which is suitable for the high

doi:10.6342/NTU202204241

wind power potential area in the Taiwan Strait where the water depth ranges from 50 m to 70 m. Moreover, the early researches on the performance of floating offshore wind turbine in the Taiwan Strait mainly focused on the NREL 5-MW [15] and the DTU 10-MW [16] wind turbines. The IEA 15-MW offshore wind turbine [17] is rarely employed in the related studies for the Taiwan Strait. Therefore, the performance of a wind turbine system equipped with an IEA 15-MW wind turbine under the metocean conditions of the Hsinchu offshore area which is one of the most potential sites in the Taiwan Strait, requires a further study.

A numerical framework for predicting the motion response and generator power of a floating wind turbine system under the metocean conditions of the Hsinchu offshore area is discussed in [12]. The potential component of hydrodynamic properties is predicted by Ansys Aqwa via a potential flow approach. The forced motion of the platform is simulated by STAR-CCM+ in order to obtain the hydrodynamic properties considering viscous effects. The aerodynamics and the dynamics of the mooring system are calculated by OrcaFlex via blade element momentum theory and finite element method. With all these results, the equations of motion are solved and the motion response and generator power of the wind turbine system are obtained. Based on the aforementioned framework, [13] successfully investigated the performance of a disk-type semi-submersible floating wind turbine system installed in the Taiwan Strait. The same framework is also adopted in this study.

doi:10.6342/NTU202204241

1.2 Motivation

To decrease the dependence on fossil fuel and pollution caused by the thermal power generation, the development of renewable energy has become one of the main global issues, among which wind energy is an industry growing rapidly. In April 2022, the Global Wind Energy Council (GWEC) reported that more than 93.6 GW of onshore and offshore wind energy capacity has been newly installed in 2021, and the total amount of global wind energy capacity has exceeded 837 GW, which is the second highest record over the years. Compared to onshore wind energy, the capacity of offshore wind energy is still low, but its growth rate is significantly higher. The global offshore wind energy capacity is expected to exceed 90 GW from 2022 to 2026. [18].

According to [19] that classifies the global wind energy potential into seven classes, the Taiwan Strait is found in the highest class, which indicates that the Taiwan Strait is one of the richest wind resources in the world. The average wind speed at 100 m above mean sea level (MSL) in the Taiwan Strait ranges between 9.32 m/s and 11.24 m/s, and the wind power density ranges between 1079 W/m^2 and 2665 W/m^2 [20]. Figure 1 and Figure 2 show the annual average wind speed and wind power density at 80 m above MSL around Taiwan [21]. Having an extraordinary wind power potential, the Taiwan Strait is a promising site for developing offshore wind energy.

doi:10.6342/NTU202204241

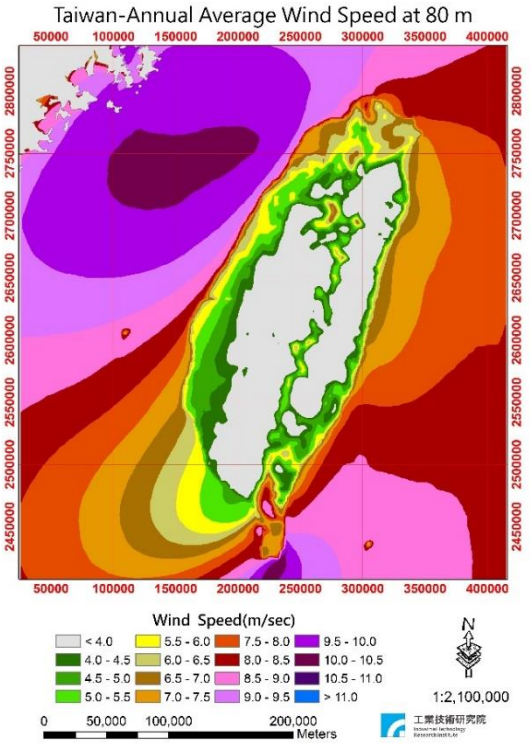

Figure 1 Taiwan annual average wind speed at 80 m above MSL [21]

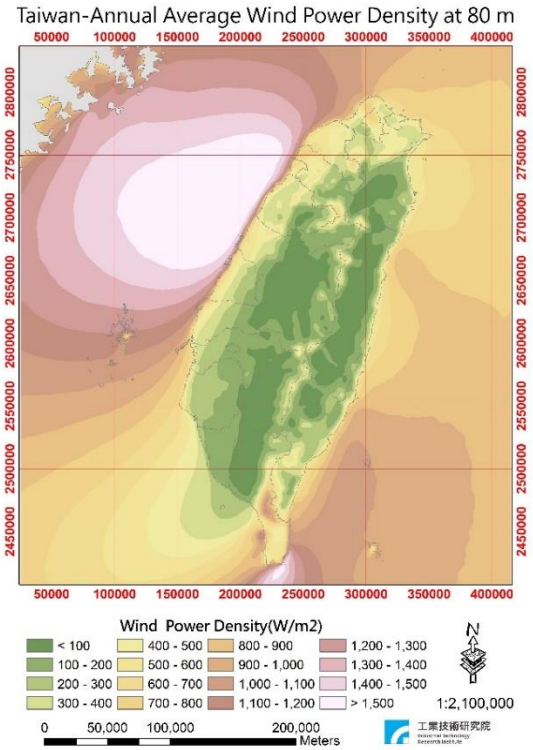

Figure 2 Taiwan annual average wind power density at 80 m above MSL [21]

doi:10.6342/NTU202204241

The government of Taiwan aims to install an offshore wind energy capacity of 20 GW by 2035 [22]. Despite a high wind power potential, there are still some limits for developing offshore wind energy in the Taiwan Strait. According to [21], the water depth of the offshore area around Taiwan is classified into shallow, deep, and deeper water, representing 5 m to 20 m, 20 m to 50 m, and greater than 50 m, respectively. As shown in Figure 3, the high wind potential area of the Taiwan Strait is mostly located in the deeper water area, which indicates that a bottom-fixed offshore wind turbine becomes a less favorable choice in the Taiwan Strait due to the high cost and technical difficulty for its installation and maintenance in deep waters [23]. A floating wind turbine is instead a relatively economical design in deep waters. Therefore, the research on the operating performance of floating offshore wind turbine becomes an important task to efficiently explore the offshore wind energy in the Taiwan Strait.

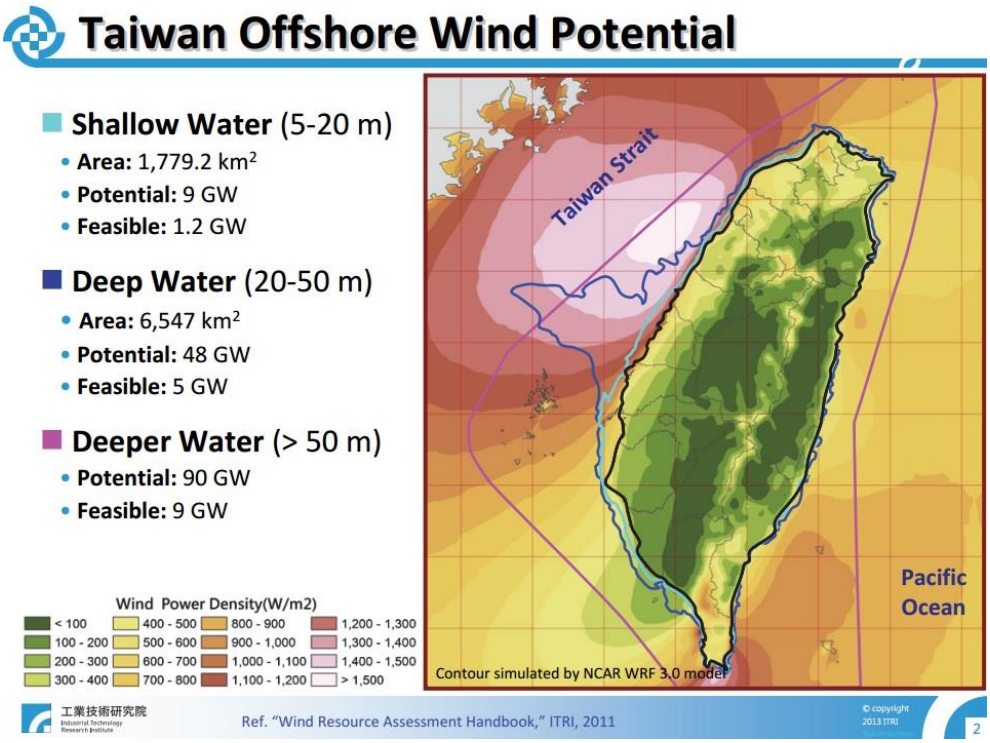

Figure 3 Taiwan offshore wind potential [21]

doi:10.6342/NTU202204241

To lower the cost and adapt the system to the metocean conditions in the Taiwan Strait, designing an indigenous floating offshore wind turbine is an essential task for Taiwan. TaidaFloat platform [24] is an original delta-shaped semi-submersible platform designed by a research team at National Taiwan University. This study aims to predict the motion response, generator power and mooring line tension of a 15 MW floating wind turbine system equipped with a TaidaFloat platform, an IEA 15-MW offshore wind turbine and a 3×2 mooring design under the metocean conditions in the Hsinchu offshore area in the Taiwan Strait. According to [25], the wind is most likely coming from the northeast with the probability of 40%, followed by north-northeast with the probability of 30% in the Taiwan Strait. This study also aims to find a recommended angle between the leading mooring line of the system and the dominant wind direction.

doi:10.6342/NTU202204241

2 Wind Turbine System Design

2.1 Floating Platform Design

The TaidaFloat platform which is designed to carry a 15 MW wind turbine, is considered as the target platform in this study. According to the design basis of a 15 MW wind turbine system mentioned in [24] and [26], the characteristic length of the TaidaFloat platform is limited by 85 m to fit in the drydock of a potential Taiwanese shipyard for production, the wind turbine system is limited by a pitch angle between -10° and 10°, as well as a mean pitch angle between -5° and 5° during the normal operation.

The TaidaFloat platform is a three-column delta-shaped semi-submersible floating platform with a characteristic length of 81.6 m, a height of 35 m and a draft of 20 m. The column under the turbine is 60% wider than the other two columns with the same size. The total displacement of the system is 23.683 kt. The specifications and dimensions of the TaidaFloat platform are shown in Table 1 and Figure 4, where the origin is located on the free surface.

Table 1 Specifications of the TaidaFloat platform

Draft (m)		20
Total System Displacement (kt)		23.683
CG (m)		(4.117, 0, -2.29)
Principal Inertias about CG (kg·m^2)	I_{xx}	4.932×10^{10}
	I_{yy}	5.335×10^{10}
	I_{zz}	2.834×10^{10}
	I_{xy}	-6.734×10^{5}
	I_{xz}	-9.954×10^{9}
	I_{yz}	-3.047×10^{6}

doi:10.6342/NTU202204241

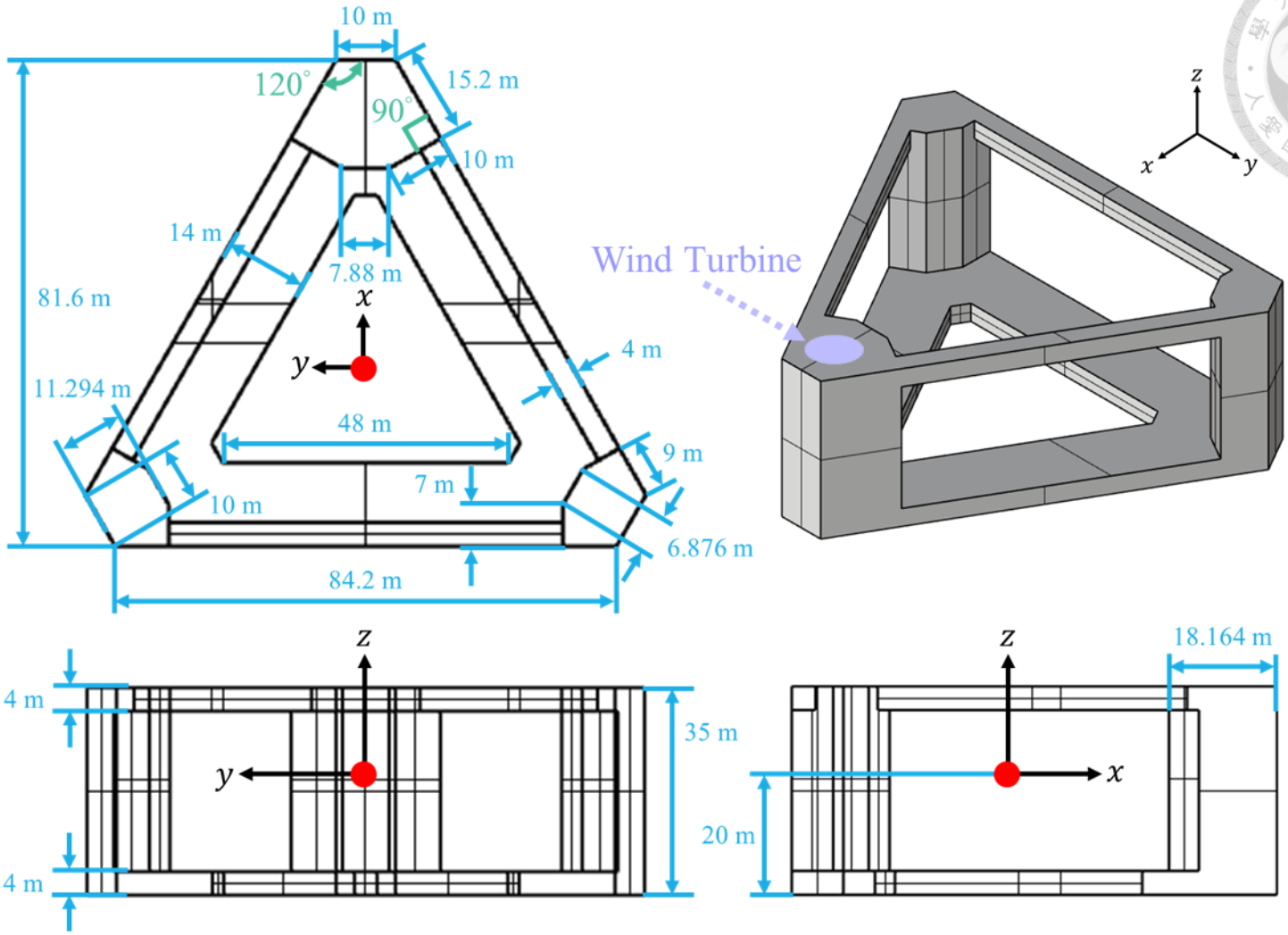

Figure 4 Dimensions of the TaidaFloat platform

doi:10.6342/NTU202204241

2.2 Mooring Design

A 3×2 mooring design is employed in this study. The mooring line is designed with the following limitations [27]: the allowable offset of the wind turbine system is 30% of the water depth, which is 21 m, to protect the dynamic cables, the anchor weight is preferably less than 16.329 t and the mooring chain is limited by a diameter of 16.51 cm.

Table 2 shows the specifications of the mooring lines. The TaidaFloat platform is equipped with two mooring lines on each column and the angle between these two mooring lines is 10°, as shown in Figure 5. The fairleads are 18 m below the free surface. The water depth is assumed to be 70 m. The length of a unstretched mooring line is 448 m. The break load of the mooring line is 14.96 MN.

Table 2 Specifications of the mooring lines

Number of Mooring Lines	3×2
Angle between Adjacent Lines (°)	10 / 119.8
Depth to Anchors below SWL (m)	70
Depth to Fairleads below SWL (m)	18
Radius Measured from the Centroid of the Platform to the Anchors (m)	484.3
Radius Measured from the Centroid of the Platform to the Fairleads (m)	47.1
Unstretched Mooring Line Length (m)	448
Mooring Line Diameter (m)	0.229
Mooring Nominal Diameter (m)	0.127
Mooring Line Mass Density (kg/m)	321
Mooring Line Break Load (MN)	14.96
Mooring Line Axial Stiffness (GN)	1.377

doi:10.6342/NTU202204241

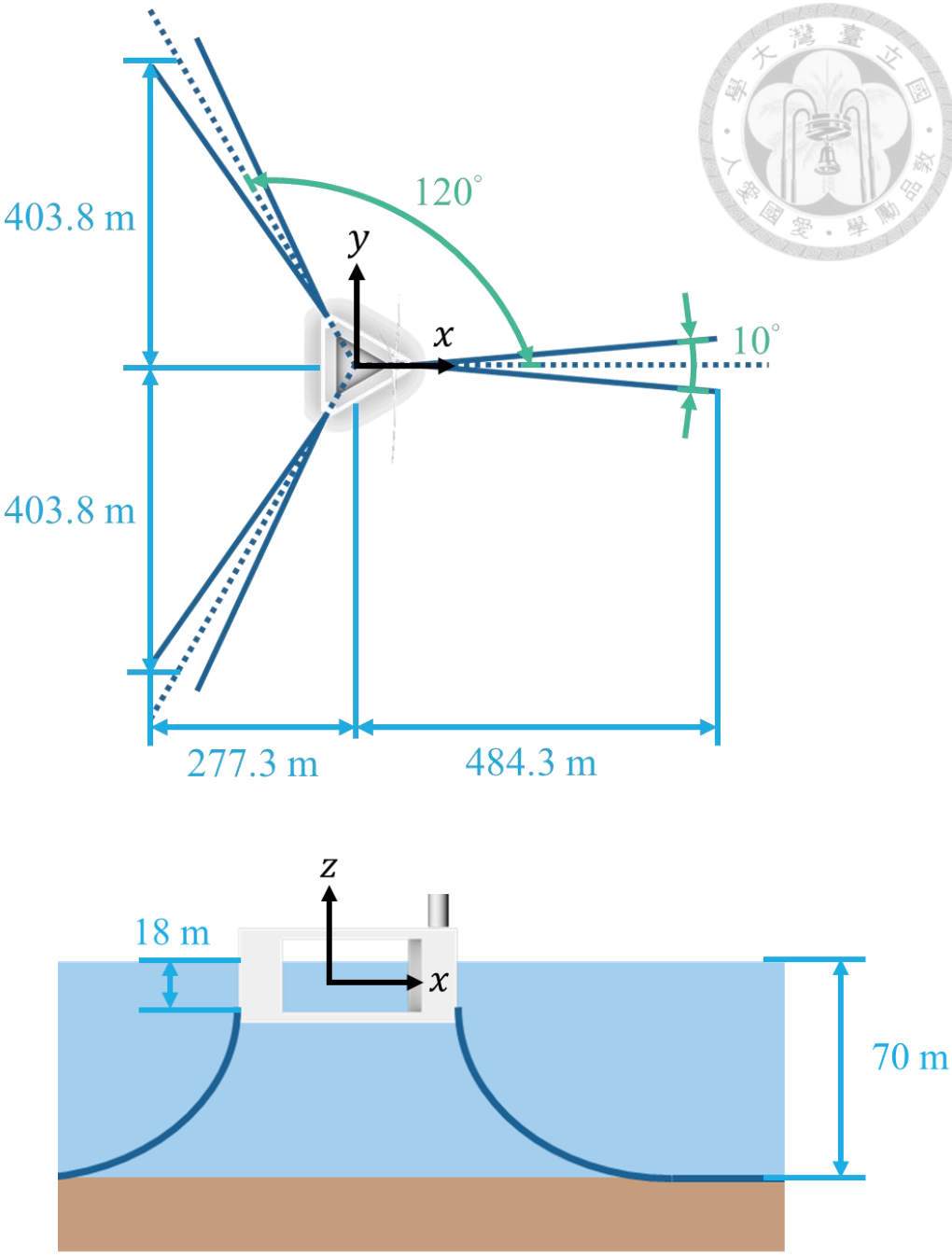

Figure 5 Mooring design of the wind turbine system

doi:10.6342/NTU202204241

2.3 Wind Turbine Design

An IEA 15-MW offshore wind turbine is employed in this study. The detailed design is given in [17],[28]. The specifications and dimensions of the IEA 15-MW wind turbine are shown in Table 3 and Figure 6. The cut-in, rated, and cut-out wind speed are 3 m/s, 10.59 m/s, and 25 m/s, respectively. The cut-in and rated rotor speed are 5 RPM and 7.56 RPM. The hub height and rotor diameter are 150 m and 240 m, respectively.

The DTU FFA-W3 airfoil series are used in the blade design of the IEA 15-MW offshore wind turbine. The shape of the airfoils and the blade are shown in Figure 7 and Figure 8. The aerodynamic data of the corresponding airfoils are shown in Figure 9. The definition of the blade geometry is described in Table 4. Figure 10 shows the dependence of the blade pitch angle β_b, generator power P_g, rotor speed Ω_r and rotor thrust force T_r on the wind speed at hub height U_w.

doi:10.6342/NTU202204241

Table 3 Specifications of the IEA 15-MW offshore wind turbine

Rated Power (MW)	15
Rotor Orientation	Upwind
Configuration	3 Blades
Blade Length (m)	120
Hub Height (m)	150
Hub / Rotor Diameter (m)	7.94 / 240
Tower Base Diameter (m)	10
Hub Overhang (m)	11.35
Cut-in / Rated / Cut-out Wind Speed (m/s)	3 / 10.59 / 25
Cut-in / Rated Rotor Speed (RPM)	5 / 7.56
Shaft Tilt / Pre-Cone Angle (°)	6 / 4
Rotor Nacelle Assembly Mass (t)	1016.6
Tower Mass (t)	860

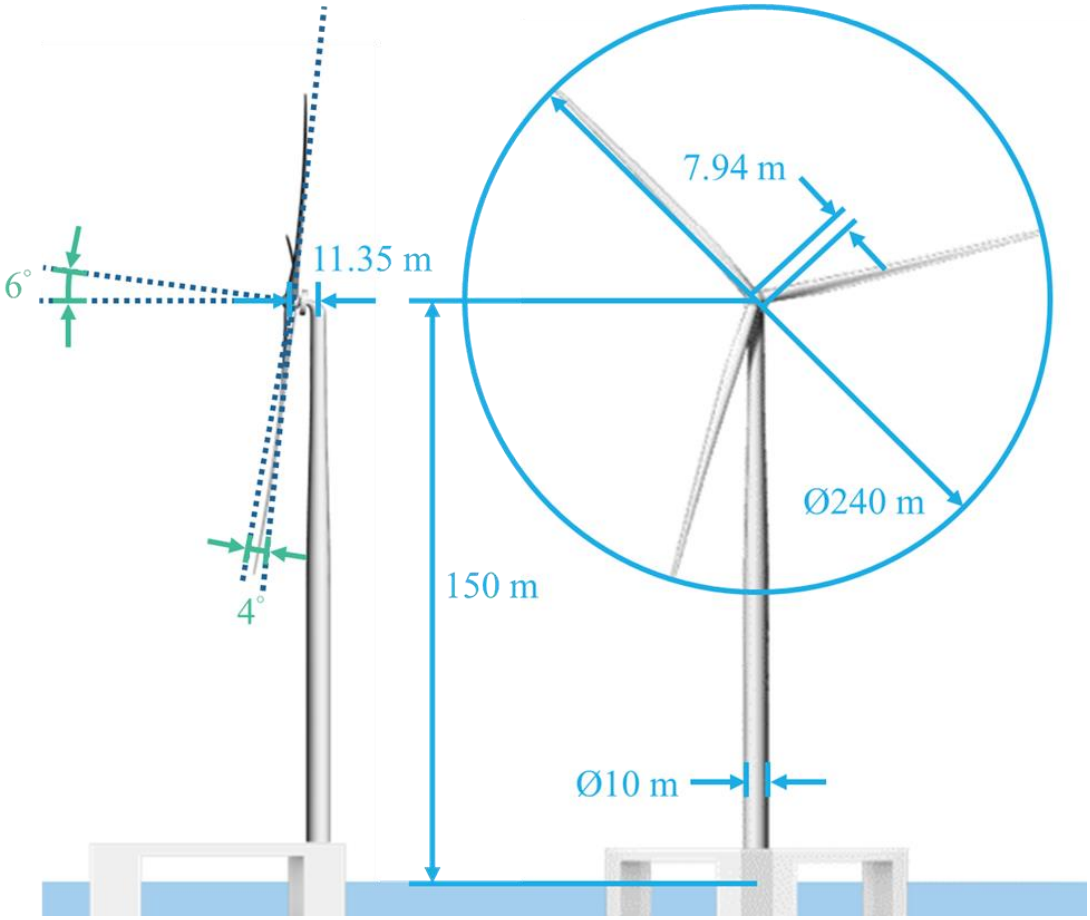

Figure 6 Dimensions of the IEA 15-MW offshore wind turbine

doi:10.6342/NTU202204241

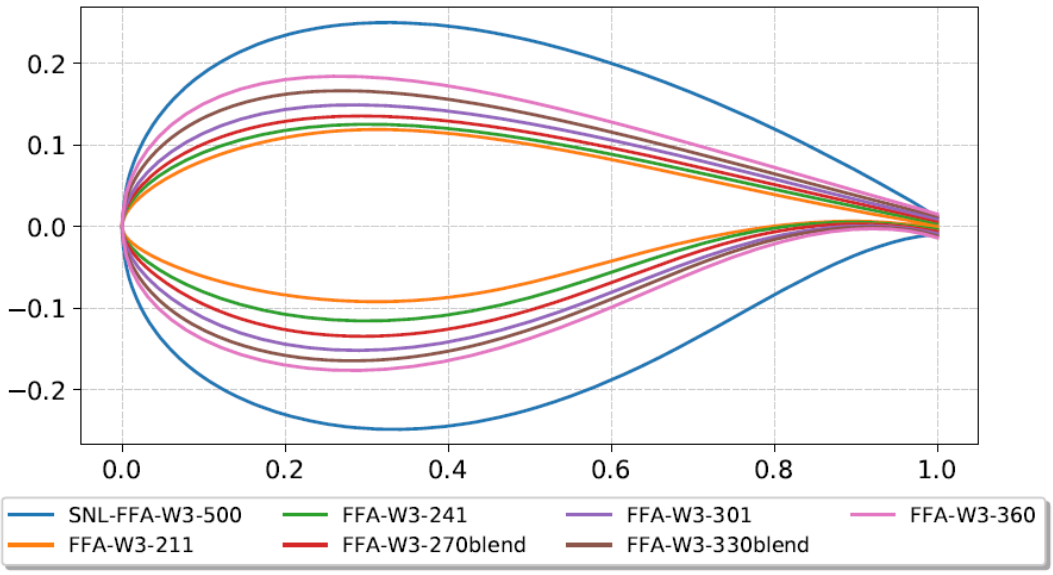

Figure 7 The DTU FFA-W3 airfoils used in the IEA 15-MW blade design [17]

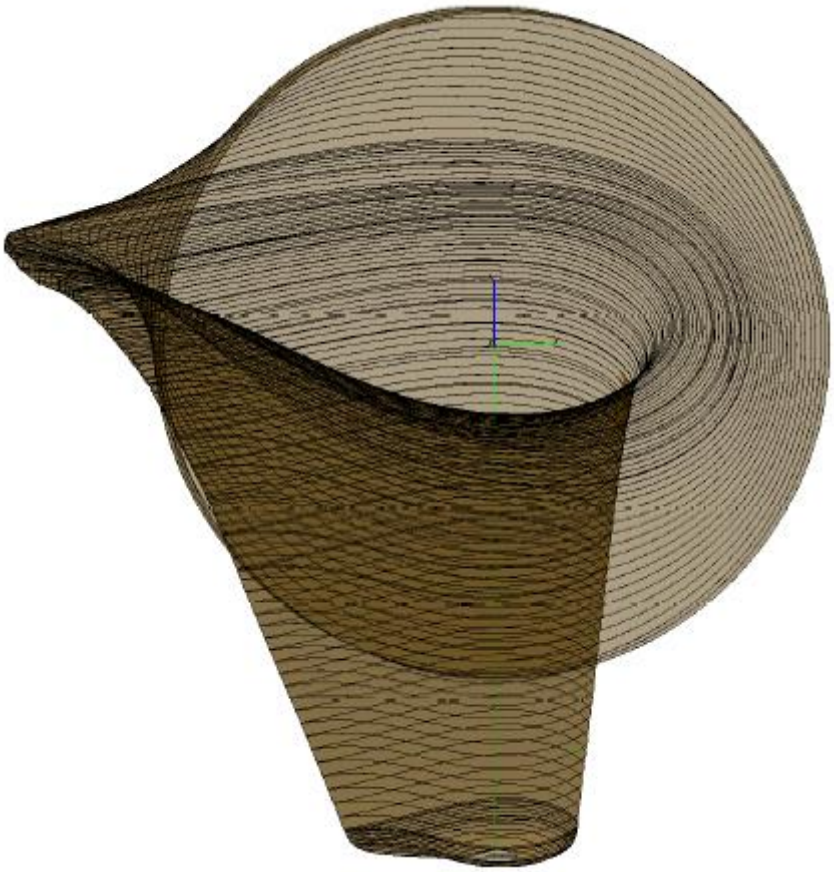

Figure 8 Lofted blade shape of the IEA 15-MW offshore wind turbine [17]

doi:10.6342/NTU202204241

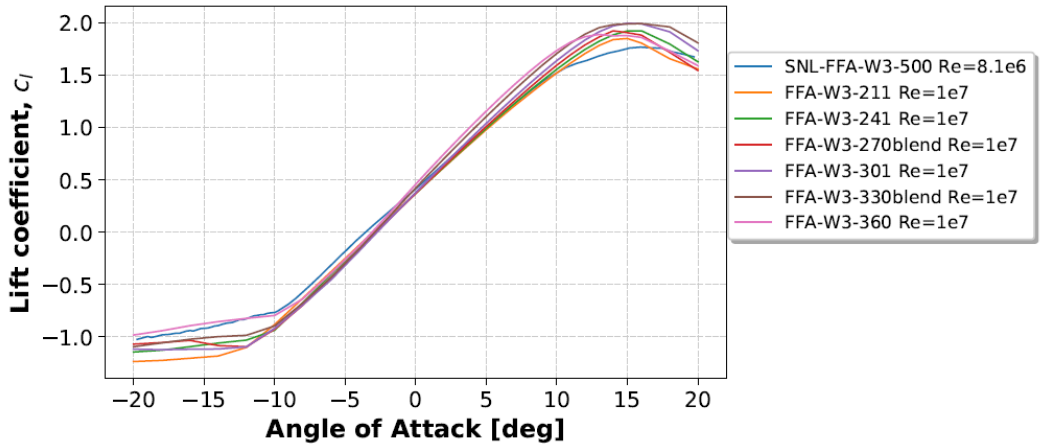

(a)

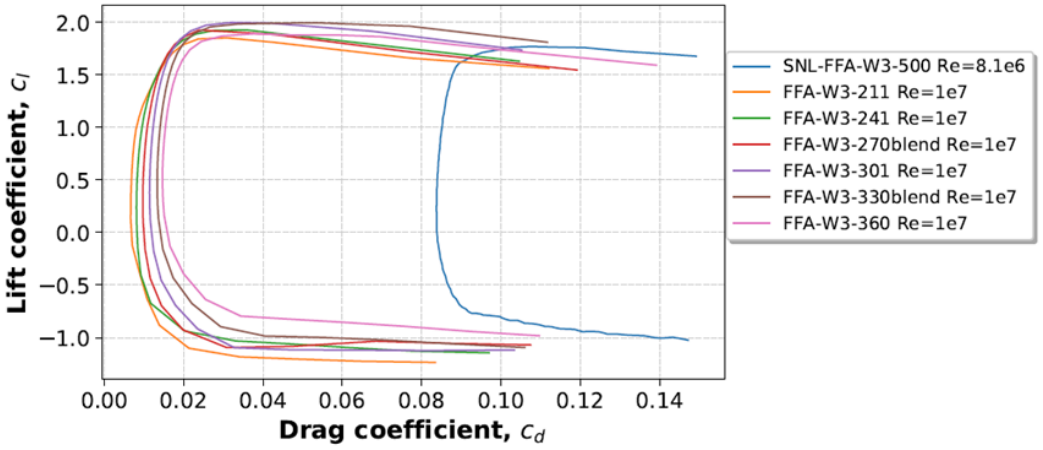

(b)

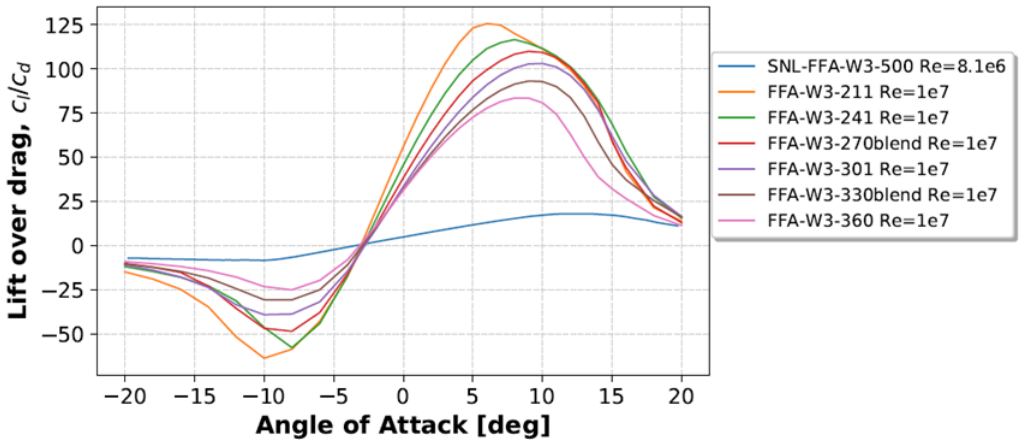

(c)

Figure 9 Aerodynamic data of the DTU FFA-W3 airfoils [17]: (a) Airfoil lift coefficients, (b) Airfoil lift-drag polars, (c) Airfoil lift-to-drag coefficients

doi:10.6342/NTU202204241

Table 4 Blade geometry definition of the IEA 15-MW offshore wind turbine [28]

Blade Fraction	Chord (m)	Twist (°)	Twist Axis Fraction	Airfoil Description
0.000	5.200	7.787	0.505	Circular
0.041	5.238	7.695	0.473	Transition
0.082	5.367	7.119	0.435	Transition
0.122	5.540	6.203	0.398	Transition
0.163	5.693	5.178	0.365	SNL-FFA-W3-500
0.204	5.765	4.270	0.340	SNL-FFA-W3-500
0.245	5.703	3.591	0.324	FFA-W3-360
0.286	5.472	2.963	0.315	FFA-W3-360
0.327	5.166	2.395	0.309	FFA-W3-330 Blend
0.367	4.886	1.921	0.304	FFA-W3-330 Blend
0.408	4.655	1.536	0.299	FFA-W3-330 Blend
0.449	4.428	1.204	0.294	FFA-W3-301
0.490	4.208	0.913	0.290	FFA-W3-301
0.531	3.999	0.650	0.288	FFA-W3-270 Blend
0.571	3.803	0.421	0.288	FFA-W3-270 Blend
0.612	3.617	0.218	0.290	FFA-W3-270 Blend
0.653	3.434	0.020	0.293	FFA-W3-241
0.694	3.249	-0.203	0.298	FFA-W3-241
0.735	3.065	-0.499	0.304	FFA-W3-241
0.776	2.881	-0.811	0.310	FFA-W3-211
0.816	2.691	-1.042	0.316	FFA-W3-211
0.857	2.489	-1.086	0.325	FFA-W3-211
0.898	2.276	-1.050	0.335	FFA-W3-211
0.939	2.053	-0.947	0.346	FFA-W3-211
0.980	1.820	-0.753	0.360	FFA-W3-211
0.990	1.708	-0.689	0.364	FFA-W3-211
1.000	0.500	-0.620	0.368	FFA-W3-211

doi:10.6342/NTU202204241

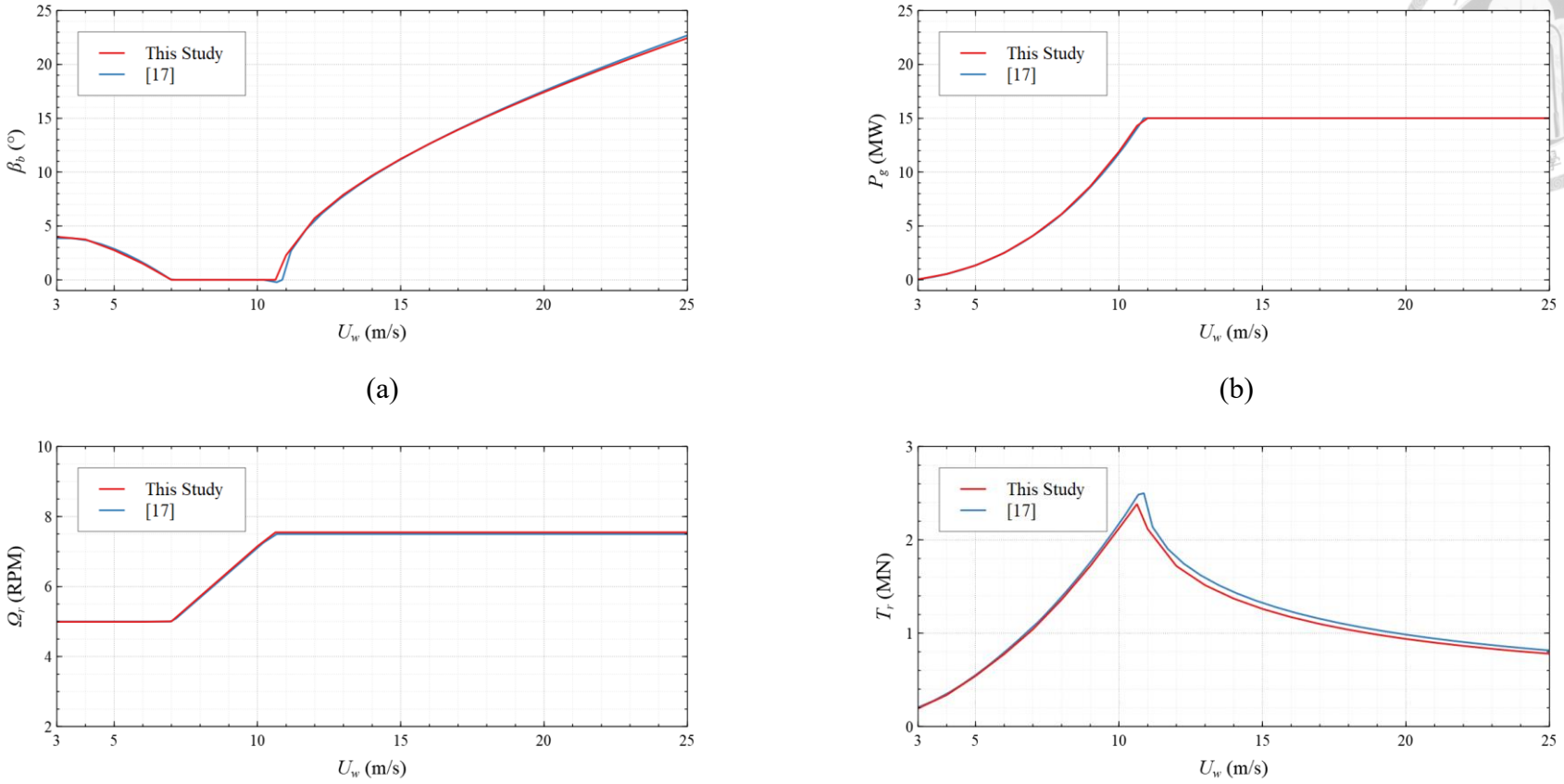

Figure 10 Comparison of wind turbine performance between this study and [17]: (a) Blade pitch angle, (b) Generator power, (c) Rotor speed, (d) Rotor thrust force

doi:10.6342/NTU202204241

3 Numerical Methods

3.1 Numerical Framework

To predict the motion response and generator power of a floating wind turbine system, the equations of motion with coupled effects are solved in OrcaFlex. The equations of motion of a floating body are given as follows:

$$\sum_{j=1}^{6}\left(M_{ij}+A_{ij}\right)\ddot{x}_j+B_{ij}\dot{x}_j+C_{ij}x_j=F_{e,i}+F_{o,i}, \tag{1}$$

where M_{ij} is the body mass, A_{ij} is the added mass, B_{ij} is the damping, C_{ij} is the stiffness of the floating body, x_j is the displacement, $\dot{x}_j$ is the velocity, and $\ddot{x}_j$ is the acceleration. On the right-hand side of the equations, $F_{e,i}$ is the wave exciting force and $F_{o,i}$ is the force other than fluid force, such as aerodynamic loading and mooring tension. The subscripts $i,j=1,2,\dots,6$ refer to the surge, sway, heave, roll, pitch, and yaw motions, respectively. A_{ij}, B_{ij}, C_{ij}, and $F_{e,i}$ come from the result of Ansys Aqwa, as well as the prediction of hydrodynamic properties. The wave drift force, which is a kind of second order force, is considered while the motion response is solved in the time domain. $F_{o,i}$ is obtained from other force models in OrcaFlex. The hydrodynamic properties, i.e., A_{ij} and B_{ij}, consist of potential and viscous components. The hydrodynamic properties obtained from Aqwa are predicted via a potential flow approach, i.e. the potential components. Therefore, a viscous flow modeling in STAR-CCM+ and a prediction of hydrodynamic properties are necessary for predicting A_{ij} and B_{ij}. The predicted viscous components are used in Aqwa to obtain the response amplitude operators considering viscous effect.

doi:10.6342/NTU202204241

The fluid force is divided into hydrostatic force and hydrodynamic force. The wave exciting force $F_{e,i}$, and radiation force composed of added inertia force $A_{ij}\ddot{x}_j$ and radiation damping force $B_{ij}\dot{x}_j$ are kinds of hydrodynamic force, while the restoring force $C_{ij}x_j$ is a kind of hydrostatic force. The wave exciting force is a combination of the Froude-Krylov force and diffraction force, which is provided by incoming waves under the condition that the floating body is stationary, while the radiation force is caused by the forced motion of the floating body without considering incoming waves. The Froude-Krylov force on the floating body is introduced by the unsteady pressure field generated by undisturbed waves, while the diffraction force is due to the disturbance of the floating body to the incoming waves.

Figure 11 shows the numerical framework for predicting the motion response and generator power of a floating wind turbine system. The numerical details of Ansys Aqwa, STAR-CCM+, and OrcaFlex are elaborated in the following sections.

doi:10.6342/NTU202204241

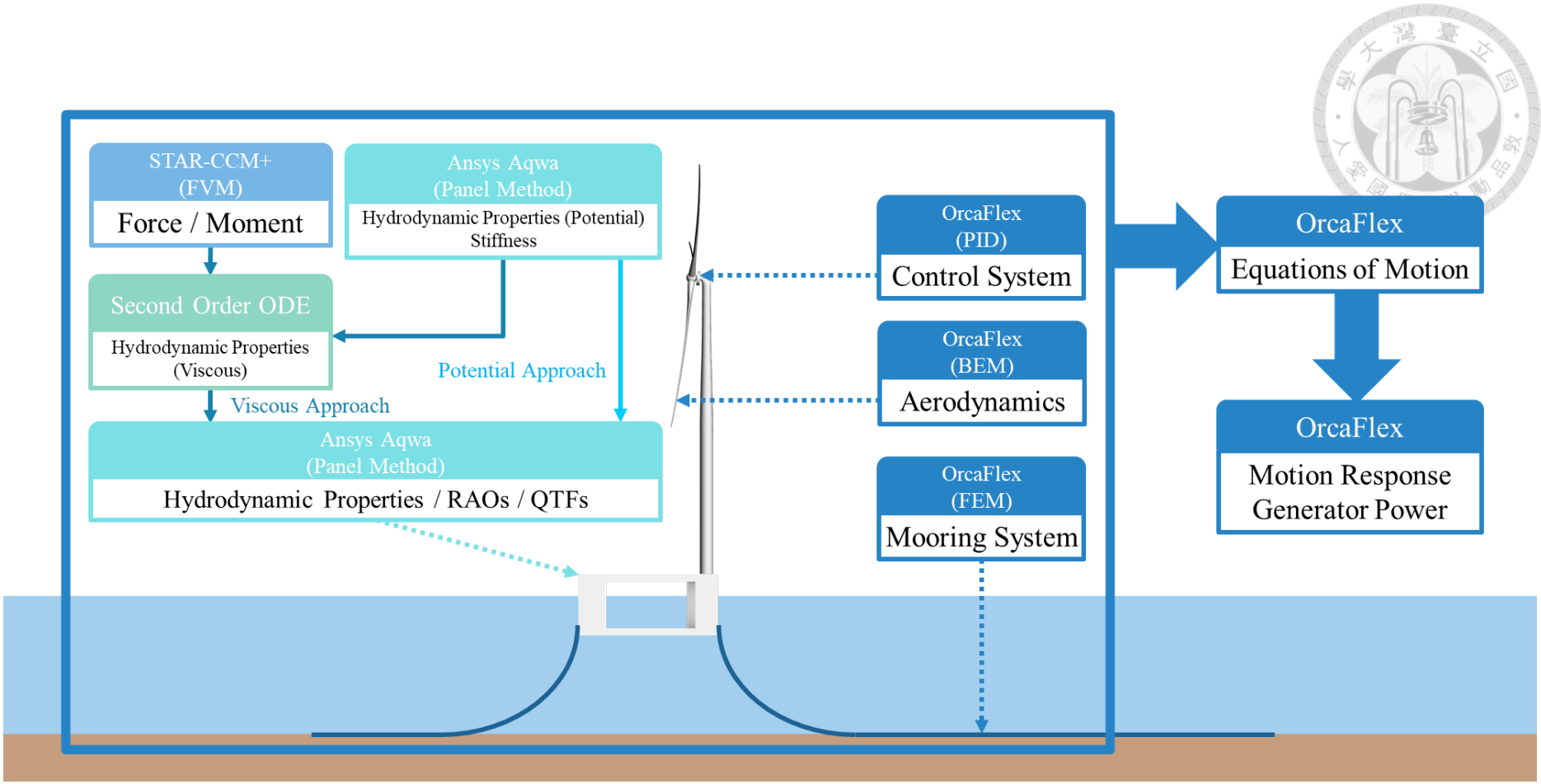

Figure 11 Numerical framework for floating wind turbine performance prediction

doi:10.6342/NTU202204241

3.2 Potential Flow Modeling of Floating Body

Under the assumption of linear small-amplitude waves, the potential components of hydrodynamic properties of a floating body are predicted in Ansys Aqwa via the panel method which is based on the three-dimensional potential flow theory. The flow field is assumed to be inviscid, irrotational and incompressible in potential flow. The coordinate system for the potential flow formulation is shown in Figure 12.

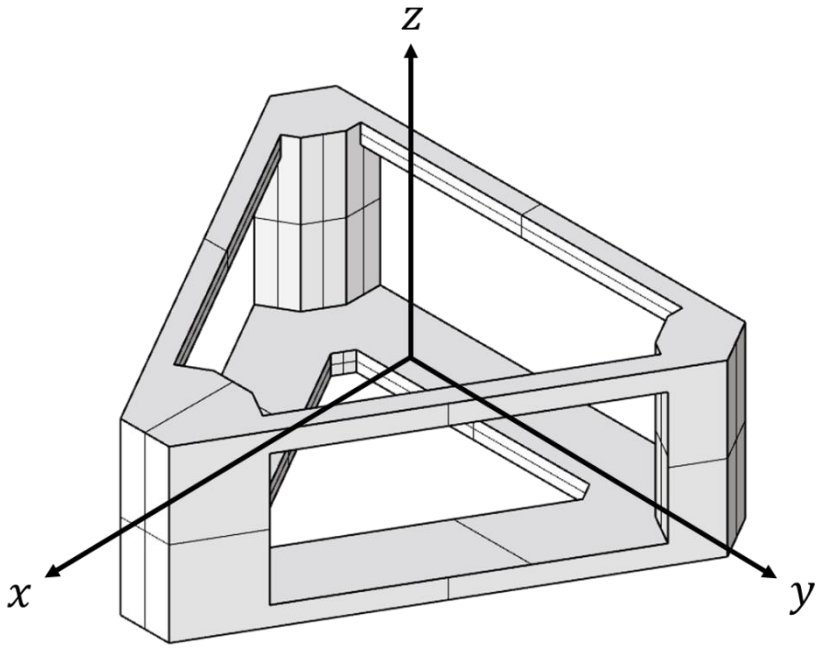

Figure 12 Coordinate system for the potential flow formulation

The velocity potential $\boldsymbol{\Phi}(x, y, z, t)$ in the flow field is expressed as

$$\boldsymbol{\Phi}(x, y, z, t) = \Phi(x, y, z)e^{-i\omega_a t}, \tag{2}$$

where $\Phi(x, y, z)$ is the amplitude of velocity potential, ω_a is the angular frequency of wave, and t is the time. According to Haskind's theory [29],[30], when the amplitude of the incident wave and the motion of the floating body are very small, the velocity potential is expressed as

doi:10.6342/NTU202204241

$$\Phi(x,y,z) = \Phi_i(x,y,z) + \Phi_d(x,y,z) + \sum_{j=1}^{6} x_j \Phi_j\,(x,y,z), \tag{3}$$

where $\Phi_i(x,y,z)$ is the incident wave velocity potential, $\Phi_d(x,y,z)$ is the diffraction wave velocity potential, $\Phi_j(x,y,z)$ is the radiation velocity potential, and x_j is the motion amplitude of a floating body. The subscripts $i,j = 1,2,\ldots,6$ refer to the surge, sway, heave, roll, pitch, and yaw motions, respectively.

Assuming that the angle between the incident wave and the x-axis is α_w, and the incident wave frequency is ω_0, Φ_i is expressed as

$$\Phi_i = \frac{-igA_w}{\omega_0}\frac{\cosh k_0(y-h)}{\cosh k_0 h} e^{i(k_0 x\cos\alpha_w + k_0 y \sin\alpha_w)}, \tag{4}$$

$$k_0 = \frac{{\omega_0}^2}{g}, \tag{5}$$

where g is the gravitational acceleration, A_w is the amplitude of the incident wave, and k_0 is the wave number of the incident wave. The floating body is assumed to have no forward speed in this study, and therefore the $\omega_a = \omega_0$. Under the assumption of potential flow theory, the velocity potential must satisfy the Laplace equation

$$\nabla^2 \boldsymbol{\Phi}(x,y,z,t) = 0. \tag{6}$$

With the wave number denoted by $k_w = \frac{{\omega_a}^2}{g}$ and the radius of the flow field by R_w, the boundary conditions of far field for Φ_d and Φ_j are

$$\lim_{R_w\to\infty} {R_w}^{\frac{1}{2}}\left(\frac{\partial}{\partial R_w} - ik_w\right)\Phi_d = 0, \tag{7}$$

$$\lim_{R_w\to\infty} {R_w}^{\frac{1}{2}}\left(\frac{\partial}{\partial R_w} - ik_w\right)\Phi_j = 0. \tag{8}$$

The boundary condition at the bottom of the flow field is

$$\frac{\partial \Phi}{\partial z} = 0 \text{ at } z \to -h, \tag{9}$$

where h is the water depth. The boundary conditions on the free surface are

doi:10.6342/NTU202204241

$$(i\omega_a)^2\Phi_i + g\frac{\partial}{\partial z}\Phi_i = 0 \text{ at } z = 0, \tag{10}$$

$$(i\omega_a)^2\Phi_d + g\frac{\partial}{\partial z}\Phi_d = 0 \text{ at } z = 0, \tag{11}$$

$$(i\omega_a)^2\Phi_j + g\frac{\partial}{\partial z}\Phi_j = 0 \text{ at } z = 0. \tag{12}$$

The boundary conditions on the surface of the floating body are

$$\frac{\partial}{\partial \mathbf{n}}(\Phi_i + \Phi_d) = 0, \tag{13}$$

$$\frac{\partial}{\partial \mathbf{n}}\Phi_j = -i\omega_a \mathbf{n}_j, \tag{14}$$

where $\mathbf{n}$ is the normal vector on the body surface. Source distribution method is used to solve the equations of boundary conditions above in this study. According to Wehausen and Laitone [31], the three-dimensional Green's function $G(p,q)$ is expressed as

$$G(p,q) = -\frac{1}{4\pi}\left(\frac{1}{r_1} + \frac{1}{r_2}\right) - \frac{k_w}{2\pi}\lim_{\mu_0 \to 0}\int_0^\infty \frac{e^{-l(z_1+z_2)}J_o(lr_3)}{l-(k-i\mu_0)}dl\,, \tag{15}$$

$$p = (x_1, y_1, z_1), \tag{16}$$

$$q = (x_2, y_2, z_2), \tag{17}$$

$$r_1 = \sqrt{(x_1-x_2)^2 + (y_1-y_2)^2 + (z_1-z_2)^2}, \tag{18}$$

$$r_2 = \sqrt{(x_1-x_2)^2 + (y_1-y_2)^2 + (z_1+z_2)^2}, \tag{19}$$

$$r_3 = \sqrt{(x_1-x_2)^2 + (y_1-y_2)^2}, \tag{20}$$

where μ_0 is the integral constant and $J_o(x)$ is the Bessel function of the first kind. Therefore, the velocity potential at any point p is expressed as

$$\Phi_d(p) = \iint_S \sigma_d(q)G(p,q)dS\,, \tag{21}$$

doi:10.6342/NTU202204241

$$\Phi_j(p) = \iint_S \sigma_j(q) G(p,q) dS\,, \tag{22}$$

where σ_d is the diffraction strength of the source point, σ_j is the radiation strength of the source point, and S is the immersed area of the floating body. Then by applying the boundary conditions, velocity potential is obtained as

$$-\frac{\partial \Phi_i(p)}{\partial \mathbf{n}_p} = 2\pi\sigma_d(p) + \iint_S \sigma_d(q) G(p,q) dS\,, \tag{23}$$

$$-\mathrm{i}\omega_a \mathbf{n}_j = 2\pi\sigma_j(p) + \iint_S \sigma_j(q) G(p,q) dS\,. \tag{24}$$

After the velocity potential is obtained, the dynamic pressure on the surface of the floating body is derived through the Bernoulli Equation:

$$P_d(x,y,z,t) = -\rho \frac{\partial \mathbf{\Phi}(x,y,z,t)}{\partial t} - \frac{1}{2}\rho[\nabla \mathbf{\Phi}(x,y,z,t)]^2 - \rho g z, \tag{25}$$

where ρ is the fluid density. When the higher order terms and time independent terms are ignored, P_d is expressed as

$$\begin{aligned} P_d(x,y,z,t) = i\omega_a \rho \Bigg[& \Phi_i(x,y,z) e^{-i\omega_a t} + \Phi_d(x,y,z) e^{-i\omega_a t} \\ & + \sum_{j=1}^{6} x_j \Phi_j(x,y,z) e^{-i\omega_a t} \Bigg]. \end{aligned} \tag{26}$$

The first, second, and third terms on the right-hand side of the equation are defined as $p_i(x,y,z)$, $p_d(x,y,z)$ and $p_r(x,y,z)$. Through the integration of $p_i(x,y,z)$ and $p_d(x,y,z)$ along the immersed surface of the floating body, the wave exciting force F_i is obtained, and through the integration of $p_r(x,y,z)$, the radiation force F_r, as well as the added mass and damping are obtained, as shown below.

doi:10.6342/NTU202204241

$$F_i = \rho \iint_S i\omega_a \left[\Phi_i(x,y,z)e^{-i\omega_a t} + \Phi_d(x,y,z)e^{-i\omega_a t}\right]\mathbf{n}_i(x,y,z)dS, \quad (27)$$

$$\begin{aligned} F_r &= \iint_S \sum_{j=1}^{6} i\omega_a x_j \Phi_j(x,y,z)\, e^{-i\omega_a t}\mathbf{n}_i(x,y,z)dS \\ &= \sum_{j=1}^{6} A_{ij}x_j'' + B_{ij}x_j'. \end{aligned} \quad (28)$$

After the imposing of the quadratic transfer function (QTF) to a number of wave components, the second order wave drift force is expressed as

$$F_d = \sum_{i=1}^{n}\sum_{j=1}^{n} \mathrm{Re}\left[Q_d(B_{w,i}, B_{w,j}, T_i, T_j)D_i D_j e^{i(\omega_i-\omega_j)t-(\varphi_i-\varphi_j)}\right], \quad (29)$$

$$Q_d\left(B_{w,1}, B_{w,2}, T_1, T_2\right) = D\left(B_{w,1}, B_{w,2}, T_1, T_2\right)e^{-i\varphi(B_{w,1},B_{w,2},T_1,T_2)}. \quad (30)$$

where Q_d is the wave drift QTF, B_w is the wave direction, T is the wave period, D is the wave drift amplitude, and φ is the phase lag.

doi:10.6342/NTU202204241

3.3 Viscous Flow Modeling of Floating Body

3.3.1 Governing Equations

To obtain the hydrodynamic properties with viscous effects, the load response of the floating body is required and hence a forced motion simulation of the platform under a specific frequency is carried out in STAR-CCM+ [32]. The coordinate system for the viscous flow formulation is shown in Figure 13.

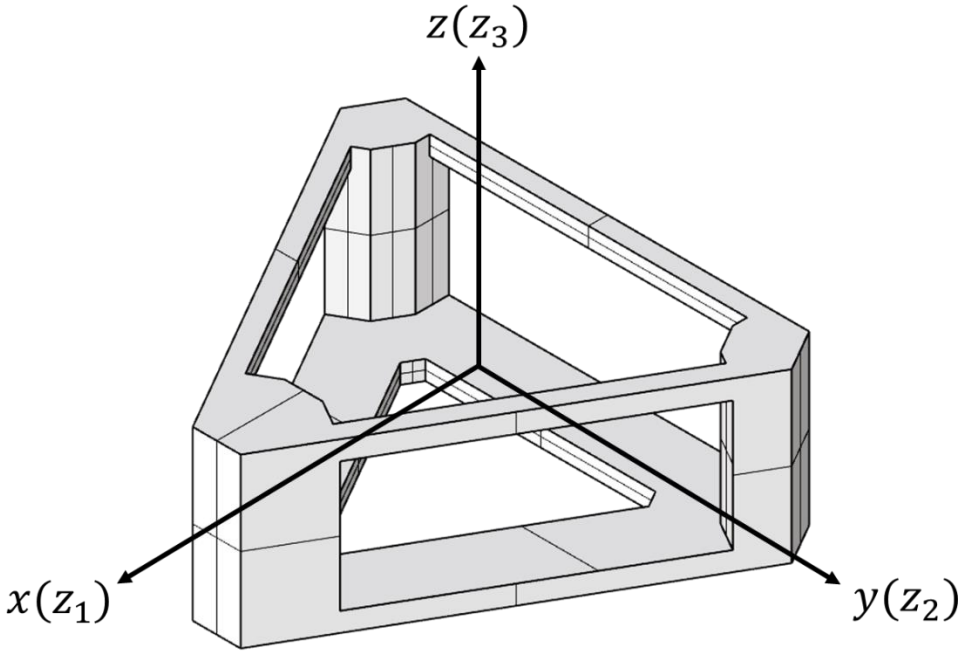

Figure 13 Coordinate system for the viscous flow formulation

Under the assumption of an incompressible fluid, the time-averaged continuity equation is expressed as

$$\frac{\partial \bar{u}_i}{\partial z_i} = 0, \tag{31}$$

where $\bar{u}_i$ is the mean velocity component in the z_i-direction, and momentum equations are expressed as

doi:10.6342/NTU202204241

$$\frac{\partial \rho \bar{u}_i}{\partial t} + \frac{\partial (\rho \bar{u}_i \bar{u}_j)}{\partial z_j} = -\frac{\partial \bar{p}}{\partial z_i} + \frac{\partial}{\partial z_j}\left[\mu\left(\frac{\partial \bar{u}_i}{\partial z_j} + \frac{\partial \bar{u}_j}{\partial z_i}\right)\right] - \frac{\partial \rho \overline{u_i' u_j'}}{\partial z_j} + \rho g_i, \quad (32)$$

where $\bar{p}$ is the mean pressure of the fluid, μ is the viscosity of the fluid, u_i' is the turbulent velocity component in the z_i-direction, and g_i is the gravity component in the z_i-direction. The subscripts $i = 1,2,3$ refers to the x-, y- and z-direction. $-\rho\overline{u_i' u_j'}$ in Equation (32) is the Reynolds stress. According to the Boussinesq eddy viscosity assumption [33], the Reynolds stress is proportional to the mean strain rate tensor, and the proportional constant is the eddy viscosity μ_t, which is calculated by SST k–ω model [32] in this study and defined as

$$\mu_t = \min\left\{\frac{\rho k}{\max(\frac{\omega}{\alpha^*}, \frac{|\mathbf{S}|F_2}{a_1})}, \frac{\rho k C_T}{\sqrt{3|\mathbf{S}|}}\right\}, \quad (33)$$

where k is the turbulent kinetic energy, ω is the specific dissipation rate, $\bar{\mathbf{v}}$ is the mean velocity, and $\mathbf{S}$ is the mean strain rate tensor defined as

$$\mathbf{S} = \frac{1}{2}(\nabla \bar{\mathbf{v}} + \nabla \bar{\mathbf{v}}^{\mathrm{T}}). \quad (34)$$

The other key model constants and functions used in are listed in Table 5, where d is the distance to the wall, ν is the kinematic viscosity, and $CD_{k\omega}$ is the cross-diffusion coefficient. The turbulent kinetic energy equation and the specific dissipation rate equation are shown below:

$$\frac{\partial (\rho k)}{\partial t} + \frac{\partial (\rho \bar{u}_j k)}{\partial z_j} = \tau_{ij}\frac{\partial \bar{u}_i}{\partial z_j} - \beta^* \rho \omega k + \frac{\partial}{\partial z_j}\left[(\mu + \sigma_k \mu_t)\frac{\partial k}{\partial z_j}\right], \quad (35)$$

$$\frac{\partial (\rho \omega)}{\partial t} + \frac{\partial (\rho \bar{u}_j \omega)}{\partial z_j} = \frac{\rho \gamma}{\mu_t}\tau_{ij}\frac{\partial \bar{u}_i}{\partial z_j} - \beta \rho \omega^2 + \frac{\partial}{\partial z_j}\left[(\mu + \sigma_\omega \mu_t)\frac{\partial \omega}{\partial z_j}\right] + 2(1 - F_1)\frac{\rho \sigma_{\omega 2}}{\omega}\frac{\partial k}{\partial z_j}\frac{\partial \omega}{\partial z_j}, \quad (36)$$

where τ_{ij} is the shear stress.

doi:10.6342/NTU202204241

The SST $k-\omega$ model is a combination of the standard $k-\omega$ models and the standard $k-\varepsilon$ models. The blending function F_1 combines the coefficients of the $k-\omega$ equation in the boundary layer and the coefficients of the $k-\varepsilon$ equation in the free shear layer and the free flow domain, where F_1 equals unity on a no-slip wall, approaches unity in the boundary layer, and equals zero at the margin of the boundary layer.

Table 5 Model constants used in the SST $k-\omega$ model [32]

a_1	0.31	β^*	$F_1\beta_1^* + (1-F_1)\beta_2^*$
$CD_{k\omega}$	$\max\left(\frac{1}{\omega}\nabla k \cdot \nabla\omega, 10^{-20}\right)$	β_1^*	0.09
C_T	0.6	β_2^*	0.09
F_1	$\tanh({f_1}^4)$	γ	$F_1\gamma_1 + (1-F_1)\gamma_2$
f_1	$\min\left[\max\left(\frac{\sqrt{k}}{0.09\omega d}, \frac{500\nu}{d^2\omega}\right), \frac{2k}{d^2 CD_{k\omega}}\right]$	γ_1	$\frac{\beta_1}{\beta^*} - \sigma_{\omega_1}\frac{\kappa^2}{\sqrt{\beta^*}}$
F_2	$\tanh({f_2}^2)$	γ_2	$\frac{\beta_2}{\beta^*} - \sigma_{\omega_2}\frac{\kappa^2}{\sqrt{\beta^*}}$
f_2	$\max\left(\frac{2\sqrt{k}}{\beta^*\omega d}, \frac{500\nu}{d^2\omega}\right)$	κ	0.41
α^*	$F_1\alpha_1^* + (1-F_1)\alpha_2^*$	σ_k	$F_1\sigma_{k_1} + (1-F_1)\sigma_{k_2}$
α_1^*	1	σ_{k_1}	0.85
α_2^*	1	σ_{k_2}	1
β	$F_1\beta_1 + (1-F_1)\beta_2$	σ_ω	$F_1\sigma_{\omega_1} + (1-F_1)\sigma_{\omega_2}$
β_1	0.075	σ_{ω_1}	0.5
β_2	0.0828	σ_{ω_2}	0.856

The employed volume of fluid (VOF) method [34] is used for the simulation of free surface flow. When multiple fluids are present in a cell, the volume fraction of the i-th fluid is expressed as

$$\alpha_i = \frac{V_i}{V}, \tag{37}$$

doi:10.6342/NTU202204241

where V_i is the volume of the i-th fluid in a cell, and V is the cell volume. Therefore, the volume fraction of all the fluids in each cell must satisfy the following formula:

$$\sum_{i=1}^{N} \alpha_i = 1, \tag{38}$$

where N is the number of the fluids. When $\alpha_i = 0$, it means that there is no i-th fluid present in the cell. When $\alpha_i = 1$, it means that there is only the i-th fluid present in the cell. When $0 < \alpha_i < 1$, it means that there are other fluids in addition to the i-th fluid present in the cell, and there is a free surface in the cell. As a result, the density ρ and viscosity μ in a cell are the weighted averages of such fluid properties in a cell.

$$\rho = \sum_{i=1}^{N} \rho_i \alpha_i , \tag{39}$$

$$\mu = \sum_{i=1}^{N} \mu_i \alpha_i , \tag{40}$$

where ρ_i and μ_i are the density and viscosity of the i-th fluid. The continuity equation of the i-th fluid is formulated as

$$\frac{\partial \alpha_i}{\partial t} + u_k \frac{\partial \alpha_i}{\partial z_k} + \nabla \cdot (\alpha_i \mathbf{v}_{d,i}) + \nabla \cdot [\alpha_i (1 - \alpha_i) \mathbf{v}_{c,i}] = 0, \tag{41}$$

where $\mathbf{v}_{d,i}$ is the diffusion velocity of the i-th fluid and $\mathbf{v}_{c,i}$ is the boundary sharpening velocity of the i-th fluid, which is defined as

$$\mathbf{v}_{c,i} = C_\alpha |\mathbf{v}| \frac{\nabla \alpha_i}{|\nabla \alpha_i|}, \tag{42}$$

where C_α is the sharpening factor, and $\mathbf{v}$ is the flow field velocity. Based on the normalized variable diagram, the normalized volume fraction value at the cell interface between the central cell and the downwind cell ξ_f is defined in Equation (43) and Figure 14 [13], where $\mathbf{a}$ is the area vector of the cell interface and $\mathbf{n}$ is the normal vector of the fluid interface.

doi:10.6342/NTU202204241

$$\xi_f = \begin{cases} \xi_c & \text{for} \quad \xi_C \notin [0,1] \\ 2\xi_c & \text{for} \quad \xi_C \in [0,0.5] \\ 1 & \text{for} \quad \xi_C \in [0.5,1] \end{cases}, \tag{43}$$

where the normalized volume fraction of the central cell ξ_c is defined as

$$\xi_c = \frac{\alpha_c - \alpha_u}{\alpha_d - \alpha_u}, \tag{44}$$

where α_u, α_c, and α_d are the volume fraction of the upwind, central, and downwind cells, respectively. ξ_f is further modified to ξ_f^* via Courant number Co:

$$\xi_f^* = \begin{cases} \xi_f & \text{for} \quad Co < Co_l \\ \xi_c + (\xi_f - \xi_C)\dfrac{Co_u - Co}{Co_u - Co_l} & \text{for} \quad Co_l \le Co < Co_u \\ \xi_c & \text{for} \quad Co_u \le Co \end{cases}, \tag{45}$$

where the upper bound of Courant number Co_u is unity, and the lower bound of Courant number Co_l is 0.5. The Courant number Co is defined as

$$Co = \frac{\mathbf{v} \cdot \mathbf{a}}{V_c}\delta t, \tag{46}$$

where V_c is the characteristic velocity, and δt is the time step size. When $Co < Co_l$, Equation (43) is used. When $Co_l \le Co < Co_u$, Equation (43) and the first-order upwind method is used. When $Co_u \le Co$, the first-order upwind method is used. ξ_f^* is then modified to ξ_f^{**} via the angle between the fluid interface and the cell interface θ_p:

$$\xi_f^{**} = \xi_f^*(\cos\theta_p)^{C_\theta} + \xi_c\left(1 - (\cos\theta_p)^{C_\theta}\right), \tag{47}$$

where the angle factor C_θ is set to 0.05. The modified volume fraction α_f^{HRIC} at the cell interface is obtained from the equation below:

$$\alpha_f^{HRIC} = \xi_f^{**}(\alpha_d - \alpha_u) + \alpha_u. \tag{48}$$

doi:10.6342/NTU202204241

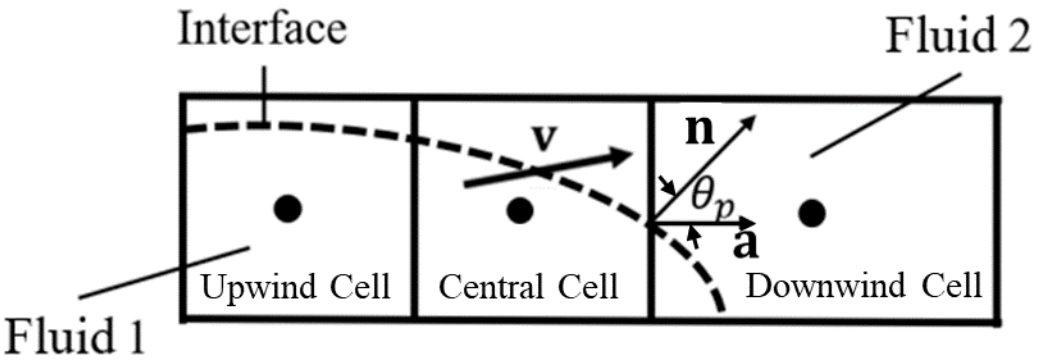

Figure 14 Schematic of fluid interface and cells [13]

doi:10.6342/NTU202204241

3.3.2 Setup of Modeling

The platform undergoes a forced motion in which the velocity of a forced motion is given as

$$V_f = \zeta \omega_a \sin(\omega_a t), \tag{49}$$

where V_f is the generalized velocity of motion, ω_a is the angular frequency of motion, and ζ is the generalized amplitude of motion which is assumed as 1 m for translation and 1° for rotation in this study.

Overset mesh is used to simulate the forced motion of the floating platform in this study. Compared to the dynamic mesh that is prone to give a negative volume of cells, the overset mesh is relatively simple to use, and easily maintains a fine mesh quality during the body movement. The whole mesh is mainly composed of background and component meshes. The former is arranged in the whole computational domain, and the latter is arranged in the overset domain. The entire component mesh is forced to translate or rotate during the simulation. The boundary condition of the object surface is a no-slip wall. The boundary condition of the lower boundary of the computational domain is assumed to be a no-slip wall, and that of the other boundaries is assumed to be velocity inlets where the initial velocity of the flow field is set to be zero.

The upper and lower boundary of the computational domain is located 70 m above and below the water surface, which is the typical water depth of the Hsinchu offshore area. The height of the overset boundary is 80 m, which is close to the characteristic length L of the TaidaFloat platform. The length of the computational domain and overset domain is proportional to the wave length λ which is estimated by the following equations:

doi:10.6342/NTU202204241

$$\lambda = \begin{cases} \sqrt{ghT} & \text{for} \quad \frac{h}{\lambda} < 0.05 \\ \frac{gT^2}{2\pi}\tanh\left(\frac{2\pi h}{\lambda}\right) & \text{for} \quad 0.05 < \frac{h}{\lambda} < 0.5 \\ \frac{gT^2}{2\pi} & \text{for} \quad \frac{h}{\lambda} > 0.5 \end{cases} . \tag{50}$$

The computational domain has a length of 20λ, and the overset domain has a length of 3λ. For the two wave conditions discussed in this study, i.e., common wave condition and high wave condition, hereinafter referred as 'CW condition' and 'HW condition'. Their zero-crossing period is 5.5 s and 7.5 s, and their wave length is 48 m and 92 m, respectively. Therefore, the lengths of the computational domain and overset domain of the CW condition are 960 m and 144 m, and those of the HW condition is 1840 m and 276 m, respectively. The dimensions and boundary conditions of the computational domain is shown in Figure 15.

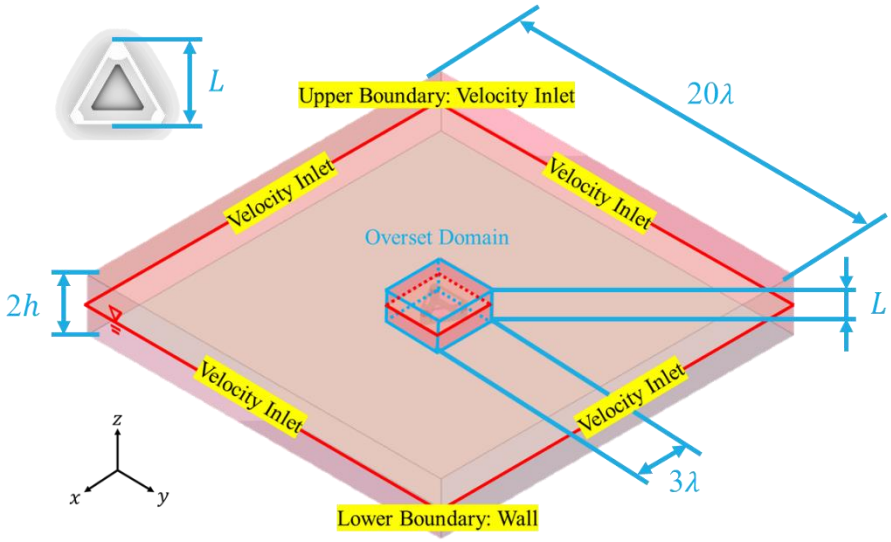

Figure 15 Computational domain of the viscous flow modeling

The mesh arrangement is shown in Table 6 and Figure 16. The size of the background mesh cells is refined with three grid levels. The refinement conditions are shown in Table 6(b). The size of the region of refinement is only arranged in the x- and

doi:10.6342/NTU202204241

y-direction, and remain the same as computational domain in z-direction. To better capture the volume fraction of the cells, the cell size at the free surface needs to be refined in the z-direction. As shown in Figure 16(c), the refinement region of the component mesh must be thicker than that of the background mesh, especially in heave, roll and pitch motions due to the displacement of the component mesh in the z-direction. Moreover, the peripheral part of the background mesh has to be further refined to capture the free surface due to the rapid decay of the waves. The conditions of the mesh refinement at the free surface are shown in Table 6(c).

doi:10.6342/NTU202204241

Table 6 Mesh arrangement for the viscous flow modeling: (a) Details of meshes, (b) Background mesh refinement, (c) Mesh refinement at free surface

(a)

Wave Condition		CW	HW
Platform Surface Mesh Faces	Surge, Sway, Yaw	2.799×10^5	2.793×10^5
	Heave, Roll, Pitch	6.459×10^5	5.937×10^5
Numerical Mesh Cells	Surge, Sway, Yaw	3.413×10^6	4.230×10^6
	Heave, Roll, Pitch	7.559×10^6	8.096×10^6
Platform Surface Mesh Size (m)		0.625	
Component Mesh Cell Size (m)		6.25	
Maximum Background Mesh Cell Size (m)		50	

(b)

Outer Boundary Shape	Outer Boundary of Refinement Region on xy-Plane from the Origin	Cell Size Scale
Cylinder	7λ	1/2
	5λ	1/4
	3λ	1/8

(c)

Wave Condition		CW	HW
Refinement Region Thickness of Component Mesh (m)	Surge, Sway, Yaw	4	4
	Heave, Roll, Pitch	11	10
Refinement Region Thickness of Background Mesh (m)		2	
Outer Boundary of Inner Refinement Region on xy-Plane		Circle with Radius of 5λ at Origin	
Cell Size in z-Direction (m)	Inner Region	0.05	
	Outer Region	0.025	

doi:10.6342/NTU202204241

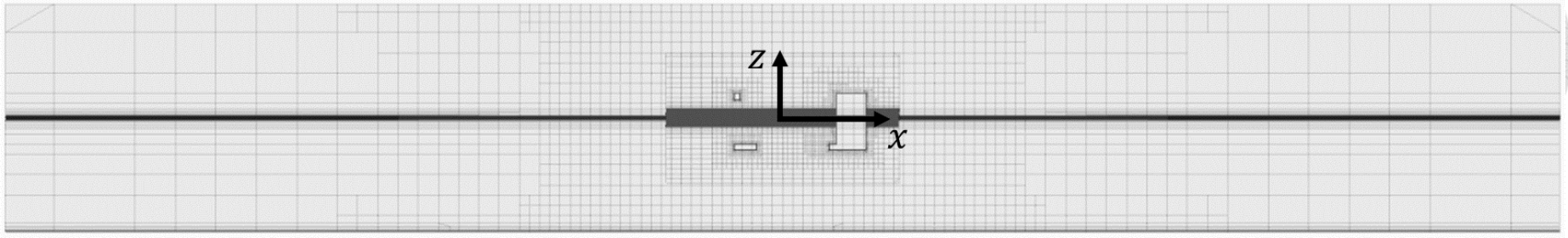

(a)

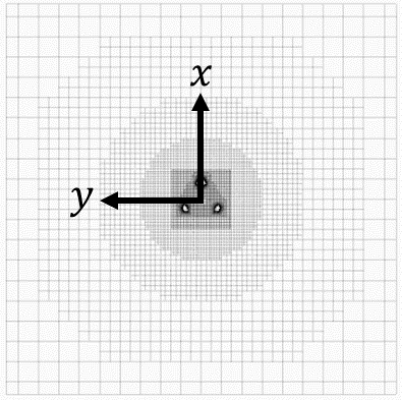

(b)

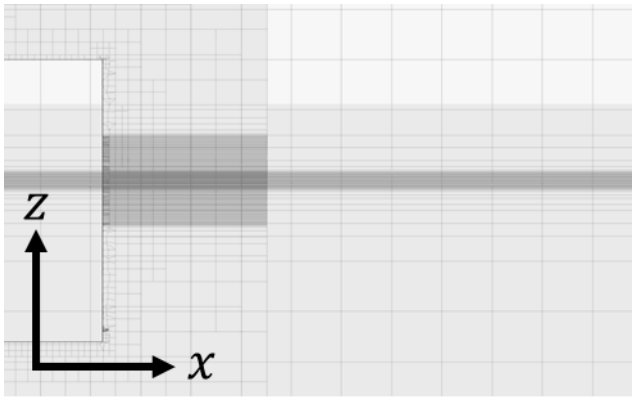

(c)

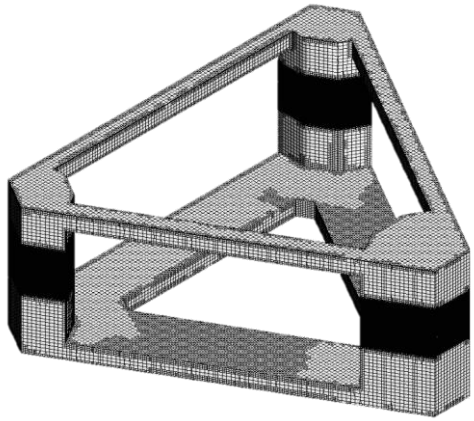

(d)

Figure 16 Mesh arrangement for the viscous flow modeling: (a) Side view of numerical mesh, (b) Top view of numerical mesh, (c) Free surface refinement of component mesh, (d) Surface mesh of the TaidaFloat platform

doi:10.6342/NTU202204241

3.4 Prediction of Hydrodynamic Properties

The hydrodynamic properties predicted by Ansys Aqwa are potential results. With the load response of the platform calculated in STAR-CCM+, the hydrodynamic properties considering viscous effect are then predicted via the following method [13].

The flow field is with zero initial velocity, which indicates that there is no wave exciting force acting on the platform. Therefore, radiation and hydrostatic forces are the only fluid forces acting on the platform. The radiation force includes the added inertia force and the radiation damping force which occurs when there is no incoming wave. The total force acting on the floating body F_o which is obtained from the result of viscous flow modeling in STAR-CCM+, is expressed in terms of the generalized displacement x_k, as shown below:

$$F_o = A_k\ddot{x}_k + B_k\dot{x}_k + C_k x_k. \tag{51}$$

where A_k is the predicted added mass, B_k is the predicted damping, C_k is the stiffness of the floating body. From Equation (49), x_k, $\dot{x}_k$ and $\ddot{x}_k$ are expressed as

$$x_k = -\zeta\cos(\omega_a t)\,, \tag{52}$$

$$\dot{x}_k = \zeta\omega_a\sin(\omega_a t)\,, \tag{53}$$

$$\ddot{x}_k = \zeta{\omega_a}^2\cos(\omega_a t)\,. \tag{54}$$

With the help of Equation (52), (53) and (54), Equation (51) is written as

$$\begin{aligned} F_o &= \zeta\big(({\omega_a}^2 A_k - C_k)\cos(\omega_a t) + \omega_a B_k\sin(\omega t)\big) \\ &= D_k\cos(\omega_a t + \varphi_k)\,, \end{aligned} \tag{55}$$

where D_k is the amplitude of F_o and φ_k is the phase difference between $\ddot{x}_k$ and F_o, as shown in Figure 17. Therefore, A_k and B_k are determined by D_k and φ_k as follows:

$$D_k = \zeta\sqrt{({\omega_a}^2 A_k - C_k)^2 + (\omega_a B_k)^2}, \tag{56}$$

doi:10.6342/NTU202204241

$$\varphi_k = \tan^{-1}\frac{-\omega_a B_k}{{\omega_a}^2 A_k - C_k}, \tag{57}$$

$$A_k = \frac{\zeta C_k + D_k \cos\varphi_k}{\zeta {\omega_a}^2}, \tag{58}$$

$$B_k = \frac{-D_k \sin\varphi_k}{\zeta \omega_a}, \tag{59}$$

where C_k comes from the result of Aqwa.

Assuming that A_{ij} is the sum of $A_{ij,p}$ and $A_{ij,v}$, as well as B_{ij} is the sum of $B_{ij,p}$ and $B_{ij,v}$, where $A_{ij,p}$ and $B_{ij,p}$ are the potential components predicted via potential flow theory in Aqwa, and $A_{ij,v}$ and $B_{ij,v}$ are the viscous components obtained by subtracting $A_{ij,p}$ and $B_{ij,p}$ from A_k and B_k. A_{ij} and B_{ij} are obtained by shifting $A_{ij,p}$ and $B_{ij,p}$ with non-negative $A_{ij,v}$ and $B_{ij,v}$.

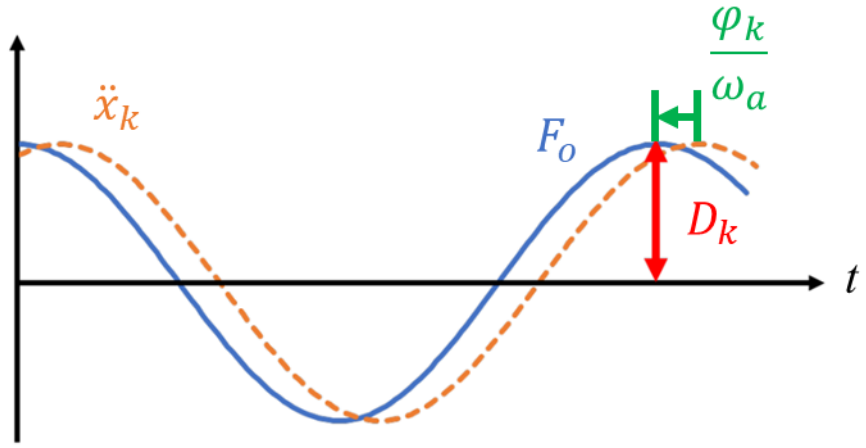

Figure 17 Schematic of the phase difference between force and acceleration [13]

doi:10.6342/NTU202204241

3.5 Modeling of Floating Wind Turbine System

3.5.1 Aerodynamics Modeling

The aerodynamic loading of a wind turbine is calculated by the blade element momentum theory in OrcaFlex. The blade element momentum theory, which is discussed in Section 3.5.1.3, is a combination of the momentum theory and the blade element theory, which is discussed in Section 3.5.1.1 and Section 3.5.1.2. The tip loss model employed in OrcaFlex and is discussed in Section 3.5.1.4.

3.5.1.1 Momentum Theory

The momentum theory is based on the conservation of mass and energy, where the difference of the momentum between the upstream and downstream flows gives the force exerted on the control volume.

The axial momentum theory assumes that the fluid is inviscid, irrotational and incompressible. The rotor plane is regarded as an actuator disk. Based on the conservation of mass, the mass flowing into the control volume equals the mass flowing out of the control volume, as shown in Figure 18 [12]. U_{in} and P_{in} are the velocity and pressure of the fluid before flows into the control volume, U_1 and P_1 are the velocity and pressure before the fluid flows into the actuator disk, U_2 and P_2 are the velocity and pressure after the fluid flows out of the actuator disk, and U_{out} and P_{out} are the velocity and pressure after the fluid flows out of the control volume, respectively. The following equations are obtained from the Bernoulli equation:

$$P_{in} + \frac{1}{2}\rho {U_{in}}^2 = P_1 + \frac{1}{2}\rho {U_1}^2, \tag{60}$$

doi:10.6342/NTU202204241

$$P_2 + \frac{1}{2}\rho {U_2}^2 = P_{out} + \frac{1}{2}\rho {U_{out}}^2. \quad (61)$$

An axial induction factor a is defined as the ratio of the reduction in fluid flow velocity after the flows into the control volume to the inflow velocity:

$$a = \frac{U_{in} - U_1}{U_{in}}. \quad (62)$$

The thrust force T_r acting on the actuator disk equals the pressure difference across the actuator disk multiplied by the disk area A, which is obtained as

$$T_r = \frac{1}{2}\rho A {U_{in}}^2 4a(1-a). \quad (63)$$

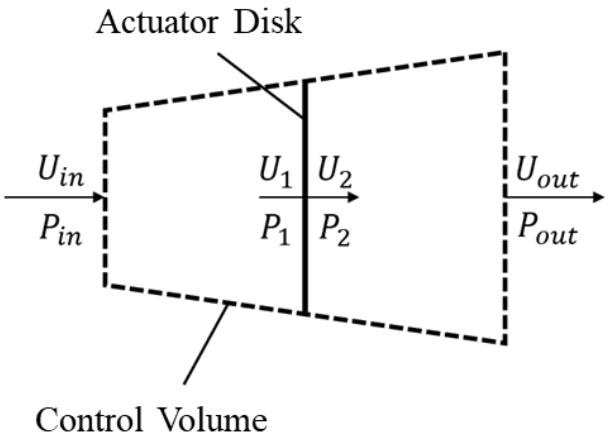

Figure 18 Axial momentum theory [12]

The angular momentum theory is based on the axial momentum theory, and it incorporates the angular velocity of the fluid generated by the rotation of the rotor to calculate the torque acting on the actuator disk caused by the fluid. When the rotor rotates at an angular velocity ω_a, a reduced axial velocity ($U_1 = U_{in}(1-a)$) arises in front of the rotor. The change of the angular velocity of the fluid due to the rotor is ω'. Assuming that r is the radius of the cross section, the moment Q is expressed as

doi:10.6342/NTU202204241

$$Q = \frac{d(I\omega')}{dt} = \dot{m}r^2\omega', \tag{64}$$

where I is the moment of inertia. The angular velocity induction factor is defined as

$$a' = \frac{\omega'}{2\omega_a}. \tag{65}$$

As shown in Figure 19, the moment dQ contributed by the annulus of size dr is obtained as

$$dQ = 4a'(1-a)\frac{1}{2}\rho U_{in}\omega_a r^2 2\pi r dr. \tag{66}$$

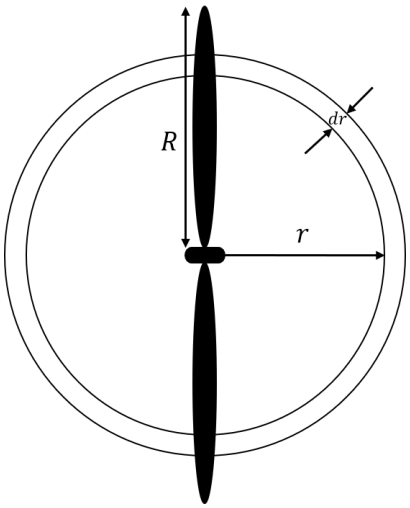

Figure 19 Angular momentum theory [12]

3.5.1.2 Blade Element Theory

The blade element theory first divides a blade into finite blade sections along the span direction. The force acting on each section depends on the drag and lift coefficients of the local airfoil, and all sections are assumed to be aerodynamically independent of each other. Figure 20 shows the geometrical definition of a blade section [12], where the blade length is R, the radial location of a blade section is r, the length of the blade section is dr, and the chord length of the blade section is c.

doi:10.6342/NTU202204241

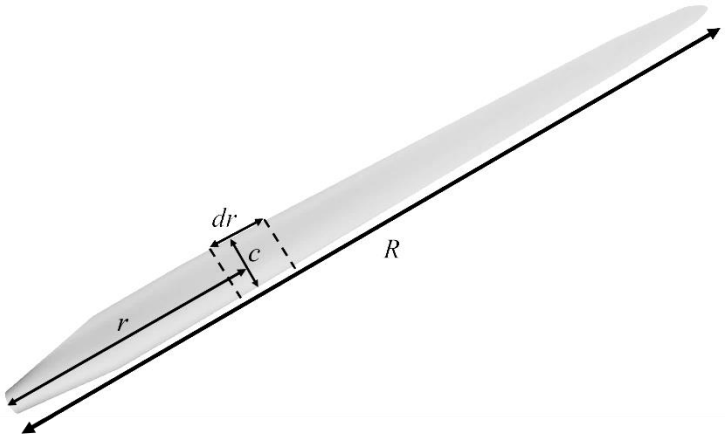

Figure 20 Geometrical definition of a blade section [12]

Each blade section has a relative inflow velocity U which includes the wind speed, tangential rotor speed, axial induced velocity and tangential induced velocity. As shown in Figure 21, for the wind velocity U_{in} the axial induced velocity is $-U_{in}a$, and the vector sum of tangential rotor speed and tangential induced velocity is

$$\omega_a r + \frac{\omega'}{2} r = \omega_a r + \omega_a r a' = \omega_a r(1 + a'). \tag{67}$$

Therefore, the total tangential velocity of the rotor is $\omega_a r(1 + a')$ and the total axial velocity is $U_{in}(1 - a)$. Figure 21 shows the force components acting on the blade section [12], where β_b is the blade pitch angle, α is the angle of attack, and θ is the relative inflow angle.

$$\tan(\theta) = \frac{U_{in}(1 - a)}{r\omega_a(1 + a')} = \frac{1 - a}{1 + a'}\lambda_r, \tag{68}$$

where λ_r is defined as

$$\lambda_r = \frac{U_{in}}{r\omega_a}. \tag{69}$$

The relative inflow velocity is then expressed as

$$U = \frac{U_{in}(1 - a)}{\sin(\theta)}. \tag{70}$$

doi:10.6342/NTU202204241

With the number of blades n_b, the axial force F_a and tangential force F_t are derived as

$$dF_a = n_b c \frac{1}{2} \rho U^2 [C_l \cos(\theta) + C_d \sin(\theta)] dr, \quad (71)$$

$$dF_t = n_b c \frac{1}{2} \rho U^2 [C_l \sin(\theta) - C_d \cos(\theta)] dr, \quad (72)$$

where C_d and C_l are the drag and lift coefficients. The moment acting on the blade dQ is the product of the tangential force dF_t and the radius of the blade section r:

$$dQ = n_b c \frac{1}{2} \rho U^2 [C_l \sin(\theta) - C_d \cos(\theta)] r dr. \quad (73)$$

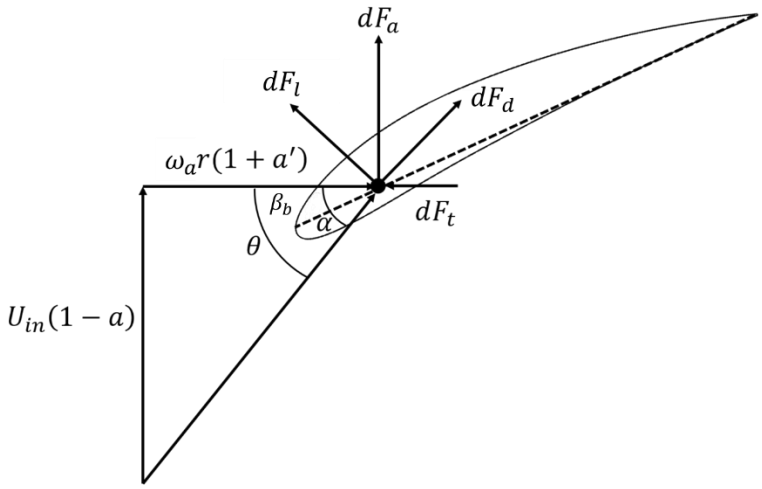

Figure 21 Force components acting on a blade section [12]

3.5.1.3 Blade Element Momentum Theory

The blade element momentum theory (BEM) is a combination of momentum theory and blade element theory. Because dT_r from axial momentum theory is equal to dF_a from blade element theory, the following equation is obtained by combining Equation (63) and (71):

doi:10.6342/NTU202204241

$$\frac{a}{1-a} = \frac{\sigma[C_l \cos(\theta) + C_d \sin(\theta)]}{4\sin^2(\theta)}, \tag{74}$$

where σ is the local solidity defined as

$$\sigma = \frac{n_b c}{2\pi}. \tag{75}$$

Because dQ from angular momentum theory is equal to dQ from blade element theory, the following equation is obtained by combining Equation (66) and (73):

$$\frac{a'}{1-a} = \frac{\sigma[C_L \sin(\theta) - C_D \cos(\theta)]}{4\lambda_r \sin^2(\theta)}. \tag{76}$$

With the help of Equation (74) and (76), a and a' are expressed as

$$a = \frac{1}{1 + \frac{4\sin^2\theta}{\sigma[C_l \cos(\theta) + C_d \sin(\theta)]}}, \tag{77}$$

$$a' = \frac{1}{\frac{2\sin(\theta)\cos(\theta)}{\sigma[C_l \cos(\theta) + C_d \sin(\theta)]} - 1}. \tag{78}$$

The total thrust force and mechanical power are subsequently obtained:

$$T_r = \int_{r_h}^{R_r} dT_r\,, \tag{79}$$

$$P = \int_{r_h}^{R_r} \omega_a dQ\,, \tag{80}$$

where r_h is the hub radius and R_r is the rotor radius.

3.5.1.4 Tip Loss Model

There are many simplifications in BEM, so the predicted power is generally higher than the measured power. The rotor is assumed to have an infinite number of blades in the momentum theory, but it usually has only three blades. Therefore, the energy loss due to vortices at the blade tip arises for finite number of blades. The lifting surface

doi:10.6342/NTU202204241

method [35] is employed to improve the prediction accuracy in OrcaFlex. The correction term F is found between zero and unity.

$$F = \frac{2}{\pi}\cos^{-1}\left\{\exp\left[-\frac{\frac{n_b}{2}\left(1-\frac{r}{R}\right)}{\frac{r}{R}\sin(\theta)}\right]\right\}. \tag{81}$$

The axial induction factor a and angular velocity induction factor a' are then corrected as

$$a = \frac{1}{1+\frac{4F\sin^2(\theta)}{\sigma[C_l\cos(\theta)+C_d\sin(\theta)]}}, \tag{82}$$

$$a' = \frac{1}{\frac{2F\sin(\theta)\cos(\theta)}{\sigma[C_l\cos(\theta)+C_d\sin(\theta)]}-1}. \tag{83}$$

doi:10.6342/NTU202204241

3.5.2 Control System Modeling

3.5.2.1 Governing Equations

The control system modeling for the wind turbine in OrcaFlex is supported through Python. It involves the design of two controllers: the generator torque controller and the full-span rotor-collective blade pitch controller. The former is designed for the below-rated-wind-speed range while the latter is designed for the above-rated-wind-speed range. Figure 22 shows the schematic of the employed control system.

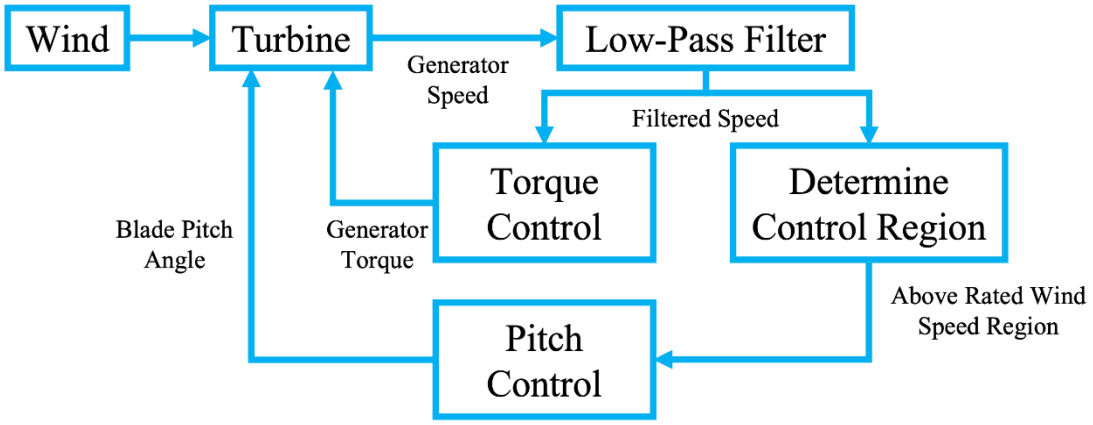

Figure 22 Schematic of the employed control system

A recursive, single-pole low-pass filter with exponential smoothing is employed in the model to avoid the effects of high-frequency excitation. The discrete-time recursion equation for the filter is given as

$$y_{f,n} = (1 - \alpha_f)u_{f,n} + \alpha_f y_{f,(n-1)}, \tag{84}$$

$$\alpha_f = e^{-2\pi T_s \omega_s}, \tag{85}$$

where $y_{f,n}$ is the filtered generator speed, $u_{f,n}$ is the unfiltered generator speed, α_f is the low-pass filter coefficient, n is the discrete-time-step counter, T_s is the discrete time step, and ω_s is the corner frequency. The start-up region is relatively complicated.

doi:10.6342/NTU202204241

Therefore, it is not considered in this study. An optimal constant of proportionality is used to estimate the moment acting on the rotor, which is assumed to be proportional to the square of the generator speed. Within the below-rated-wind-speed range, a single-degree-of-freedom model is employed to control the generator speed. The equation of motion is shown below:

$$T_a - N_g T_g = I_d \Delta\dot{\Omega}, \tag{86}$$

where T_a is the low-speed shaft aerodynamic torque, T_g is the high-speed shaft generator torque, N_g is the high-speed to low-speed gearbox ratio, I_d is the low-speed shaft drivetrain inertia, and $\Delta\dot{\Omega}$ is the low-speed shaft rotational acceleration. The inertia I_d is expressed as

$$I_d = I_r + {N_g}^2 I_g, \tag{87}$$

where I_r is the rotor inertia and I_g is the generator inertia relative to the high-speed shaft. Within the above-rated wind-speed range, the equation of motion of the single-degree-of-freedom model is modified as

$$T_a - N_g T_g = \left(I_r + {N_g}^2 I_g\right) \frac{d}{dt}(\Omega_0 + \Delta\Omega), \tag{88}$$

where Ω_0 is the rated low-speed shaft rotational speed, and $\Delta\Omega$ is the small perturbation of low-speed shaft rotational speed about the rated speed. The generator power P_g is written as

$$P_g = T_g N_g \Omega, \tag{89}$$

where Ω is the low-speed shaft rotational speed. T_g and T_a are obtained as

$$T_g\left(N_g\Omega\right) = \frac{P_0}{N_g\Omega}, \tag{90}$$

$$T_a(\beta_b) = \frac{P(\beta_b, \Omega_0)}{\Omega_0}, \tag{91}$$

doi:10.6342/NTU202204241

where P_0 is the rated mechanical power and β_b is the blade pitch angle. Through the first-order Taylor series expansion, Equation (90) and (91) are expressed as

$$T_g \approx \frac{P_0}{N_g \Omega_0} - \frac{P_0}{N_g \Omega_0^2} \Delta\Omega, \tag{92}$$

$$T_a \approx \frac{P_0}{\Omega_0} + \frac{1}{\Omega_0}\left(\frac{\partial P}{\partial \beta_b}\right) \Delta\beta_b, \tag{93}$$

where $\Delta\beta_b$ is the small perturbation of the blade pitch angle about the operating point, which is shown in Equation (94) with a proportional integral derivative (PID) control.

$$\Delta\beta_b = K_p N_g \Delta\Omega + K_i \int_0^t N_g \Delta\Omega dt + K_d N_g \Delta\dot{\Omega}, \tag{94}$$

where K_p, K_i, K_d are the blade pitch controller proportional, integral, and derivative gains. Assuming that $\dot{\varphi} = \Delta\Omega$, the equation of motion is obtained as

$$\begin{aligned}\left[I_d + \frac{1}{\Omega_0}\left(-\frac{\partial P}{\partial \beta_b} N_g K_d\right)\right]\ddot{\varphi} + \left[\frac{1}{\Omega_0}\left(-\frac{\partial P}{\partial \beta_b}\right) N_g K_p - \frac{P_0}{{\Omega_0}^2}\right]\dot{\varphi} \\ + \left[\frac{1}{\Omega_0}\left(-\frac{\partial P}{\partial \beta_b}\right) N_g K_i\right]\varphi = 0.\end{aligned} \tag{95}$$

From [36], when K_d is set to zero, K_p and K_i are obtained as

$$K_p = \frac{2 I_d \Omega_0 \zeta_\varphi \omega_n}{N_g\left(-\frac{\partial P}{\partial \beta_b}\right)}, \tag{96}$$

$$K_i = \frac{I_d \Omega_0 {\omega_n}^2}{N_g\left(-\frac{\partial P}{\partial \beta_b}\right)}, \tag{97}$$

where ω_n is the natural frequency and ζ_φ is the damping ratio which are obtained from

$$\omega_n = \sqrt{\frac{K_\varphi}{m_\varphi}}, \tag{98}$$

doi:10.6342/NTU202204241

$$\zeta_\varphi = \frac{C_\varphi}{2\sqrt{K_\varphi M_\varphi}} = \frac{C_\varphi}{2M_\varphi \omega_n}, \tag{99}$$

The pitch sensitivity is assumed to nearly linearly vary with blade pitch angle.

$$\frac{\partial P}{\partial \beta_b} = \frac{\partial P}{\partial \beta_b}(\beta_b = 0)\left(1 + \frac{\beta_b}{\beta_{b,k}}\right), \tag{100}$$

where $\beta_{b,k}$ is the blade pitch angle when the pitch sensitivity has doubled from its value at the rated operating point, i.e.,

$$\frac{\partial P}{\partial \beta_b}\left(\beta_b = \beta_{b,k}\right) = 2\frac{\partial P}{\partial \beta_b}(\beta_b = 0). \tag{101}$$

With the help of Equation (100) and (101), Equation (96) and (97) are derived as

$$K_p = \frac{2I_d \Omega_0 \zeta_\varphi \omega_n}{N_g\left[\left(-\frac{\partial P}{\partial \beta_b}\right)(\beta_b = 0)\right]} GK(\beta_b), \tag{102}$$

$$K_i = \frac{I_d \Omega_0 {\omega_n}^2}{N_g\left[\left(-\frac{\partial P}{\partial \beta_b}\right)(\beta_b = 0)\right]} GK(\beta_b), \tag{103}$$

where $GK(\beta_b)$ is the dimensionless gain correction factor defined as

$$GK(\beta_b) = \frac{1}{1 + \frac{\beta_b}{\beta_{b,k}}}. \tag{104}$$

3.5.2.2 Control System Parameters

In this study, the turbine controller source code for IEA 15-MW wind turbine, i.e., NREL's Reference Open Source Controller (ROSCO), is compiled as a dynamic link library (DLL). The referenced blade pitch and variable-speed controllers are both modified to adjust the target wind turbine. The control system parameters are summarized in Table 7. K_p and K_i used in the blade pitch controller are shown in Table 8, and K_d is set to be zero. Table 9 shows the minimum blade pitch as a function of the wind speed.

doi:10.6342/NTU202204241

Table 7 Control system parameters

Corner Frequency of Low-Pass Filter (Hz)	0.16
Rated Generator Torque (MN·m)	19.624
Max Generator Torque (MN·m)	21.586
Generator Torque Constant [MN·m/(rad/s)^2]	33.732
Generator Efficiency	96.55%
Minimum Blade Pitch Angle (°)	0
Maximum Blade Pitch Angle (°)	90
Maximum Blade Pitch Rate (°/s)	1
Rated Rotor Speed (RPM)	7.56

Table 8 Gain-scheduling table

β_b (°)	K_p (s)	K_i	β_b (°)	K_p (s)	K_i
3.671	-1.273	-0.133	15.724	-0.214	-0.052
5.239	-1.100	-0.120	16.311	-0.185	-0.050
6.482	-0.958	-0.109	16.900	-0.159	-0.048
7.557	-0.840	-0.100	17.463	-0.135	-0.046
8.525	-0.740	-0.092	18.031	-0.112	-0.045
9.414	-0.653	-0.086	18.571	-0.091	-0.043
10.244	-0.579	-0.080	19.124	-0.072	-0.042
11.028	-0.513	-0.075	19.642	-0.054	-0.040
11.772	-0.455	-0.071	20.170	-0.037	-0.039
12.485	-0.404	-0.067	20.687	-0.021	-0.038
13.172	-0.358	-0.063	21.187	-0.006	-0.037
13.840	-0.317	-0.060	21.701	0.008	-0.035
14.482	-0.279	-0.057	22.189	0.022	-0.034
15.106	-0.245	-0.055	22.671	0.034	-0.033

doi:10.6342/NTU202204241

Table 9 Minimum blade pitch as a function of wind speed

U_w (m/s)	β_b (°)	U_w (m/s)	β_b (°)
3.00	2.000	14.09	1.928
3.50	2.000	14.59	2.543
4.00	1.875	15.09	3.122
4.50	1.625	15.59	3.671
5.00	1.375	16.09	4.191
5.50	1.000	16.59	4.686
6.00	0.750	17.09	5.162
6.50	0.250	17.59	5.622
7.00	-0.500	18.09	6.066
7.50	-0.500	18.59	6.496
8.00	-0.500	19.09	6.911
8.50	-0.500	19.59	7.321
9.00	-0.314	20.09	7.722
9.50	-5.932	20.59	8.106
10.00	-6.155	21.09	8.486
10.50	-6.515	21.59	8.860
11.09	-4.649	22.09	9.226
11.59	-2.568	22.59	9.583
12.09	-1.315	23.09	9.931
12.59	-0.332	23.59	10.279
13.09	0.509	24.09	10.622
13.59	1.254	24.59	10.958

doi:10.6342/NTU202204241

3.5.3 Mooring Modeling

The finite element method is used for the mooring line modeling in OrcaFlex as shown in Figure 23 [37]. The line is divided into a series of straight massless model segments with a node at each end, where each segment models only the axial and torsional properties of the line. It turns out that the axial force predominates in the mooring system. Each line segment is divided into two sub-segments and the properties, such as mass, weight, buoyancy of each sub-segment, are lumped to the neighboring node.

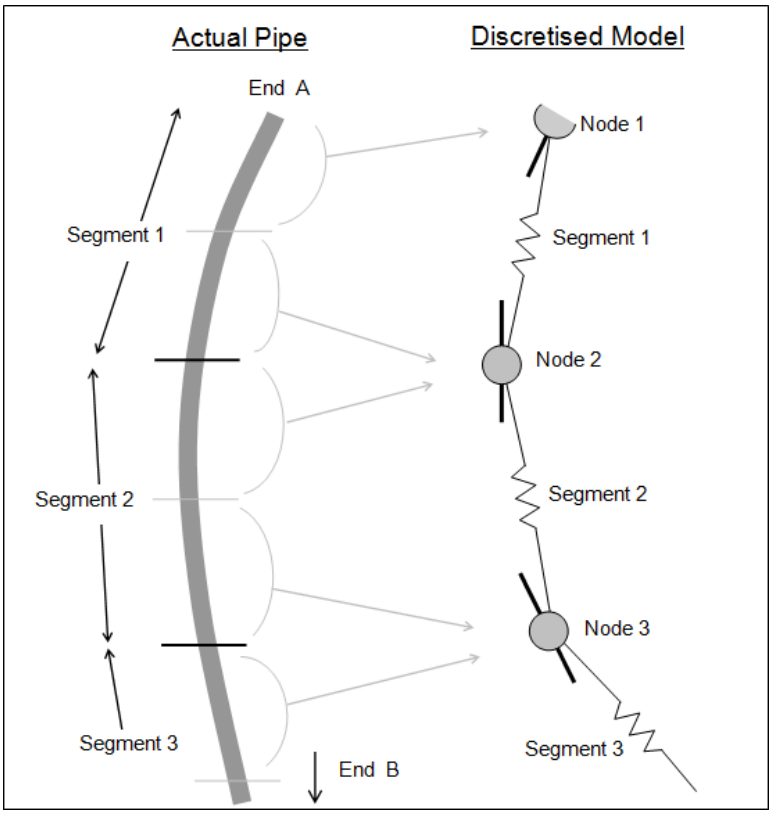

Figure 23 Finite element model for mooring lines [37]

The axial force contains the effective tension T_e and the wall tension T_w, where they are corelated using the following equation:

doi:10.6342/NTU202204241

$$T_e = T_w + (p_{ex}a_{ex} - p_{in}a_{in}) \tag{105}$$

where p_{ex} and p_{in} are the external and internal pressure, and a_{ex} and a_{in} are the external and internal cross-sectional stress area, respectively, and the wall tension is obtained as

$$T_w = EA\varepsilon - 2\nu_P(p_{ex}a_{ex} - p_{in}a_{in}) + k_{tt}\frac{\tau}{l_0} + EAc_d\frac{dl}{dt}\frac{1}{l_0}, \tag{106}$$

$$\varepsilon = \frac{l - \lambda_s l_0}{\lambda_s l_0}, \tag{107}$$

where EA is the axial stiffness of the line, ε is the total mean axial strain, ν_P is the Poisson ratio, k_{tt} is the coefficient for torque coupling tension, τ is the segment twist angle, l is the segment length, l_0 is the initial segment length, λ_s is the expansion factor of segment, and c_d is the damping coefficient for the mooring line defined as

$$c_d = \frac{\lambda_a}{100}c_c, \tag{108}$$

$$c_c = \sqrt{\frac{2ml_0}{EA}}, \tag{109}$$

where λ_a is the target tension damping, c_c is the critical damping value for a segment, and m is the segment mass including contents but not of any attachment.

doi:10.6342/NTU202204241

4 Performance Prediction

4.1 Cases Description

The performance of a 15 MW floating wind turbine system using the semi-submersible TaidaFloat platform equipped with the IEA 15-MW offshore wind turbine predicted via a potential flow approach, hereinafter referred as 'PF approach', which only considers the potential result, and a viscous flow approach, hereinafter referred as 'VF approach', which additionally considers the effects of viscosity, in the Hsinchu offshore area is presented in this study. The global coordinate system of the floating wind turbine system, as well as the definition of six degrees of motion in this study is shown in Figure 24. The irregular wave conditions discussed in this study is corresponding to the wave scatter diagram of the Hsinchu offshore area which is shown in Table 10 [25]. In this study, the CW condition, i.e., $(H_s, T_z) = (1.5\ \text{m}, 5.5\ \text{s})$, and the HW condition, i.e., $(H_s, T_z) = (4.5\ \text{m}, 7.5\ \text{s})$, are both considered. According to [38], the JONSWAP spectrum with $\gamma = 2.08$ is chosen as the wave spectrum in this study. As shown in Figure 25, the wind profile of an offshore area is defined as

$$U_{in}^{w} = U_w \left(\frac{z}{H_h}\right)^{\frac{1}{10}}, \tag{110}$$

where U_w is the wind velocity at the hub height, U_{in}^{w} is the wind velocity, z is the height above the mean sea level, and H_h is the hub height of the IEA 15-MW wind turbine ($H_h = 150$ m). The wind velocity obtained from the Beaufort scale U_B is the wind velocity defined at 10 m above MSL, which is 8.11 m/s and 17.8 m/s for the CW condition and the HW condition, respectively. U_w for the CW condition and the HW condition are then calculated via Equation (110). According to [25], the surface current

doi:10.6342/NTU202204241

speed U_c is assumed to be 0.93 m/s, which occurs in the Taiwan Strait with a probability of 75%, and the current profile is defined as

$$U_{in}^{c} = U_c \left(\frac{z+h}{h}\right)^{\frac{1}{7}}, \tag{111}$$

where U_c is the current velocity at the free surface, U_{in}^{c} is the current velocity, h is the water depth ($h = 70$ m). The metocean conditions adopted in this study are summarized in Table 11. The wave is assumed to have a direction consistent with the wind. In this study, seven wind and wave directions ($\theta_w = 0°, 30°, \ldots, 180°$), and four current directions ($\theta_c = 0°, 90°, 180°, 270°$) are discussed. The wind, wave and current directions are defined as the angles measured clockwise from the negative x-axis to the incoming wind or current directions, as shown in Figure 26.

There are totally 112 cases investigated in this study as shown in Table 12. The hydrodynamic properties are discussed in Section 4.2, the response amplitude operator is discussed in Section 4.3, the motion response and generator power are discussed in Section 4.4, and the mooring line tension is discussed in Section 4.5.

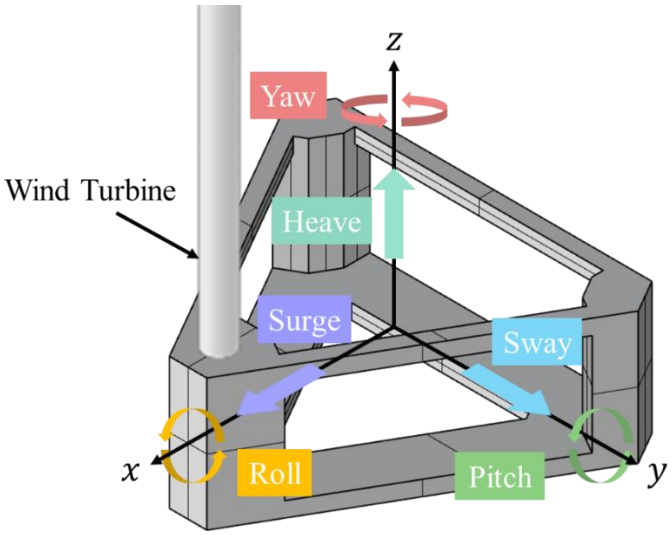

Figure 24 Global coordinate system of the floating wind turbine system

doi:10.6342/NTU202204241

Table 10 Wave scatter diagram of the Hsinchu offshore area [25]

H_s (m) \ T_z (s)	3.5	4.5	5.5	6.5	7.5	Sum
0.5	14.79%	41.96%	5.49%	0.44%	0.02%	62.70%
1.5	0.31%	12.23%	18.31%	0.70%		31.55%
2.5		0.02%	4.35%	0.90%	0.04%	5.32%
3.5				0.35%	0.04%	0.39%
4.5				0.04%	0.02%	0.06%
Sum	15.10%	54.21%	28.15%	2.43%	0.11%	100%

Table 11 Metocean conditions of the two irregular wave conditions

Irregular Wave Condition	CW	HW
Wave Spectrum	JONSWAP ($\gamma = 2.08$)	
H_s (m)	1.5	4.5
T_z (s)	5.5	7.5
U_B (m/s)	8.11	17.80
U_w (m/s)	10.63	23.34
U_c (m/s)	0.93	

Table 12 Case definition

Wave Condition	CW				HW		
Approach	PF				VF		
θ_w (°)	0	30	60	90	120	150	180
θ_c (°)	0		90		180		270

doi:10.6342/NTU202204241

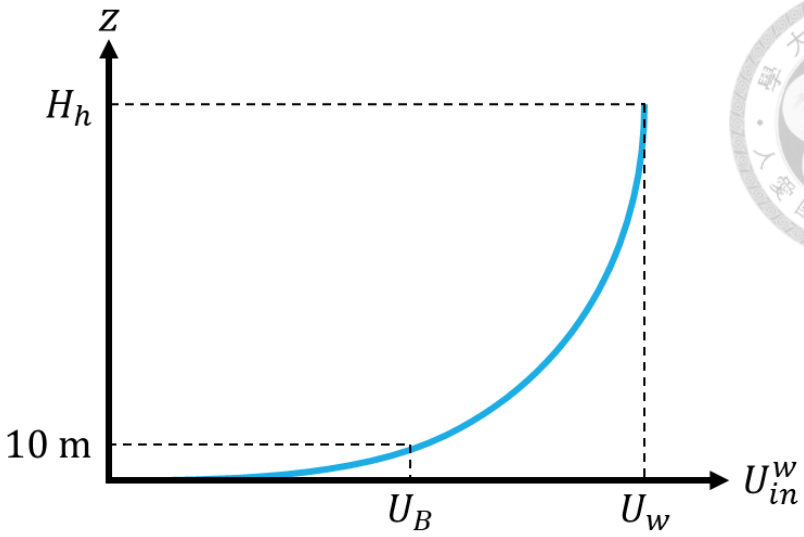

Figure 25 Schematic of the wind profile

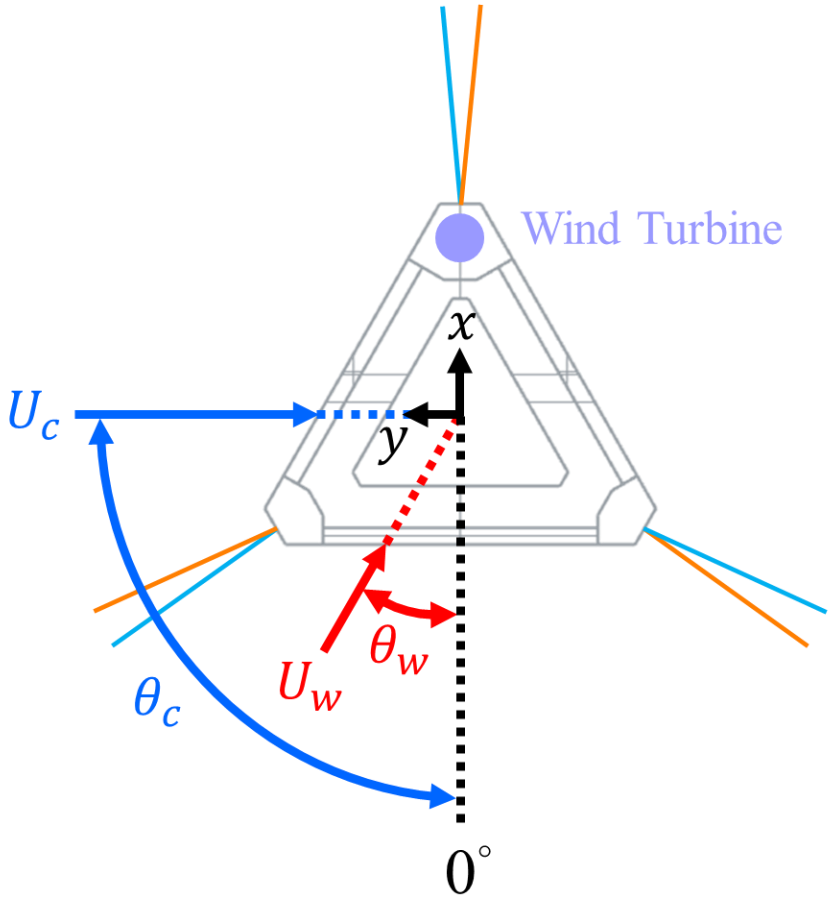

Figure 26 Definition of the wind, wave and current directions

doi:10.6342/NTU202204241

4.2 Hydrodynamic Properties

This study estimates the potential components of hydrodynamic properties of the TaidaFloat platform in the frequency domain of 0 Hz to 0.5 Hz via Aqwa. STAR-CCM+ is then employed to obtain the load response of the platform under a forced motion in the viscous flow field to predict the hydrodynamic properties considering viscous effect. The mean values of the predicted hydrodynamic properties of the last 5 periods of a forced motion with a frequency of 0.182 Hz for CW condition, as well as 0.133 Hz for HW condition, are employed, and only the non-negative predicted viscous components are used, i.e., A_{ij} and B_{ij} are obtained by shifting $A_{ij,p}$ and $B_{ij,p}$ with non-negative $A_{ij,v}$ and $B_{ij,v}$. The stiffnesses calculated by Aqwa in heave, roll, and pitch motion C_{33}, C_{44}, and C_{55} are 6.342 MN/m, 75.628 MN/m, and 43.674 MN/m, respectively. The hydrodynamic properties calculated via the PF approach and VF approach, i.e., $A_{ij,p}$ vs. A_{ij}, and $B_{ij,p}$ vs. B_{ij}, in six degrees of freedom motions are shown in Figure 27 to Figure 32. The values are shown in Table 13 and Table 14.

Under the CW condition ($T_z = 5.5$ s), the heave motion has an added mass of 50.678 kt, that is the largest one among the translation motions, while the surge and sway motions have an added mass of 11.657 kt and 9.908 kt. Among the rotation motions, the roll and pitch motions have an added mass of 22.626 Mt·m^2/rad and 22.804 Mt·m^2/rad, while the yaw motion has an added mass of 12.682 Mt·m^2/rad. The heave motion has a damping of 13.63 MN·s/m, that is the largest one among the translation motions, while the surge and sway motions have a damping of 9.787 MN·s/m and 7.909 MN·s/m. The yaw motion has a damping of 10.807 GN·m·s/rad, that is the largest one among the rotation motions, while the roll and pitch motions has a damping of 2.861 GN·m·s/rad and 3.553 GN·m·s/rad. The

doi:10.6342/NTU202204241

added mass in the heave motion predicted via the PF approach is underestimated by up to 13.035%. The damping in the roll motion predicted via the PF approach is underestimated by up to 93.044%.

Under the HW condition ($T_z = 7.5$ s), the heave motion has an added mass of 49.619 kt, that is the largest one among the translation motions, while the surge and sway motions have an added mass of 18.13 kt and 19.456 kt. The roll motion has an added mass of 20.888 Mt·m^2/rad, that is the largest one among the rotation motions, while the pitch and yaw motions have an added mass of 20.371 Mt·m^2/rad and 20.149 Mt·m^2/rad. The sway motion has a damping of 12.803 MN·s/m, that is the largest one among translation motions, while the surge and heave motions have a damping of around 11.641 MN·s/m and 10.072 MN·s/m. The yaw motion has a damping of 11.351 GN·m·s/rad, that is the largest one among rotation motions, while the roll and pitch motions have a damping of 4.549 GN·m·s/rad and 4.927 GN·m·s/rad. The added mass in the heave motion predicted via the PF approach is underestimated by up to 12.34%. The damping in the heave motion predicted via the PF approach is underestimated by up to 86.606%.

The results show that the viscous effect has a larger impact on the hydrodynamic properties in the heave, roll, and pitch motions than in the surge, sway, and yaw motions. The hydrodynamic properties are underestimated without considering viscous effect, especially under the CW condition.

doi:10.6342/NTU202204241

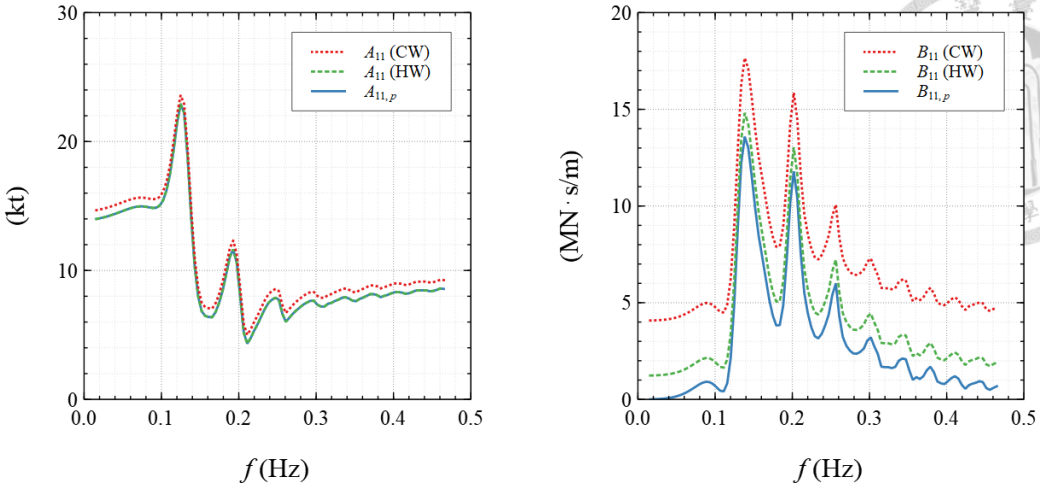

(a) (b)

Figure 27 Hydrodynamic properties in surge motion: (a) Added mass, (b) Damping

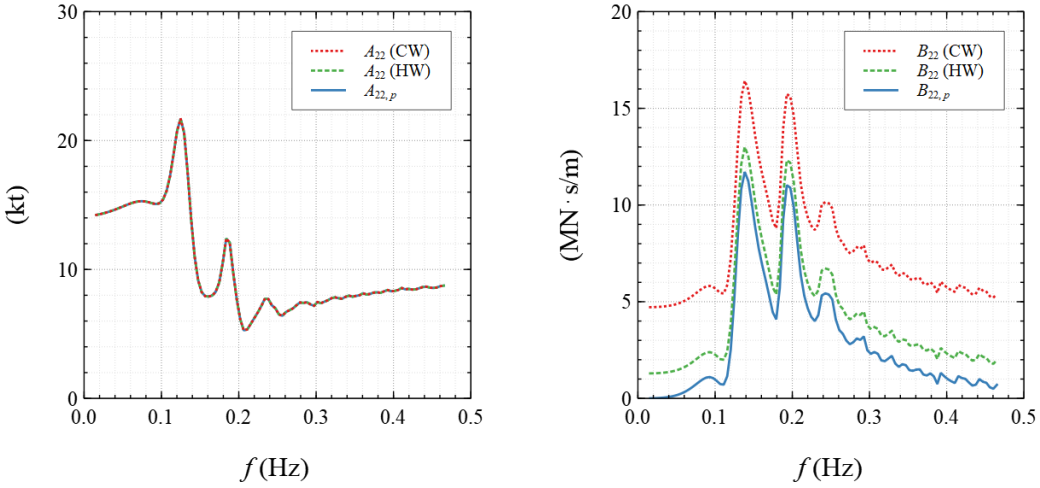

(a) (b)

Figure 28 Hydrodynamic properties in sway motion: (a) Added mass, (b) Damping

doi:10.6342/NTU202204241

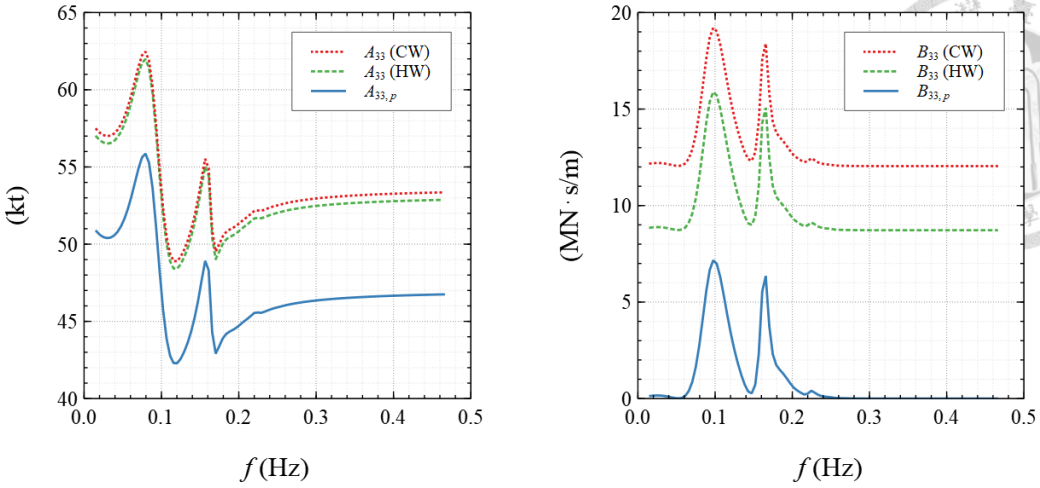

(a) (b)

Figure 29 Hydrodynamic properties in heave motion: (a) Added mass, (b) Damping

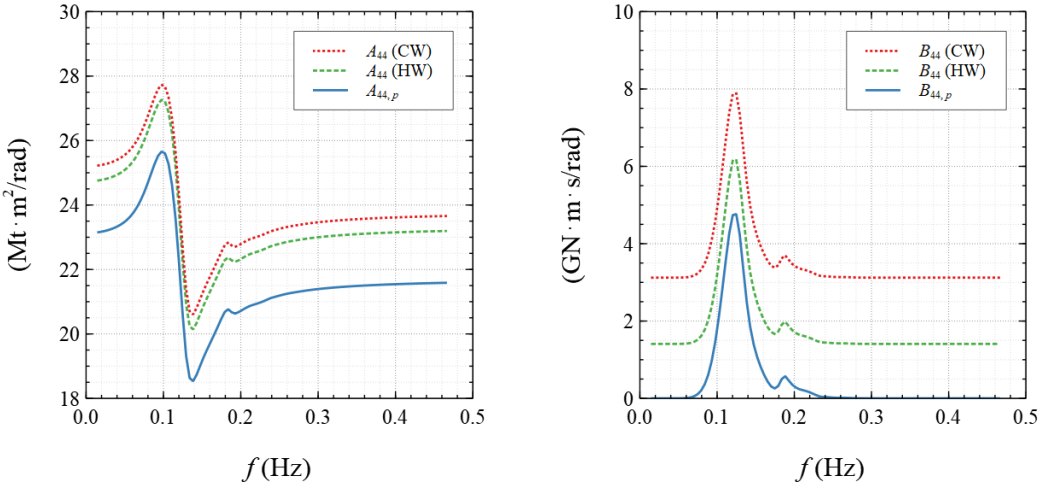

(a) (b)

Figure 30 Hydrodynamic properties in roll motion: (a) Added mass, (b) Damping

doi:10.6342/NTU202204241

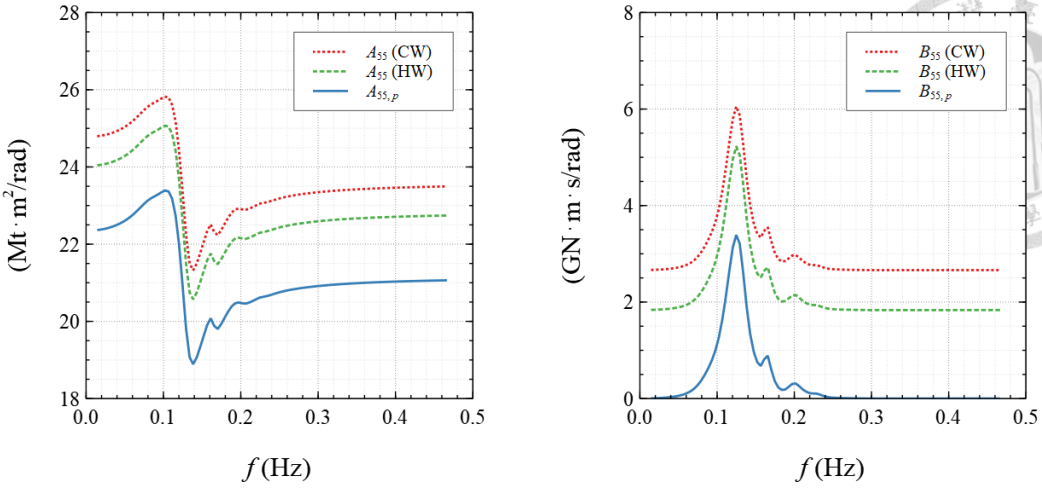

(a) (b)

Figure 31 Hydrodynamic properties in pitch motion: (a) Added mass, (b) Damping

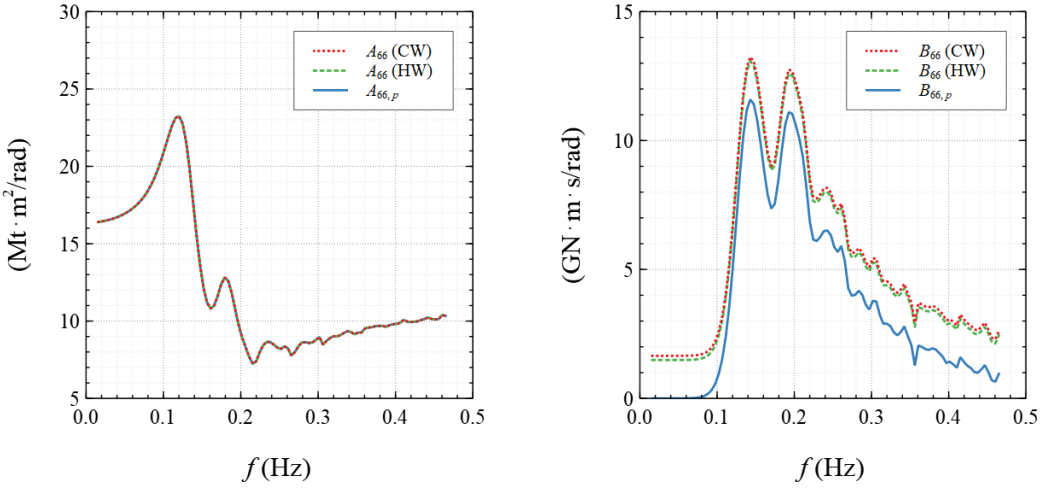

(a) (b)

Figure 32 Hydrodynamic properties in yaw motion: (a) Added mass, (b) Damping

doi:10.6342/NTU202204241

Table 13 Hydrodynamic properties under CW condition ($T_z = 5.5$ s): (a) Added mass, (b) Damping

(a)

Motion	PF Approach	VF Approach
Surge (kt)	11.657	11.657
Sway (kt)	9.228	9.908
Heave (kt)	44.072	50.678
Roll (Mt·m^2/rad)	20.194	22.626
Pitch (Mt·m^2/rad)	20.732	22.804
Yaw (Mt·m^2/rad)	12.682	12.682

(b)

Motion	PF Approach	VF Approach
Surge (MN·s/m)	5.075	9.787
Sway (MN·s/m)	3.833	7.909
Heave (MN·s/m)	1.586	13.630
Roll (GN·m·s/rad)	0.199	2.861
Pitch (GN·m·s/rad)	0.431	3.553
Yaw (GN·m·s/rad)	9.157	10.807

Table 14 Hydrodynamic properties under HW condition ($T_z = 7.5$ s): (a) Added mass, (b) Damping

(a)

Motion	PF Approach	VF Approach
Surge (kt)	18.130	18.130
Sway (kt)	19.456	19.456
Heave (kt)	43.496	49.619
Roll (Mt·m^2/rad)	19.209	20.888
Pitch (Mt·m^2/rad)	18.763	20.371
Yaw (Mt·m^2/rad)	20.149	20.149

(b)

Motion	PF Approach	VF Approach
Surge (MN·s/m)	10.352	11.641
Sway (MN·s/m)	11.572	12.803
Heave (MN·s/m)	1.349	10.072
Roll (GN·m·s/rad)	2.715	4.549
Pitch (GN·m·s/rad)	3.519	4.927
Yaw (GN·m·s/rad)	9.863	11.351

doi:10.6342/NTU202204241

4.3 Response Amplitude Operator

In this study, the response amplitude operator (RAO) of the wind turbine system without mooring system is calculated by Ansys Aqwa. The comparisons of RAO in six degrees of freedom motions among different incoming wave directions which is defined in Figure 26, are shown in Figure 33 to Figure 38, where the subscripts $i, j = 1, 2, \ldots, 6$ refer to the surge, sway, heave, roll, pitch, and yaw motions, respectively. The RAOs calculated via the PF approach are similar at $\theta_w = 0°$ and $180°$, at $\theta_w = 30°$ and $150°$, and at $\theta_w = 60°$ and $120°$ in the six degrees of freedom motions, while those calculated via the VF approach are similar for the same combinations of wave directions except those in the roll motion. The largest RAOs obtained via the PF approach are 3.709 m/m, 3.71 m/m, 3.998 m/m, 9.045°/m, 11.614°/m, and 1.93°/m, respectively, those obtained via the VF approach under the CW condition are 2.499 m/m, 2.324 m/m, 1.012 m/m, 1.049°/m, 2.998°/m, and 0.537°/m, respectively, and those obtained via the VF approach under the HW condition are 3.528 m/m, 3.512 m/m, 1.108 m/m, 2.405°/m, 3.654°/m, and 0.539°/m, respectively, at $\theta_w = 0°, 90°, 0°, 90°, 180°$, and $90°$ in surge, sway, heave, roll, pitch, and yaw motions, respectively. The RAO in the roll motion obtained via the PF approach is overestimated by about 8 times and 3 times those obtained via the VF approach under the CW and HW conditions, respectively.

The results show that the viscous effect has a significant impact on the RAO in the roll motion, followed by those in heave, pitch, and yaw motions, and has a minor impact on those in surge and sway motions. The RAO is overestimated without considering viscous effect, especially under the CW condition.

doi:10.6342/NTU202204241

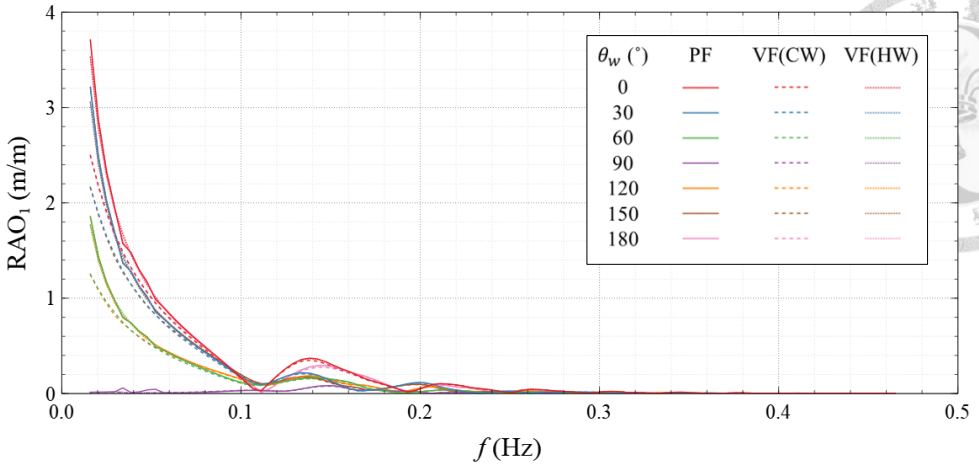

Figure 33 Comparison of response amplitude operator in surge motion

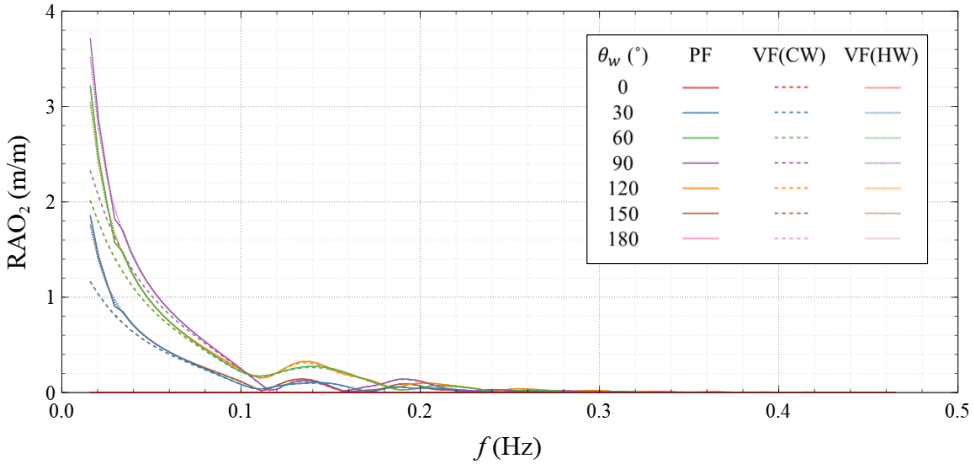

Figure 34 Comparison of response amplitude operator in sway motion

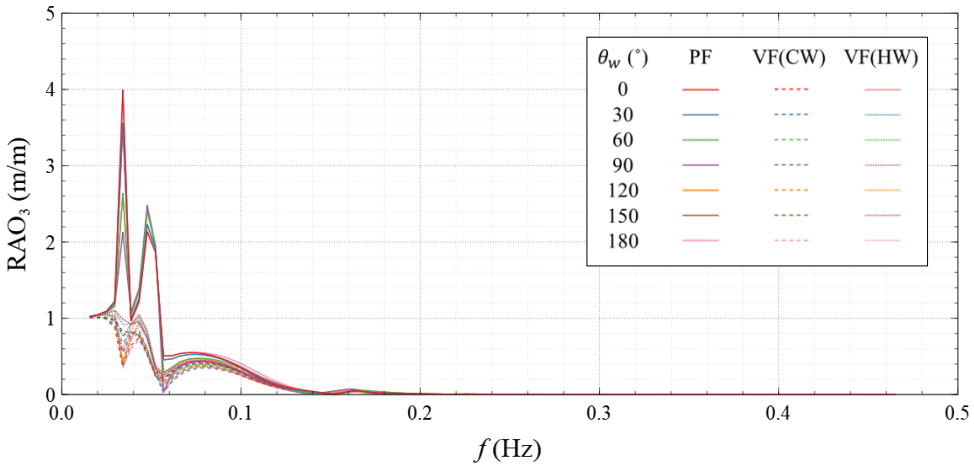

Figure 35 Comparison of response amplitude operator in heave motion

doi:10.6342/NTU202204241

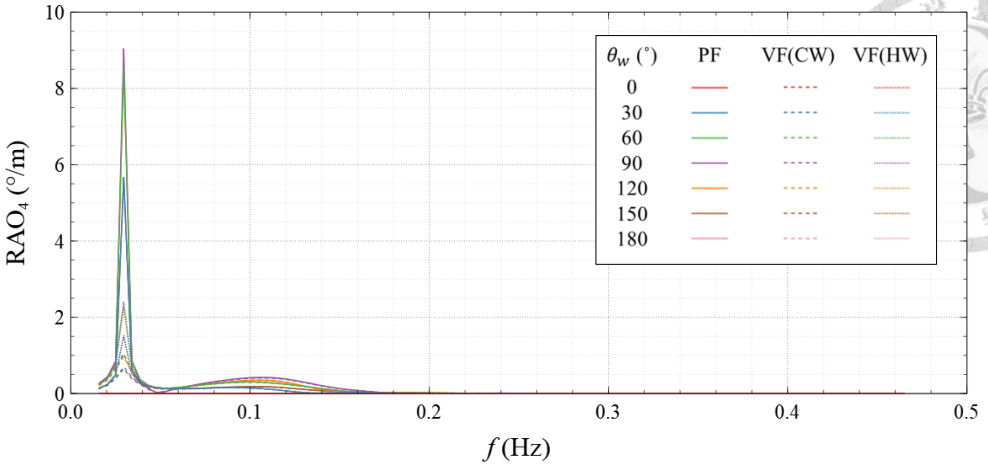

Figure 36 Comparison of response amplitude operator in roll motion

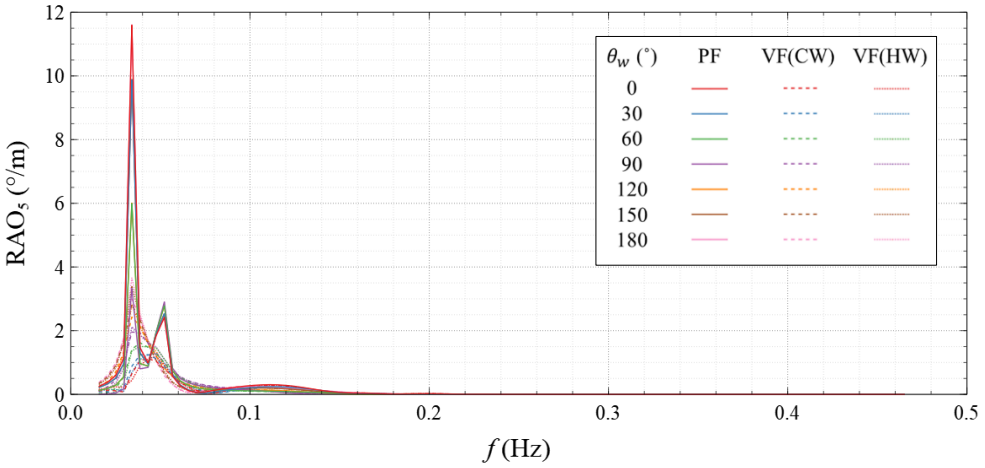

Figure 37 Comparison of response amplitude operator in pitch motion

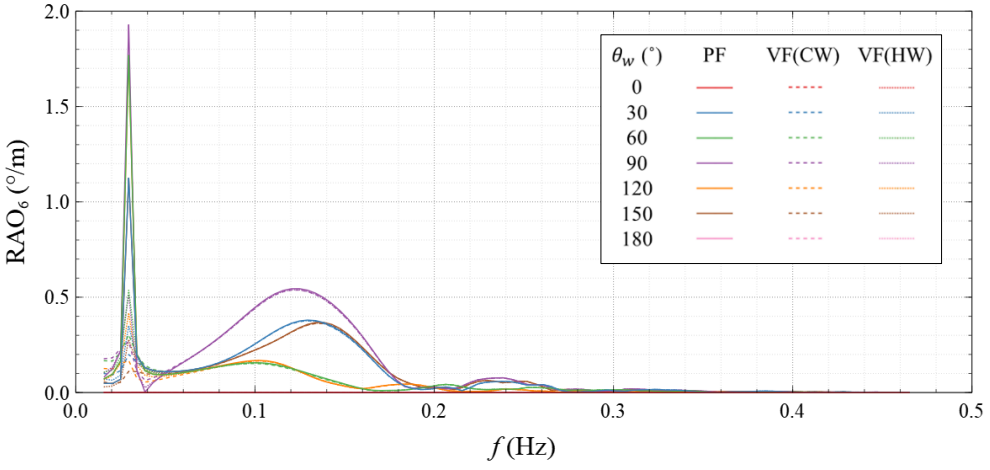

Figure 38 Comparison of response amplitude operator in yaw motion

doi:10.6342/NTU202204241

4.4 Motion Response and Generator Power

The motion response and generator power are obtained by solving the equations of motion in OrcaFlex. The mean and standard deviation are analyzed from the time-domain result of OrcaFlex, where the time histories of the generator electrical power at $\theta_w = 0°$ is shown in Figure 39. In this study, η_i is regarded as the linear and angular displacement, where $i = 1, 2, \ldots, 6$ refers to the surge, sway, heave, roll, pitch, and yaw motions, respectively.

The results under the CW condition are discussed in Section 4.4.1, while those under the HW condition are discussed in Section 4.4.2.

doi:10.6342/NTU202204241

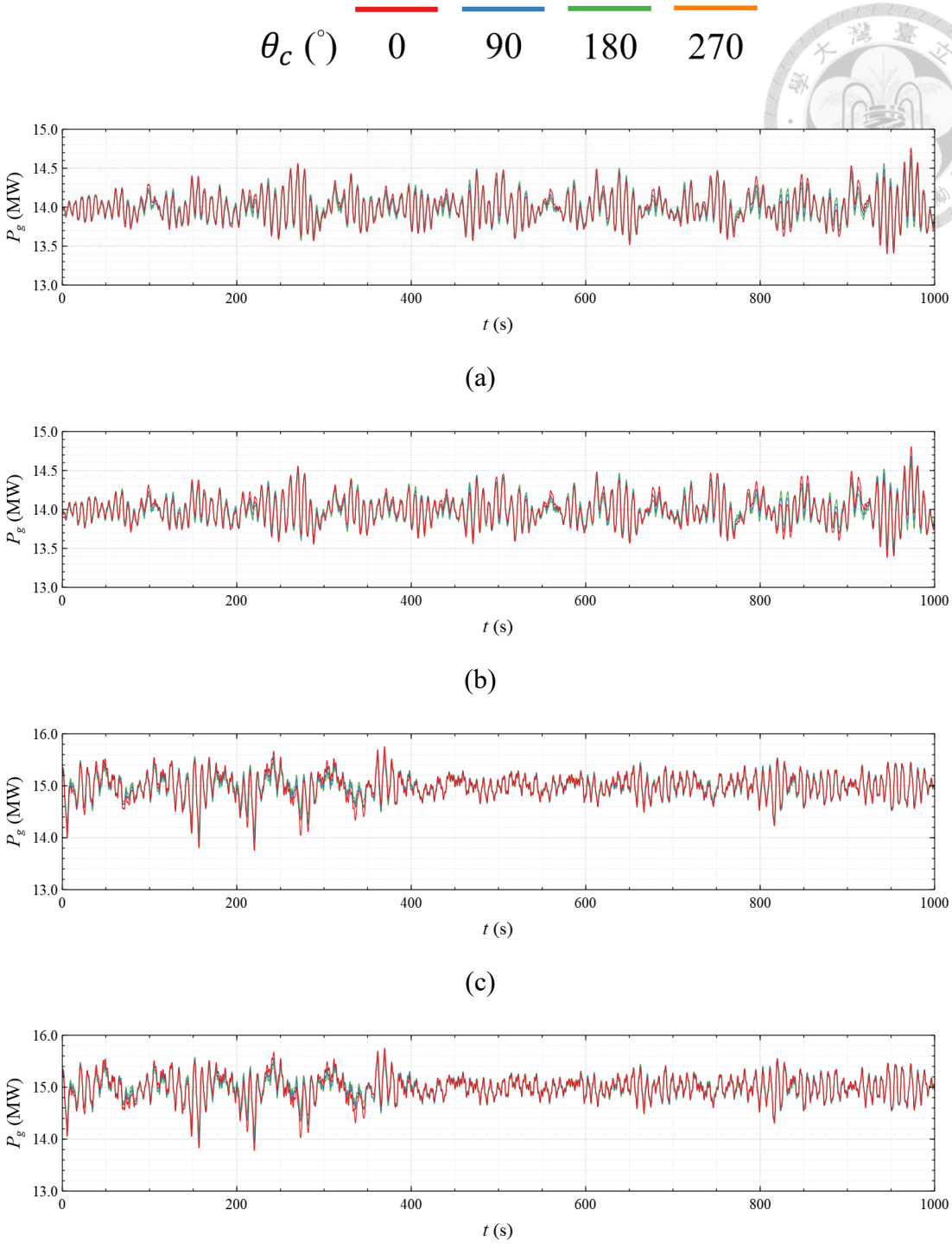

Figure 39 Generator electrical power predicted in time domain ($\theta_w = 0°$): (a) PF approach under CW condition, (b) VF approach under CW condition, (c) PF approach under HW condition, (d) VF approach under HW condition

doi:10.6342/NTU202204241

4.4.1 Common Wave Condition

The trajectories of the platform on xy-plane are shown in Figure 40 and Figure 41, those on xz-plane are shown in Figure 42 and Figure 43, and those on yz-plane are shown in Figure 44 and Figure 45. The maximums, minimums, and variations of the platform translation motions in time history under the CW condition are shown in Table 15 to Table 17. The trajectories of the platform between the two modeling approaches as well as among the four current directions are similar under the CW condition. The platform at $(\theta_w, \theta_c) = (0°, 0°)$ has the largest surge variation of 1.32 m which is found between 4.284 m and 5.604 m, and the platform at $(\theta_w, \theta_c) = (90°, 270°)$ has the smallest surge variation of 0.187 m which is found between -4.8 m and -4.613 m. The platform at $(\theta_w, \theta_c) = (120°, 90°)$ has the largest sway variation of 0.731 m which is found between -4.975 m and -4.244 m, and the platform at $(\theta_w, \theta_c) = (0°, 180°)$ has the smallest sway variation of 0.015 m which is found between -0.045 m and -0.03 m. The platform at $(\theta_w, \theta_c) = (180°, 180°)$ has the largest heave variation of 0.259 m which is found between -1.171 m and -0.912 m, and the platform at $(\theta_w, \theta_c) = (120°, 180°)$ has the smallest heave variation of 0.164 m which is found between -1.01 m and -0.846 m.

The mean values and standard deviations of the nacelle motions are shown in Figure 46 to Figure 51, and Table 18 to Table 23. The largest mean values of surge, sway, and heave motion of nacelle appear at $(\theta_w, \theta_c) = (180°, 180°)$, $(90°, 90°)$, and $(0°, 180°)$, and they are -21.274 m, -29.282 m, and -2.512 m, respectively. The smallest mean values of surge, sway, and heave motion of nacelle appear at $(\theta_w, \theta_c) = (60°, 0°)$, $(0°, 90°)$, and $(120°, 180°)$, and they are -4.139 m, -0.957 m, and 0.553 m, respectively. The largest standard deviations of surge, sway, and heave motion of

doi:10.6342/NTU202204241

nacelle appear at $(\theta_w, \theta_c) = (0°, 0°)$, $(180°, 270°)$, and $(0°, 0°)$, and they are 0.285 m, 0.197 m, and 0.061 m, respectively. The smallest standard deviations of surge, sway, and heave motion of nacelle appear at $(\theta_w, \theta_c) = (90°, 270°)$, $(0°, 180°)$, and $(120°, 90°)$, and they are 0.069 m, 0.054 m, and 0.023 m, respectively.

The mean values and standard deviations of the platform motions are shown in Figure 52 to Figure 63, and Table 24 to Table 35. The largest mean values of surge, sway, heave, roll, pitch, and yaw motions of platform appear at $(\theta_w, \theta_c) = (180°, 180°)$, $(90°, 90°)$, $(180°, 0°)$, $(90°, 180°)$, $(0°, 180°)$, and $(90°, 0°)$, and they are -7.507 m, -5.055 m, -1.037 m, 6.998°, 4.7°, and -10.848°, respectively. The smallest mean values of surge, sway, heave, roll, pitch, and yaw motions of platform appear at $(\theta_w, \theta_c) = (60°, 0°)$, $(0°, 270°)$, $(0°, 180°)$, $(180°, 270°)$, $(90°, 90°)$, and $(0°, 270°)$, and they are -2.09 m, -0.014 m, -0.331 m, -0.431°, -0.516°, and 0.237°, respectively. The largest standard deviations of surge, sway, heave, roll, pitch, and yaw motions of platform appear at $(\theta_w, \theta_c) = (0°, 0°)$, $(180°, 270°)$, $(180°, 180°)$, $(120°, 90°)$, $(0°, 0°)$, and $(120°, 90°)$, and they are 0.206 m, 0.188 m, 0.034 m, 0.062°, 0.055°, and 0.158°, respectively. The smallest standard deviations of surge, sway, heave, roll, pitch, and yaw motions of platform appear at $(\theta_w, \theta_c) = (90°, 270°)$, $(0°, 180°)$, $(120°, 90°)$, $(180°, 0°)$, $(90°, 0°)$, and $(0°, 180°)$, and they are 0.03 m, 0.003 m, 0.025 m, 0.009°, 0.017°, and 0.007°, respectively.

The mean values and standard deviations of the generator power are shown in Figure 64 and Figure 65, and Table 36 and Table 37. The largest mean value of generator power appears at $(\theta_w, \theta_c) = (0°, 0°)$, and it is 14.005 MW, while the smallest one appears at $(\theta_w, \theta_c) = (90°, 0°)$, and it is 12.602 MW. The largest standard deviation

doi:10.6342/NTU202204241

of generator power appears at $(\theta_w, \theta_c) = (0°, 0°)$, and it is 0.191 MW, while the smallest one appears at $(\theta_w, \theta_c) = (90°, 270°)$, and it is 0.097 MW.

The results show that the mean value and standard deviation of the motion response and generator power are sensitive to the wind direction. The difference of the mean value of the motion response and generator power between the two approaches as well as among the four current directions is small, while the difference of the standard deviation is relatively substantial. The offset of the wind turbine system remains under 21 m, and the mean pitch angle remains between -5° and 5° at all studied wind directions. Under the CW condition, $\theta_w = 0°$ delivering the highest mean generator power of up to 14.005 MW, is the most favorable wind direction for the wind turbine system to operate in the Hsinchu offshore area.

doi:10.6342/NTU202204241

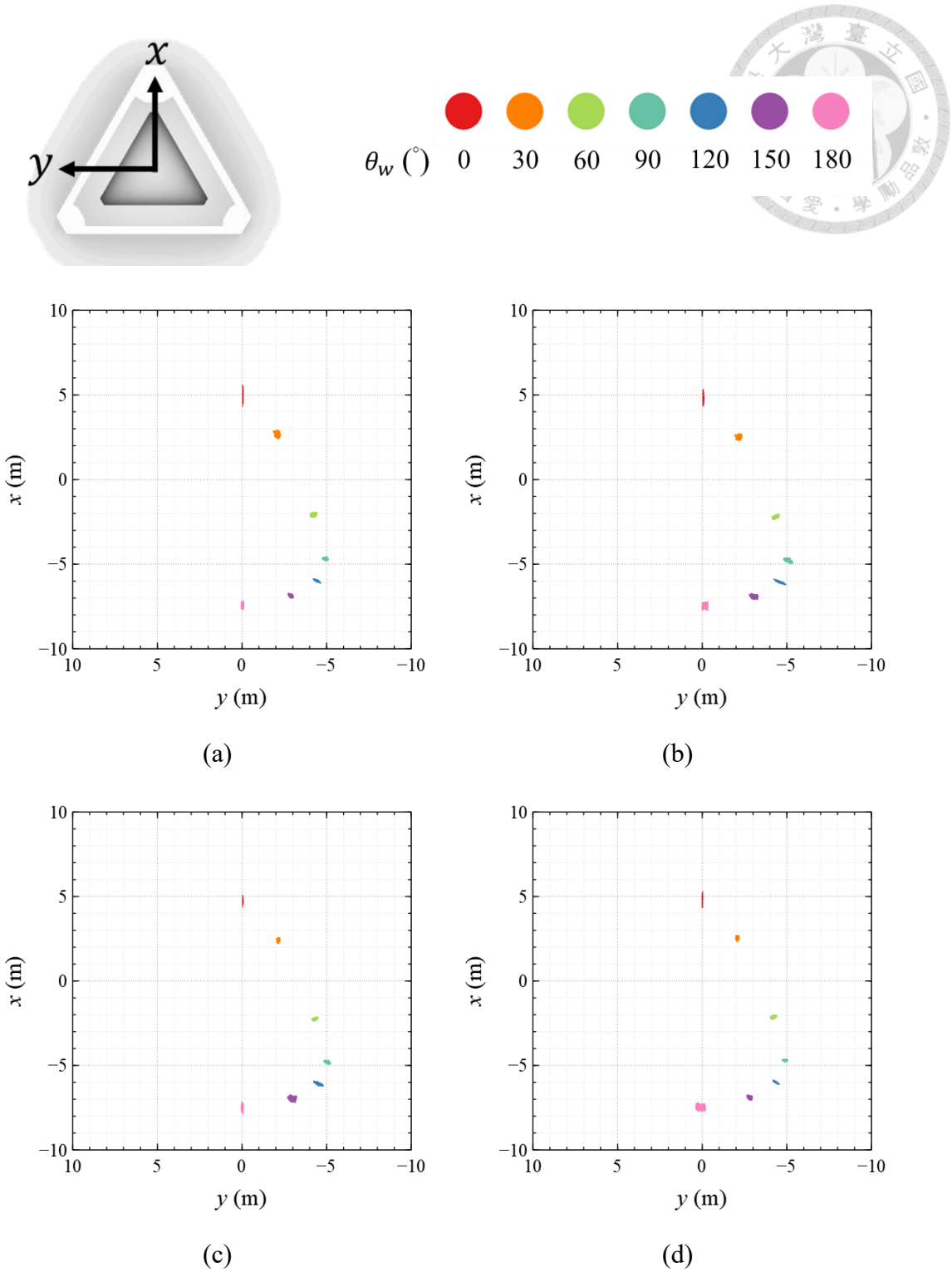

Figure 40 Platform trajectory on xy-plane via PF approach under CW condition: (a) $\theta_c = 0°$, (b) $\theta_c = 90°$, (c) $\theta_c = 180°$, (d) $\theta_c = 270°$

doi:10.6342/NTU202204241

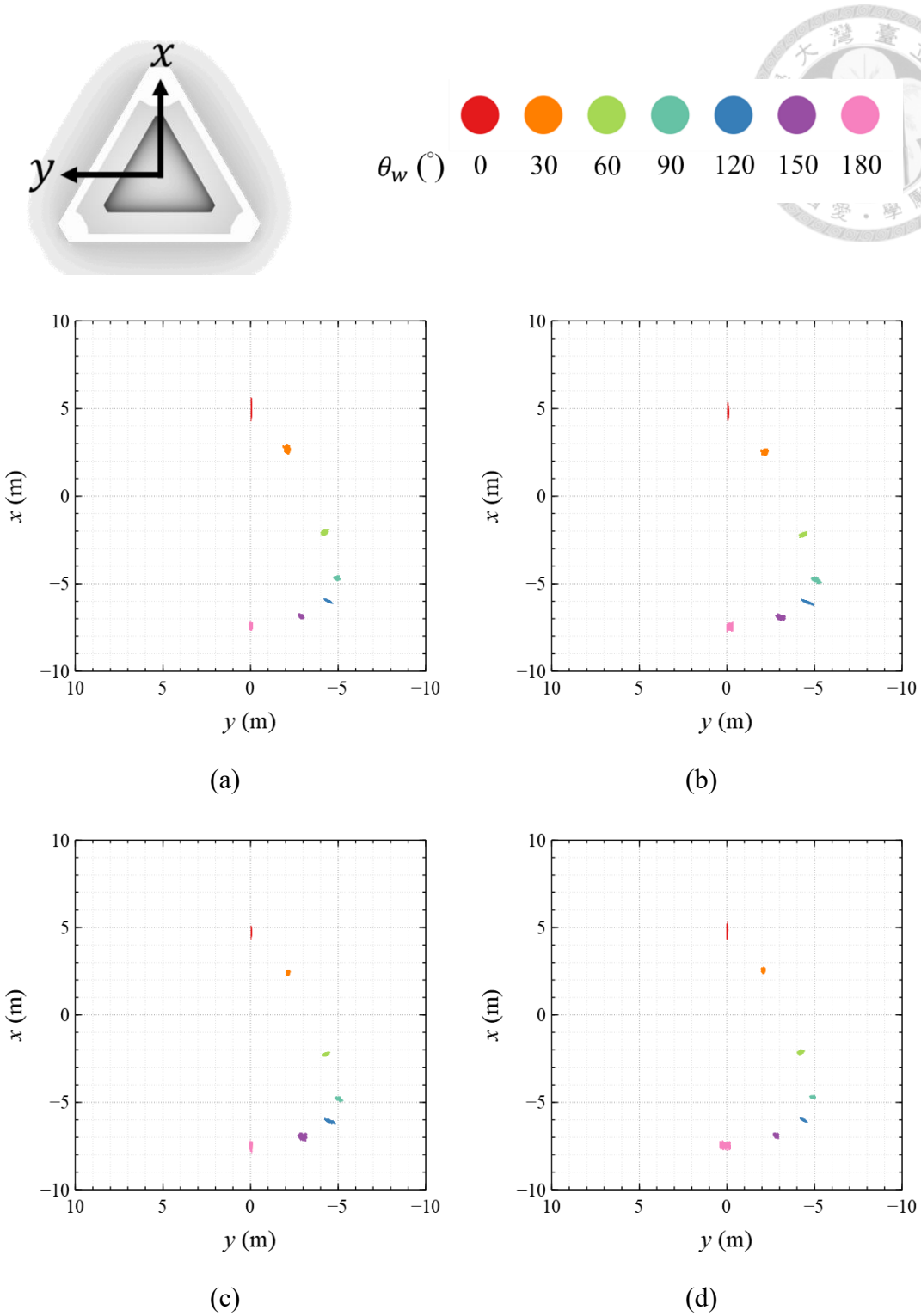

Figure 41 Platform trajectory on xy-plane via VF approach under CW condition: (a) $\theta_c = 0°$, (b) $\theta_c = 90°$, (c) $\theta_c = 180°$, (d) $\theta_c = 270°$

doi:10.6342/NTU202204241

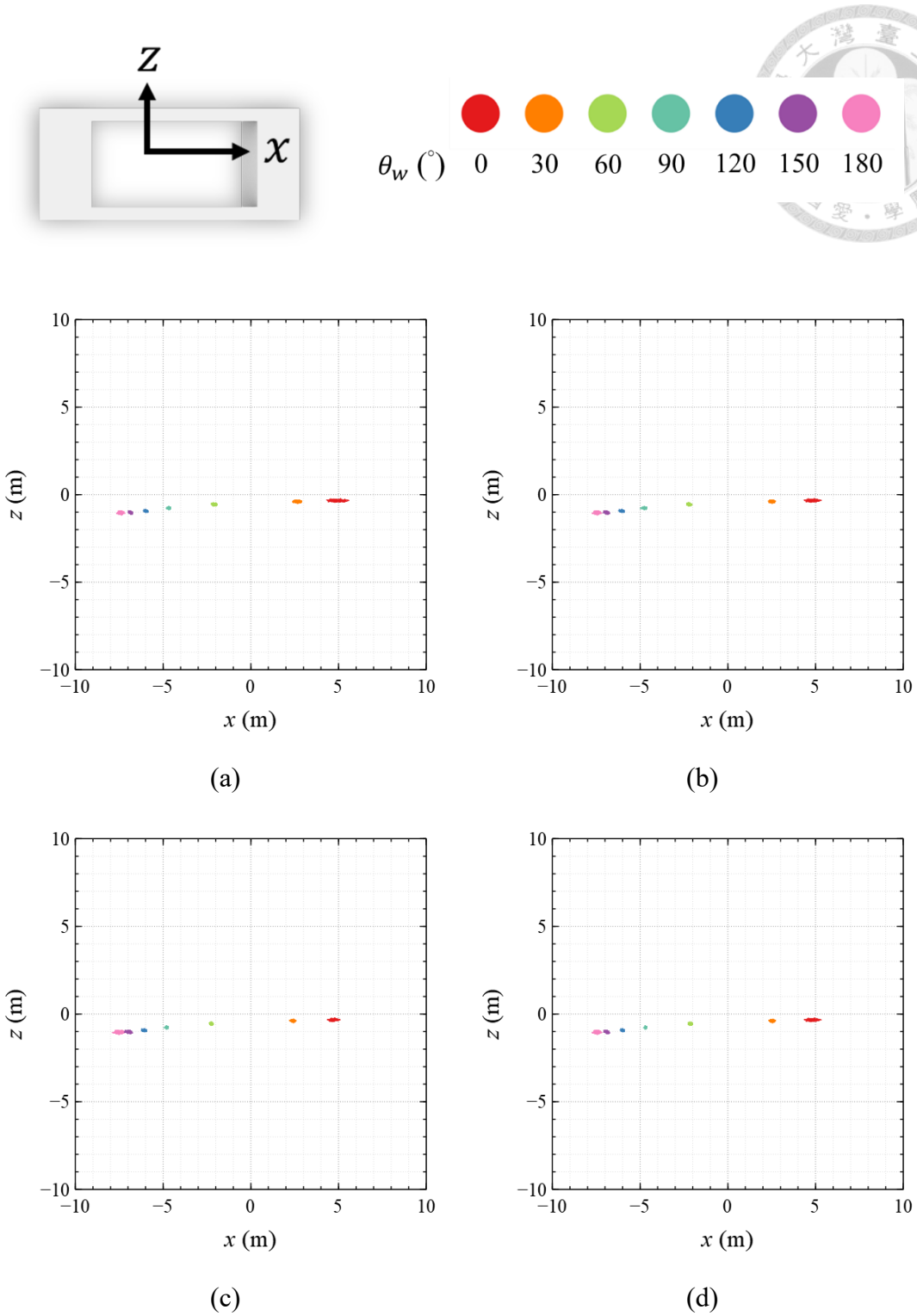

Figure 42 Platform trajectory on xz-plane via PF approach under CW condition: (a) $\theta_c = 0°$, (b) $\theta_c = 90°$, (c) $\theta_c = 180°$, (d) $\theta_c = 270°$

doi:10.6342/NTU202204241

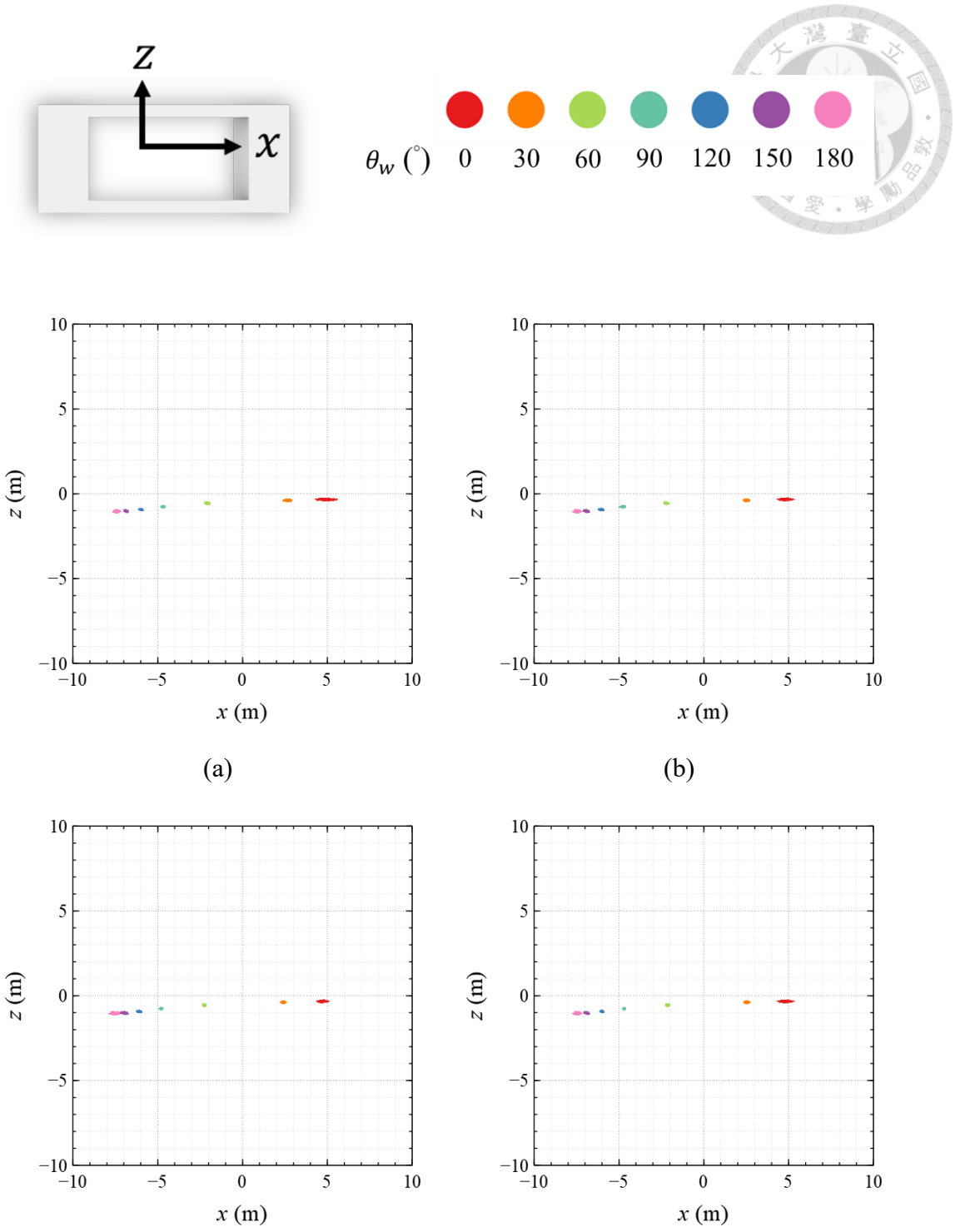

Figure 43 Platform trajectory on xz-plane via VF approach under CW condition: (a) $\theta_c = 0°$, (b) $\theta_c = 90°$, (c) $\theta_c = 180°$, (d) $\theta_c = 270°$

doi:10.6342/NTU202204241

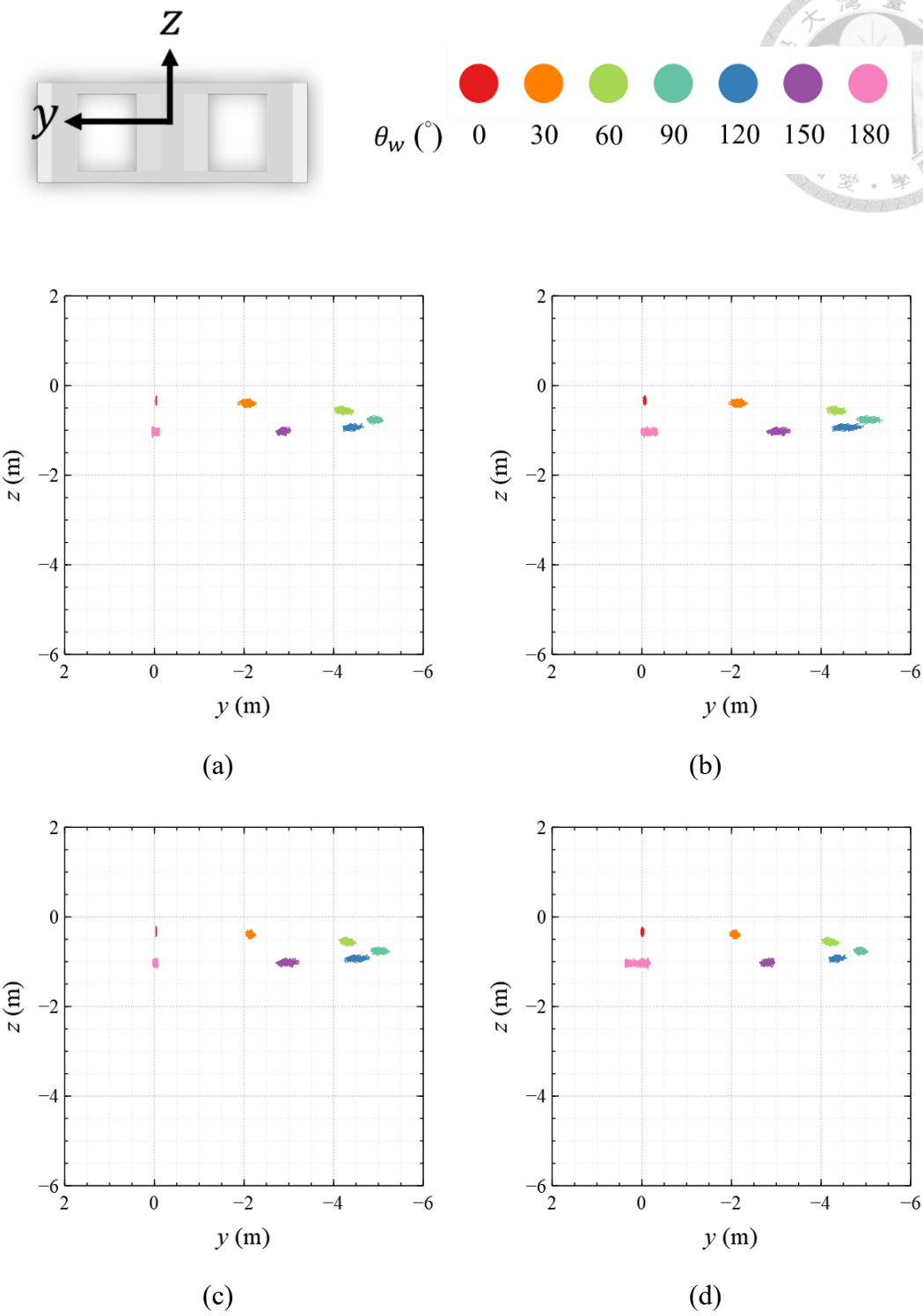

Figure 44 Platform trajectory on yz-plane via PF approach under CW condition: (a) $\theta_c = 0°$, (b) $\theta_c = 90°$, (c) $\theta_c = 180°$, (d) $\theta_c = 270°$

doi:10.6342/NTU202204241

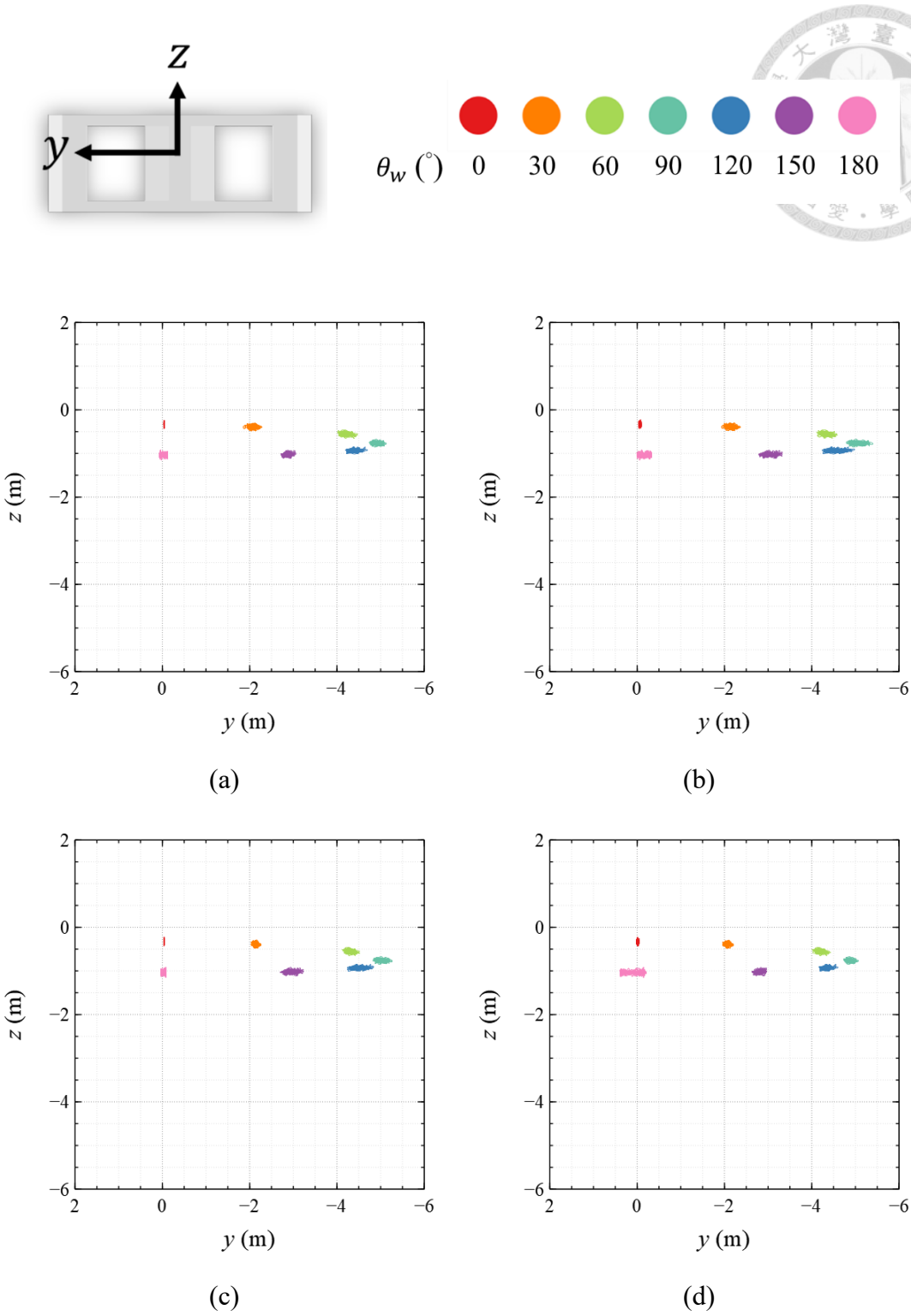

Figure 45 Platform trajectory on yz-plane via VF approach under CW condition: (a) $\theta_c = 0°$, (b) $\theta_c = 90°$, (c) $\theta_c = 180°$, (d) $\theta_c = 270°$

doi:10.6342/NTU202204241

Table 15 Platform surge motion in time history under CW condition: (a) Maximum, (b) Minimum, (c) Variation

(a)

	θ_c \ θ_w	0°	30°	60°	90°	120°	150°	180°
PF	0°	5.588	2.912	-1.918	-4.563	-5.858	-6.724	-7.160
VF		5.604	2.919	-1.921	-4.548	-5.862	-6.721	-7.178
PF	90°	5.323	2.714	-2.031	-4.626	-5.881	-6.732	-7.182
VF		5.330	2.715	-2.026	-4.615	-5.885	-6.726	-7.200
PF	180°	5.089	2.577	-2.124	-4.687	-5.920	-6.750	-7.156
VF		5.099	2.581	-2.135	-4.683	-5.929	-6.746	-7.173
PF	270°	5.314	2.714	-2.005	-4.613	-5.884	-6.743	-7.174
VF		5.320	2.723	-1.995	-4.608	-5.890	-6.739	-7.191

(b)

	θ_c \ θ_w	0°	30°	60°	90°	120°	150°	180°
PF	0°	4.318	2.393	-2.247	-4.816	-6.128	-7.003	-7.665
VF		4.284	2.392	-2.244	-4.830	-6.141	-7.008	-7.658
PF	90°	4.344	2.309	-2.357	-4.980	-6.230	-7.102	-7.753
VF		4.322	2.318	-2.367	-4.992	-6.246	-7.113	-7.755
PF	180°	4.354	2.205	-2.374	-4.950	-6.239	-7.205	-7.896
VF		4.352	2.218	-2.373	-4.959	-6.264	-7.218	-7.906
PF	270°	4.347	2.328	-2.272	-4.800	-6.136	-7.067	-7.754
VF		4.327	2.340	-2.270	-4.808	-6.152	-7.078	-7.758

(c)

	θ_c \ θ_w	0°	30°	60°	90°	120°	150°	180°
PF	0°	1.270	0.520	0.329	0.254	0.270	0.279	0.505
VF		1.320	0.527	0.323	0.282	0.279	0.287	0.479
PF	90°	0.978	0.405	0.325	0.354	0.350	0.369	0.571
VF		1.008	0.397	0.341	0.378	0.360	0.387	0.555
PF	180°	0.735	0.372	0.251	0.264	0.318	0.455	0.740
VF		0.747	0.362	0.239	0.277	0.335	0.472	0.734
PF	270°	0.966	0.386	0.267	0.187	0.252	0.325	0.580
VF		0.992	0.383	0.276	0.199	0.262	0.339	0.568

doi:10.6342/NTU202204241

Table 16 Platform sway motion in time history under CW condition: (a) Maximum, (b) Minimum, (c) Variation

(a)

	θ_c \ θ_w	0°	30°	60°	90°	120°	150°	180°
PF	0°	-0.028	-1.857	-4.005	-4.737	-4.197	-2.712	0.056
VF		-0.028	-1.854	-4.013	-4.741	-4.197	-2.714	0.067
PF	90°	-0.030	-1.940	-4.113	-4.789	-4.246	-2.782	0.025
VF		-0.029	-1.934	-4.118	-4.795	-4.244	-2.784	0.007
PF	180°	-0.030	-2.039	-4.113	-4.830	-4.239	-2.698	0.029
VF		-0.030	-2.036	-4.123	-4.829	-4.239	-2.703	0.030
PF	270°	0.018	-1.960	-4.000	-4.728	-4.173	-2.626	0.380
VF		0.019	-1.957	-4.005	-4.732	-4.171	-2.633	0.396

(b)

	θ_c \ θ_w	0°	30°	60°	90°	120°	150°	180°
PF	0°	-0.053	-2.279	-4.457	-5.111	-4.675	-3.047	-0.112
VF		-0.053	-2.282	-4.470	-5.129	-4.694	-3.060	-0.124
PF	90°	-0.095	-2.357	-4.574	-5.372	-4.946	-3.312	-0.349
VF		-0.099	-2.362	-4.584	-5.396	-4.975	-3.326	-0.337
PF	180°	-0.045	-2.256	-4.506	-5.247	-4.798	-3.233	-0.086
VF		-0.047	-2.259	-4.516	-5.267	-4.835	-3.228	-0.090
PF	270°	-0.042	-2.203	-4.428	-5.055	-4.578	-2.970	-0.188
VF		-0.044	-2.202	-4.428	-5.070	-4.600	-2.965	-0.203

(c)

	θ_c \ θ_w	0°	30°	60°	90°	120°	150°	180°
PF	0°	0.024	0.421	0.452	0.374	0.478	0.336	0.169
VF		0.025	0.428	0.456	0.388	0.497	0.346	0.191
PF	90°	0.065	0.417	0.460	0.583	0.700	0.530	0.373
VF		0.070	0.428	0.466	0.601	0.731	0.542	0.344
PF	180°	0.015	0.217	0.393	0.416	0.559	0.535	0.115
VF		0.017	0.223	0.393	0.438	0.596	0.525	0.120
PF	270°	0.060	0.243	0.427	0.327	0.404	0.344	0.568
VF		0.064	0.245	0.423	0.338	0.429	0.332	0.599

doi:10.6342/NTU202204241

Table 17 Platform heave motion in time history under CW condition: (a) Maximum, (b) Minimum, (c) Variation

(a)

	θ_c \ θ_w	0°	30°	60°	90°	120°	150°	180°
PF	0°	-0.232	-0.292	-0.450	-0.670	-0.847	-0.922	-0.912
VF		-0.243	-0.303	-0.457	-0.677	-0.850	-0.928	-0.924
PF	90°	-0.223	-0.291	-0.449	-0.670	-0.847	-0.922	-0.912
VF		-0.235	-0.301	-0.455	-0.675	-0.849	-0.927	-0.923
PF	180°	-0.217	-0.281	-0.448	-0.668	-0.843	-0.919	-0.912
VF		-0.228	-0.292	-0.457	-0.674	-0.846	-0.922	-0.921
PF	270°	-0.223	-0.284	-0.449	-0.669	-0.844	-0.920	-0.913
VF		-0.235	-0.295	-0.459	-0.675	-0.846	-0.926	-0.923

(b)

	θ_c \ θ_w	0°	30°	60°	90°	120°	150°	180°
PF	0°	-0.445	-0.499	-0.665	-0.865	-1.024	-1.121	-1.167
VF		-0.429	-0.484	-0.652	-0.854	-1.015	-1.111	-1.152
PF	90°	-0.444	-0.495	-0.664	-0.866	-1.023	-1.122	-1.168
VF		-0.430	-0.480	-0.650	-0.854	-1.015	-1.115	-1.152
PF	180°	-0.441	-0.495	-0.661	-0.863	-1.021	-1.121	-1.171
VF		-0.429	-0.482	-0.651	-0.851	-1.010	-1.115	-1.152
PF	270°	-0.444	-0.498	-0.662	-0.862	-1.021	-1.119	-1.168
VF		-0.430	-0.485	-0.652	-0.850	-1.011	-1.111	-1.152

(c)

	θ_c \ θ_w	0°	30°	60°	90°	120°	150°	180°
PF	0°	0.213	0.207	0.215	0.195	0.176	0.199	0.255
VF		0.186	0.181	0.195	0.177	0.165	0.184	0.227
PF	90°	0.221	0.204	0.215	0.197	0.177	0.199	0.256
VF		0.195	0.179	0.195	0.179	0.165	0.188	0.229
PF	180°	0.224	0.213	0.213	0.195	0.178	0.202	0.259
VF		0.201	0.190	0.194	0.177	0.164	0.193	0.231
PF	270°	0.220	0.214	0.213	0.193	0.177	0.199	0.256
VF		0.195	0.190	0.194	0.175	0.165	0.186	0.229

doi:10.6342/NTU202204241

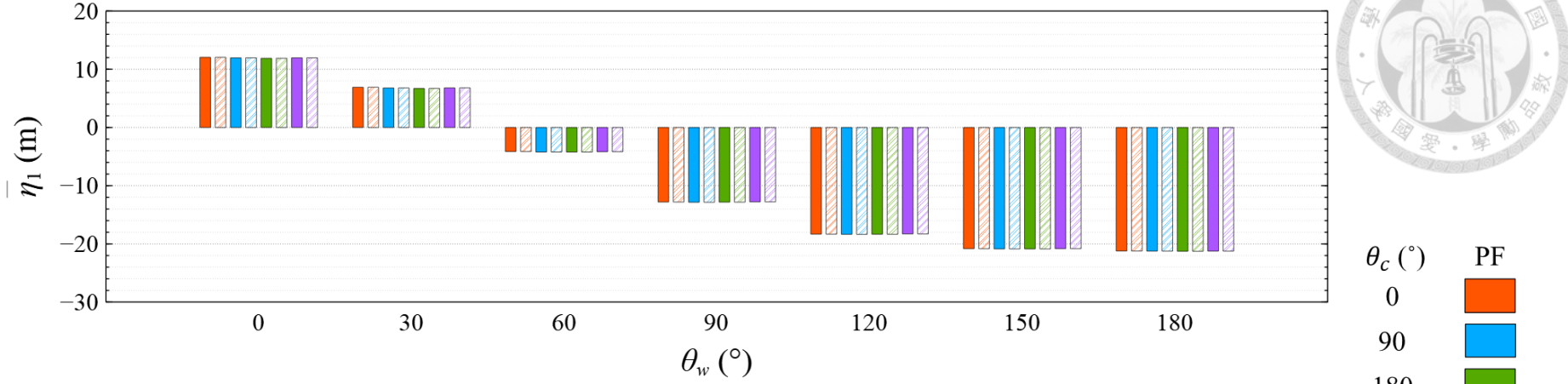

Figure 46 Comparison of mean value of nacelle surge motion under CW condition

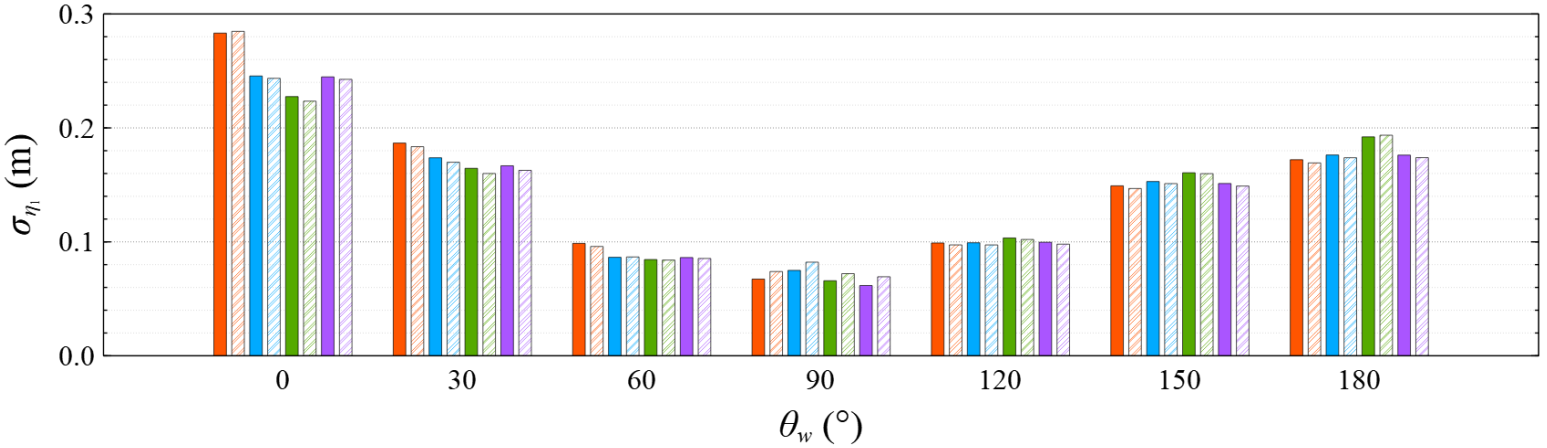

Figure 47 Comparison of standard deviation of nacelle surge motion under CW condition

doi:10.6342/NTU202204241

Table 18 Mean value of nacelle surge motion under CW condition

	θ_c \ θ_w	0°	30°	60°	90°	120°	150°	180°
PF (m)	0°	12.049	6.906	-4.141	-12.813	-18.328	-20.832	-21.228
VF (m)		12.047	6.911	-4.139	-12.815	-18.332	-20.835	-21.231
Difference (%)		0.010	-0.080	0.028	-0.016	-0.022	-0.016	-0.015
PF (m)	90°	11.960	6.787	-4.222	-12.851	-18.355	-20.865	-21.245
VF (m)		11.960	6.791	-4.220	-12.852	-18.360	-20.868	-21.248
Difference (%)		0.005	-0.054	0.031	-0.009	-0.023	-0.016	-0.016
PF (m)	180°	11.879	6.700	-4.226	-12.832	-18.342	-20.869	-21.271
VF (m)		11.880	6.704	-4.226	-12.833	-18.347	-20.872	-21.274
Difference (%)		-0.006	-0.062	0.003	-0.014	-0.026	-0.013	-0.014
PF (m)	270°	11.960	6.798	-4.162	-12.780	-18.291	-20.826	-21.246
VF (m)		11.960	6.803	-4.161	-12.782	-18.296	-20.829	-21.250
Difference (%)		0.004	-0.079	0.026	-0.015	-0.026	-0.014	-0.016

Table 19 Standard deviation of nacelle surge motion under CW condition

	θ_c \ θ_w	0°	30°	60°	90°	120°	150°	180°
PF (m)	0°	0.283	0.187	0.099	0.067	0.099	0.149	0.172
VF (m)		0.285	0.184	0.096	0.074	0.097	0.147	0.169
Difference (%)		-0.548	1.725	2.841	-8.944	1.736	1.623	1.671
PF (m)	90°	0.246	0.174	0.086	0.075	0.099	0.153	0.176
VF (m)		0.244	0.170	0.087	0.082	0.097	0.151	0.174
Difference (%)		0.838	2.316	-0.354	-8.768	1.955	1.214	1.384
PF (m)	180°	0.227	0.165	0.084	0.066	0.103	0.161	0.192
VF (m)		0.223	0.160	0.084	0.072	0.102	0.160	0.194
Difference (%)		1.794	2.852	0.560	-8.617	1.297	0.488	-0.738
PF (m)	270°	0.245	0.167	0.086	0.062	0.100	0.151	0.176
VF (m)		0.243	0.163	0.085	0.069	0.098	0.149	0.174
Difference (%)		0.885	2.464	0.938	-11.077	1.711	1.498	1.275

doi:10.6342/NTU202204241

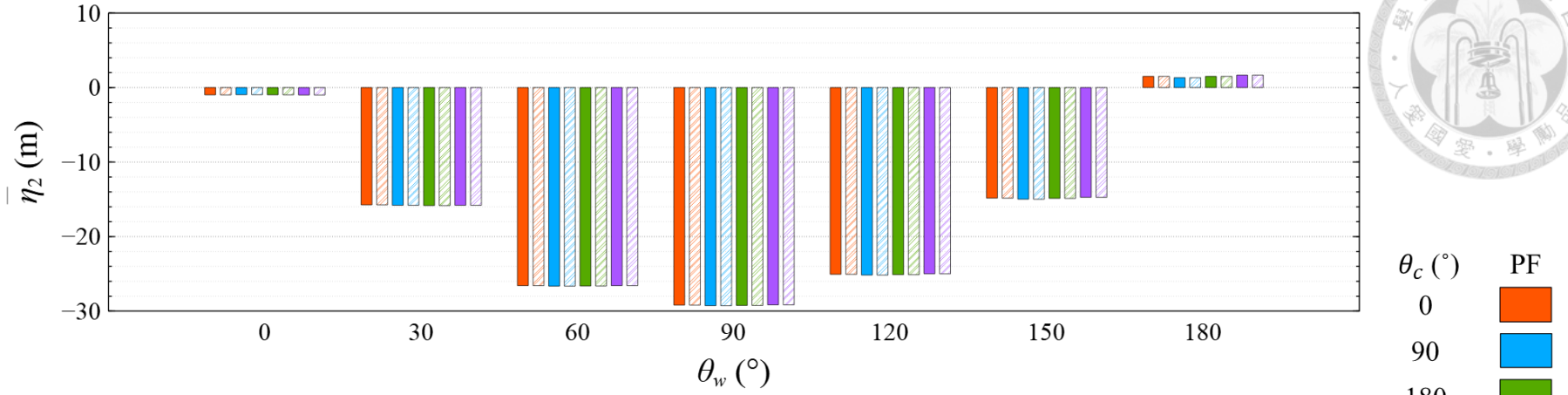

Figure 48 Comparison of mean value of nacelle sway motion under CW condition

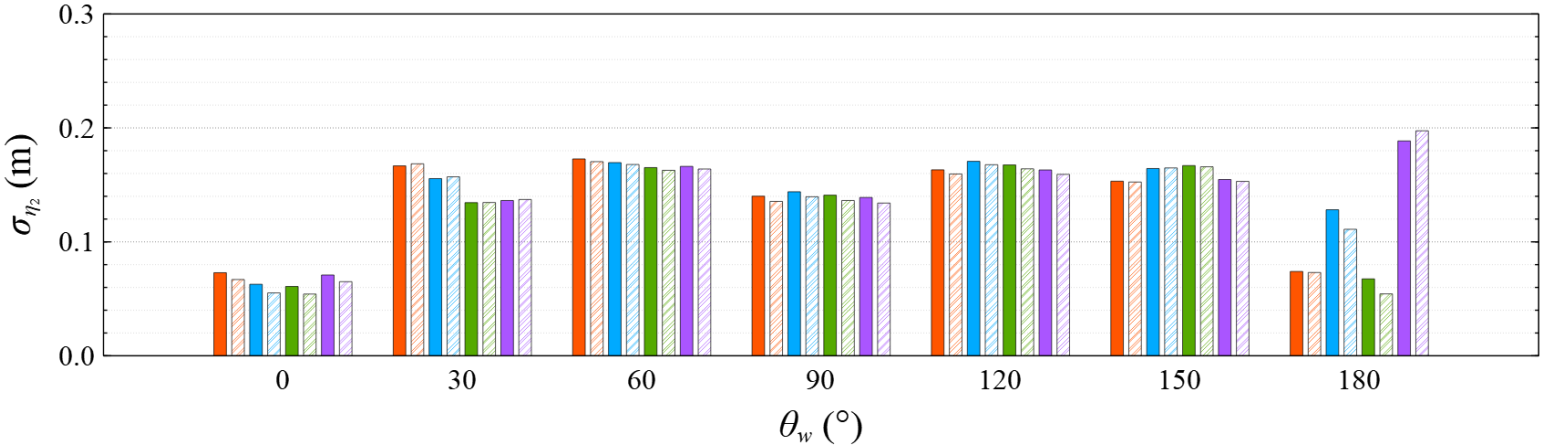

Figure 49 Comparison of standard deviation of nacelle sway motion under CW condition

doi:10.6342/NTU202204241

Table 20 Mean value of nacelle sway motion under CW condition

	θ_c \ θ_w	0°	30°	60°	90°	120°	150°	180°
PF (m)	0°	-0.976	-15.741	-26.588	-29.200	-25.059	-14.835	1.508
VF (m)		-0.979	-15.740	-26.592	-29.206	-25.066	-14.843	1.511
Difference (%)		-0.321	0.002	-0.015	-0.021	-0.025	-0.054	-0.161
PF (m)	90°	-0.954	-15.798	-26.654	-29.277	-25.159	-14.979	1.332
VF (m)		-0.957	-15.800	-26.658	-29.282	-25.165	-14.987	1.331
Difference (%)		-0.354	-0.012	-0.016	-0.018	-0.027	-0.057	0.039
PF (m)	180°	-0.969	-15.834	-26.635	-29.243	-25.107	-14.869	1.509
VF (m)		-0.971	-15.836	-26.641	-29.249	-25.114	-14.877	1.509
Difference (%)		-0.176	-0.014	-0.024	-0.021	-0.029	-0.050	-0.002
PF (m)	270°	-0.993	-15.798	-26.587	-29.162	-24.990	-14.727	1.676
VF (m)		-0.993	-15.800	-26.592	-29.167	-24.997	-14.732	1.677
Difference (%)		0.000	-0.008	-0.019	-0.019	-0.027	-0.034	-0.050

Table 21 Standard deviation of nacelle sway motion under CW condition

	θ_c \ θ_w	0°	30°	60°	90°	120°	150°	180°
PF (m)	0°	0.073	0.167	0.173	0.140	0.163	0.153	0.074
VF (m)		0.067	0.169	0.170	0.136	0.160	0.153	0.073
Difference (%)		8.938	-1.072	1.406	3.375	2.284	0.470	1.273
PF (m)	90°	0.063	0.156	0.170	0.144	0.171	0.164	0.128
VF (m)		0.055	0.157	0.168	0.140	0.168	0.165	0.111
Difference (%)		13.750	-0.990	0.986	3.149	1.765	-0.319	15.450
PF (m)	180°	0.061	0.134	0.165	0.141	0.168	0.167	0.067
VF (m)		0.054	0.135	0.163	0.136	0.164	0.166	0.054
Difference (%)		12.295	-0.080	1.481	3.433	2.083	0.637	24.235
PF (m)	270°	0.071	0.136	0.166	0.139	0.163	0.155	0.189
VF (m)		0.065	0.137	0.164	0.134	0.159	0.153	0.197
Difference (%)		9.000	-0.649	1.398	3.662	2.417	1.082	-4.517

doi:10.6342/NTU202204241

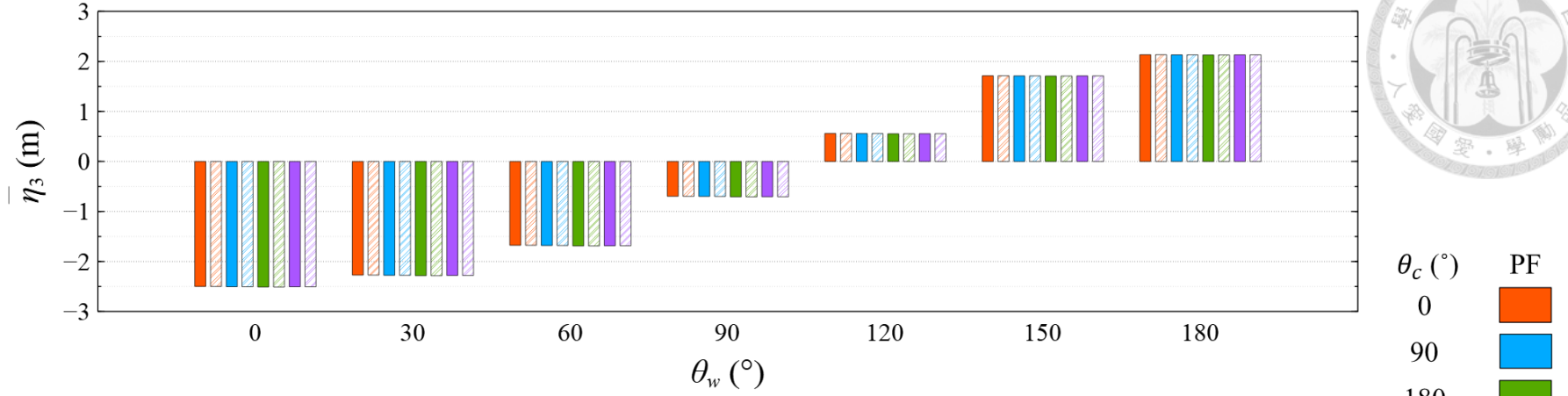

Figure 50 Comparison of mean value of nacelle heave motion under CW condition

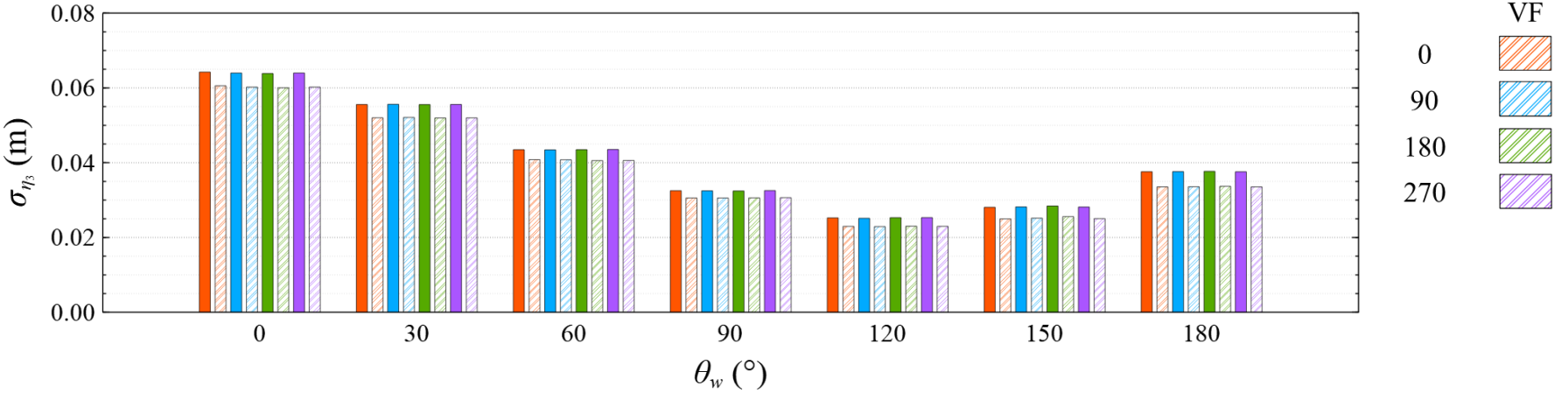

Figure 51 Comparison of standard deviation of nacelle heave motion under CW condition

doi:10.6342/NTU202204241

Table 22 Mean value of nacelle heave motion under CW condition

	θ_c \ θ_w	0°	30°	60°	90°	120°	150°	180°
PF (m)	0°	-2.499	-2.272	-1.677	-0.697	0.560	1.714	2.135
VF (m)		-2.500	-2.272	-1.677	-0.697	0.560	1.714	2.135
Difference (%)		-0.032	-0.031	-0.012	-0.044	0.026	-0.004	-0.008
PF (m)	90°	-2.505	-2.276	-1.680	-0.699	0.558	1.711	2.132
VF (m)		-2.506	-2.277	-1.681	-0.699	0.558	1.711	2.132
Difference (%)		-0.037	-0.030	-0.014	-0.041	0.032	-0.003	-0.008
PF (m)	180°	-2.511	-2.284	-1.689	-0.706	0.553	1.708	2.129
VF (m)		-2.512	-2.284	-1.689	-0.707	0.553	1.708	2.129
Difference (%)		-0.037	-0.032	-0.019	-0.054	0.039	-0.003	-0.004
PF (m)	270°	-2.505	-2.279	-1.685	-0.705	0.555	1.711	2.132
VF (m)		-2.506	-2.280	-1.686	-0.705	0.555	1.711	2.132
Difference (%)		-0.036	-0.031	-0.017	-0.049	0.033	-0.006	-0.008

Table 23 Standard deviation of nacelle heave motion under CW condition

	θ_c \ θ_w	0°	30°	60°	90°	120°	150°	180°
PF (m)	0°	0.064	0.056	0.043	0.033	0.025	0.028	0.038
VF (m)		0.061	0.052	0.041	0.031	0.023	0.025	0.034
Difference (%)		6.024	6.822	6.522	6.358	9.899	12.485	12.053
PF (m)	90°	0.064	0.056	0.043	0.032	0.025	0.028	0.038
VF (m)		0.060	0.052	0.041	0.031	0.023	0.025	0.034
Difference (%)		6.254	6.777	6.510	6.275	9.618	11.963	12.038
PF (m)	180°	0.064	0.056	0.043	0.032	0.025	0.028	0.038
VF (m)		0.060	0.052	0.041	0.031	0.023	0.026	0.034
Difference (%)		6.366	6.912	7.234	6.010	9.883	11.104	11.887
PF (m)	270°	0.064	0.056	0.044	0.033	0.025	0.028	0.038
VF (m)		0.060	0.052	0.041	0.031	0.023	0.025	0.034
Difference (%)		6.250	6.904	7.252	6.174	10.143	12.381	12.035

doi:10.6342/NTU202204241

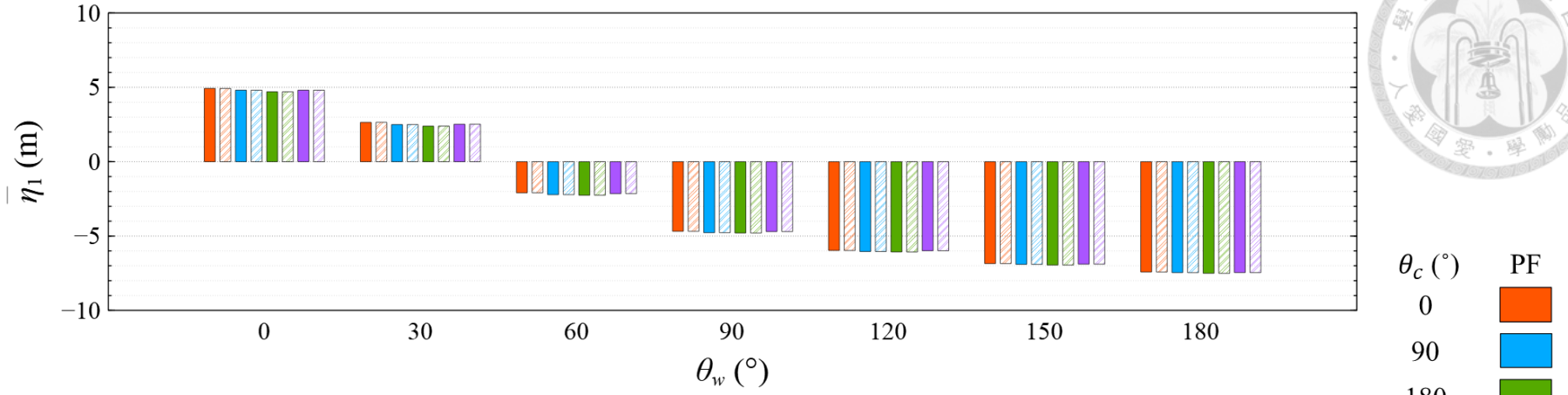

Figure 52 Comparison of mean value of platform surge motion under CW condition

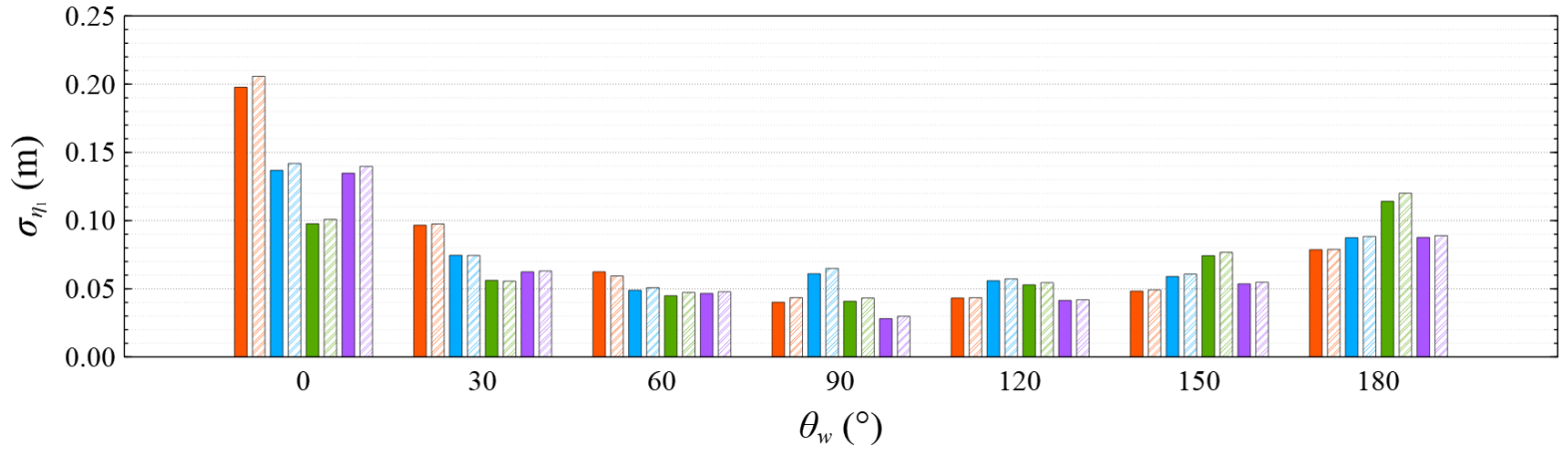

Figure 53 Comparison of standard deviation of platform surge motion under CW condition

doi:10.6342/NTU202204241

Table 24 Mean value of platform surge motion under CW condition

	θ_w / θ_c	0°	30°	60°	90°	120°	150°	180°
PF (m)	0°	4.929	2.644	-2.093	-4.681	-5.970	-6.851	-7.417
VF (m)		4.925	2.647	-2.090	-4.682	-5.973	-6.851	-7.419
Difference (%)		0.075	-0.123	0.108	-0.024	-0.045	0.005	-0.024
PF (m)	90°	4.812	2.498	-2.218	-4.772	-6.041	-6.905	-7.458
VF (m)		4.809	2.500	-2.217	-4.774	-6.043	-6.906	-7.460
Difference (%)		0.072	-0.069	0.080	-0.029	-0.046	-0.005	-0.029
PF (m)	180°	4.703	2.391	-2.259	-4.795	-6.070	-6.950	-7.505
VF (m)		4.701	2.394	-2.257	-4.796	-6.074	-6.949	-7.507
Difference (%)		0.045	-0.102	0.060	-0.029	-0.061	0.006	-0.031
PF (m)	270°	4.812	2.521	-2.148	-4.697	-5.987	-6.889	-7.455
VF (m)		4.808	2.524	-2.145	-4.698	-5.990	-6.890	-7.457
Difference (%)		0.072	-0.139	0.116	-0.021	-0.055	-0.011	-0.027

Table 25 Standard deviation of platform surge motion under CW condition

	θ_w / θ_c	0°	30°	60°	90°	120°	150°	180°
PF (m)	0°	0.198	0.097	0.062	0.040	0.043	0.048	0.079
VF (m)		0.206	0.097	0.059	0.044	0.043	0.049	0.079
Difference (%)		-3.893	-0.912	5.224	-7.738	-0.690	-1.695	-0.295
PF (m)	90°	0.137	0.075	0.049	0.061	0.056	0.059	0.087
VF (m)		0.142	0.074	0.051	0.065	0.057	0.061	0.088
Difference (%)		-3.595	0.154	-3.765	-6.001	-2.380	-2.929	-1.045
PF (m)	180°	0.098	0.056	0.045	0.041	0.053	0.074	0.114
VF (m)		0.101	0.056	0.047	0.043	0.054	0.077	0.120
Difference (%)		-3.165	1.079	-5.041	-5.458	-2.902	-3.134	-4.990
PF (m)	270°	0.135	0.062	0.047	0.028	0.041	0.054	0.088
VF (m)		0.140	0.063	0.048	0.030	0.042	0.055	0.089
Difference (%)		-3.574	-0.990	-2.623	-5.618	-1.092	-2.186	-1.455

doi:10.6342/NTU202204241

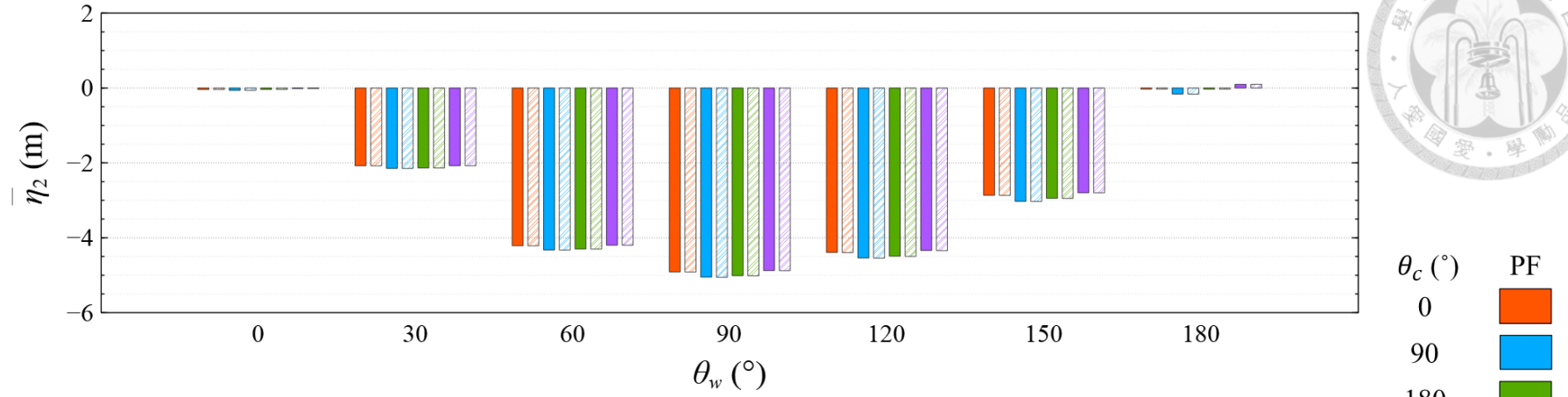

Figure 54 Comparison of mean value of platform sway motion under CW condition

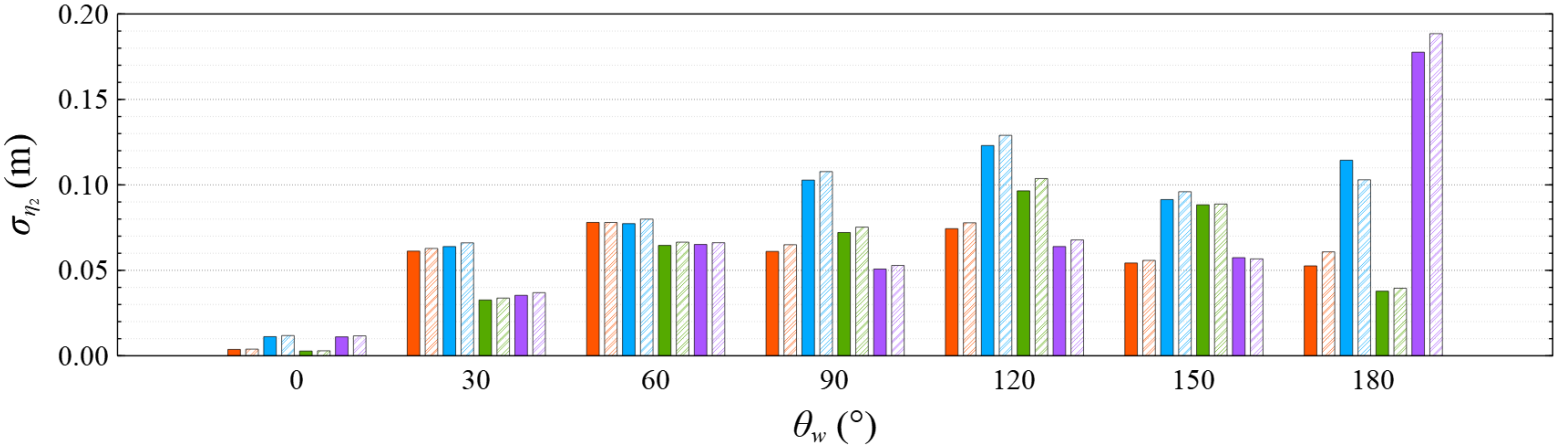

Figure 55 Comparison of standard deviation of platform sway motion under CW condition

doi:10.6342/NTU202204241

Table 26 Mean value of platform sway motion under CW condition

	θ_c \ θ_w	0°	30°	60°	90°	120°	150°	180°
PF (m)	0°	-0.040	-2.077	-4.213	-4.911	-4.391	-2.866	-0.028
VF (m)		-0.040	-2.077	-4.214	-4.915	-4.395	-2.868	-0.028
Difference (%)		-1.061	0.006	-0.016	-0.069	-0.086	-0.066	1.397
PF (m)	90°	-0.064	-2.147	-4.326	-5.050	-4.539	-3.027	-0.161
VF (m)		-0.064	-2.147	-4.328	-5.055	-4.543	-3.031	-0.161
Difference (%)		-0.997	-0.029	-0.043	-0.090	-0.091	-0.123	-0.413
PF (m)	180°	-0.038	-2.136	-4.300	-5.011	-4.492	-2.947	-0.029
VF (m)		-0.038	-2.136	-4.302	-5.015	-4.497	-2.948	-0.029
Difference (%)		-1.295	0.006	-0.047	-0.077	-0.110	-0.049	-1.793
PF (m)	270°	-0.014	-2.076	-4.197	-4.875	-4.339	-2.798	0.098
VF (m)		-0.014	-2.075	-4.198	-4.878	-4.343	-2.800	0.098
Difference (%)		-1.701	0.012	-0.014	-0.053	-0.092	-0.070	-0.055

Table 27 Standard deviation of platform sway motion under CW condition

	θ_c \ θ_w	0°	30°	60°	90°	120°	150°	180°
PF (m)	0°	0.004	0.061	0.078	0.061	0.074	0.054	0.053
VF (m)		0.004	0.063	0.078	0.065	0.078	0.056	0.061
Difference (%)		-4.362	-2.497	0.017	-6.027	-4.425	-2.745	-13.509
PF (m)	90°	0.011	0.064	0.077	0.103	0.123	0.091	0.114
VF (m)		0.012	0.066	0.080	0.108	0.129	0.096	0.103
Difference (%)		-5.359	-3.287	-3.291	-4.613	-4.627	-4.775	11.127
PF (m)	180°	0.003	0.033	0.065	0.072	0.097	0.088	0.038
VF (m)		0.003	0.034	0.066	0.075	0.104	0.089	0.040
Difference (%)		-5.044	-3.315	-2.840	-4.181	-6.939	-0.499	-4.330
PF (m)	270°	0.011	0.035	0.065	0.051	0.064	0.057	0.178
VF (m)		0.012	0.037	0.066	0.053	0.068	0.057	0.188
Difference (%)		-5.014	-4.207	-1.564	-3.996	-5.707	1.267	-5.756

doi:10.6342/NTU202204241

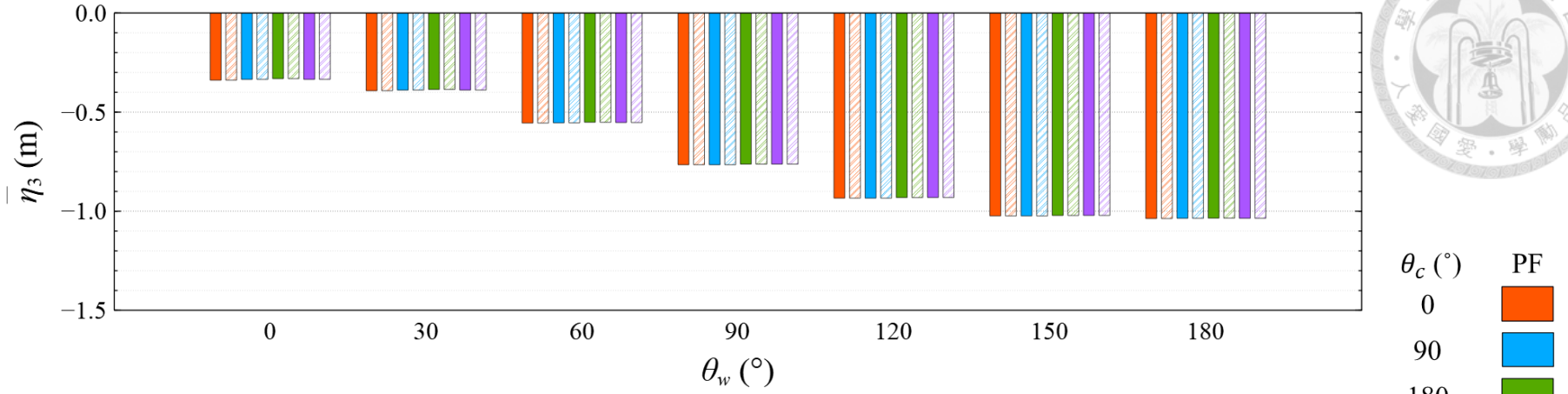

Figure 56 Comparison of mean value of platform heave motion under CW condition

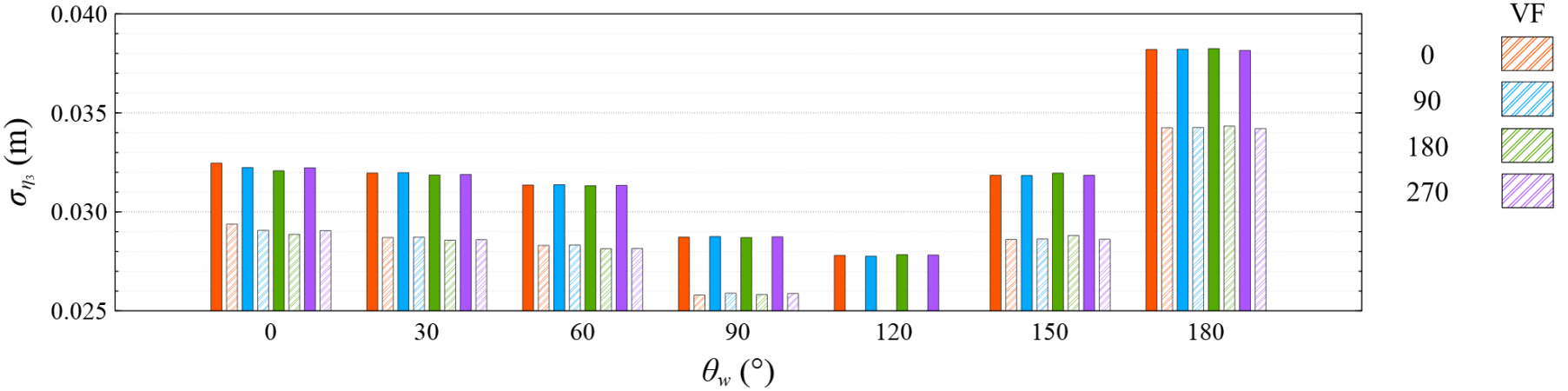

Figure 57 Comparison of standard deviation of platform heave motion under CW condition

doi:10.6342/NTU202204241

Table 28 Mean value of platform heave motion under CW condition

	θ_c \ θ_w	0°	30°	60°	90°	120°	150°	180°
PF (m)	0°	-0.339	-0.392	-0.555	-0.765	-0.934	-1.024	-1.037
VF (m)		-0.339	-0.392	-0.555	-0.765	-0.934	-1.024	-1.037
Difference (%)		0.018	0.000	0.002	-0.005	-0.007	-0.011	-0.006
PF (m)	90°	-0.335	-0.389	-0.554	-0.765	-0.934	-1.024	-1.036
VF (m)		-0.335	-0.389	-0.554	-0.766	-0.934	-1.024	-1.036
Difference (%)		0.018	0.007	0.002	-0.011	-0.011	-0.010	-0.006
PF (m)	180°	-0.331	-0.386	-0.551	-0.762	-0.931	-1.021	-1.035
VF (m)		-0.331	-0.386	-0.551	-0.762	-0.931	-1.021	-1.035
Difference (%)		0.006	0.004	-0.001	-0.010	-0.012	-0.008	-0.003
PF (m)	270°	-0.335	-0.389	-0.552	-0.762	-0.931	-1.021	-1.036
VF (m)		-0.335	-0.389	-0.552	-0.762	-0.931	-1.021	-1.036
Difference (%)		0.018	-0.001	0.000	-0.006	-0.008	-0.007	-0.006

Table 29 Standard deviation of platform heave motion under CW condition

	θ_c \ θ_w	0°	30°	60°	90°	120°	150°	180°
PF (m)	0°	0.032	0.032	0.031	0.029	0.028	0.032	0.038
VF (m)		0.029	0.029	0.028	0.026	0.025	0.029	0.034
Difference (%)		10.473	11.338	10.766	11.340	11.529	11.317	11.560
PF (m)	90°	0.032	0.032	0.031	0.029	0.028	0.032	0.038
VF (m)		0.029	0.029	0.028	0.026	0.025	0.029	0.034
Difference (%)		10.911	11.351	10.727	11.041	11.454	11.189	11.544
PF (m)	180°	0.032	0.032	0.031	0.029	0.028	0.032	0.038
VF (m)		0.029	0.029	0.028	0.026	0.025	0.029	0.034
Difference (%)		11.118	11.523	11.298	11.155	11.514	10.922	11.395
PF (m)	270°	0.032	0.032	0.031	0.029	0.028	0.032	0.038
VF (m)		0.029	0.029	0.028	0.026	0.025	0.029	0.034
Difference (%)		10.917	11.507	11.328	11.079	11.480	11.279	11.548

doi:10.6342/NTU202204241

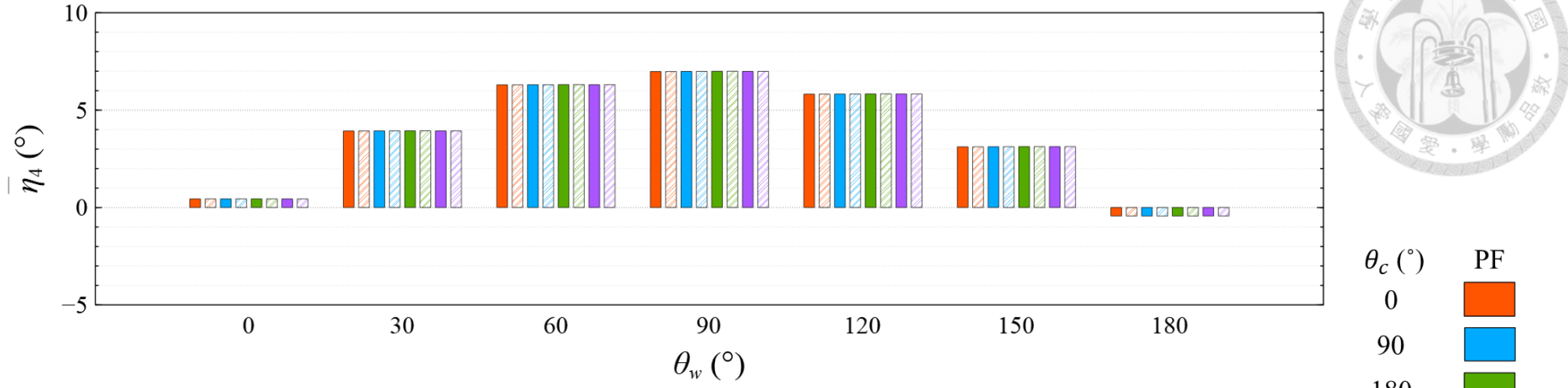

Figure 58 Comparison of mean value of platform roll motion under CW condition

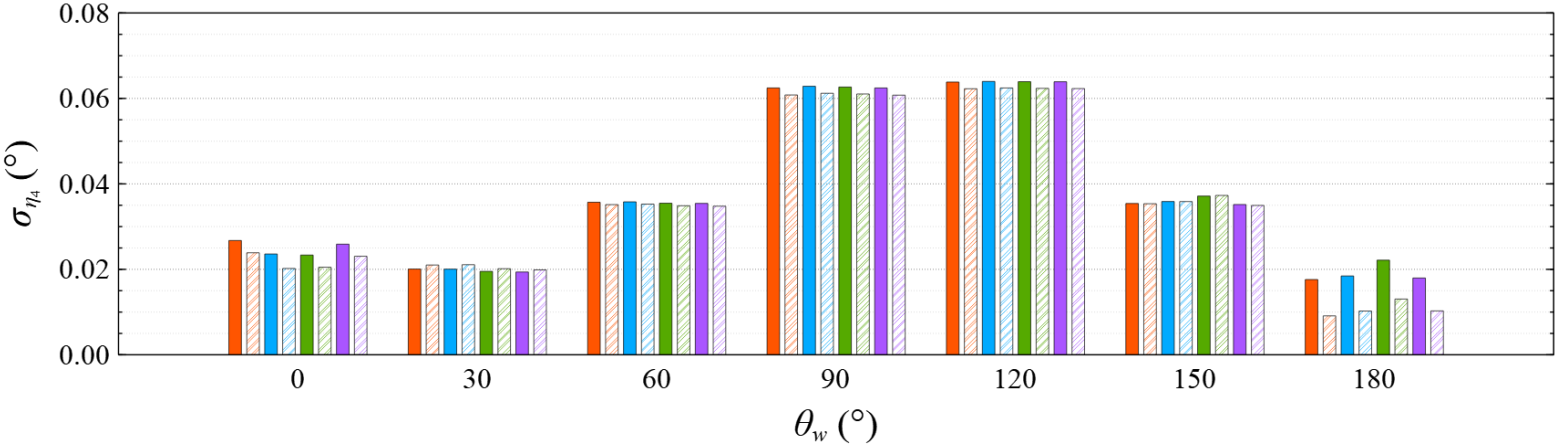

Figure 59 Comparison of standard deviation of platform roll motion under CW condition condition

doi:10.6342/NTU202204241

Table 30 Mean value of value of platform roll motion under CW condition

	θ_w / θ_c	0°	30°	60°	90°	120°	150°	180°
PF (°)	0°	0.442	3.929	6.299	6.981	5.820	3.117	-0.434
VF (°)		0.442	3.929	6.299	6.982	5.821	3.117	-0.435
Difference (%)		-0.013	-0.010	-0.004	-0.014	-0.013	-0.002	-0.019
PF (°)	90°	0.444	3.933	6.304	6.989	5.828	3.121	-0.438
VF (°)		0.444	3.933	6.304	6.990	5.829	3.121	-0.439
Difference (%)		0.001	-0.010	-0.005	-0.015	-0.012	-0.004	-0.063
PF (°)	180°	0.444	3.935	6.311	6.997	5.835	3.126	-0.435
VF (°)		0.444	3.936	6.311	6.998	5.836	3.126	-0.436
Difference (%)		-0.009	-0.014	-0.007	-0.017	-0.015	0.003	-0.079
PF (°)	270°	0.442	3.932	6.306	6.990	5.830	3.125	-0.431
VF (°)		0.442	3.932	6.306	6.991	5.831	3.125	-0.431
Difference (%)		0.002	-0.011	-0.006	-0.015	-0.014	-0.011	-0.056

Table 31 Standard deviation of platform roll motion under CW condition

	θ_w / θ_c	0°	30°	60°	90°	120°	150°	180°
PF (°)	0°	0.027	0.020	0.036	0.062	0.064	0.035	0.018
VF (°)		0.024	0.021	0.035	0.061	0.062	0.035	0.009
Difference (%)		12.018	-4.487	1.584	2.709	2.512	0.165	93.340
PF (°)	90°	0.024	0.020	0.036	0.063	0.064	0.036	0.018
VF (°)		0.020	0.021	0.035	0.061	0.062	0.036	0.010
Difference (%)		16.778	-4.929	1.498	2.673	2.445	0.042	80.141
PF (°)	180°	0.023	0.020	0.035	0.063	0.064	0.037	0.022
VF (°)		0.020	0.020	0.035	0.061	0.062	0.037	0.013
Difference (%)		13.919	-3.073	1.687	2.655	2.512	-0.401	69.742
PF (°)	270°	0.026	0.019	0.035	0.062	0.064	0.035	0.018
VF (°)		0.023	0.020	0.035	0.061	0.062	0.035	0.010
Difference (%)		12.279	-2.528	1.863	2.768	2.564	0.609	74.895

doi:10.6342/NTU202204241

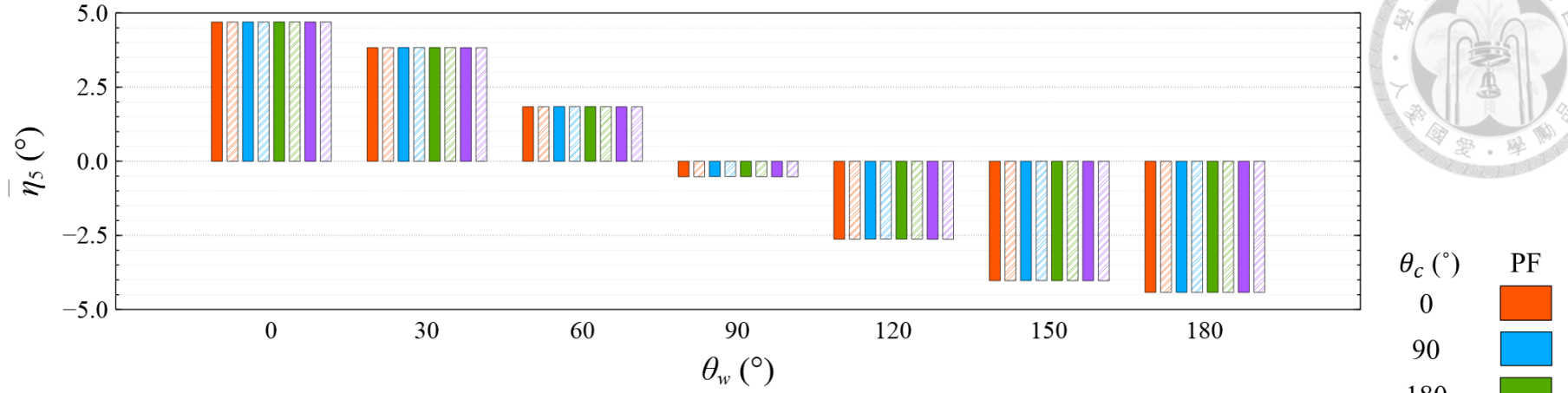

Figure 60 Comparison of mean value of platform pitch motion under CW condition

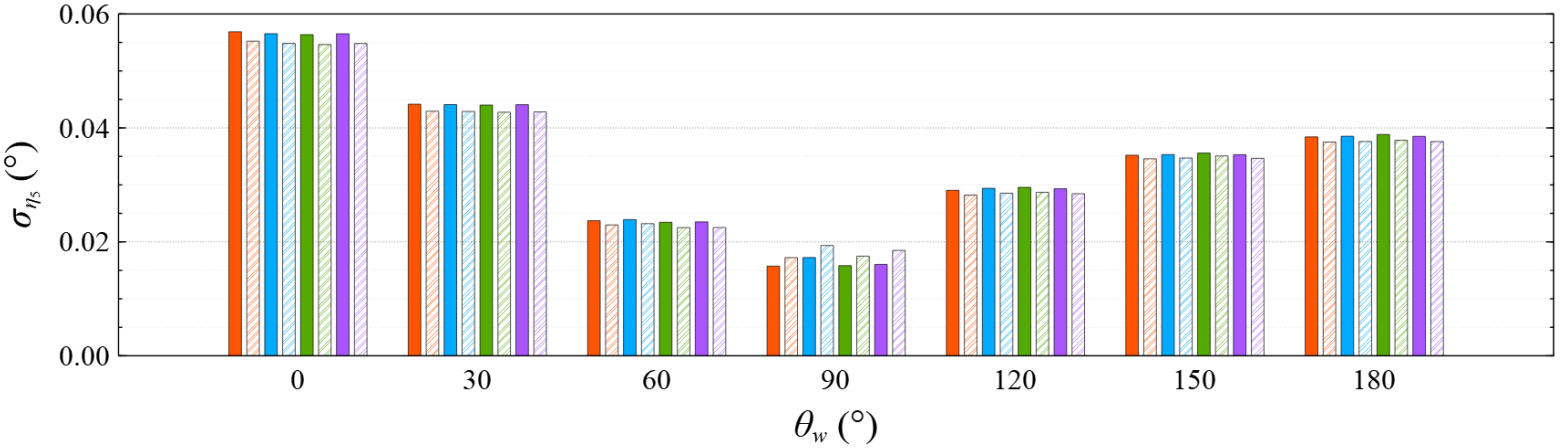

Figure 61 Comparison of standard deviation of platform pitch motion under CW condition

doi:10.6342/NTU202204241

Table 32 Mean value of platform pitch motion under CW condition

	θ_w / θ_c	0°	30°	60°	90°	120°	150°	180°
PF (°)	0°	4.694	3.832	1.839	-0.522	-2.630	-4.026	-4.424
VF (°)		4.695	3.833	1.839	-0.522	-2.630	-4.027	-4.424
Difference (%)		-0.020	-0.023	0.006	-0.070	-0.015	-0.016	-0.010
PF (°)	90°	4.697	3.836	1.845	-0.516	-2.625	-4.024	-4.424
VF (°)		4.698	3.836	1.845	-0.516	-2.625	-4.024	-4.425
Difference (%)		-0.023	-0.022	0.002	-0.058	-0.015	-0.013	-0.010
PF (°)	180°	4.699	3.835	1.844	-0.518	-2.627	-4.026	-4.424
VF (°)		4.700	3.836	1.844	-0.518	-2.628	-4.026	-4.424
Difference (%)		-0.023	-0.022	0.004	-0.061	-0.014	-0.011	-0.004
PF (°)	270°	4.697	3.830	1.837	-0.523	-2.631	-4.028	-4.424
VF (°)		4.698	3.831	1.837	-0.523	-2.632	-4.029	-4.424
Difference (%)		-0.023	-0.022	0.006	-0.063	-0.015	-0.011	-0.010

Table 33 Standard deviation of platform pitch motion under CW condition

	θ_w / θ_c	0°	30°	60°	90°	120°	150°	180°
PF (°)	0°	0.057	0.044	0.024	0.016	0.029	0.035	0.038
VF (°)		0.055	0.043	0.023	0.017	0.028	0.035	0.038
Difference (%)		2.983	2.887	3.199	-8.665	2.970	1.819	2.434
PF (°)	90°	0.057	0.044	0.024	0.017	0.029	0.035	0.039
VF (°)		0.055	0.043	0.023	0.019	0.029	0.035	0.038
Difference (%)		3.116	2.807	3.077	-10.910	3.008	1.765	2.456
PF (°)	180°	0.056	0.044	0.023	0.016	0.030	0.036	0.039
VF (°)		0.055	0.043	0.023	0.017	0.029	0.035	0.038
Difference (%)		3.183	2.937	4.132	-9.572	3.064	1.455	2.690
PF (°)	270°	0.057	0.044	0.024	0.016	0.029	0.035	0.039
VF (°)		0.055	0.043	0.023	0.019	0.028	0.035	0.038
Difference (%)		3.122	2.964	4.394	-13.310	3.068	1.852	2.444

doi:10.6342/NTU202204241

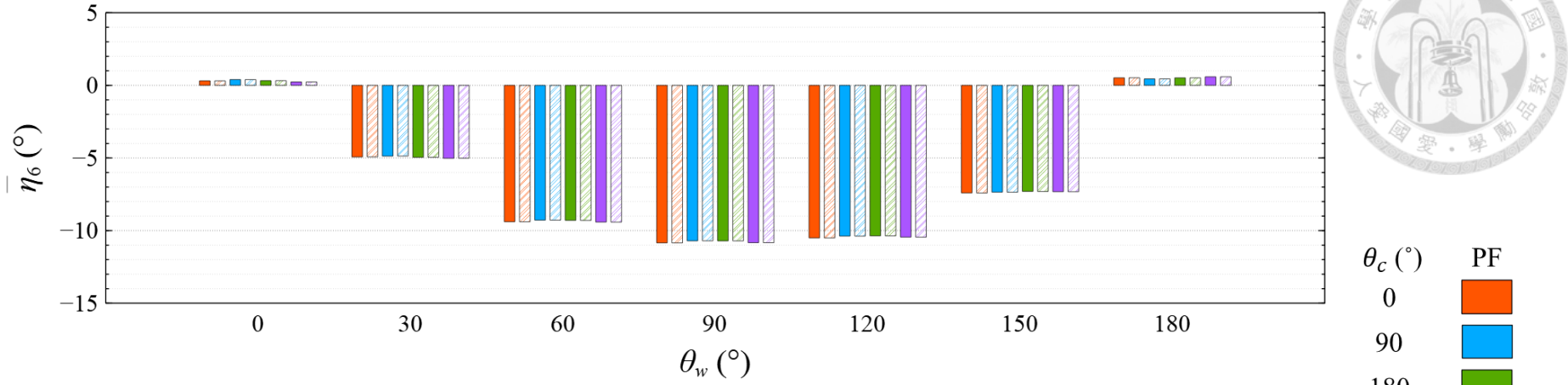

Figure 62 Comparison of mean value of platform yaw motion under CW condition

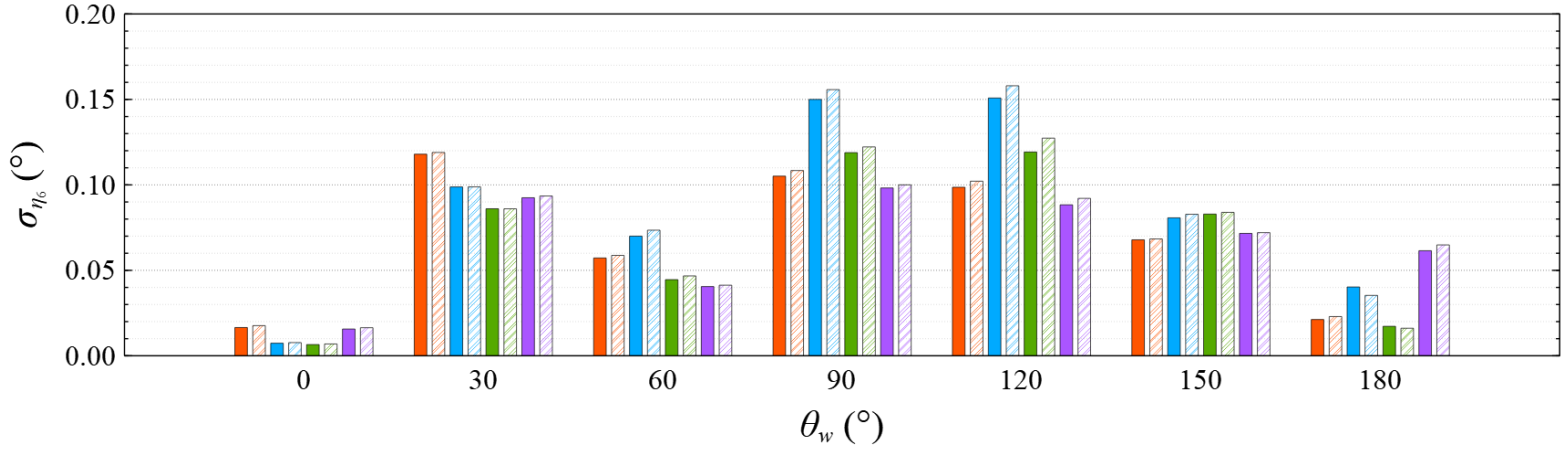

Figure 63 Comparison of standard deviation of platform yaw motion under CW condition

doi:10.6342/NTU202204241

Table 34 Mean value of platform yaw motion under CW condition

	θ_w / θ_c	0°	30°	60°	90°	120°	150°	180°
PF (°)	0°	0.313	-4.930	-9.388	-10.846	-10.502	-7.405	0.520
VF (°)		0.310	-4.923	-9.392	-10.848	-10.503	-7.411	0.523
Difference (%)		0.987	0.131	-0.038	-0.015	-0.008	-0.088	-0.553
PF (°)	90°	0.400	-4.873	-9.280	-10.705	-10.379	-7.352	0.446
VF (°)		0.396	-4.868	-9.282	-10.703	-10.380	-7.356	0.445
Difference (%)		0.840	0.101	-0.023	0.014	-0.013	-0.054	0.202
PF (°)	180°	0.323	-4.955	-9.297	-10.708	-10.362	-7.301	0.517
VF (°)		0.322	-4.951	-9.301	-10.708	-10.362	-7.308	0.516
Difference (%)		0.416	0.082	-0.048	-0.006	-0.002	-0.094	0.102
PF (°)	270°	0.236	-5.023	-9.412	-10.831	-10.448	-7.323	0.587
VF (°)		0.237	-5.018	-9.416	-10.833	-10.449	-7.323	0.588
Difference (%)		-0.125	0.095	-0.048	-0.020	-0.013	-0.007	-0.040

Table 35 Standard deviation of platform yaw motion under CW condition

	θ_w / θ_c	0°	30°	60°	90°	120°	150°	180°
PF (°)	0°	0.017	0.118	0.057	0.105	0.099	0.068	0.021
VF (°)		0.018	0.119	0.059	0.108	0.102	0.068	0.023
Difference (%)		-6.278	-0.845	-2.576	-3.021	-3.473	-0.737	-7.480
PF (°)	90°	0.007	0.099	0.070	0.150	0.151	0.081	0.040
VF (°)		0.008	0.099	0.073	0.156	0.158	0.083	0.035
Difference (%)		-4.650	-0.027	-4.720	-3.676	-4.526	-2.515	13.918
PF (°)	180°	0.007	0.086	0.045	0.119	0.119	0.083	0.017
VF (°)		0.007	0.086	0.047	0.122	0.127	0.084	0.016
Difference (%)		-5.230	0.053	-4.660	-2.735	-6.372	-1.213	6.925
PF (°)	270°	0.016	0.092	0.041	0.098	0.088	0.072	0.061
VF (°)		0.016	0.094	0.041	0.100	0.092	0.072	0.065
Difference (%)		-4.672	-1.109	-1.950	-1.824	-4.098	-0.596	-5.232

doi:10.6342/NTU202204241

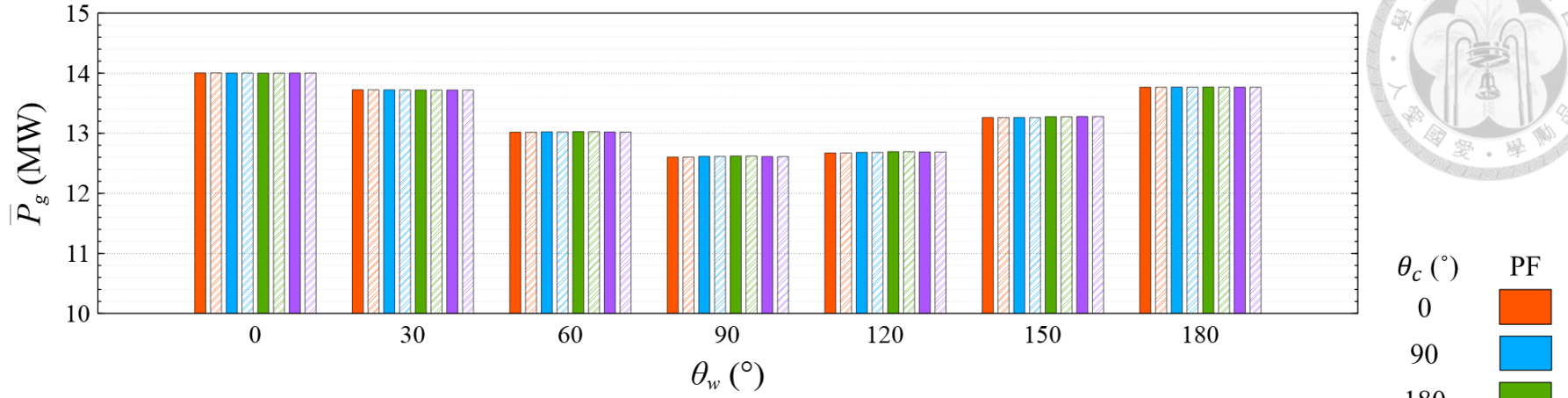

Figure 64 Comparison of mean value of generator electrical power under CW condition

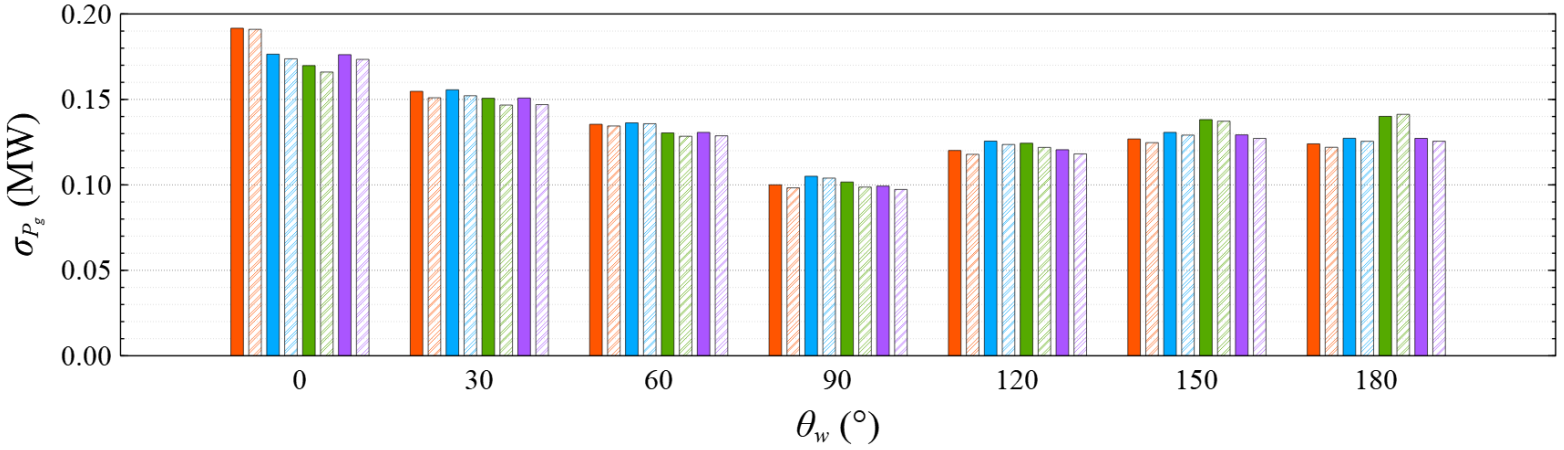

Figure 65 Comparison of standard deviation of generator electrical power under CW condition

doi:10.6342/NTU202204241

Table 36 Mean value of generator electrical power under CW condition

	θ_c \ θ_w	0°	30°	60°	90°	120°	150°	180°
PF (MW)	0°	14.005	13.724	13.019	12.603	12.672	13.264	13.767
VF (MW)		14.005	13.724	13.018	12.602	12.672	13.262	13.767
Difference (%)		0.002	0.003	0.008	0.007	0.005	0.012	0.003
PF (MW)	90°	14.003	13.723	13.024	12.615	12.682	13.263	13.769
VF (MW)		14.003	13.722	13.023	12.614	12.681	13.262	13.769
Difference (%)		0.003	0.004	0.006	0.003	0.006	0.009	0.003
PF (MW)	180°	14.001	13.719	13.028	12.622	12.693	13.277	13.770
VF (MW)		14.001	13.719	13.027	12.621	12.693	13.275	13.769
Difference (%)		0.003	0.005	0.010	0.006	0.005	0.012	0.003
PF (MW)	270°	14.003	13.720	13.022	12.612	12.689	13.280	13.767
VF (MW)		14.003	13.720	13.020	12.611	12.688	13.279	13.766
Difference (%)		0.003	0.004	0.009	0.007	0.006	0.007	0.003

Table 37 Standard deviation of generator electrical power under CW condition

	θ_c \ θ_w	0°	30°	60°	90°	120°	150°	180°
PF (MW)	0°	0.192	0.155	0.135	0.100	0.120	0.127	0.124
VF (MW)		0.191	0.151	0.134	0.098	0.118	0.125	0.122
Difference (%)		0.341	2.502	0.734	1.801	1.917	1.729	1.650
PF (MW)	90°	0.176	0.156	0.136	0.105	0.126	0.131	0.127
VF (MW)		0.174	0.152	0.136	0.104	0.124	0.129	0.125
Difference (%)		1.555	2.277	0.376	1.044	1.593	1.240	1.417
PF (MW)	180°	0.170	0.151	0.130	0.102	0.124	0.138	0.140
VF (MW)		0.166	0.147	0.128	0.099	0.122	0.137	0.141
Difference (%)		2.282	2.700	1.523	3.000	2.009	0.683	-0.830
PF (MW)	270°	0.176	0.151	0.131	0.099	0.121	0.129	0.127
VF (MW)		0.173	0.147	0.129	0.097	0.118	0.127	0.126
Difference (%)		1.588	2.612	1.541	2.013	2.049	1.641	1.323

doi:10.6342/NTU202204241

Table 38 Performance of mean generator power based on the rated power of the system under CW condition

θ_c \ θ_w	0°	30°	60°	90°	120°	150°	180°
0°	93.365%	91.492%	86.785%	84.013%	84.478%	88.414%	91.777%
90°	93.350%	91.480%	86.823%	84.097%	84.541%	88.415%	91.792%
180°	93.338%	91.458%	86.846%	84.142%	84.619%	88.502%	91.795%
270°	93.351%	91.463%	86.803%	84.076%	84.585%	88.527%	91.776%

doi:10.6342/NTU202204241

4.4.2 High Wave Condition

The trajectories of the platform on xy-plane are shown in Figure 66 and Figure 67, those on xz-plane are shown in Figure 68 and Figure 69, and those on yz-plane are shown in Figure 70 and Figure 71. The maximums, minimums, and variations of the platform translation motions in time history under the HW condition are shown in Table 39 to Table 41. The trajectories of the platform between the two modeling approaches as well as among the four current directions are similar under the HW condition. The platform at $(\theta_w, \theta_c) = (0°, 0°)$ has the largest surge variation of 8.748 m which is found between -2.567 m and 6.182 m, and the platform at $(\theta_w, \theta_c) = (60°, 180°)$ has the smallest surge variation of 1.275 m which is found between - -2.5 m and -1.224 m. The platform at $(\theta_w, \theta_c) = (150°, 90°)$ has the largest sway variation of 5.557 m which is found between -4.753 m and 0.804 m, and the platform at $(\theta_w, \theta_c) = (180°, 0°)$ has the smallest sway variation of 0.122 m which is found between 0.149 m and 0.27 m. The platform at $(\theta_w, \theta_c) = (180°, 180°)$ has the largest heave variation of 2.1 m which is found between -1.869 m and 0.231 m, and the platform at $(\theta_w, \theta_c) = (120°, 270°)$ has the smallest heave variation of 1.433 m which is found between -1.449 m and -0.016 m.

The mean values and standard deviations of the nacelle motions are shown in Figure 72 to Figure 77, and Table 42 to Table 47. The largest mean values of surge, sway, and heave motion of nacelle appear at $(\theta_w, \theta_c) = (180°, 180°)$, $(90°, 90°)$, and $(180°, 0°)$, and they are -12.738 m, -15.074 m, and 1.074 m, respectively. The smallest mean values of surge, sway, and heave motion of nacelle appear at $(\theta_w, \theta_c) = (30°, 0°)$, $(180°, 90°)$, and $(60°, 0°)$, and they are -0.972 m, 0.825 m, and -0.041 m, respectively. The largest standard deviations of surge, sway, and heave motion of nacelle appear at

doi:10.6342/NTU202204241

$(\theta_w, \theta_c) = (0°, 0°)$, $(150°, 90°)$, and $(0°, 0°)$, and they are 1.82 m, 1.161 m, and 0.335 m, respectively. The smallest standard deviations of surge, sway, and heave motion of nacelle appear at $(\theta_w, \theta_c) = (60°, 180°)$, $(180°, 0°)$, and $(120°, 270°)$, and they are 0.341 m, 0.067 m, and 0.166 m, respectively.

The mean values and standard deviations of the platform motions are shown in Figure 78 to Figure 89, and Table 48 to Table 59. The largest mean values of surge, sway, heave, roll, pitch, and yaw motions of platform appear at $(\theta_w, \theta_c) = (180°, 180°)$, $(90°, 90°)$, $(150°, 90°)$, $(60°, 270°)$, $(150°, 0°)$, and $(90°, 0°)$, and they are -5.83 m, -3.23 m, -0.739 m, 0.995°, -0.67°, and -3.362°, respectively. The smallest mean values of surge, sway, heave, roll, pitch, and yaw motions of platform appear at $(\theta_w, \theta_c) = (30°, 180°)$, $(180°, 90°)$, $(0°, 180°)$, $(150°, 90°)$, $(60°, 0°)$, and $(0°, 90°)$, and they are 0.184 m, 0.029 m, -0.497 m, 0.081°, 0.045°, and -0.977°, respectively. The largest standard deviations of surge, sway, heave, roll, pitch, and yaw motions of platform appear at $(\theta_w, \theta_c) = (0°, 0°)$, $(150°, 90°)$, $(180°, 180°)$, $(90°, 90°)$, $(0°, 0°)$, and $(30°, 0°)$, and they are 1.637 m, 1.035 m, 0.29 m, 0.305°, 0.21°, and 0.986°, respectively. The smallest standard deviations of surge, sway, heave, roll, pitch, and yaw motions of platform appear at $(\theta_w, \theta_c) = (60°, 180°)$, $(180°, 0°)$, $(120°, 270°)$, $(180°, 0°)$, $(60°, 180°)$, and $(180°, 0°)$, and they are 0.208 m, 0.024 m, 0.229 m, 0.015°, 0.119°, and 0.047°, respectively.

The mean values and standard deviations of the generator power are shown in Figure 90 and Figure 91, and Table 60 and Table 61. The largest mean value of generator power appears at $(\theta_w, \theta_c) = (180°, 0°)$, and it is 14.999 MW, while the smallest one appears at $(\theta_w, \theta_c) = (120°, 90°)$, and it is 14.891 MW. The largest standard deviation

doi:10.6342/NTU202204241

of generator power appears at $(\theta_w, \theta_c) = (120°, 90°)$, and it is 0.317 MW, while the smallest one appears at $(\theta_w, \theta_c) = (180°, 0°)$, and it is 0.148 MW.

Similar to the CW condition, the mean value and standard deviation of the motion response and generator power are sensitive to the wind direction. The difference of the motion response and generator power between the two approaches as well as among the four current directions mainly reflects in the standard deviation, rather than in the mean value. The offset of the wind turbine system remains under 21 m, and the mean pitch angle remains between -5° and 5° at all studied wind directions. Under the HW condition, all studied wind directions deliver a mean generator power that approaches the rated power.

doi:10.6342/NTU202204241

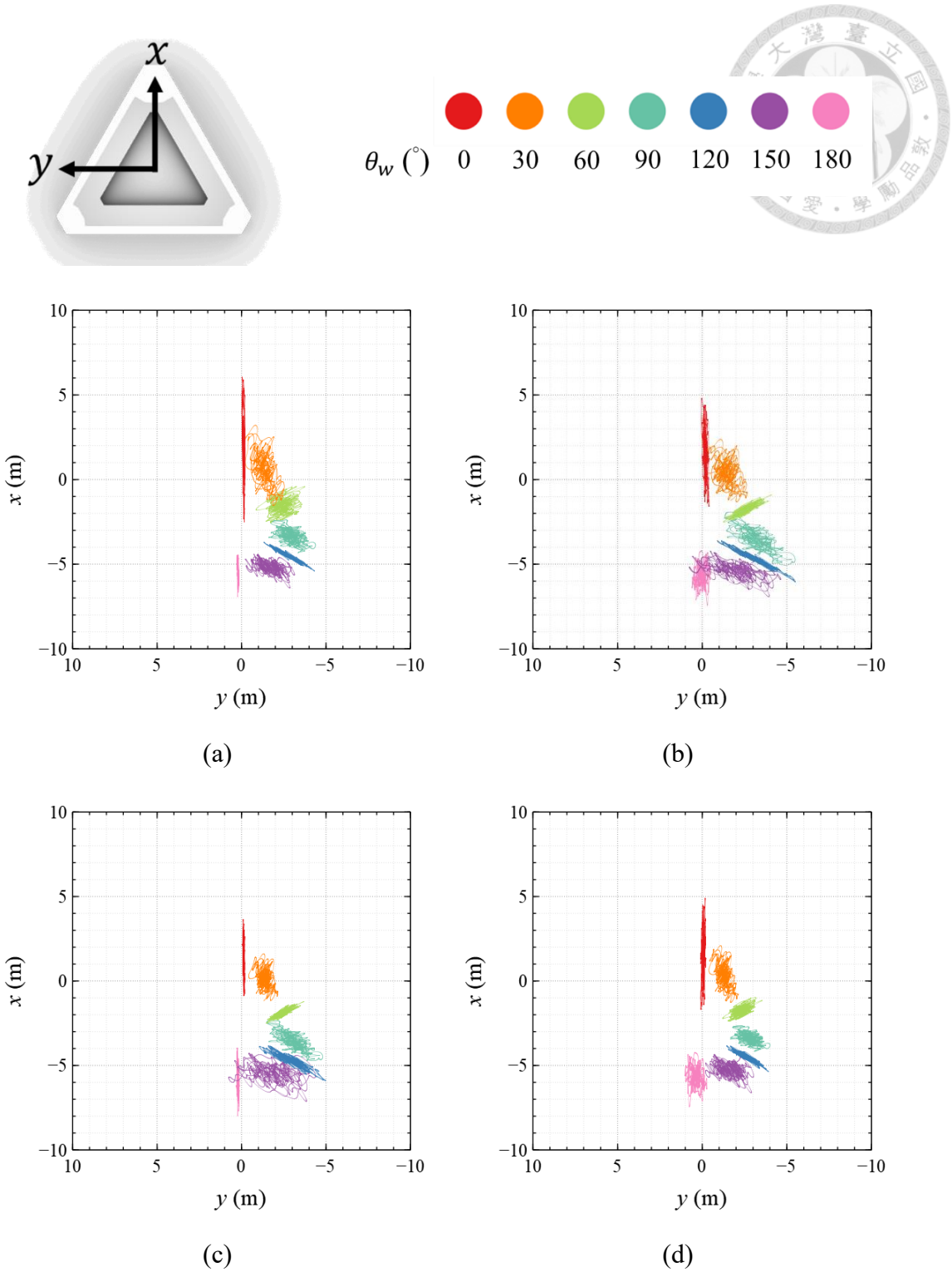

Figure 66 Platform trajectory on xy-plane via PF approach under HW condition: (a) $\theta_c = 0°$, (b) $\theta_c = 90°$, (c) $\theta_c = 180°$, (d) $\theta_c = 270°$

doi:10.6342/NTU202204241

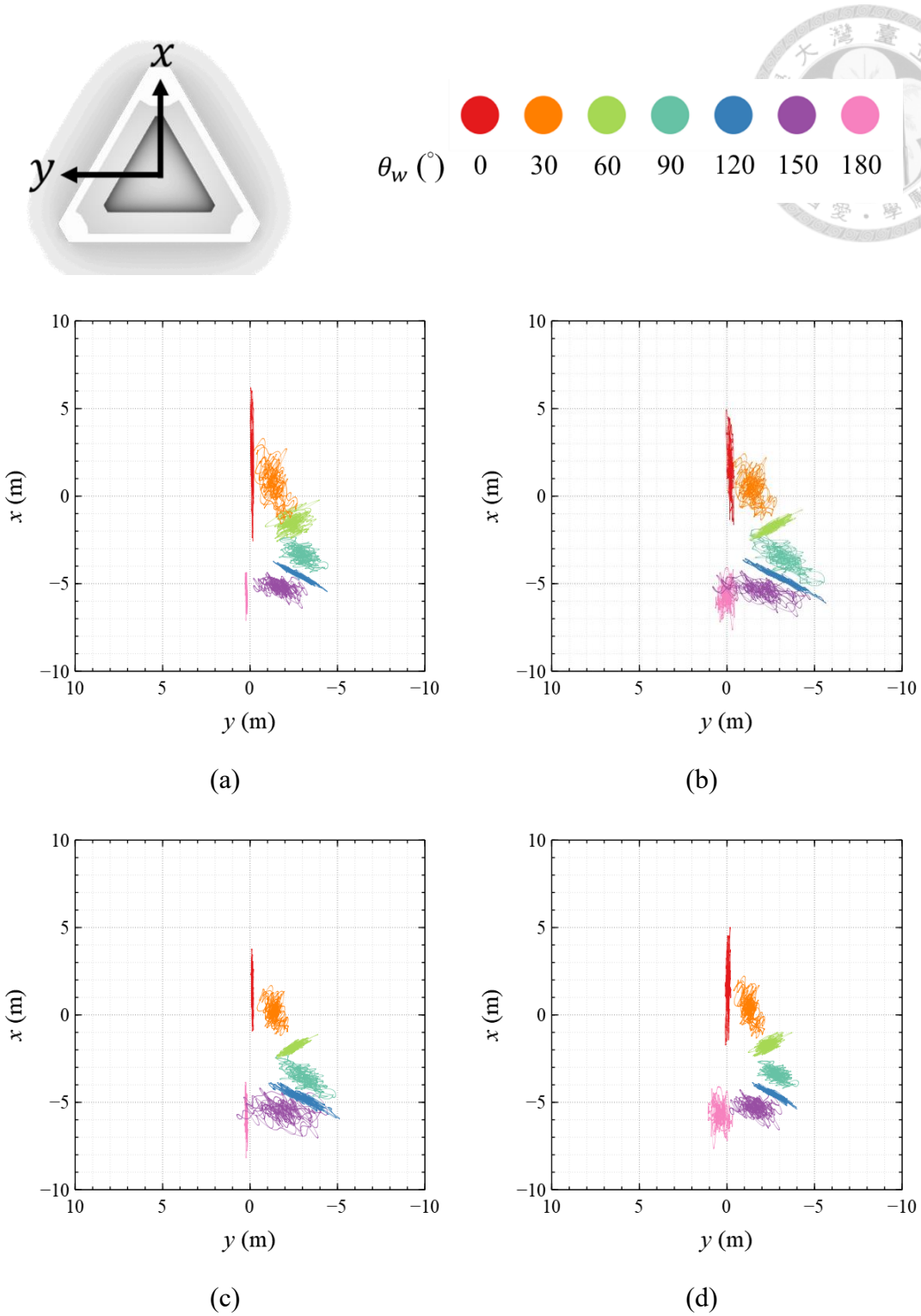

Figure 67 Platform trajectory on xy-plane via VF approach under HW condition: (a) $\theta_c = 0°$, (b) $\theta_c = 90°$, (c) $\theta_c = 180°$, (d) $\theta_c = 270°$

doi:10.6342/NTU202204241

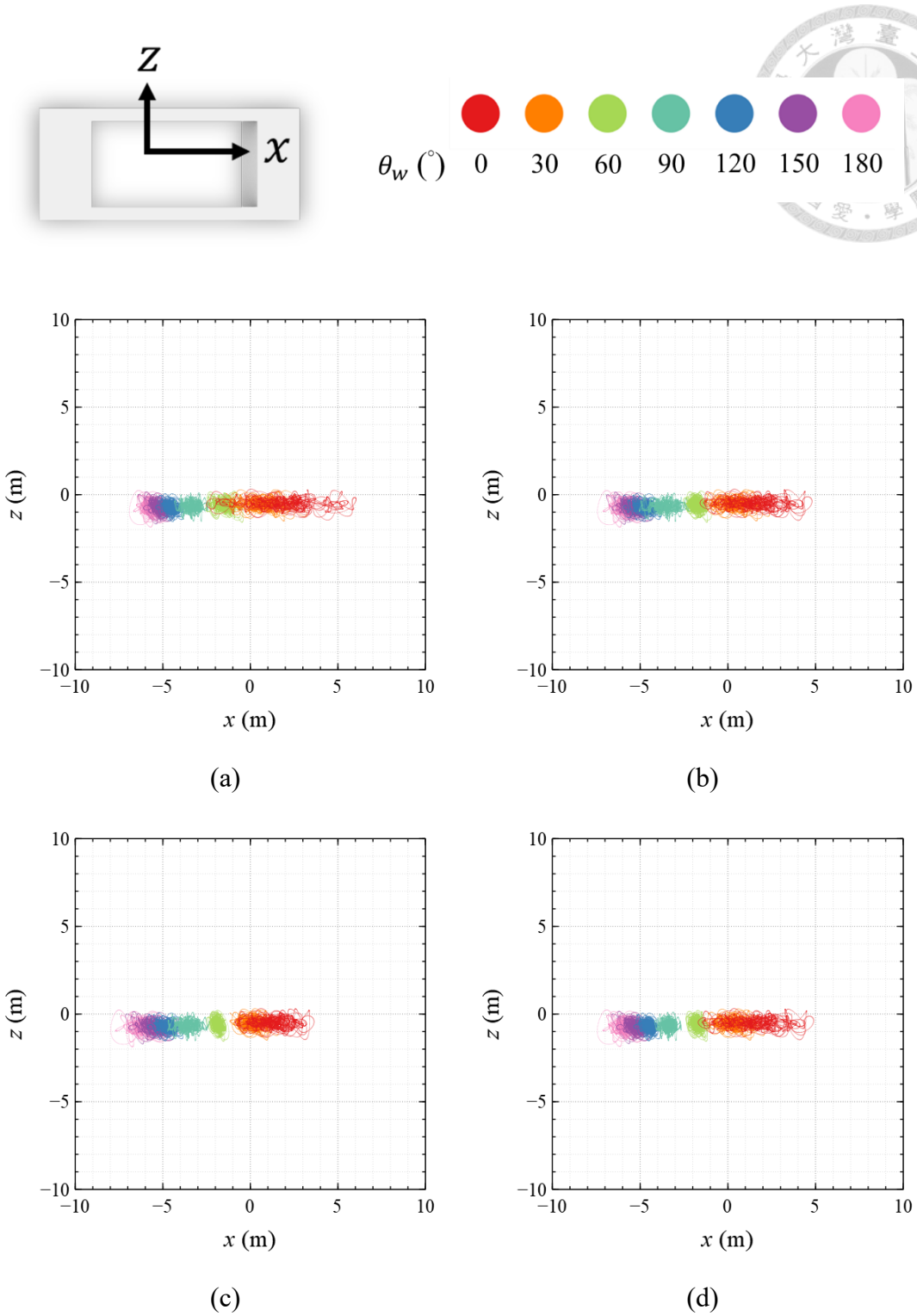

Figure 68 Platform trajectory on xz-plane via PF approach under HW condition: (a) $\theta_c = 0°$, (b) $\theta_c = 90°$, (c) $\theta_c = 180°$, (d) $\theta_c = 270°$

doi:10.6342/NTU202204241

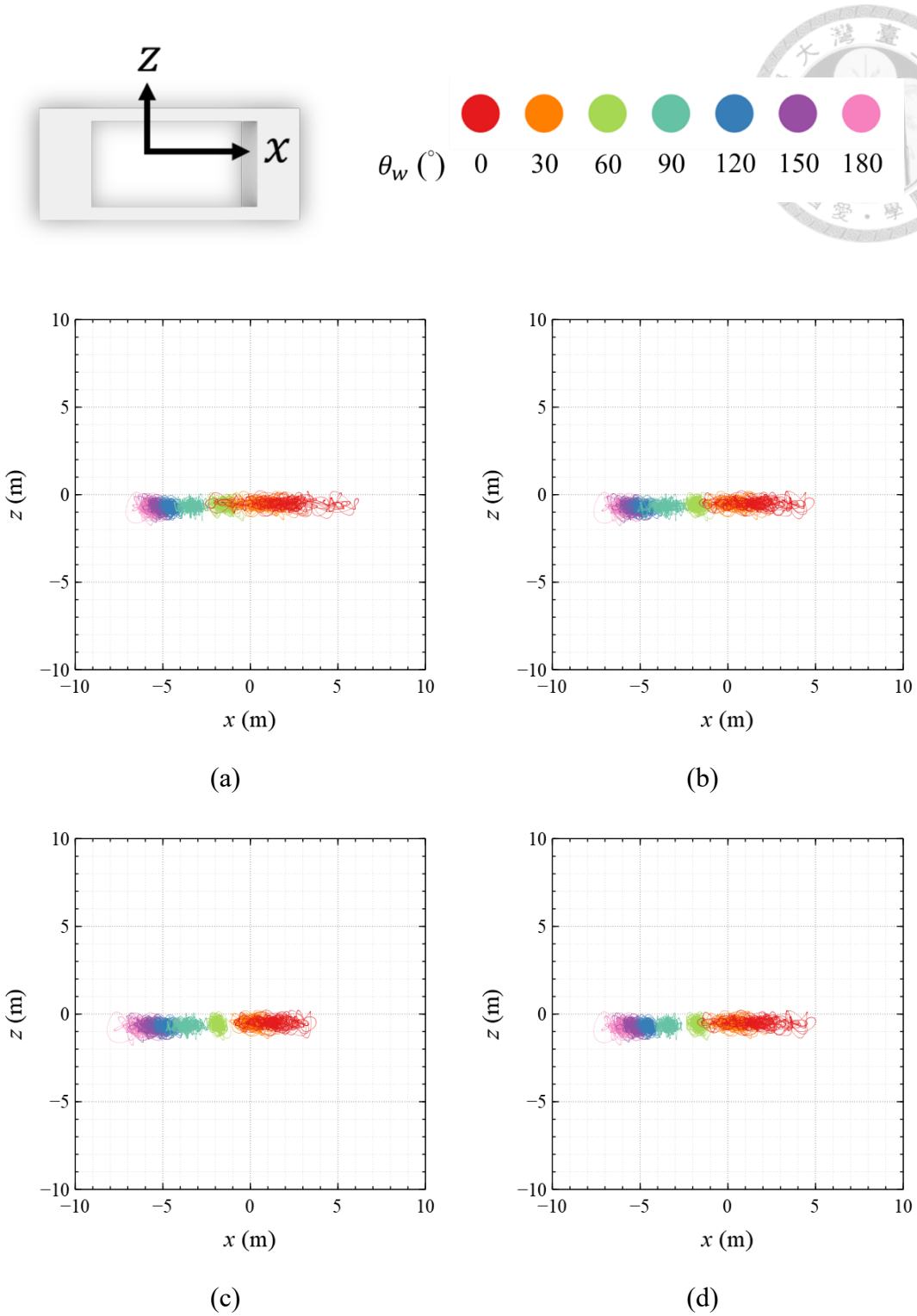

Figure 69 Platform trajectory on xz-plane via VF approach under HW condition: (a) $\theta_c = 0°$, (b) $\theta_c = 90°$, (c) $\theta_c = 180°$, (d) $\theta_c = 270°$

doi:10.6342/NTU202204241

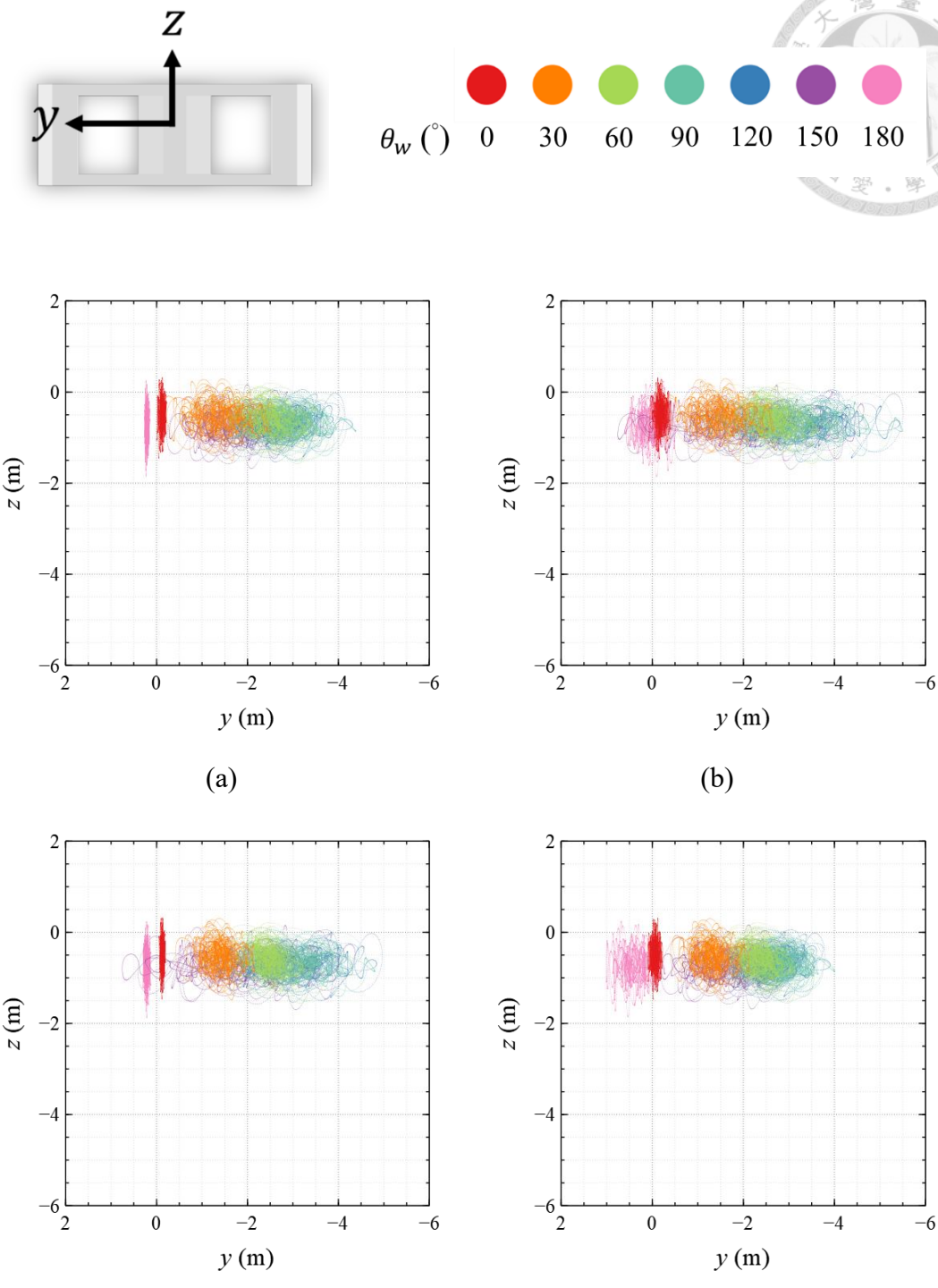

Figure 70 Platform trajectory on yz-plane via PF approach under HW condition: (a) $\theta_c = 0°$, (b) $\theta_c = 90°$, (c) $\theta_c = 180°$, (d) $\theta_c = 270°$

doi:10.6342/NTU202204241

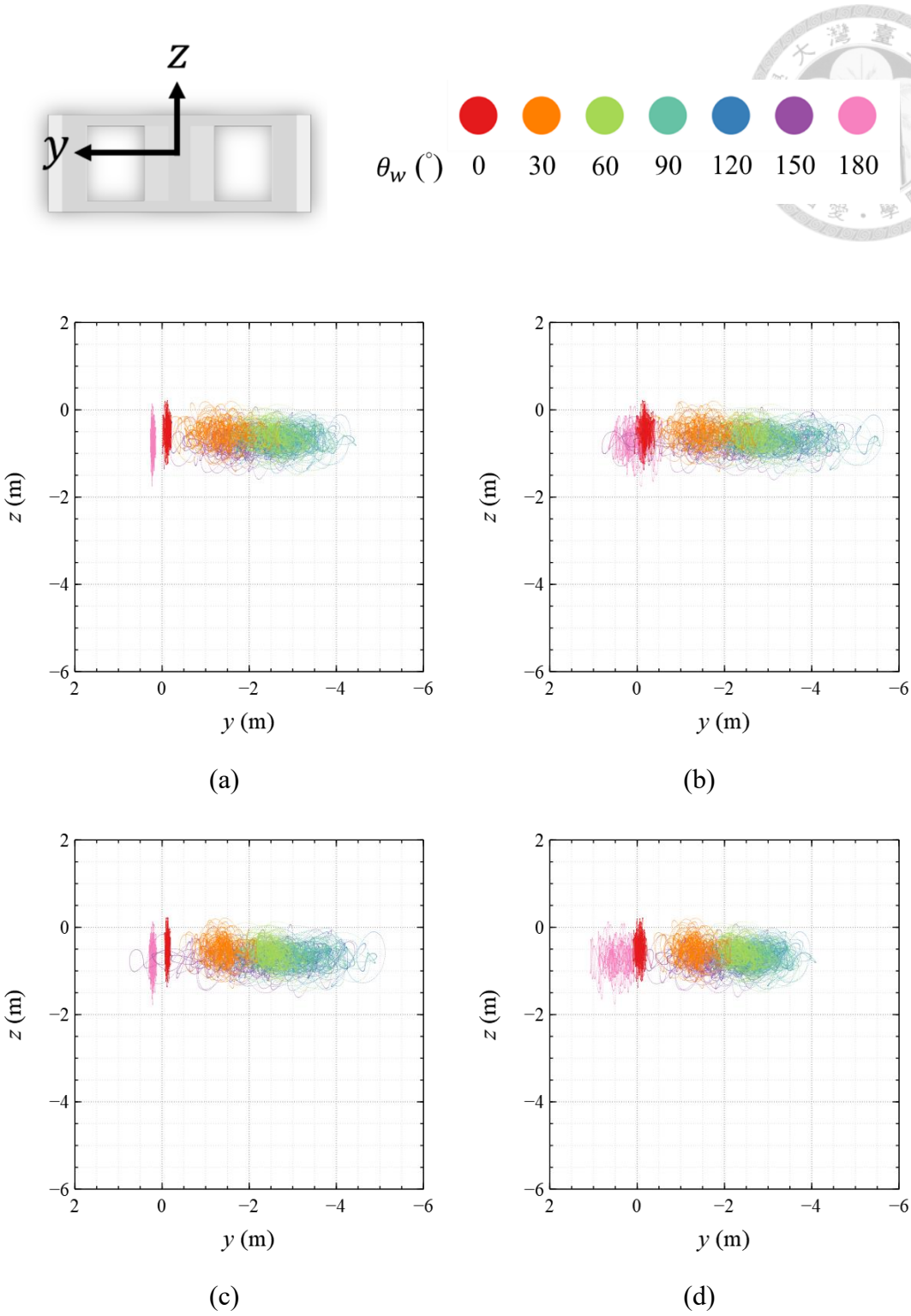

Figure 71 Platform trajectory on yz-plane via VF approach under HW condition: (a) $\theta_c = 0°$, (b) $\theta_c = 90°$, (c) $\theta_c = 180°$, (d) $\theta_c = 270°$

doi:10.6342/NTU202204241

Table 39 Platform surge motion in time history under HW condition: (a) Maximum, (b) Minimum, (c) Variation

(a)

	θ_w / θ_c	0°	30°	60°	90°	120°	150°	180°
PF	0°	6.042	3.209	-0.413	-2.387	-3.711	-4.409	-4.466
VF		6.182	3.298	-0.229	-2.339	-3.723	-4.359	-4.367
PF	90°	4.795	2.377	-0.910	-1.897	-3.621	-4.238	-4.207
VF		4.917	2.420	-0.783	-1.852	-3.574	-4.259	-4.089
PF	180°	3.636	1.610	-1.224	-2.349	-3.844	-4.280	-3.980
VF		3.762	1.683	-1.122	-2.309	-3.869	-4.187	-3.859
PF	270°	4.891	2.092	-0.978	-2.653	-3.840	-4.346	-4.237
VF		5.009	2.214	-0.987	-2.640	-3.870	-4.285	-4.117

(b)

	θ_w / θ_c	0°	30°	60°	90°	120°	150°	180°
PF	0°	-2.508	-1.537	-2.530	-4.330	-5.400	-6.411	-6.914
VF		-2.567	-1.580	-2.596	-4.357	-5.445	-6.400	-7.110
PF	90°	-1.583	-1.324	-2.518	-5.057	-6.040	-6.919	-7.427
VF		-1.626	-1.350	-2.520	-5.124	-6.105	-6.871	-7.638
PF	180°	-0.882	-1.164	-2.500	-4.716	-5.894	-7.124	-7.973
VF		-0.930	-1.183	-2.510	-4.803	-5.938	-7.038	-8.178
PF	270°	-1.686	-1.265	-2.385	-4.161	-5.356	-6.620	-7.438
VF		-1.726	-1.330	-2.360	-4.202	-5.387	-6.580	-7.650

(c)

	θ_w / θ_c	0°	30°	60°	90°	120°	150°	180°
PF	0°	8.550	4.746	2.117	1.944	1.689	2.002	2.448
VF		8.748	4.878	2.367	2.018	1.723	2.041	2.743
PF	90°	6.377	3.701	1.608	3.160	2.420	2.681	3.220
VF		6.543	3.771	1.737	3.272	2.531	2.612	3.548
PF	180°	4.518	2.774	1.275	2.367	2.049	2.845	3.993
VF		4.693	2.866	1.388	2.494	2.068	2.851	4.320
PF	270°	6.577	3.357	1.407	1.507	1.517	2.274	3.201
VF		6.734	3.544	1.373	1.562	1.517	2.295	3.532

doi:10.6342/NTU202204241

Table 40 Platform sway motion in time history under HW condition: (a) Maximum, (b) Minimum, (c) Variation

(a)

	θ_c \ θ_w	0°	30°	60°	90°	120°	150°	180°
PF	0°	-0.007	-0.163	-0.855	-1.610	-1.332	-0.230	0.270
VF		-0.008	-0.166	-0.871	-1.673	-1.335	-0.195	0.267
PF	90°	0.068	-0.122	-1.253	-1.319	-0.900	0.757	0.604
VF		0.062	-0.163	-1.301	-1.305	-0.929	0.804	0.650
PF	180°	-0.057	-0.419	-1.469	-1.480	-1.063	0.756	0.300
VF		-0.057	-0.406	-1.525	-1.443	-1.079	0.748	0.301
PF	270°	0.093	-0.397	-1.207	-1.672	-1.453	-0.196	1.009
VF		0.097	-0.384	-1.222	-1.736	-1.464	-0.172	1.070

(b)

	θ_c \ θ_w	0°	30°	60°	90°	120°	150°	180°
PF	0°	-0.219	-2.533	-3.750	-4.379	-4.310	-3.142	0.149
VF		-0.221	-2.705	-3.954	-4.453	-4.410	-3.273	0.144
PF	90°	-0.412	-2.661	-4.089	-5.489	-5.506	-4.642	-0.514
VF		-0.410	-2.838	-4.309	-5.569	-5.644	-4.753	-0.575
PF	180°	-0.194	-2.152	-3.682	-4.799	-4.965	-4.371	0.130
VF		-0.194	-2.187	-3.886	-4.890	-5.121	-4.424	0.128
PF	270°	-0.223	-2.126	-3.538	-4.003	-3.905	-3.041	-0.275
VF		-0.226	-2.160	-3.715	-4.090	-3.984	-3.118	-0.320

(c)

	θ_c \ θ_w	0°	30°	60°	90°	120°	150°	180°
PF	0°	0.212	2.370	2.895	2.769	2.978	2.912	0.122
VF		0.213	2.539	3.082	2.780	3.075	3.078	0.124
PF	90°	0.480	2.539	2.836	4.170	4.606	5.400	1.118
VF		0.472	2.675	3.008	4.264	4.715	5.557	1.224
PF	180°	0.137	1.733	2.213	3.319	3.901	5.127	0.170
VF		0.137	1.781	2.361	3.448	4.042	5.172	0.173
PF	270°	0.315	1.729	2.331	2.331	2.453	2.845	1.283
VF		0.323	1.777	2.493	2.354	2.520	2.945	1.390

doi:10.6342/NTU202204241

Table 41 Platform heave motion in time history under HW condition: (a) Maximum, (b) Minimum, (c) Variation

(a)

	θ_c \ θ_w	0°	30°	60°	90°	120°	150°	180°
PF	0°	0.312	0.288	0.200	0.101	0.053	0.161	0.243
VF		0.219	0.194	0.120	0.043	-0.021	0.067	0.132
PF	90°	0.310	0.294	0.208	0.105	0.051	0.149	0.238
VF		0.219	0.201	0.126	0.050	-0.020	0.059	0.129
PF	180°	0.312	0.305	0.213	0.097	0.056	0.150	0.231
VF		0.223	0.214	0.131	0.038	-0.015	0.063	0.120
PF	270°	0.309	0.298	0.210	0.113	0.058	0.162	0.238
VF		0.218	0.206	0.128	0.045	-0.016	0.070	0.129

(b)

	θ_c \ θ_w	0°	30°	60°	90°	120°	150°	180°
PF	0°	-1.451	-1.508	-1.571	-1.517	-1.534	-1.680	-1.843
VF		-1.352	-1.422	-1.501	-1.471	-1.454	-1.591	-1.743
PF	90°	-1.467	-1.498	-1.571	-1.522	-1.535	-1.693	-1.854
VF		-1.375	-1.416	-1.502	-1.470	-1.454	-1.603	-1.754
PF	180°	-1.459	-1.480	-1.553	-1.514	-1.534	-1.698	-1.869
VF		-1.367	-1.395	-1.480	-1.459	-1.452	-1.609	-1.771
PF	270°	-1.468	-1.485	-1.553	-1.514	-1.529	-1.685	-1.855
VF		-1.375	-1.398	-1.481	-1.464	-1.449	-1.597	-1.755

(c)

	θ_c \ θ_w	0°	30°	60°	90°	120°	150°	180°
PF	0°	1.763	1.796	1.772	1.617	1.587	1.841	2.086
VF		1.570	1.616	1.621	1.514	1.433	1.657	1.875
PF	90°	1.778	1.792	1.779	1.627	1.586	1.842	2.092
VF		1.594	1.617	1.628	1.520	1.434	1.662	1.883
PF	180°	1.772	1.785	1.766	1.611	1.590	1.848	2.100
VF		1.589	1.609	1.611	1.497	1.438	1.672	1.891
PF	270°	1.777	1.783	1.762	1.627	1.587	1.848	2.094
VF		1.593	1.604	1.609	1.509	1.433	1.667	1.884

doi:10.6342/NTU202204241

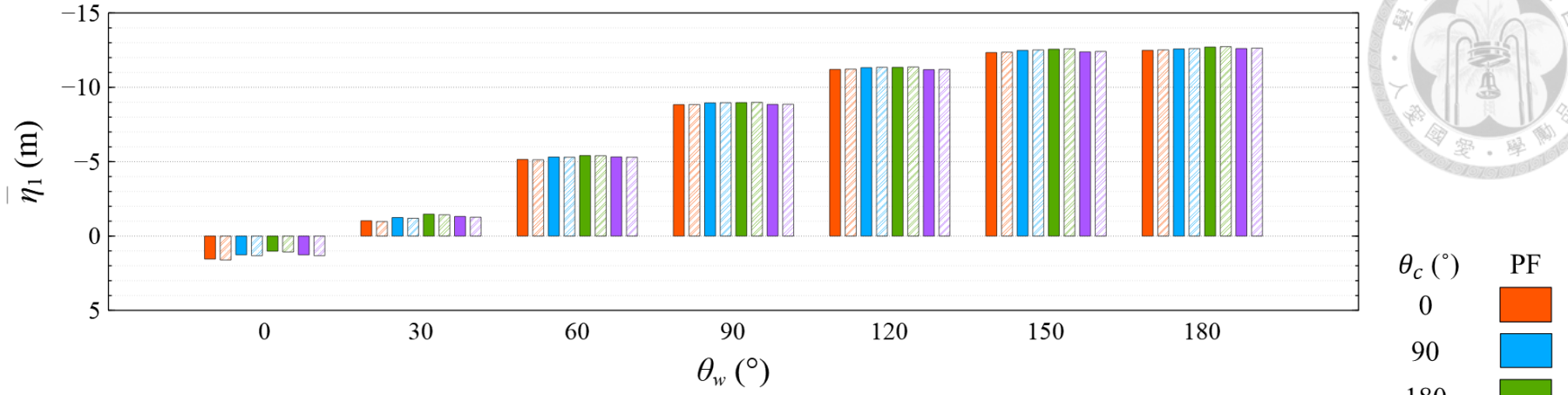

Figure 72 Comparison of mean value of nacelle surge motion under HW condition

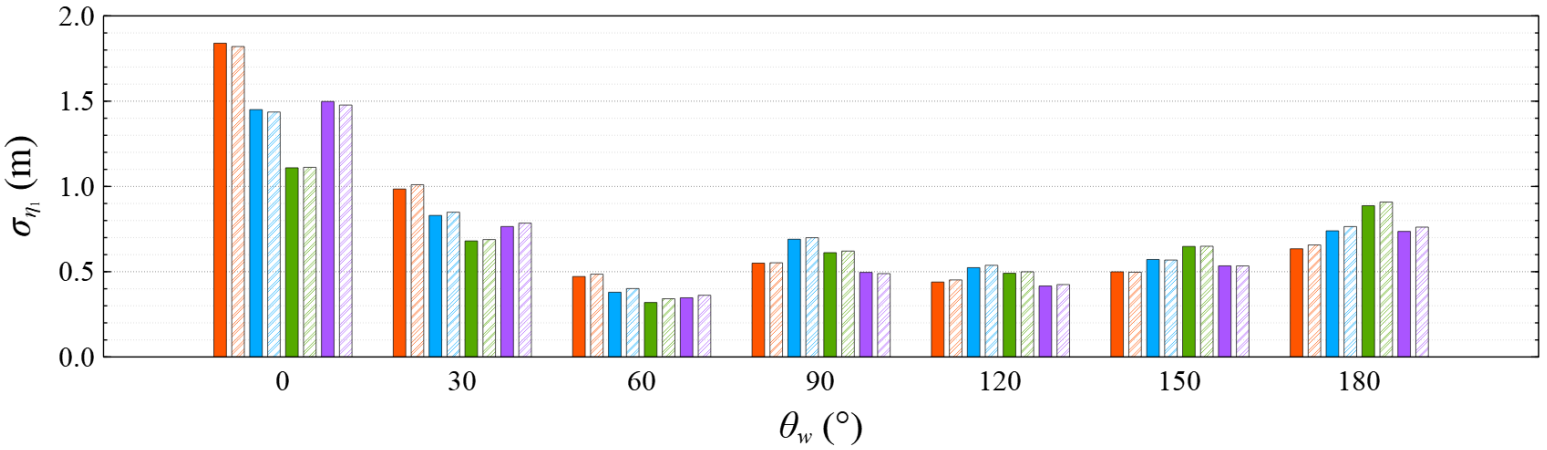

Figure 73 Comparison of standard deviation of nacelle surge motion under HW condition

doi:10.6342/NTU202204241

Table 42 Mean value of nacelle surge motion under HW condition

	θ_c \ θ_w	0°	30°	60°	90°	120°	150°	180°
PF (m)	0°	1.547	-1.027	-5.152	-8.836	-11.207	-12.339	-12.491
VF (m)		1.613	-0.972	-5.128	-8.843	-11.227	-12.363	-12.518
Difference (%)		-4.061	5.566	0.462	-0.076	-0.181	-0.191	-0.213
PF (m)	90°	1.260	-1.246	-5.314	-8.956	-11.325	-12.488	-12.581
VF (m)		1.322	-1.197	-5.301	-8.969	-11.347	-12.514	-12.608
Difference (%)		-4.690	4.123	0.245	-0.138	-0.194	-0.207	-0.215
PF (m)	180°	1.019	-1.473	-5.411	-8.975	-11.343	-12.565	-12.711
VF (m)		1.075	-1.431	-5.401	-8.990	-11.369	-12.592	-12.738
Difference (%)		-5.230	2.931	0.179	-0.173	-0.227	-0.219	-0.213
PF (m)	270°	1.259	-1.320	-5.322	-8.854	-11.189	-12.386	-12.609
VF (m)		1.320	-1.269	-5.302	-8.863	-11.211	-12.413	-12.637
Difference (%)		-4.650	4.044	0.376	-0.101	-0.197	-0.218	-0.220

Table 43 Standard deviation of nacelle surge motion under HW condition

	θ_c \ θ_w	0°	30°	60°	90°	120°	150°	180°
PF (m)	0°	1.840	0.985	0.472	0.550	0.439	0.499	0.634
VF (m)		1.820	1.010	0.485	0.552	0.452	0.497	0.657
Difference (%)		1.055	-2.577	-2.904	-0.373	-2.828	0.454	-3.533
PF (m)	90°	1.450	0.830	0.379	0.690	0.524	0.572	0.740
VF (m)		1.436	0.849	0.401	0.699	0.538	0.568	0.765
Difference (%)		0.970	-2.256	-5.703	-1.305	-2.636	0.565	-3.372
PF (m)	180°	1.109	0.680	0.320	0.612	0.491	0.648	0.887
VF (m)		1.112	0.688	0.341	0.621	0.500	0.649	0.909
Difference (%)		-0.250	-1.184	-6.864	-1.512	-1.748	-0.166	-2.414
PF (m)	270°	1.498	0.765	0.347	0.496	0.416	0.534	0.736
VF (m)		1.477	0.785	0.362	0.489	0.425	0.534	0.762
Difference (%)		1.399	-2.604	-4.279	1.447	-1.985	0.059	-3.426

doi:10.6342/NTU202204241

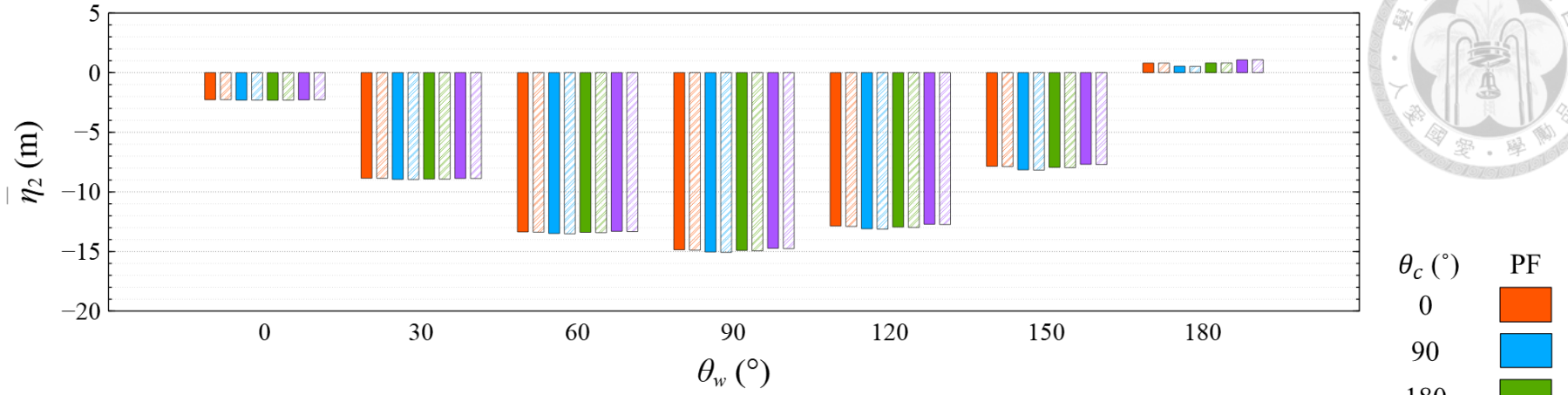

Figure 74 Comparison of mean value of nacelle sway motion under HW condition

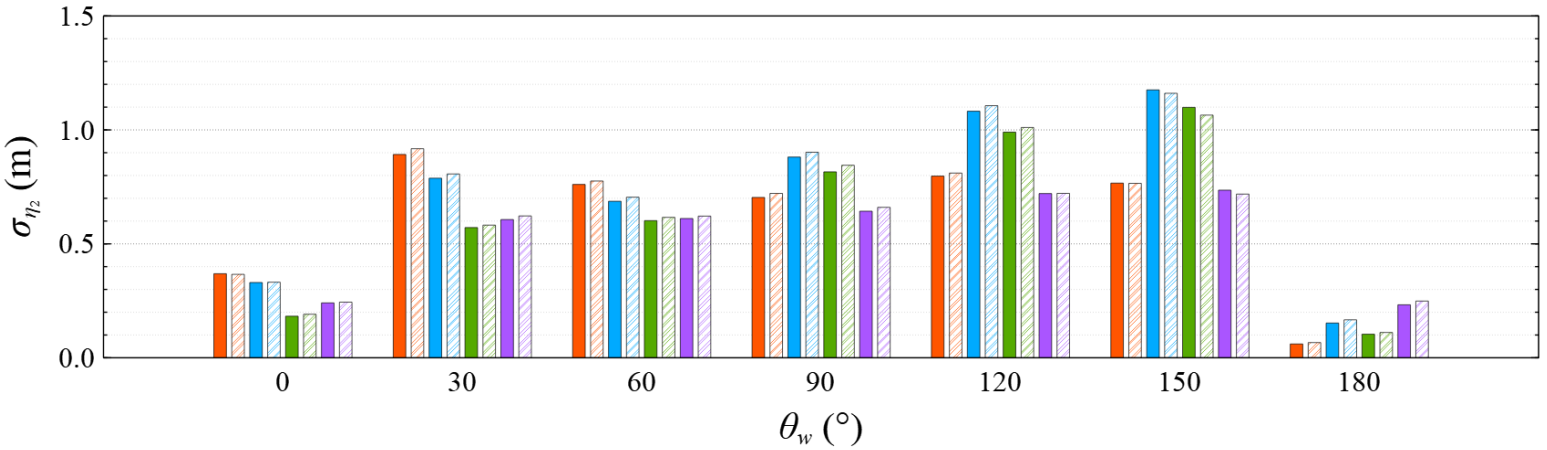

Figure 75 Comparison of standard deviation of nacelle sway motion under HW condition

doi:10.6342/NTU202204241

Table 44 Mean value of nacelle sway motion under HW condition

	θ_c \ θ_w	0°	30°	60°	90°	120°	150°	180°
PF (m)	0°	-2.270	-8.855	-13.357	-14.853	-12.861	-7.854	0.810
VF (m)		-2.268	-8.859	-13.378	-14.890	-12.896	-7.876	0.809
Difference (%)		0.089	-0.040	-0.160	-0.250	-0.265	-0.281	0.091
PF (m)	90°	-2.307	-8.947	-13.489	-15.036	-13.093	-8.150	0.542
VF (m)		-2.306	-8.956	-13.513	-15.073	-13.128	-8.172	0.528
Difference (%)		0.040	-0.093	-0.175	-0.252	-0.264	-0.267	2.666
PF (m)	180°	-2.313	-8.917	-13.391	-14.907	-12.949	-7.943	0.817
VF (m)		-2.309	-8.929	-13.419	-14.942	-12.981	-7.963	0.816
Difference (%)		0.170	-0.134	-0.213	-0.237	-0.241	-0.247	0.137
PF (m)	270°	-2.282	-8.868	-13.306	-14.729	-12.710	-7.686	1.075
VF (m)		-2.277	-8.874	-13.329	-14.759	-12.738	-7.705	1.086
Difference (%)		0.201	-0.064	-0.173	-0.206	-0.218	-0.253	-1.069

Table 45 Standard deviation of nacelle sway motion under HW condition

	θ_c \ θ_w	0°	30°	60°	90°	120°	150°	180°
PF (m)	0°	0.369	0.892	0.761	0.704	0.797	0.767	0.061
VF (m)		0.366	0.918	0.776	0.721	0.811	0.765	0.067
Difference (%)		0.787	-2.829	-1.968	-2.512	-1.654	0.138	-10.161
PF (m)	90°	0.330	0.788	0.687	0.881	1.082	1.176	0.153
VF (m)		0.332	0.807	0.705	0.902	1.106	1.161	0.167
Difference (%)		-0.423	-2.370	-2.621	-2.413	-2.251	1.266	-9.289
PF (m)	180°	0.183	0.572	0.602	0.816	0.990	1.099	0.104
VF (m)		0.191	0.582	0.616	0.845	1.011	1.065	0.111
Difference (%)		-4.705	-1.862	-2.382	-3.559	-2.054	3.101	-7.266
PF (m)	270°	0.241	0.607	0.611	0.643	0.721	0.736	0.233
VF (m)		0.244	0.623	0.622	0.660	0.722	0.718	0.249
Difference (%)		-1.392	-2.618	-1.730	-2.637	-0.117	2.335	-7.061

doi:10.6342/NTU202204241

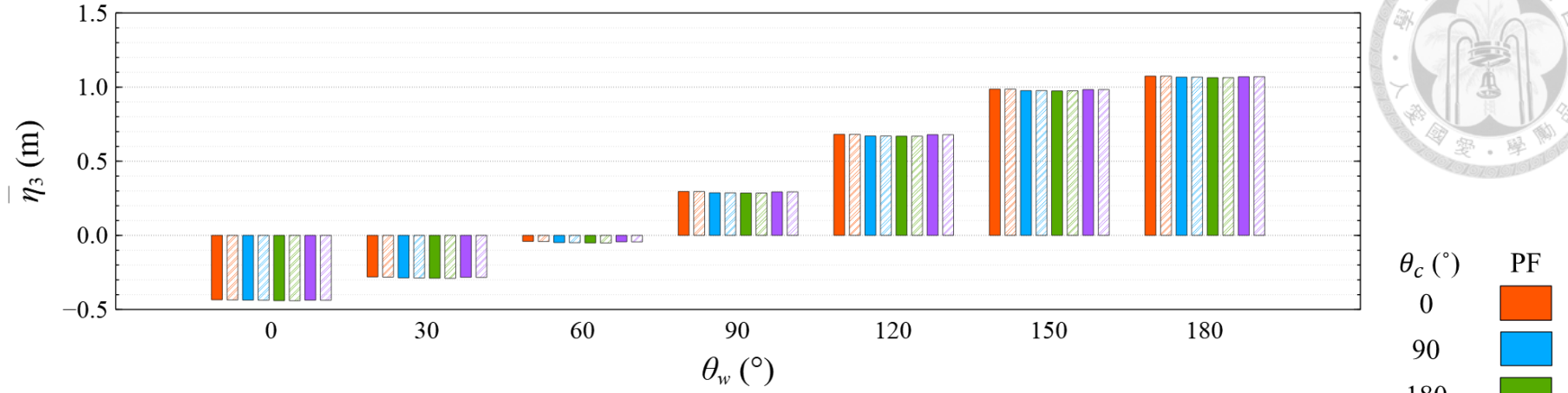

Figure 76 Comparison of mean value of nacelle heave motion under HW condition

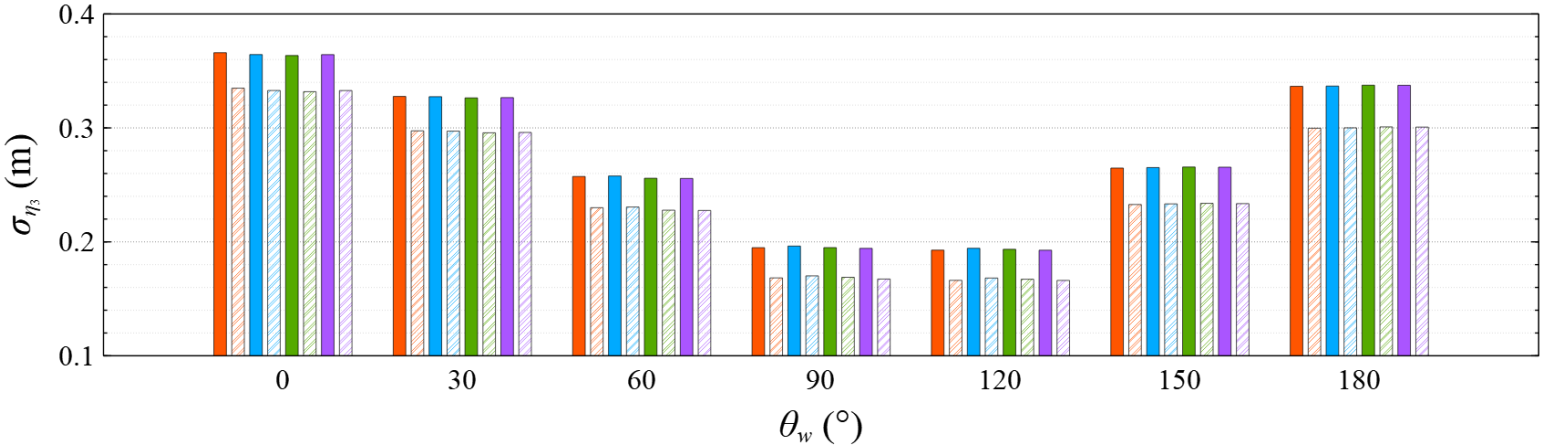

Figure 77 Comparison of standard deviation of nacelle heave motion under HW condition

doi:10.6342/NTU202204241

Table 46 Mean value of nacelle heave motion under HW condition

	θ_w / θ_c	0°	30°	60°	90°	120°	150°	180°
PF (m)	0°	-0.434	-0.280	-0.040	0.296	0.682	0.987	1.074
VF (m)		-0.435	-0.281	-0.041	0.296	0.681	0.987	1.074
Difference (%)		-0.225	-0.416	-2.134	0.131	0.053	0.009	0.002
PF (m)	90°	-0.437	-0.286	-0.048	0.287	0.670	0.976	1.067
VF (m)		-0.437	-0.287	-0.049	0.287	0.670	0.977	1.068
Difference (%)		-0.195	-0.353	-1.558	0.190	0.038	-0.013	-0.009
PF (m)	180°	-0.440	-0.289	-0.050	0.285	0.669	0.974	1.064
VF (m)		-0.441	-0.290	-0.051	0.285	0.669	0.975	1.064
Difference (%)		-0.156	-0.251	-1.223	0.075	0.017	-0.044	-0.029
PF (m)	270°	-0.437	-0.282	-0.043	0.293	0.679	0.983	1.070
VF (m)		-0.438	-0.283	-0.044	0.293	0.679	0.983	1.070
Difference (%)		-0.172	-0.309	-1.471	-0.007	0.025	-0.016	-0.013

Table 47 Standard deviation of nacelle heave motion under HW condition

	θ_w / θ_c	0°	30°	60°	90°	120°	150°	180°
PF (m)	0°	0.366	0.328	0.257	0.195	0.193	0.265	0.336
VF (m)		0.335	0.297	0.230	0.168	0.166	0.233	0.300
Difference (%)		8.500	9.216	10.635	13.614	13.760	12.083	10.920
PF (m)	90°	0.364	0.327	0.258	0.196	0.194	0.265	0.337
VF (m)		0.333	0.297	0.231	0.170	0.168	0.233	0.300
Difference (%)		8.654	9.238	10.563	13.318	13.441	12.023	10.886
PF (m)	180°	0.364	0.326	0.256	0.195	0.193	0.266	0.337
VF (m)		0.332	0.296	0.228	0.169	0.167	0.234	0.301
Difference (%)		8.726	9.390	10.961	13.369	13.581	12.008	10.842
PF (m)	270°	0.364	0.327	0.256	0.194	0.193	0.266	0.337
VF (m)		0.333	0.296	0.228	0.167	0.166	0.234	0.301
Difference (%)		8.654	9.362	10.987	13.854	13.772	12.046	10.874

doi:10.6342/NTU202204241

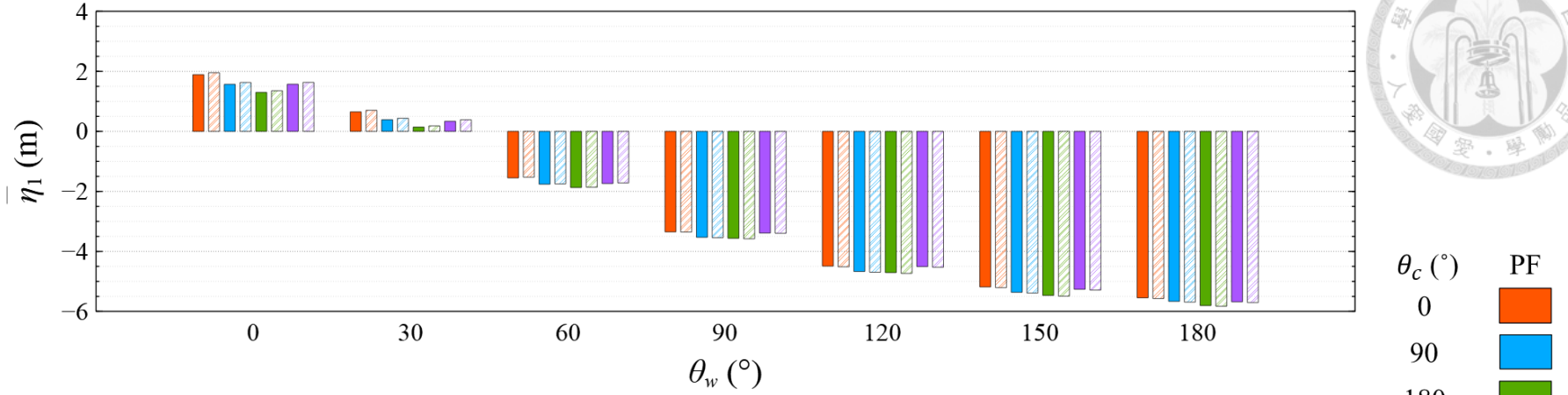

Figure 78 Comparison of mean value of platform surge motion under HW condition

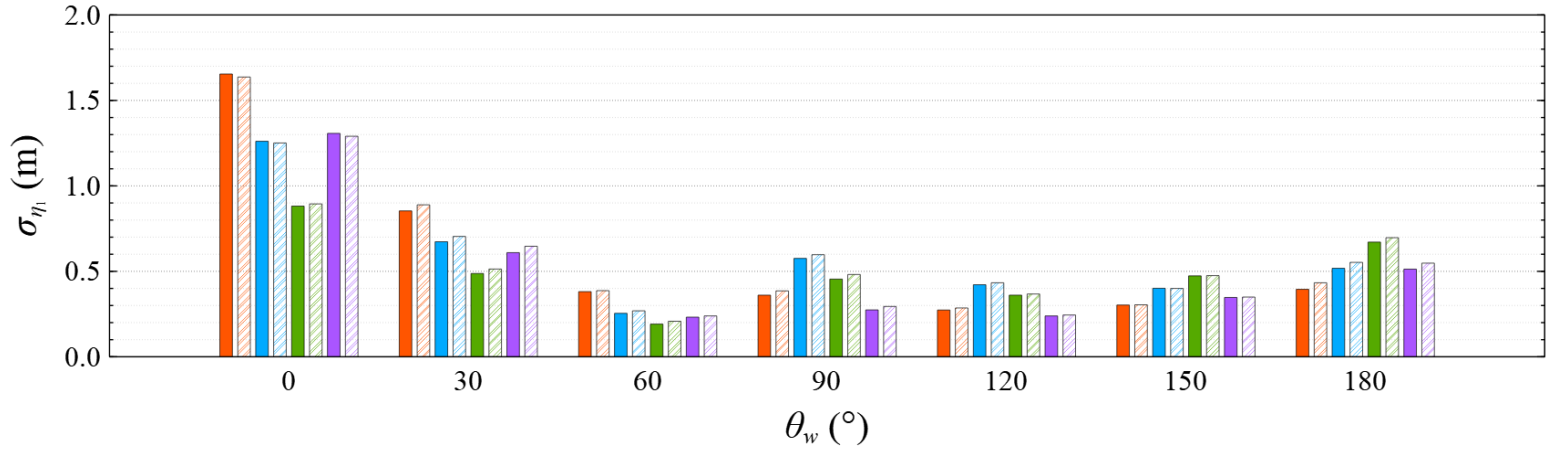

Figure 79 Comparison of standard deviation of platform surge motion under HW condition

doi:10.6342/NTU202204241

Table 48 Mean value of platform surge motion under HW condition

	θ_w / θ_c	0°	30°	60°	90°	120°	150°	180°
PF (m)	0°	1.891	0.651	-1.551	-3.350	-4.492	-5.185	-5.546
VF (m)		1.954	0.703	-1.527	-3.356	-4.513	-5.209	-5.572
Difference (%)		-3.251	-7.399	1.542	-0.176	-0.486	-0.447	-0.450
PF (m)	90°	1.570	0.389	-1.762	-3.531	-4.670	-5.364	-5.666
VF (m)		1.630	0.436	-1.750	-3.544	-4.694	-5.390	-5.690
Difference (%)		-3.694	-10.815	0.661	-0.375	-0.501	-0.473	-0.436
PF (m)	180°	1.301	0.143	-1.873	-3.564	-4.707	-5.466	-5.806
VF (m)		1.356	0.184	-1.863	-3.580	-4.734	-5.492	-5.830
Difference (%)		-4.059	-22.289	0.504	-0.468	-0.570	-0.469	-0.408
PF (m)	270°	1.573	0.337	-1.739	-3.389	-4.506	-5.263	-5.679
VF (m)		1.633	0.387	-1.719	-3.398	-4.529	-5.289	-5.704
Difference (%)		-3.677	-12.939	1.166	-0.260	-0.510	-0.485	-0.442

Table 49 Standard deviation of platform surge motion under HW condition

	θ_w / θ_c	0°	30°	60°	90°	120°	150°	180°
PF (m)	0°	1.654	0.854	0.381	0.361	0.274	0.303	0.395
VF (m)		1.637	0.889	0.387	0.386	0.286	0.304	0.433
Difference (%)		1.059	-4.166	-1.531	-6.952	-4.406	-0.440	-9.685
PF (m)	90°	1.261	0.673	0.254	0.576	0.422	0.401	0.518
VF (m)		1.251	0.704	0.269	0.597	0.433	0.400	0.552
Difference (%)		0.789	-4.632	-5.737	-3.725	-2.734	0.263	-6.659
PF (m)	180°	0.882	0.487	0.191	0.455	0.361	0.474	0.671
VF (m)		0.894	0.513	0.208	0.482	0.367	0.475	0.697
Difference (%)		-1.428	-5.330	-8.696	-5.926	-1.851	-0.286	-3.843
PF (m)	270°	1.307	0.609	0.232	0.274	0.239	0.347	0.513
VF (m)		1.290	0.647	0.239	0.295	0.245	0.349	0.548
Difference (%)		1.295	-6.148	-3.072	-7.354	-2.269	-0.665	-6.830

doi:10.6342/NTU202204241

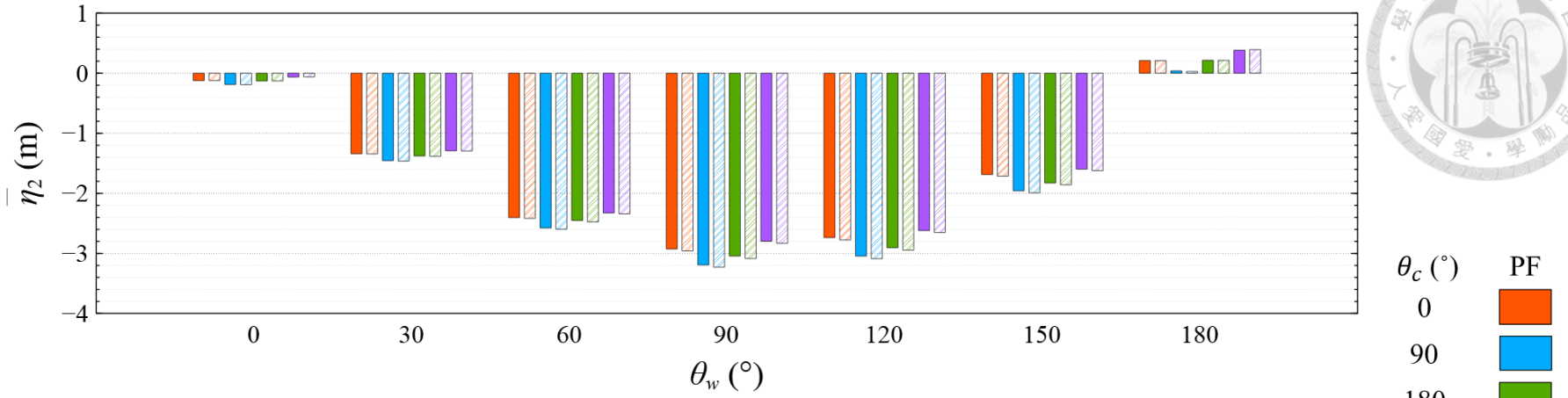

Figure 80 Comparison of mean value of platform sway motion under HW condition

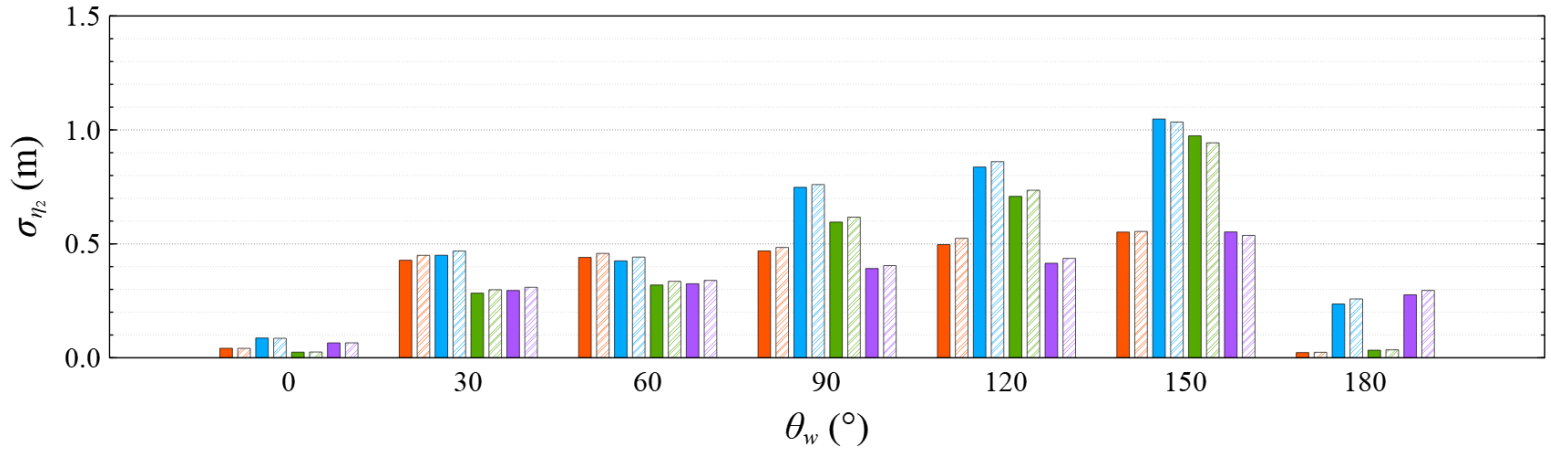

Figure 81 Comparison of standard deviation of platform sway motion under HW condition

doi:10.6342/NTU202204241

Table 50 Mean value of platform sway motion under HW condition

	θ_c \ θ_w	0°	30°	60°	90°	120°	150°	180°
PF (m)	0°	-0.123	-1.341	-2.404	-2.926	-2.737	-1.687	0.211
VF (m)		-0.122	-1.344	-2.417	-2.959	-2.777	-1.714	0.211
Difference (%)		0.249	-0.237	-0.561	-1.104	-1.413	-1.599	0.389
PF (m)	90°	-0.187	-1.456	-2.576	-3.192	-3.045	-1.958	0.040
VF (m)		-0.189	-1.463	-2.597	-3.230	-3.088	-1.991	0.029
Difference (%)		-1.301	-0.501	-0.817	-1.200	-1.395	-1.655	37.236
PF (m)	180°	-0.130	-1.376	-2.452	-3.044	-2.906	-1.828	0.215
VF (m)		-0.129	-1.384	-2.475	-3.086	-2.946	-1.858	0.214
Difference (%)		0.148	-0.511	-0.923	-1.342	-1.381	-1.601	0.596
PF (m)	270°	-0.063	-1.291	-2.326	-2.799	-2.619	-1.597	0.383
VF (m)		-0.061	-1.294	-2.342	-2.832	-2.653	-1.622	0.393
Difference (%)		4.505	-0.250	-0.689	-1.166	-1.263	-1.566	-2.498

Table 51 Standard deviation of platform sway motion under HW condition

	θ_c \ θ_w	0°	30°	60°	90°	120°	150°	180°
PF (m)	0°	0.042	0.428	0.440	0.469	0.497	0.552	0.023
VF (m)		0.041	0.450	0.458	0.484	0.524	0.554	0.024
Difference (%)		0.805	-5.045	-4.013	-3.244	-5.531	-0.488	-5.758
PF (m)	90°	0.087	0.450	0.425	0.748	0.837	1.048	0.236
VF (m)		0.086	0.468	0.442	0.760	0.861	1.035	0.258
Difference (%)		1.405	-4.043	-3.853	-1.612	-2.815	1.264	-9.334
PF (m)	180°	0.025	0.284	0.319	0.596	0.708	0.974	0.033
VF (m)		0.025	0.299	0.335	0.617	0.735	0.943	0.035
Difference (%)		-2.216	-5.272	-5.025	-3.636	-3.805	3.162	-5.003
PF (m)	270°	0.065	0.295	0.325	0.392	0.415	0.552	0.276
VF (m)		0.066	0.309	0.340	0.405	0.436	0.537	0.296
Difference (%)		-0.433	-4.718	-4.516	-3.293	-5.110	2.749	-6.904

doi:10.6342/NTU202204241

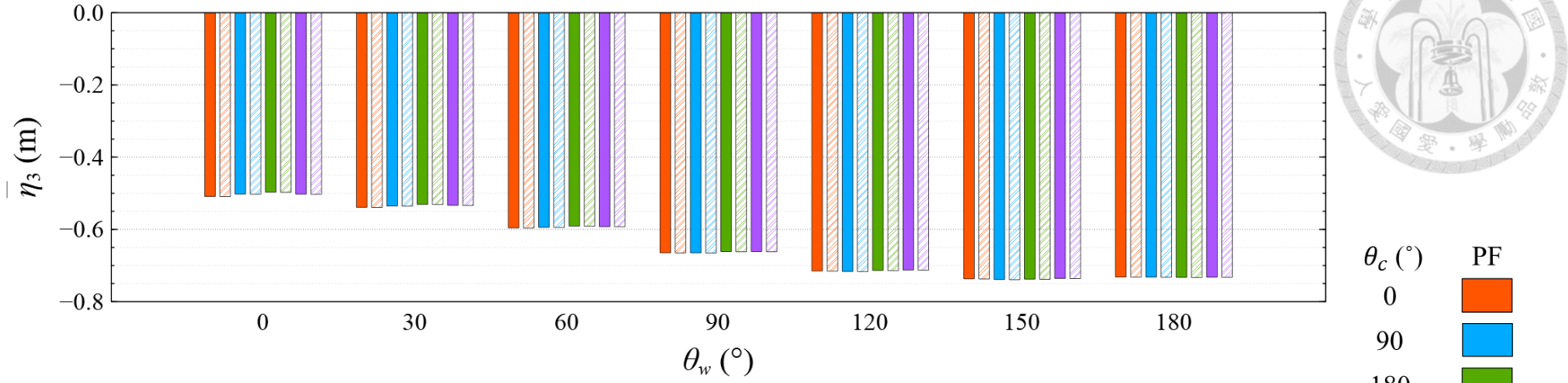

Figure 82 Comparison of mean value of platform heave motion under HW condition

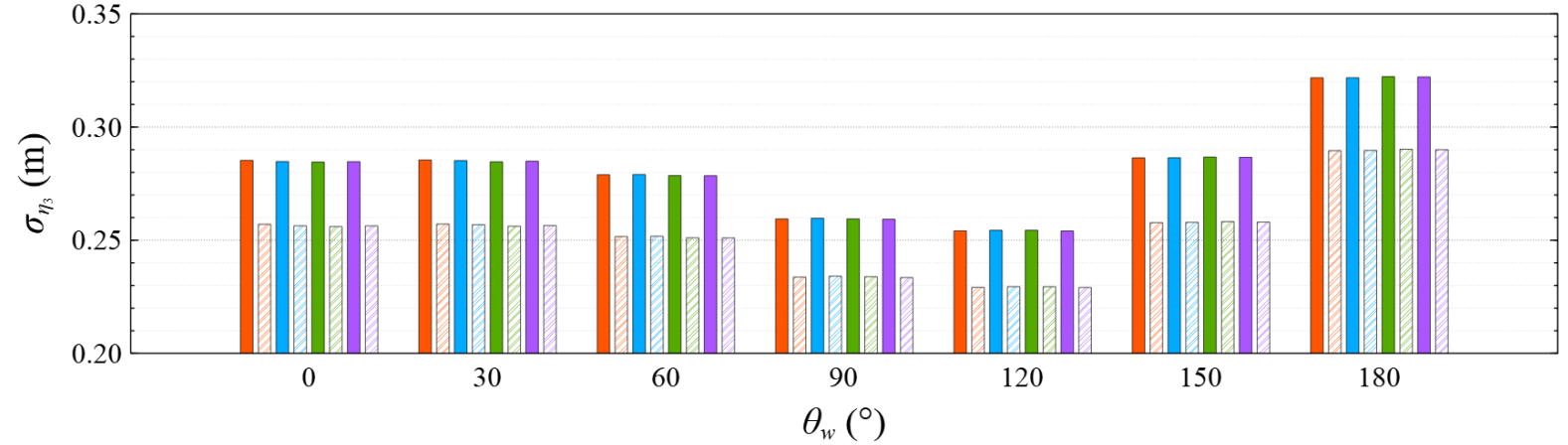

Figure 83 Comparison of standard deviation of platform heave motion under HW condition

doi:10.6342/NTU202204241

Table 52 Mean value of platform heave motion under HW condition

	θ_w / θ_c	0°	30°	60°	90°	120°	150°	180°
PF (m)	0°	-0.509	-0.539	-0.596	-0.665	-0.715	-0.737	-0.732
VF (m)		-0.509	-0.539	-0.596	-0.665	-0.715	-0.737	-0.732
Difference (%)		-0.103	-0.093	-0.042	-0.053	-0.043	-0.052	-0.061
PF (m)	90°	-0.502	-0.535	-0.594	-0.665	-0.716	-0.739	-0.732
VF (m)		-0.503	-0.536	-0.594	-0.665	-0.717	-0.739	-0.733
Difference (%)		-0.096	-0.067	-0.035	-0.072	-0.056	-0.055	-0.066
PF (m)	180°	-0.497	-0.531	-0.591	-0.661	-0.714	-0.738	-0.733
VF (m)		-0.497	-0.531	-0.591	-0.662	-0.714	-0.738	-0.733
Difference (%)		-0.095	-0.047	-0.022	-0.071	-0.055	-0.051	-0.068
PF (m)	270°	-0.502	-0.533	-0.592	-0.661	-0.712	-0.736	-0.732
VF (m)		-0.503	-0.534	-0.592	-0.662	-0.713	-0.736	-0.733
Difference (%)		-0.095	-0.074	-0.028	-0.052	-0.041	-0.054	-0.067

Table 53 Standard deviation of platform heave motion under HW condition

	θ_w / θ_c	0°	30°	60°	90°	120°	150°	180°
PF (m)	0°	0.285	0.285	0.279	0.259	0.254	0.286	0.322
VF (m)		0.257	0.257	0.252	0.234	0.229	0.258	0.290
Difference (%)		9.885	9.917	9.788	9.895	9.830	9.984	10.001
PF (m)	90°	0.285	0.285	0.279	0.260	0.254	0.286	0.322
VF (m)		0.256	0.257	0.252	0.234	0.229	0.258	0.290
Difference (%)		9.971	9.934	9.774	9.833	9.798	9.945	9.980
PF (m)	180°	0.285	0.285	0.279	0.259	0.254	0.287	0.322
VF (m)		0.256	0.256	0.251	0.234	0.229	0.258	0.290
Difference (%)		10.016	10.002	9.870	9.844	9.804	9.937	9.957
PF (m)	270°	0.285	0.285	0.278	0.259	0.254	0.287	0.322
VF (m)		0.256	0.256	0.251	0.234	0.229	0.258	0.290
Difference (%)		9.971	9.978	9.870	9.937	9.825	9.969	9.978

doi:10.6342/NTU202204241

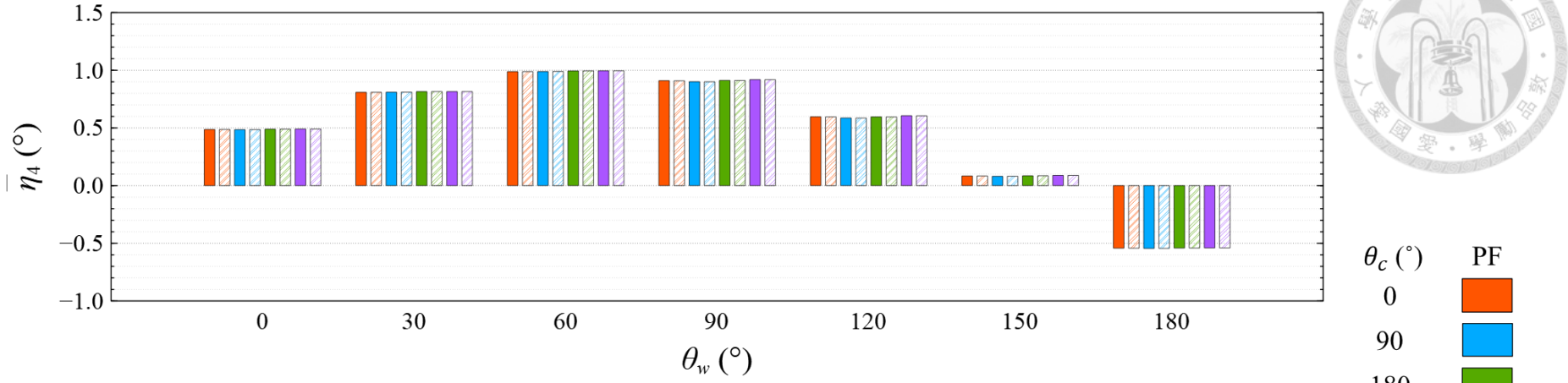

Figure 84 Comparison of mean value of platform roll motion under HW condition

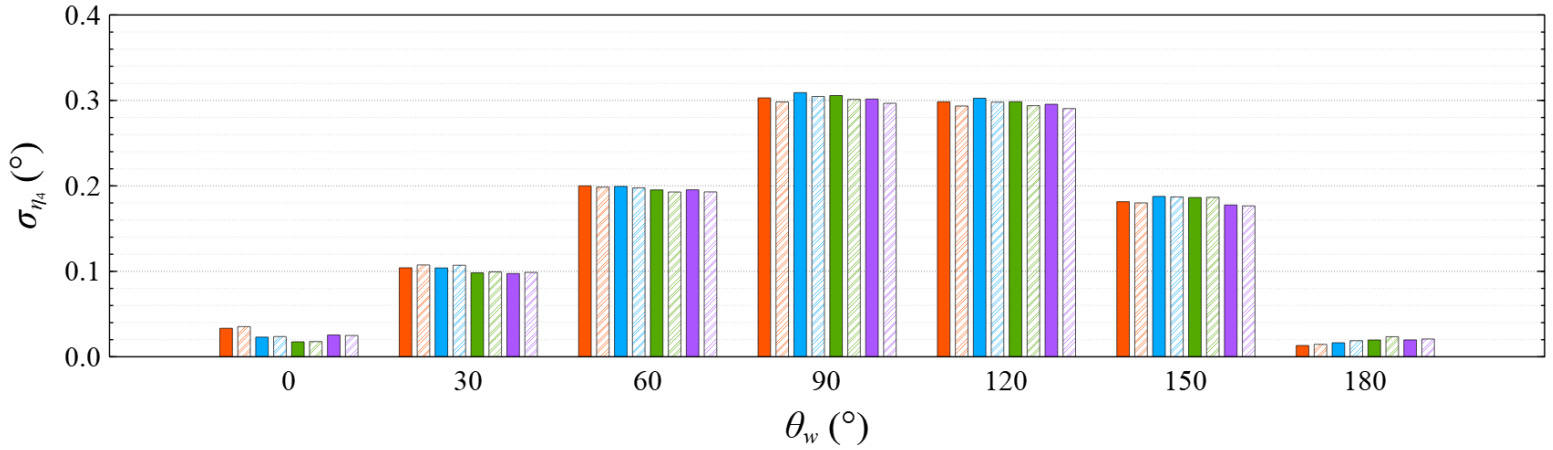

Figure 85 Comparison of standard deviation of platform roll motion under HW condition

doi:10.6342/NTU202204241

Table 54 Mean value of platform roll motion under HW condition

	θ_w / θ_c	0°	30°	60°	90°	120°	150°	180°
PF (°)	0°	0.487	0.809	0.988	0.910	0.597	0.084	-0.542
VF (°)		0.487	0.809	0.988	0.909	0.596	0.084	-0.542
Difference (%)		0.052	-0.023	-0.015	0.107	0.193	-0.278	0.019
PF (°)	90°	0.485	0.810	0.989	0.901	0.587	0.081	-0.544
VF (°)		0.485	0.810	0.990	0.901	0.586	0.081	-0.544
Difference (%)		-0.006	-0.044	-0.075	0.070	0.140	-0.786	0.035
PF (°)	180°	0.489	0.815	0.994	0.912	0.596	0.085	-0.541
VF (°)		0.489	0.815	0.995	0.911	0.595	0.086	-0.541
Difference (%)		0.027	-0.004	-0.043	0.099	0.153	-0.429	0.024
PF (°)	270°	0.491	0.815	0.995	0.919	0.606	0.089	-0.540
VF (°)		0.490	0.815	0.995	0.919	0.606	0.089	-0.540
Difference (%)		0.087	0.002	-0.010	0.059	0.142	-0.150	0.014

Table 55 Standard deviation of platform roll motion under HW condition

	θ_w / θ_c	0°	30°	60°	90°	120°	150°	180°
PF (°)	0°	0.033	0.104	0.200	0.303	0.298	0.181	0.013
VF (°)		0.035	0.107	0.199	0.298	0.293	0.180	0.015
Difference (%)		-5.836	-3.200	0.757	1.569	1.667	0.784	-10.292
PF (°)	90°	0.023	0.104	0.199	0.309	0.303	0.188	0.016
VF (°)		0.024	0.107	0.198	0.305	0.298	0.187	0.019
Difference (%)		-2.823	-3.048	0.878	1.455	1.511	0.320	-14.629
PF (°)	180°	0.018	0.098	0.195	0.306	0.298	0.186	0.020
VF (°)		0.018	0.099	0.193	0.301	0.294	0.187	0.023
Difference (%)		-1.556	-1.160	1.264	1.474	1.547	-0.131	-19.331
PF (°)	270°	0.026	0.097	0.195	0.302	0.296	0.178	0.020
VF (°)		0.025	0.099	0.193	0.297	0.290	0.177	0.021
Difference (%)		2.324	-1.360	1.239	1.629	1.713	0.582	-5.327

doi:10.6342/NTU202204241

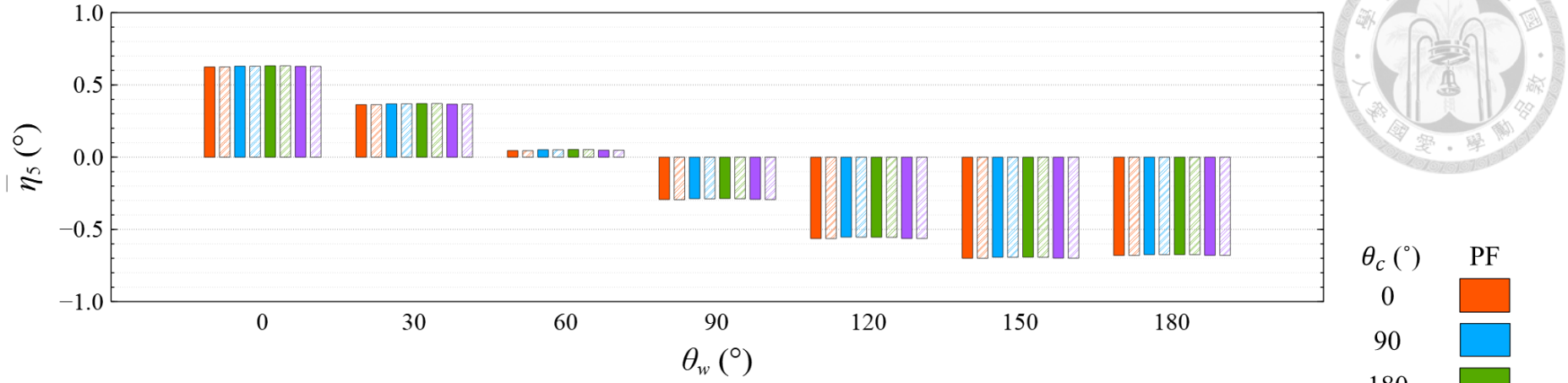

Figure 86 Comparison of mean value of platform pitch motion under HW condition

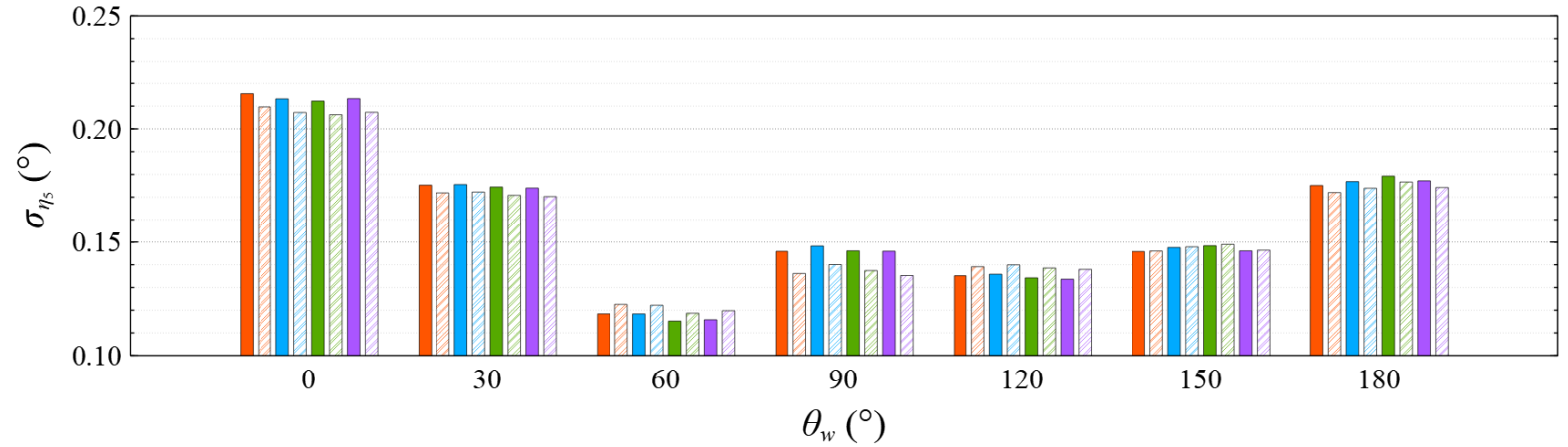

Figure 87 Comparison of standard deviation of platform pitch motion under HW condition

doi:10.6342/NTU202204241

Table 56 Mean value of platform pitch motion under HW condition

	θ_w / θ_c	0°	30°	60°	90°	120°	150°	180°
PF (°)	0°	0.624	0.363	0.045	-0.293	-0.563	-0.700	-0.680
VF (°)		0.624	0.363	0.045	-0.294	-0.564	-0.700	-0.680
Difference (%)		-0.028	-0.061	1.142	-0.447	-0.051	-0.006	0.009
PF (°)	90°	0.630	0.369	0.051	-0.287	-0.553	-0.693	-0.675
VF (°)		0.630	0.369	0.051	-0.288	-0.554	-0.693	-0.675
Difference (%)		0.002	-0.054	0.932	-0.382	-0.085	-0.038	-0.013
PF (°)	180°	0.633	0.371	0.053	-0.287	-0.554	-0.692	-0.674
VF (°)		0.633	0.371	0.052	-0.288	-0.555	-0.693	-0.675
Difference (%)		-0.001	-0.041	1.120	-0.440	-0.094	-0.080	-0.047
PF (°)	270°	0.628	0.366	0.048	-0.292	-0.563	-0.699	-0.679
VF (°)		0.628	0.367	0.048	-0.293	-0.563	-0.699	-0.679
Difference (%)		0.018	-0.062	1.090	-0.461	-0.065	-0.046	-0.029

Table 57 Standard deviation of platform pitch motion under HW condition

	θ_w / θ_c	0°	30°	60°	90°	120°	150°	180°
PF (°)	0°	0.215	0.175	0.118	0.146	0.135	0.146	0.175
VF (°)		0.210	0.172	0.123	0.136	0.139	0.146	0.172
Difference (%)		2.700	1.942	-3.522	6.691	-2.926	-0.152	1.783
PF (°)	90°	0.213	0.176	0.118	0.148	0.136	0.148	0.177
VF (°)		0.207	0.172	0.122	0.140	0.140	0.148	0.174
Difference (%)		2.811	1.885	-3.221	5.517	-3.022	-0.211	1.648
PF (°)	180°	0.212	0.174	0.115	0.146	0.134	0.148	0.179
VF (°)		0.206	0.171	0.119	0.137	0.139	0.149	0.177
Difference (%)		2.832	2.093	-3.002	5.943	-3.231	-0.420	1.437
PF (°)	270°	0.213	0.174	0.116	0.146	0.134	0.146	0.177
VF (°)		0.207	0.170	0.120	0.135	0.138	0.146	0.174
Difference (%)		2.818	2.146	-3.431	7.322	-3.237	-0.203	1.658

doi:10.6342/NTU202204241

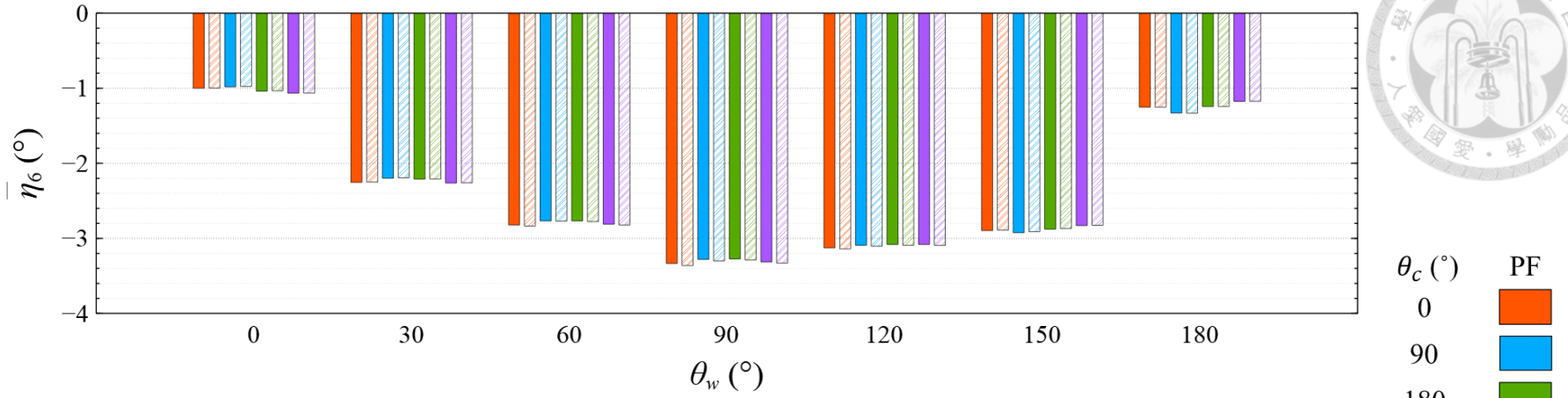

Figure 88 Comparison of mean value of platform yaw motion under HW condition

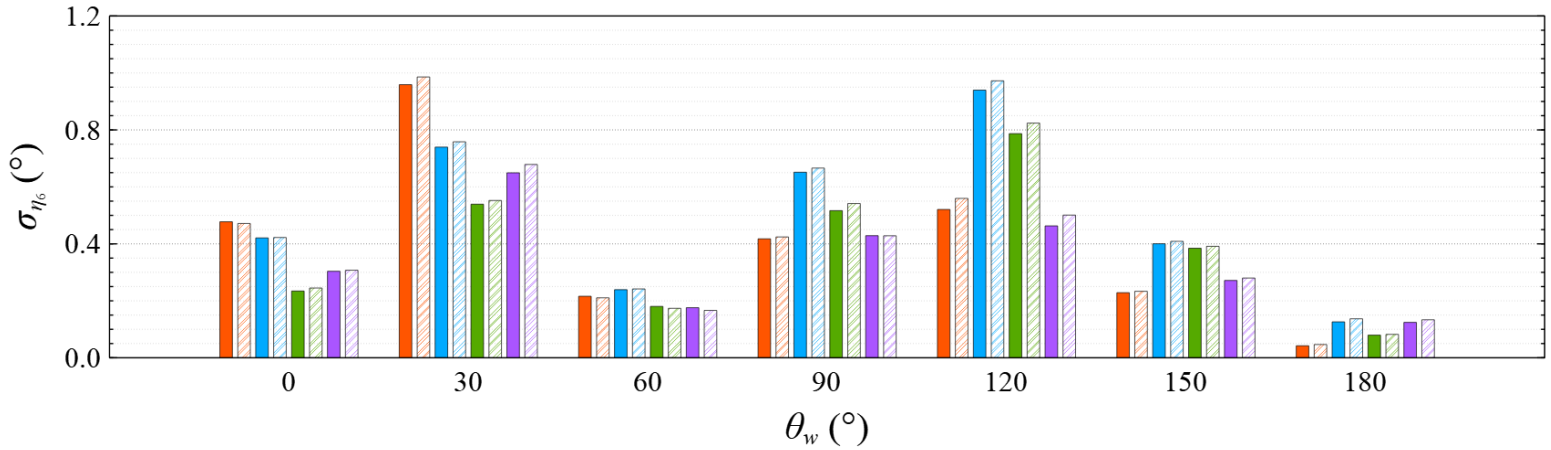

Figure 89 Comparison of standard deviation of platform yaw motion under HW condition

doi:10.6342/NTU202204241

Table 58 Mean value of platform yaw motion under HW condition

	θ_c \ θ_w	0°	30°	60°	90°	120°	150°	180°
PF (°)	0°	-1.000	-2.254	-2.821	-3.334	-3.127	-2.895	-1.252
VF (°)		-0.998	-2.250	-2.835	-3.362	-3.141	-2.890	-1.251
Difference (%)		0.125	0.195	-0.505	-0.822	-0.445	0.200	0.032
PF (°)	90°	-0.981	-2.198	-2.767	-3.280	-3.092	-2.924	-1.329
VF (°)		-0.977	-2.192	-2.770	-3.300	-3.104	-2.911	-1.332
Difference (%)		0.448	0.299	-0.120	-0.625	-0.390	0.451	-0.214
PF (°)	180°	-1.038	-2.210	-2.767	-3.274	-3.080	-2.877	-1.243
VF (°)		-1.034	-2.209	-2.776	-3.288	-3.092	-2.868	-1.243
Difference (%)		0.431	0.065	-0.319	-0.440	-0.371	0.291	0.043
PF (°)	270°	-1.066	-2.263	-2.810	-3.313	-3.080	-2.829	-1.175
VF (°)		-1.065	-2.261	-2.822	-3.330	-3.093	-2.825	-1.174
Difference (%)		0.100	0.113	-0.407	-0.499	-0.405	0.151	0.131

Table 59 Standard deviation of platform yaw motion under HW condition

	θ_c \ θ_w	0°	30°	60°	90°	120°	150°	180°
PF (°)	0°	0.478	0.959	0.216	0.418	0.521	0.229	0.042
VF (°)		0.471	0.986	0.211	0.424	0.560	0.233	0.047
Difference (%)		1.261	-2.814	2.555	-1.591	-7.455	-2.137	-10.412
PF (°)	90°	0.421	0.740	0.239	0.651	0.940	0.400	0.126
VF (°)		0.422	0.758	0.242	0.666	0.972	0.409	0.137
Difference (%)		-0.339	-2.525	-1.074	-2.241	-3.471	-2.110	-8.530
PF (°)	180°	0.234	0.539	0.180	0.517	0.787	0.385	0.080
VF (°)		0.245	0.552	0.174	0.542	0.824	0.391	0.082
Difference (%)		-4.483	-2.418	3.748	-4.841	-4.701	-1.768	-3.393
PF (°)	270°	0.304	0.649	0.176	0.429	0.463	0.272	0.124
VF (°)		0.307	0.679	0.166	0.428	0.501	0.280	0.133
Difference (%)		-1.201	-4.523	5.392	0.089	-8.176	-3.100	-7.323

doi:10.6342/NTU202204241

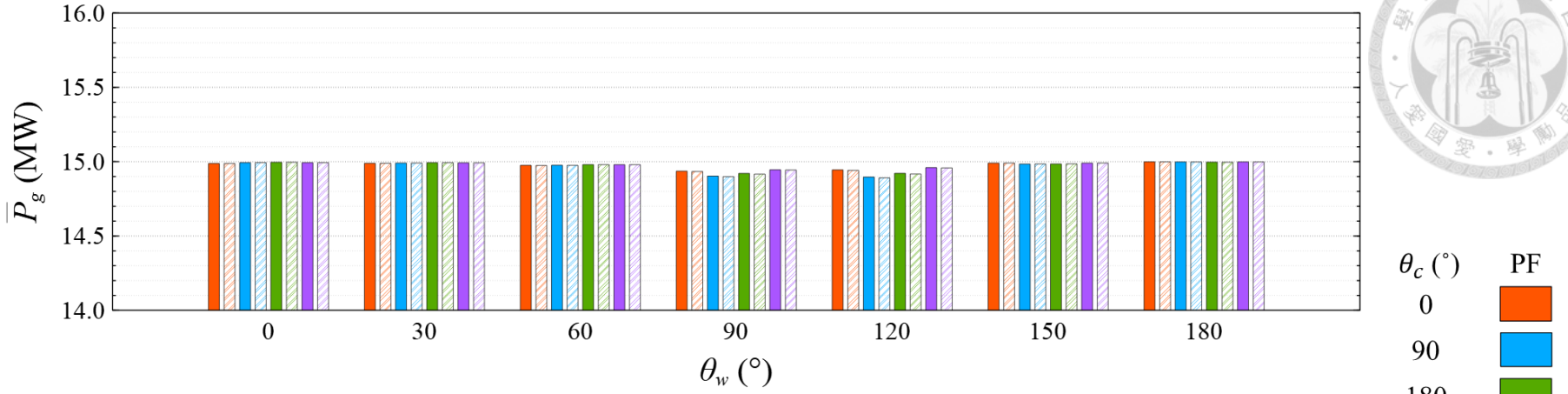

Figure 90 Comparison of mean value of generator electrical power under HW condition

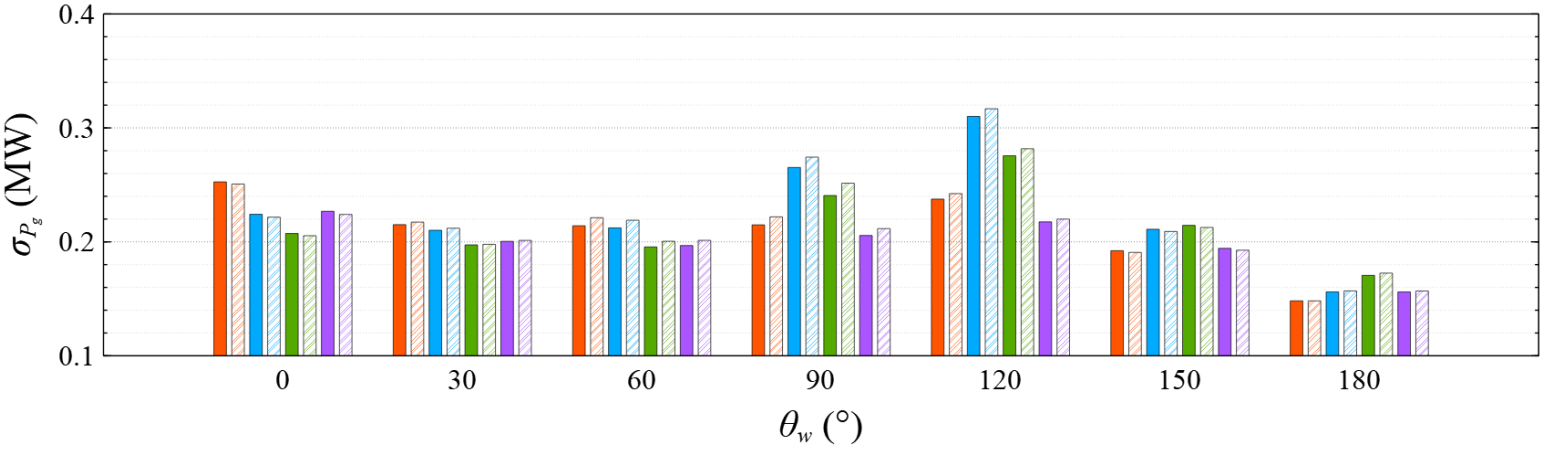

Figure 91 Comparison of standard deviation of generator electrical power under HW condition

doi:10.6342/NTU202204241

Table 60 Mean value of generator electrical power under HW condition

	θ_c \ θ_w	0°	30°	60°	90°	120°	150°	180°
PF (MW)	0°	14.988	14.989	14.975	14.936	14.945	14.991	14.999
VF (MW)		14.988	14.989	14.974	14.934	14.941	14.991	14.999
Difference (%)		0.001	0.001	0.008	0.018	0.023	-0.001	0.001
PF (MW)	90°	14.993	14.991	14.976	14.903	14.896	14.984	14.998
VF (MW)		14.993	14.991	14.975	14.899	14.891	14.985	14.998
Difference (%)		-0.001	0.001	0.006	0.024	0.035	-0.003	0.002
PF (MW)	180°	14.996	14.993	14.980	14.921	14.922	14.985	14.997
VF (MW)		14.996	14.993	14.980	14.916	14.917	14.985	14.996
Difference (%)		-0.001	0.000	0.001	0.033	0.032	-0.004	0.004
PF (MW)	270°	14.993	14.992	14.980	14.945	14.960	14.990	14.998
VF (MW)		14.993	14.992	14.980	14.944	14.958	14.991	14.998
Difference (%)		-0.001	0.001	0.000	0.010	0.013	-0.002	0.002

Table 61 Standard deviation of generator electrical power under HW condition

	θ_c \ θ_w	0°	30°	60°	90°	120°	150°	180°
PF (MW)	0°	0.253	0.215	0.214	0.215	0.238	0.192	0.148
VF (MW)		0.251	0.217	0.221	0.222	0.242	0.191	0.148
Difference (%)		0.739	-1.045	-3.311	-3.274	-2.035	0.792	0.009
PF (MW)	90°	0.224	0.210	0.212	0.265	0.310	0.211	0.156
VF (MW)		0.222	0.212	0.219	0.274	0.317	0.209	0.157
Difference (%)		1.121	-0.859	-3.164	-3.414	-2.159	0.914	-0.544
PF (MW)	180°	0.207	0.197	0.196	0.241	0.276	0.214	0.171
VF (MW)		0.205	0.198	0.201	0.251	0.282	0.213	0.173
Difference (%)		0.940	-0.249	-2.529	-4.484	-2.232	0.862	-1.147
PF (MW)	270°	0.227	0.200	0.197	0.206	0.218	0.194	0.156
VF (MW)		0.224	0.201	0.201	0.212	0.220	0.193	0.157
Difference (%)		1.227	-0.419	-2.319	-2.931	-1.088	0.845	-0.522

doi:10.6342/NTU202204241

4.5 Mooring Line Tension

The mooring line tension is calculated by finite element method in OrcaFlex. The design and specifications for the mooring lines used in this study is shown in Figure 5 and Table 2. There are six mooring lines equipped on the TaidaFloat platform in this study. Two mooring lines are equipped on each column of the platform and the angle between these two mooring lines is 10°. The definition of the mooring lines is shown in Figure 92. The results under the CW condition are discussed in Section 4.5.1, while those under the HW condition are discussed in Section 4.5.2.

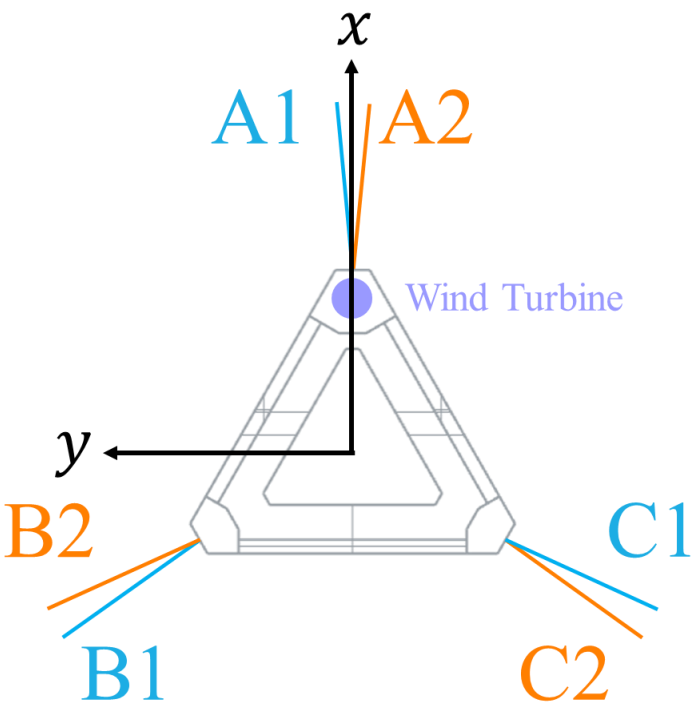

Figure 92 Definition of mooring lines

doi:10.6342/NTU202204241

4.5.1 Common Wave Condition

The mean values and standard deviations of the mooring line tension are shown in Figure 93 to Figure 104, and Table 62 to Table 73. The largest mean values of the mooring line tension of Line A1, A2, B1, B2, C1, and C2 appear at $(\theta_w, \theta_c) = (120°, 90°)$, $(180°, 180°)$, $(60°, 90°)$, $(60°, 90°)$, $(0°, 0°)$, and $(0°, 0°)$, and they are 2.135 MN, 1.763 MN, 2.114 MN, 1.68 MN, 1.433 MN, and 1.643 MN, respectively. The smallest mean values of the mooring line tension of Line A1, A2, B1, B2, C1, and C2 appear at $(\theta_w, \theta_c) = (0°, 0°)$, $(0°, 0°)$, $(180°, 270°)$, $(180°, 270°)$, $(150°, 90°)$, and $(120°, 180°)$, and they are 0.326 MN, 0.328 MN, 0.506 MN, 0.576 MN, 0.496 MN, and 0.387 MN, respectively. The largest standard deviations of the mooring line tension of Line A1, A2, B1, B2, C1, and C2 appear at $(\theta_w, \theta_c) = (180°, 180°)$, $(180°, 180°)$, $(0°, 0°)$, $(0°, 0°)$, $(0°, 0°)$, and $(0°, 0°)$, and they are 0.041 MN, 0.042 MN, 0.041 MN, 0.026 MN, 0.025 MN, and 0.041 MN, respectively. The smallest standard deviations of the mooring line tension of Line A1, A2, B1, B2, C1, and C2 appear at $(\theta_w, \theta_c) = (0°, 180°)$, $(30°, 180°)$, $(180°, 0°)$, $(180°, 0°)$, $(150°, 0°)$, and $(150°, 0°)$, and they are 0.002 MN, 0.002 MN, 0.004 MN, 0.005 MN, 0.004 MN, and 0.002 MN, respectively. Figure 105 to Figure 111 show the mean values of the mooring line tension at the seven studied wind directions. Line C2 shows the largest mean loading at $\theta_w = 0°$, which is up to 1.643 MN. Line B1 shows the largest mean loading at $\theta_w = 30°$, $60°$, and $90°$, which is up to 2.031 MN, 2.114 MN, and 1.983 MN, respectively. Line A1 shows the largest mean loading at $\theta_w = 120°$ and $150°$, which is up to 2.135 MN and 2.096 MN. Line A2 shows the largest loading at $\theta_w = 180°$, which is up to 1.763 MN.

Similar to the motion response and generator power, the difference of the mean values of mooring line tension between the two approaches as well as among the four

doi:10.6342/NTU202204241

current directions are clearly smaller than that of the standard deviations. All mooring line tensions are lower than one-sixth of the break load under the CW condition, and the smallest maximum mean mooring line tension appears at $\theta_w = 0°$.

doi:10.6342/NTU202204241

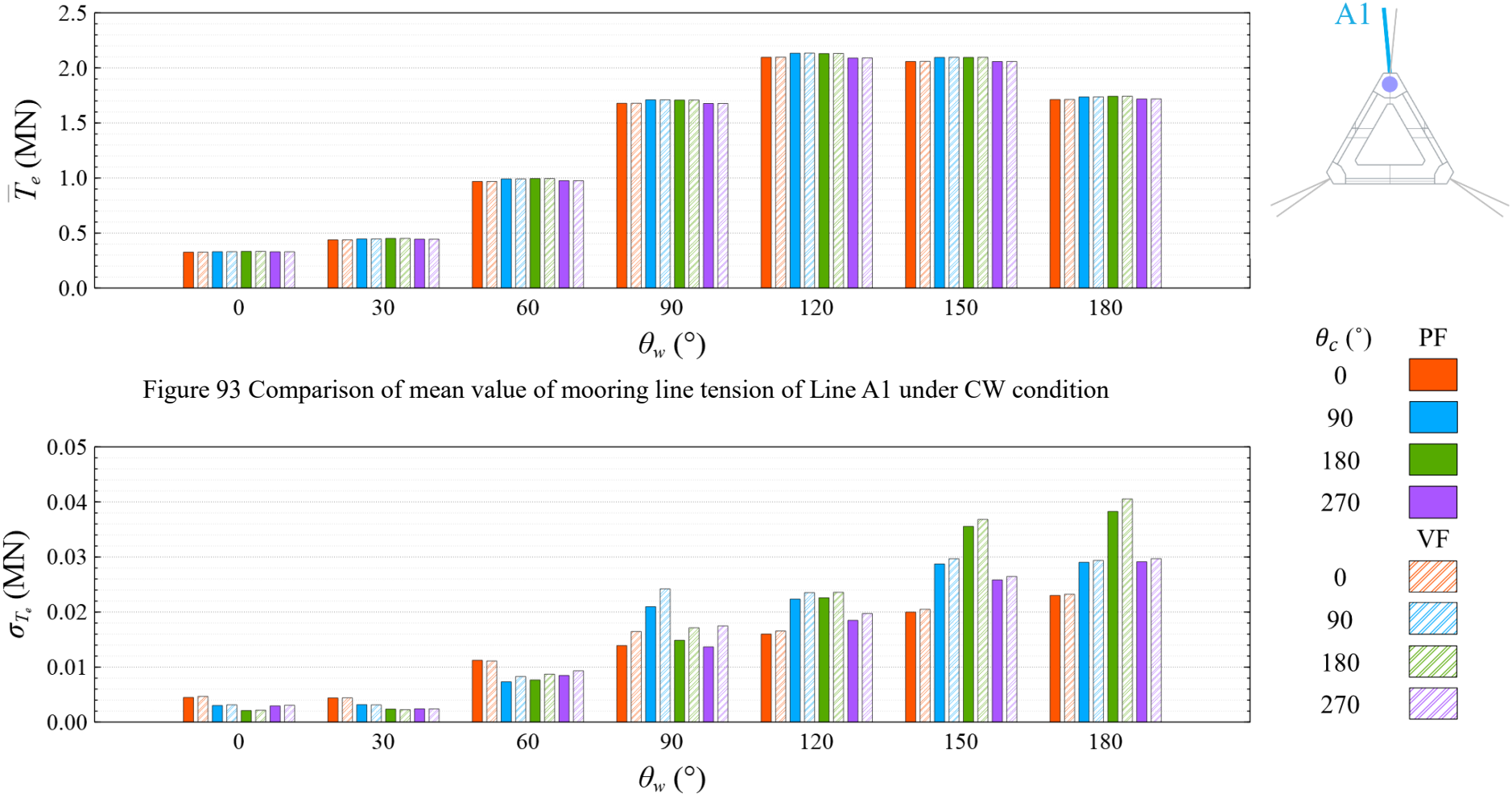

Figure 93 Comparison of mean value of mooring line tension of Line A1 under CW condition

Figure 94 Comparison of standard deviation of mooring line tension of Line A1 under CW condition

doi:10.6342/NTU202204241

Table 62 Mean value of mooring line tension of Line A1 under CW condition

	θ_w / θ_c	0°	30°	60°	90°	120°	150°	180°
PF (MN)	0°	0.326	0.438	0.969	1.679	2.096	2.058	1.713
VF (MN)		0.326	0.438	0.969	1.679	2.098	2.059	1.713
Difference (%)		-0.031	0.031	0.026	-0.011	-0.052	-0.049	-0.026
PF (MN)	90°	0.331	0.446	0.991	1.710	2.133	2.095	1.736
VF (MN)		0.331	0.446	0.991	1.710	2.135	2.096	1.737
Difference (%)		-0.029	0.016	0.013	-0.016	-0.062	-0.056	-0.039
PF (MN)	180°	0.334	0.451	0.995	1.708	2.130	2.095	1.742
VF (MN)		0.334	0.451	0.995	1.709	2.132	2.096	1.743
Difference (%)		-0.015	0.020	-0.002	-0.028	-0.075	-0.045	-0.047
PF (MN)	270°	0.330	0.444	0.976	1.677	2.089	2.058	1.718
VF (MN)		0.330	0.444	0.976	1.677	2.091	2.059	1.718
Difference (%)		-0.026	0.026	0.023	-0.015	-0.063	-0.037	-0.030

Table 63 Standard deviation of mooring line tension of Line A1 under CW condition

	θ_w / θ_c	0°	30°	60°	90°	120°	150°	180°
PF (MN)	0°	0.004	0.004	0.011	0.014	0.016	0.020	0.023
VF (MN)		0.005	0.004	0.011	0.016	0.017	0.021	0.023
Difference (%)		-4.114	-0.566	1.174	-15.519	-3.325	-2.530	-0.903
PF (MN)	90°	0.003	0.003	0.007	0.021	0.022	0.029	0.029
VF (MN)		0.003	0.003	0.008	0.024	0.024	0.030	0.029
Difference (%)		-3.945	1.195	-11.723	-13.400	-4.991	-3.196	-1.111
PF (MN)	180°	0.002	0.002	0.008	0.015	0.023	0.036	0.038
VF (MN)		0.002	0.002	0.009	0.017	0.024	0.037	0.041
Difference (%)		-3.195	4.208	-12.000	-13.221	-4.196	-3.423	-5.580
PF (MN)	270°	0.003	0.002	0.008	0.014	0.018	0.026	0.029
VF (MN)		0.003	0.002	0.009	0.017	0.020	0.026	0.030
Difference (%)		-3.873	0.191	-9.029	-21.806	-6.271	-2.357	-1.862

doi:10.6342/NTU202204241

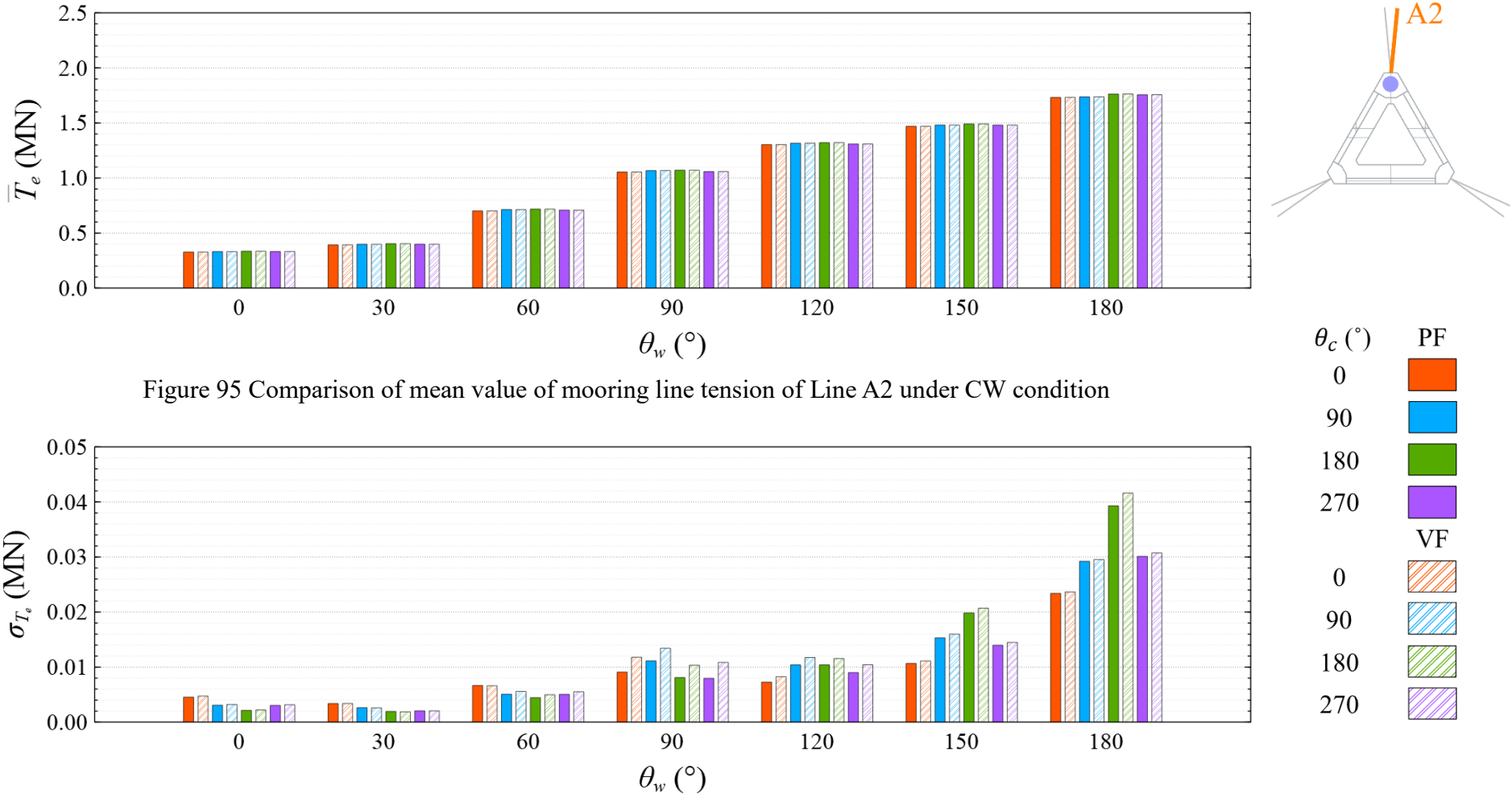

Figure 95 Comparison of mean value of mooring line tension of Line A2 under CW condition

Figure 96 Comparison of standard deviation of mooring line tension of Line A2 under CW condition

doi:10.6342/NTU202204241

Table 64 Mean value of mooring line tension of Line A2 under CW condition

	θ_w / θ_c	0°	30°	60°	90°	120°	150°	180°
PF (MN)	0°	0.328	0.393	0.702	1.054	1.303	1.469	1.732
VF (MN)		0.328	0.392	0.701	1.054	1.304	1.469	1.733
Difference (%)		-0.028	0.026	0.030	0.019	-0.016	0.006	-0.035
PF (MN)	90°	0.332	0.398	0.713	1.067	1.316	1.481	1.737
VF (MN)		0.332	0.398	0.713	1.067	1.316	1.481	1.738
Difference (%)		-0.026	0.020	0.033	0.009	-0.022	-0.001	-0.035
PF (MN)	180°	0.336	0.404	0.718	1.071	1.321	1.491	1.762
VF (MN)		0.336	0.404	0.718	1.071	1.322	1.491	1.763
Difference (%)		-0.012	0.028	0.018	0.004	-0.038	0.008	-0.041
PF (MN)	270°	0.332	0.399	0.709	1.058	1.309	1.480	1.756
VF (MN)		0.332	0.399	0.708	1.058	1.309	1.480	1.756
Difference (%)		-0.027	0.030	0.034	0.007	-0.025	-0.010	-0.037

Table 65 Standard deviation of mooring line tension of Line A2 under CW condition

	θ_w / θ_c	0°	30°	60°	90°	120°	150°	180°
PF (MN)	0°	0.005	0.003	0.007	0.009	0.007	0.011	0.023
VF (MN)		0.005	0.003	0.007	0.012	0.008	0.011	0.024
Difference (%)		-4.205	-0.422	0.717	-22.911	-12.050	-4.104	-1.090
PF (MN)	90°	0.003	0.003	0.005	0.011	0.010	0.015	0.029
VF (MN)		0.003	0.003	0.006	0.013	0.012	0.016	0.030
Difference (%)		-3.994	0.980	-9.029	-16.984	-11.455	-4.275	-1.086
PF (MN)	180°	0.002	0.002	0.004	0.008	0.010	0.020	0.039
VF (MN)		0.002	0.002	0.005	0.010	0.012	0.021	0.042
Difference (%)		-3.455	3.836	-10.768	-21.675	-10.015	-4.233	-5.581
PF (MN)	270°	0.003	0.002	0.005	0.008	0.009	0.014	0.030
VF (MN)		0.003	0.002	0.006	0.011	0.010	0.014	0.031
Difference (%)		-4.009	-0.007	-8.621	-26.689	-13.625	-3.588	-1.969

doi:10.6342/NTU202204241

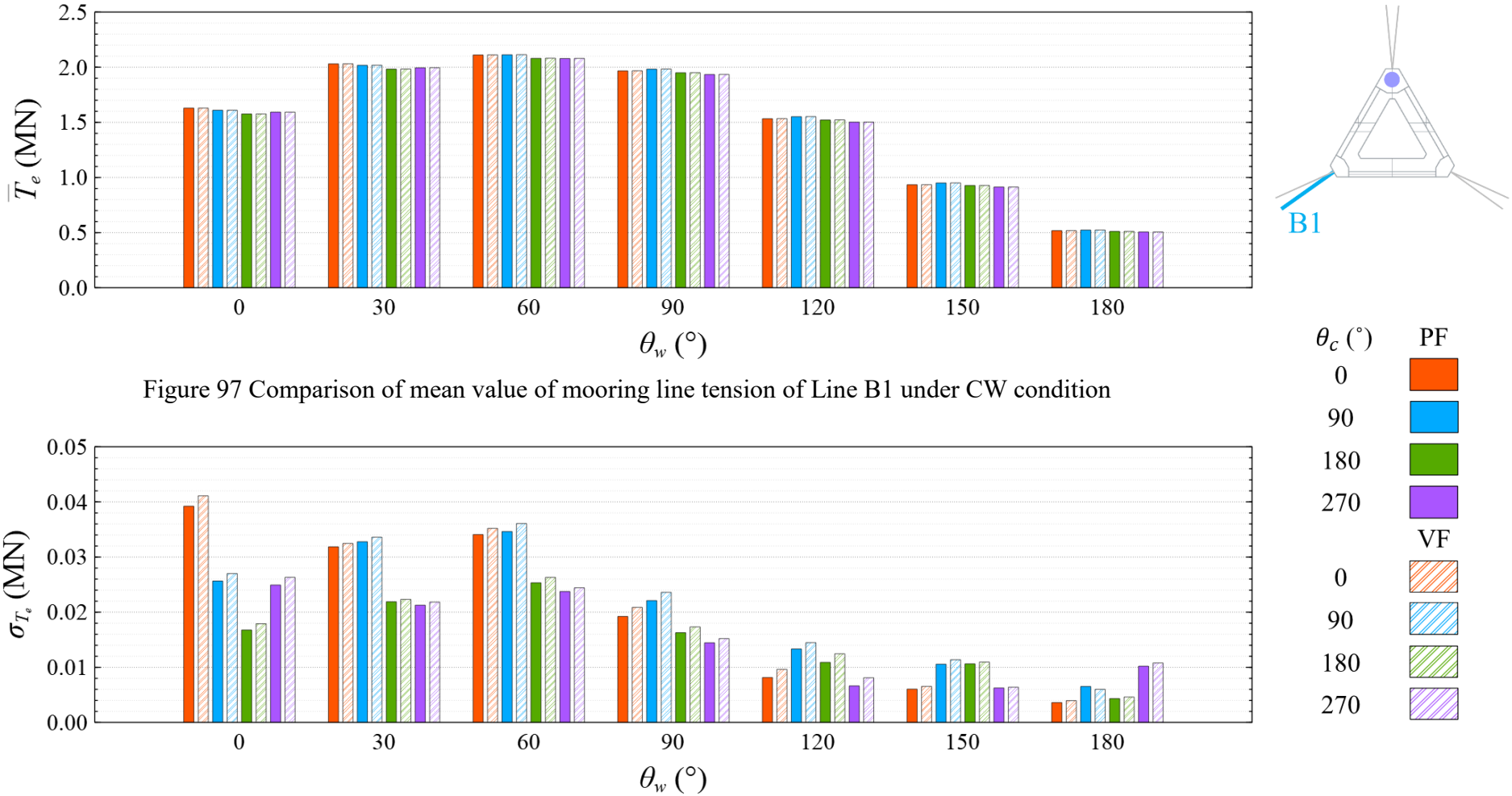

Figure 97 Comparison of mean value of mooring line tension of Line B1 under CW condition

Figure 98 Comparison of standard deviation of mooring line tension of Line B1 under CW condition

doi:10.6342/NTU202204241

Table 66 Mean value of mooring line tension of Line B1 under CW condition

	θ_c \ θ_w	0°	30°	60°	90°	120°	150°	180°
PF (MN)	0°	1.629	2.030	2.111	1.967	1.533	0.934	0.518
VF (MN)		1.629	2.031	2.112	1.968	1.534	0.935	0.518
Difference (%)		0.006	-0.041	-0.056	-0.047	-0.043	-0.045	0.017
PF (MN)	90°	1.610	2.017	2.113	1.982	1.552	0.950	0.523
VF (MN)		1.610	2.018	2.114	1.983	1.552	0.951	0.523
Difference (%)		-0.003	-0.035	-0.058	-0.044	-0.048	-0.049	0.012
PF (MN)	180°	1.576	1.983	2.080	1.949	1.521	0.927	0.511
VF (MN)		1.576	1.983	2.082	1.950	1.522	0.927	0.511
Difference (%)		-0.013	-0.033	-0.060	-0.043	-0.044	-0.030	0.012
PF (MN)	270°	1.593	1.995	2.079	1.934	1.502	0.913	0.506
VF (MN)		1.592	1.995	2.080	1.934	1.502	0.913	0.506
Difference (%)		0.013	-0.040	-0.054	-0.032	-0.039	-0.009	0.018

Table 67 Standard deviation of mooring line tension of Line B1 under CW condition

	θ_c \ θ_w	0°	30°	60°	90°	120°	150°	180°
PF (MN)	0°	0.039	0.032	0.034	0.019	0.008	0.006	0.004
VF (MN)		0.041	0.032	0.035	0.021	0.010	0.007	0.004
Difference (%)		-4.578	-1.878	-3.166	-7.908	-15.366	-7.546	-8.828
PF (MN)	90°	0.026	0.033	0.035	0.022	0.013	0.011	0.007
VF (MN)		0.027	0.034	0.036	0.024	0.014	0.011	0.006
Difference (%)		-5.014	-2.434	-4.008	-6.341	-7.991	-7.168	8.698
PF (MN)	180°	0.017	0.022	0.025	0.016	0.011	0.011	0.004
VF (MN)		0.018	0.022	0.026	0.017	0.012	0.011	0.005
Difference (%)		-6.326	-1.955	-3.715	-6.046	-12.540	-2.963	-5.902
PF (MN)	270°	0.025	0.021	0.024	0.014	0.007	0.006	0.010
VF (MN)		0.026	0.022	0.024	0.015	0.008	0.006	0.011
Difference (%)		-5.303	-2.565	-2.785	-4.912	-18.182	-2.193	-5.383

doi:10.6342/NTU202204241

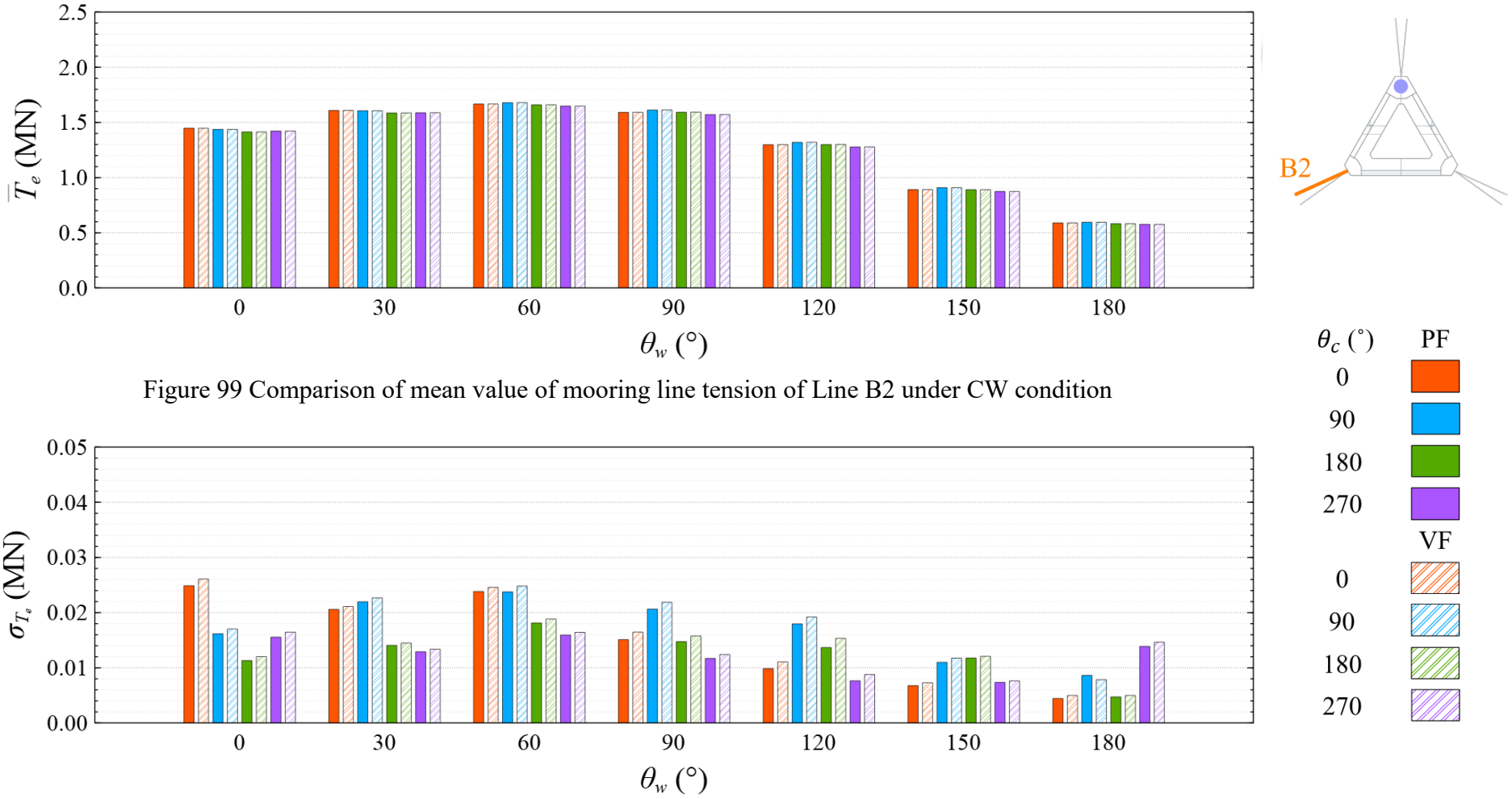

Figure 99 Comparison of mean value of mooring line tension of Line B2 under CW condition

Figure 100 Comparison of standard deviation of mooring line tension of Line B2 under CW condition

doi:10.6342/NTU202204241

Table 68 Mean value of mooring line tension of Line B2 under CW condition

	θ_w / θ_c	0°	30°	60°	90°	120°	150°	180°
PF (MN)	0°	1.448	1.608	1.667	1.591	1.298	0.891	0.589
VF (MN)		1.447	1.609	1.668	1.592	1.299	0.892	0.589
Difference (%)		0.011	-0.029	-0.017	-0.047	-0.048	-0.034	0.016
PF (MN)	90°	1.437	1.606	1.679	1.612	1.319	0.908	0.595
VF (MN)		1.437	1.606	1.680	1.613	1.320	0.909	0.595
Difference (%)		0.003	-0.018	-0.031	-0.060	-0.061	-0.038	0.007
PF (MN)	180°	1.414	1.586	1.660	1.592	1.299	0.891	0.583
VF (MN)		1.414	1.586	1.660	1.593	1.300	0.891	0.583
Difference (%)		-0.015	-0.005	-0.031	-0.041	-0.059	0.004	0.009
PF (MN)	270°	1.422	1.587	1.648	1.571	1.278	0.875	0.576
VF (MN)		1.422	1.588	1.648	1.572	1.279	0.875	0.576
Difference (%)		0.002	-0.017	-0.015	-0.035	-0.045	-0.008	0.010

Table 69 Standard deviation of mooring line tension of Line B2 under CW condition

	θ_w / θ_c	0°	30°	60°	90°	120°	150°	180°
PF (MN)	0°	0.025	0.021	0.024	0.015	0.010	0.007	0.004
VF (MN)		0.026	0.021	0.025	0.016	0.011	0.007	0.005
Difference (%)		-4.649	-2.403	-3.046	-8.335	-11.151	-7.114	-11.057
PF (MN)	90°	0.016	0.022	0.024	0.021	0.018	0.011	0.009
VF (MN)		0.017	0.023	0.025	0.022	0.019	0.012	0.008
Difference (%)		-5.102	-3.093	-4.275	-5.627	-6.468	-6.432	10.193
PF (MN)	180°	0.011	0.014	0.018	0.015	0.014	0.012	0.005
VF (MN)		0.012	0.014	0.019	0.016	0.015	0.012	0.005
Difference (%)		-5.992	-2.989	-3.867	-6.513	-10.789	-2.548	-5.298
PF (MN)	270°	0.016	0.013	0.016	0.012	0.008	0.007	0.014
VF (MN)		0.016	0.013	0.016	0.012	0.009	0.008	0.015
Difference (%)		-5.479	-3.528	-2.973	-5.688	-12.922	-3.361	-5.350

doi:10.6342/NTU202204241

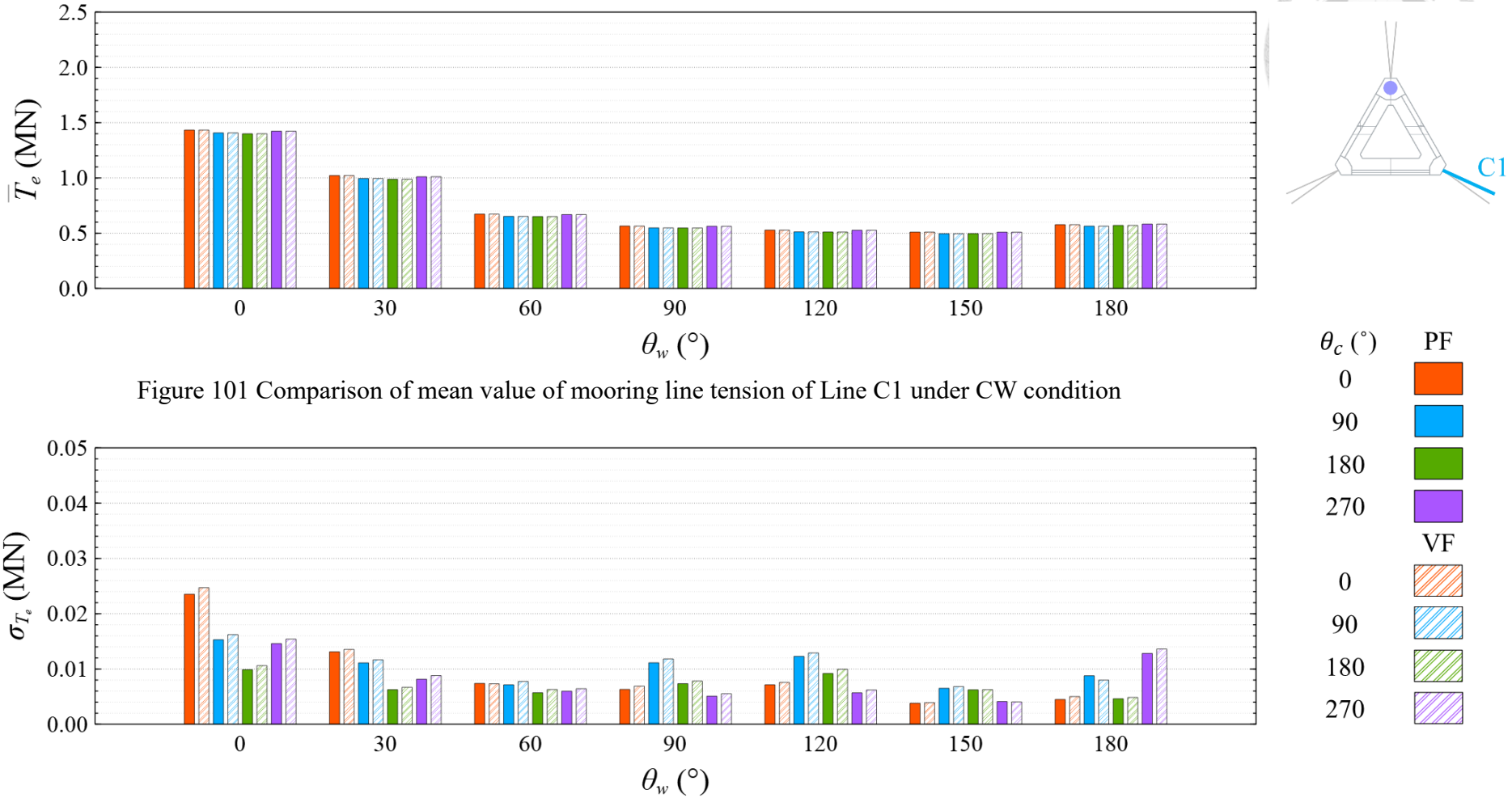

Figure 101 Comparison of mean value of mooring line tension of Line C1 under CW condition

Figure 102 Comparison of standard deviation of mooring line tension of Line C1 under CW condition

doi:10.6342/NTU202204241

Table 70 Mean value of mooring line tension of Line C1 under CW condition

	θ_w / θ_c	0°	30°	60°	90°	120°	150°	180°
PF (MN)	0°	1.433	1.021	0.673	0.565	0.528	0.510	0.577
VF (MN)		1.433	1.021	0.673	0.564	0.528	0.510	0.577
Difference (%)		-0.001	-0.010	-0.013	0.046	0.075	-0.008	0.015
PF (MN)	90°	1.407	0.994	0.652	0.548	0.512	0.496	0.564
VF (MN)		1.408	0.994	0.652	0.548	0.512	0.496	0.564
Difference (%)		-0.004	0.013	0.020	0.031	0.067	0.028	0.026
PF (MN)	180°	1.399	0.987	0.651	0.547	0.511	0.497	0.570
VF (MN)		1.400	0.988	0.651	0.547	0.511	0.497	0.570
Difference (%)		-0.023	-0.017	0.013	0.033	0.087	-0.011	0.020
PF (MN)	270°	1.423	1.011	0.669	0.563	0.527	0.510	0.583
VF (MN)		1.423	1.011	0.669	0.563	0.526	0.509	0.583
Difference (%)		-0.004	-0.024	-0.017	0.039	0.085	0.023	0.014

Table 71 Standard deviation of mooring line tension of Line C1 under CW condition

	θ_w / θ_c	0°	30°	60°	90°	120°	150°	180°
PF (MN)	0°	0.024	0.013	0.007	0.006	0.007	0.004	0.004
VF (MN)		0.025	0.014	0.007	0.007	0.008	0.004	0.005
Difference (%)		-4.747	-3.110	1.011	-8.590	-5.587	-2.681	-10.495
PF (MN)	90°	0.015	0.011	0.007	0.011	0.012	0.007	0.009
VF (MN)		0.016	0.012	0.008	0.012	0.013	0.007	0.008
Difference (%)		-5.731	-4.749	-7.718	-5.797	-4.788	-4.683	9.855
PF (MN)	180°	0.010	0.006	0.006	0.007	0.009	0.006	0.005
VF (MN)		0.011	0.007	0.006	0.008	0.010	0.006	0.005
Difference (%)		-6.811	-6.551	-9.386	-5.978	-7.753	-0.468	-4.928
PF (MN)	270°	0.015	0.008	0.006	0.005	0.006	0.004	0.013
VF (MN)		0.015	0.009	0.006	0.006	0.006	0.004	0.014
Difference (%)		-5.233	-7.401	-7.092	-8.102	-8.233	1.642	-5.868

doi:10.6342/NTU202204241

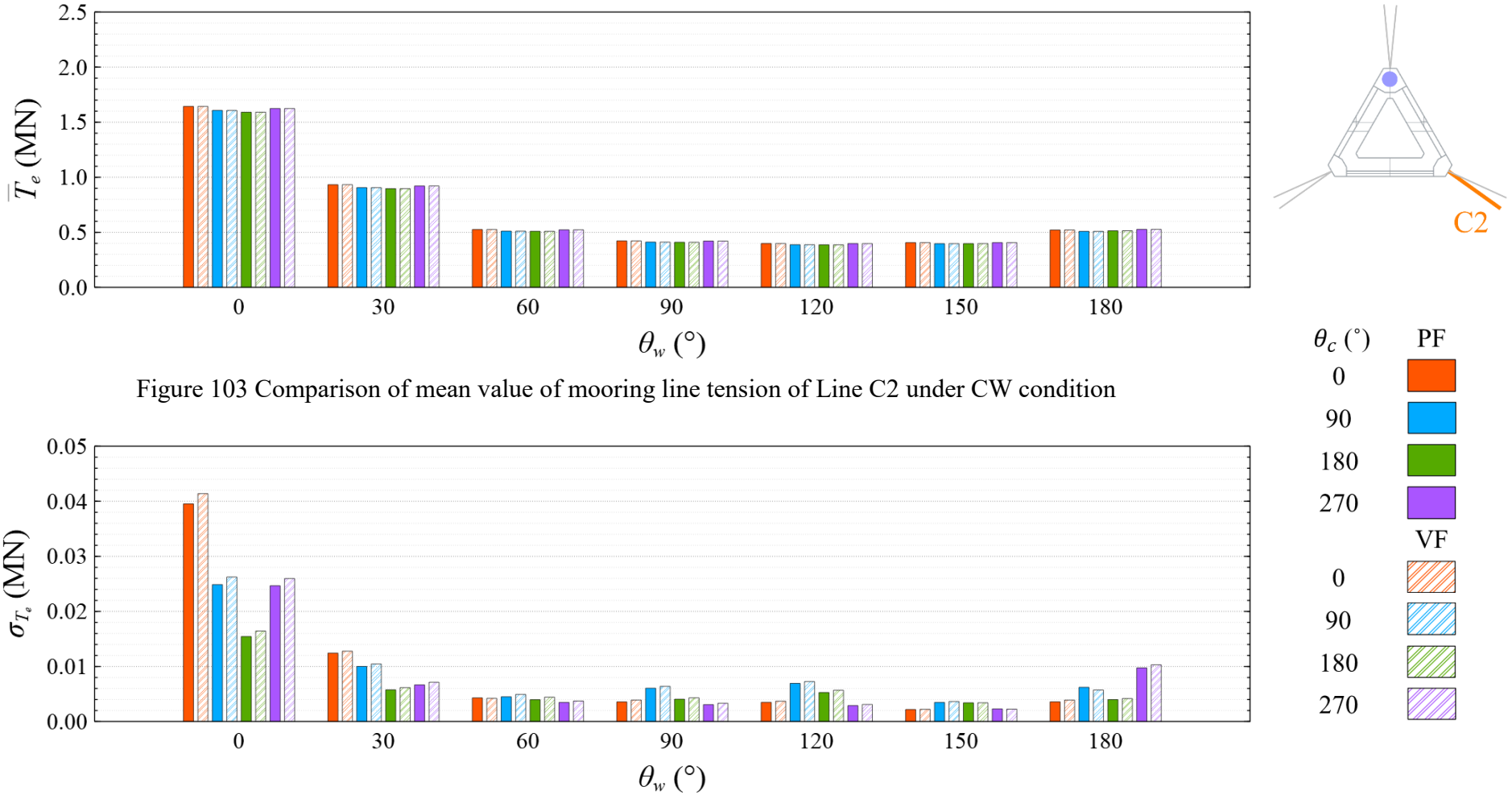

Figure 103 Comparison of mean value of mooring line tension of Line C2 under CW condition

Figure 104 Comparison of standard deviation of mooring line tension of Line C2 under CW condition

doi:10.6342/NTU202204241

Table 72 Mean value of mooring line tension of Line C2 under CW condition

	θ_c \ θ_w	0°	30°	60°	90°	120°	150°	180°
PF (MN)	0°	1.644	0.932	0.525	0.422	0.399	0.406	0.521
VF (MN)		1.643	0.933	0.525	0.422	0.398	0.407	0.521
Difference (%)		0.008	-0.025	-0.010	0.039	0.057	-0.024	0.001
PF (MN)	90°	1.607	0.906	0.511	0.411	0.388	0.397	0.509
VF (MN)		1.607	0.906	0.511	0.411	0.388	0.397	0.509
Difference (%)		0.018	0.007	0.010	0.051	0.067	0.002	0.016
PF (MN)	180°	1.591	0.897	0.510	0.410	0.387	0.397	0.514
VF (MN)		1.591	0.897	0.510	0.410	0.387	0.397	0.514
Difference (%)		-0.016	-0.019	0.011	0.045	0.080	0.000	0.019
PF (MN)	270°	1.624	0.921	0.523	0.421	0.398	0.406	0.527
VF (MN)		1.624	0.921	0.523	0.421	0.398	0.406	0.527
Difference (%)		0.004	-0.032	-0.011	0.034	0.059	0.005	0.005

Table 73 Standard deviation of mooring line tension of Line C2 under CW condition

	θ_c \ θ_w	0°	30°	60°	90°	120°	150°	180°
PF (MN)	0°	0.040	0.012	0.004	0.004	0.003	0.002	0.004
VF (MN)		0.041	0.013	0.004	0.004	0.004	0.002	0.004
Difference (%)		-4.475	-2.749	2.213	-8.590	-5.405	-1.666	-8.232
PF (MN)	90°	0.025	0.010	0.004	0.006	0.007	0.003	0.006
VF (MN)		0.026	0.010	0.005	0.006	0.007	0.004	0.006
Difference (%)		-5.258	-4.231	-8.821	-5.246	-4.492	-4.349	8.675
PF (MN)	180°	0.015	0.006	0.004	0.004	0.005	0.003	0.004
VF (MN)		0.016	0.006	0.004	0.004	0.006	0.003	0.004
Difference (%)		-6.110	-6.392	-10.181	-5.770	-7.128	-0.145	-4.750
PF (MN)	270°	0.025	0.007	0.003	0.003	0.003	0.002	0.010
VF (MN)		0.026	0.007	0.004	0.003	0.003	0.002	0.010
Difference (%)		-5.024	-6.694	-6.904	-7.439	-6.683	1.673	-5.539

doi:10.6342/NTU202204241

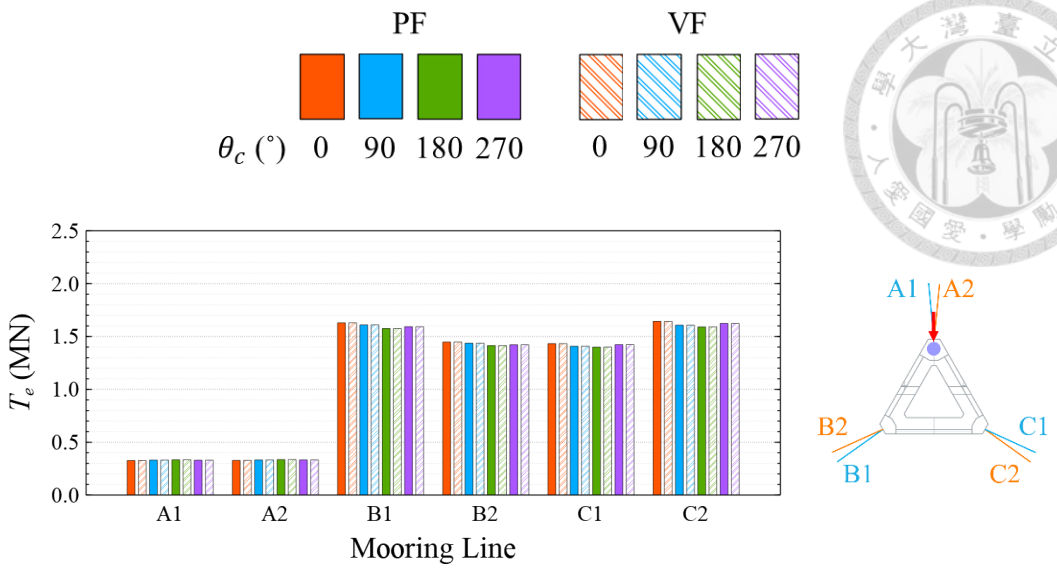

Figure 105 Comparison of mean value of mooring line tension at $\theta_w = 0°$ under CW condition

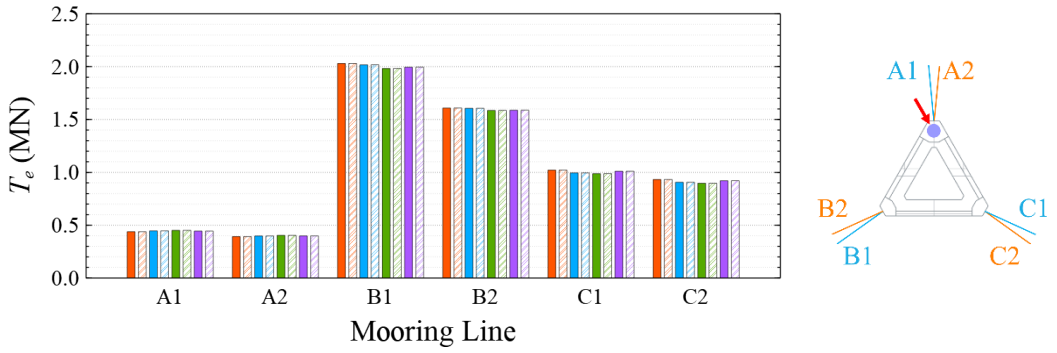

Figure 106 Comparison of mean value of mooring line tension at $\theta_w = 30°$ under CW condition

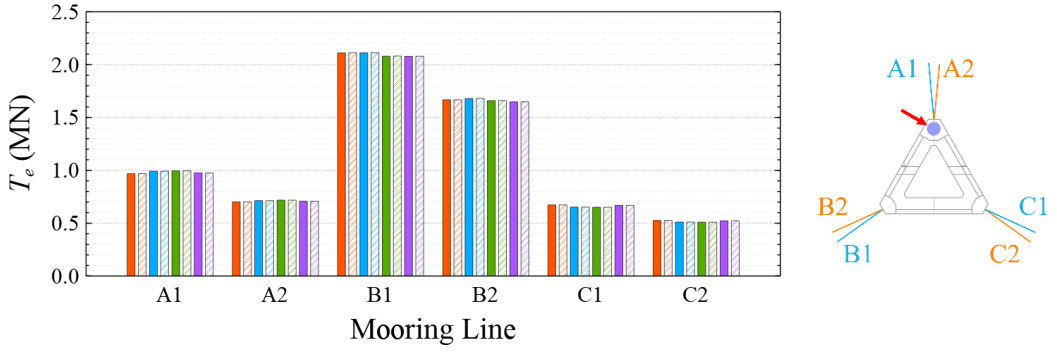

Figure 107 Comparison of mean value of mooring line tension at $\theta_w = 60°$ under CW condition

doi:10.6342/NTU202204241

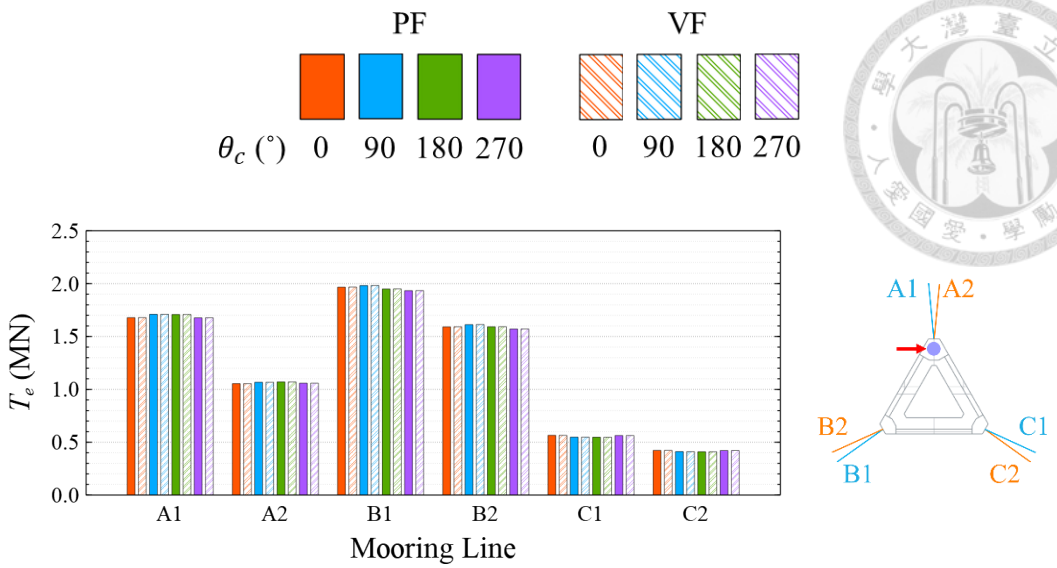

Figure 108 Comparison of mean value of mooring line tension at $\theta_w = 90°$ under CW condition

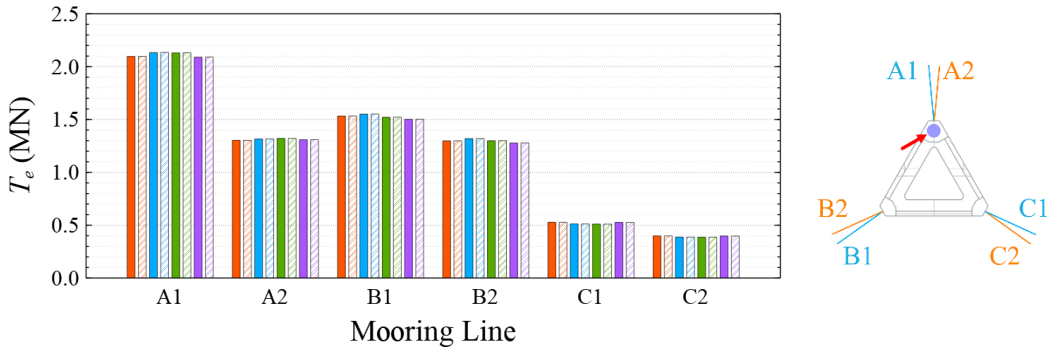

Figure 109 Comparison of mean value of mooring line tension at $\theta_w = 120°$ under CW condition

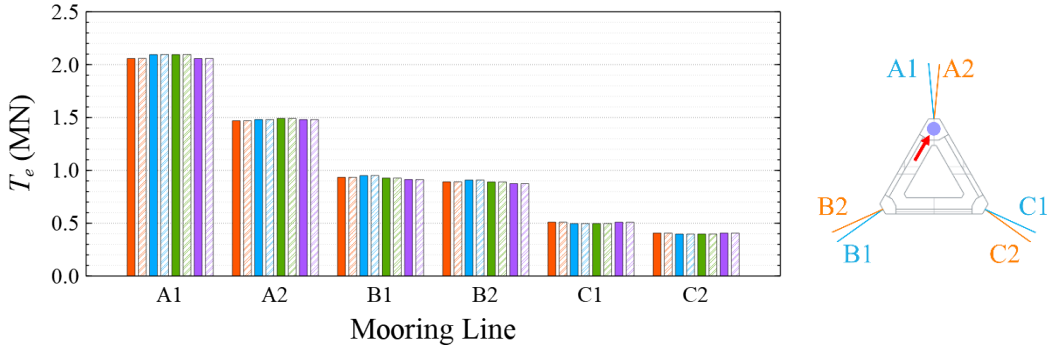

Figure 110 Comparison of mean value of mooring line tension at $\theta_w = 150°$ under CW condition

doi:10.6342/NTU202204241

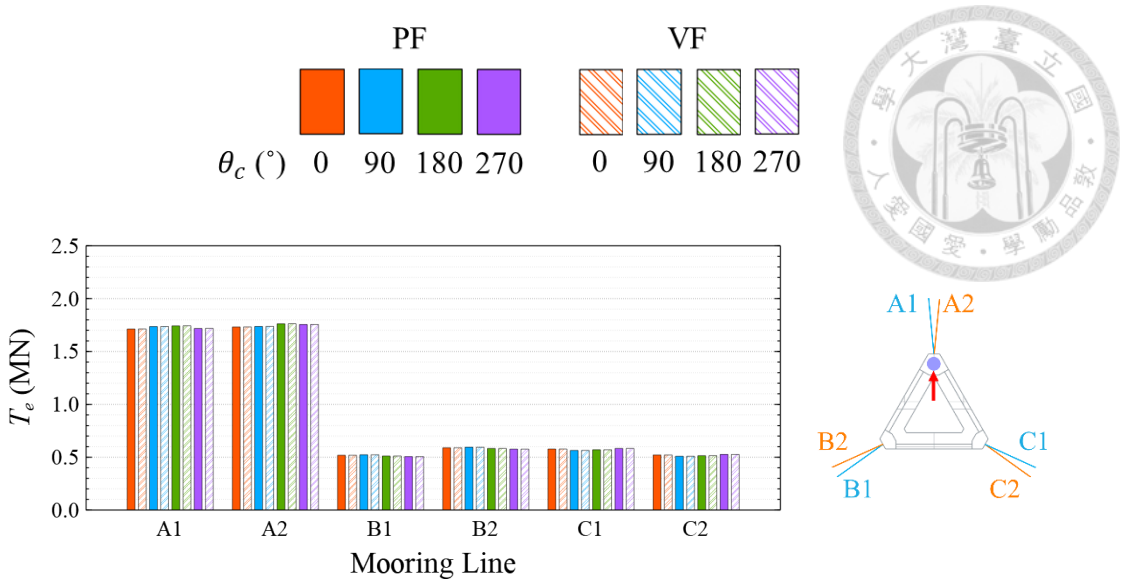

Figure 111 Comparison of mean value of mooring line tension at $\theta_w = 180°$ under CW condition

doi:10.6342/NTU202204241

4.5.2 High Wave Condition

The means and standard deviations of the mooring line tension are shown in Figure 113 to Figure 123, and Table 74 to Table 85. The largest mean values of the mooring line tension of Line A1, A2, B1, B2, C1, and C2 appear at $(\theta_w, \theta_c) = (150°, 180°)$, $(180°, 180°)$, $(60°, 90°)$, $(60°, 90°)$, $(0°, 0°)$, and $(0°, 0°)$, and they are 1.524 MN, 1.293 MN, 1.559 MN, 1.281 MN, 1.138 MN, and 1.18 MN, respectively. The smallest mean values of the mooring line tension of Line A1, A2, B1, B2, C1, and C2 appear at $(\theta_w, \theta_c) = (0°, 0°)$, $(0°, 0°)$, $(180°, 270°)$, $(180°, 270°)$, $(120°, 90°)$, and $(120°, 90°)$, and they are 0.453 MN, 0.446 MN, 0.57 MN, 0.615 MN, 0.594 MN, and 0.473 MN, respectively. The largest standard deviations of the mooring line tension of Line A1, A2, B1, B2, C1, and C2 appear at $(\theta_w, \theta_c) = (180°, 180°)$, $(180°, 180°)$, $(0°, 0°)$, $(0°, 0°)$, $(0°, 0°)$, and $(0°, 0°)$, and they are 0.177 MN, 0.166 MN, 0.237 MN, 0.146 MN, 0.157 MN, and 0.222 MN, respectively. The smallest standard deviations of the mooring line tension of Line A1, A2, B1, B2, C1, and C2 appear at $(\theta_w, \theta_c) = (60°, 180°)$, $(60°, 180°)$, $(180°, 0°)$, $(180°, 0°)$, $(180°, 0°)$, and $(60°, 180°)$, and they are 0.024 MN, 0.02 MN, 0.018 MN, 0.016 MN, 0.019 MN, and 0.017 MN, respectively. Figure 105 to Figure 111 show the mean values of the mooring line tension at the seven studied wind directions. Line B1 has the largest mean loading at $\theta_w = 0°$, $30°$, $60°$, and $90°$, which is up to 1.254 MN, 1.485 MN, 1.559 MN, and 1.503 MN, respectively. Line A1 has the largest mean loading at $\theta_w = 120°$, $150°$, and $180°$, which is up to 1.488 MN, 1.524 MN, and 1.343 MN.

Similar to the motion response and generator power, the difference of the mean values of mooring line tension between the two approaches as well as among the four current directions are clearly smaller than that of the standard deviations. All mooring

doi:10.6342/NTU202204241

line tensions are lower than one-eighth of the break load under the HW condition, and the smallest maximum mean mooring line tension appears at $\theta_w = 0°$.

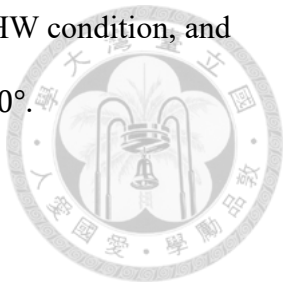

doi:10.6342/NTU202204241

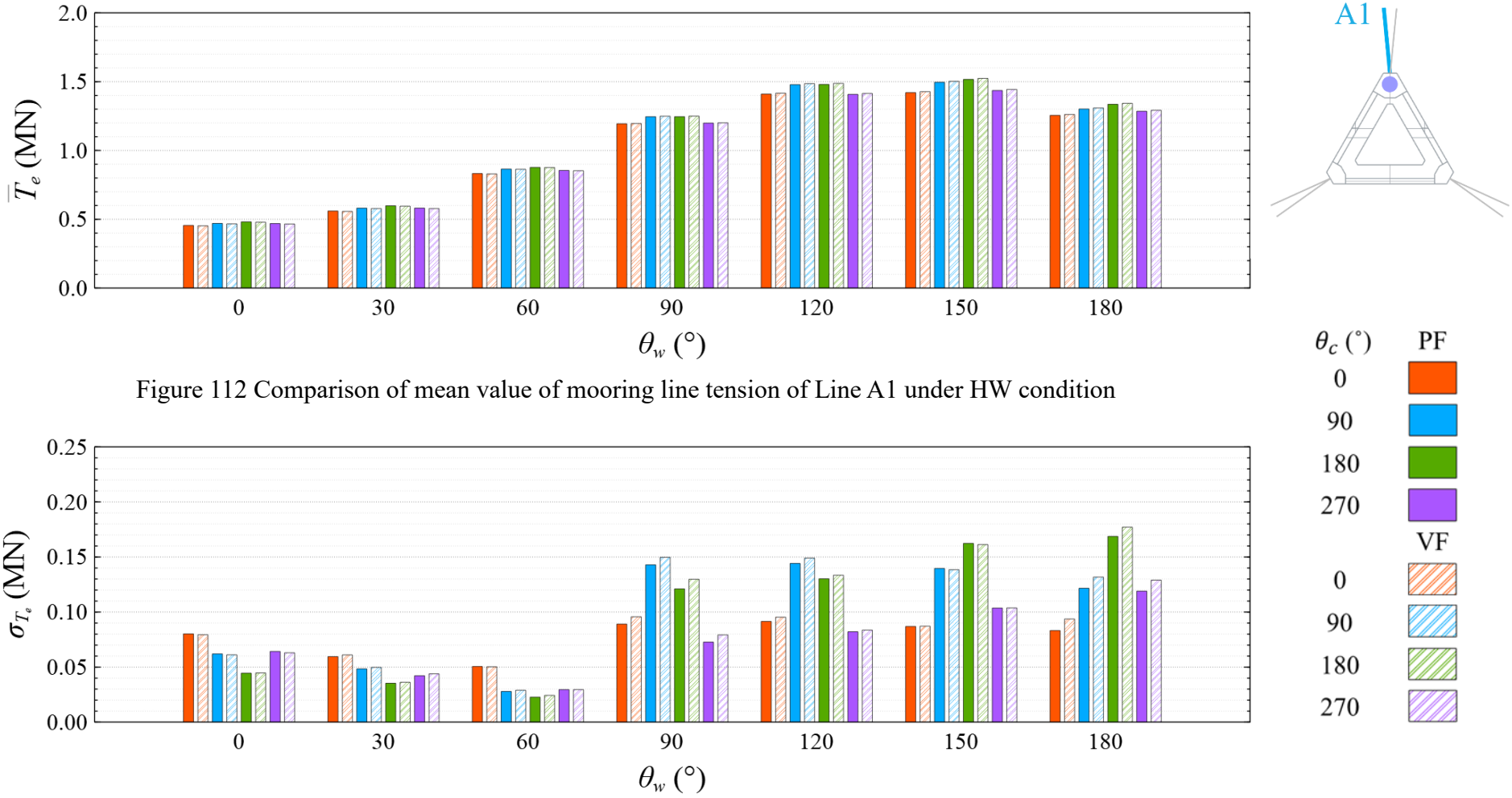

Figure 112 Comparison of mean value of mooring line tension of Line A1 under HW condition

Figure 113 Comparison of standard deviation of mooring line tension of Line A1 under HW condition

doi:10.6342/NTU202204241

Table 74 Mean value of mooring line tension of Line A1 under HW condition

	θ_c \ θ_w	0°	30°	60°	90°	120°	150°	180°
PF (MN)	0°	0.456	0.560	0.832	1.194	1.410	1.420	1.255
VF (MN)		0.453	0.557	0.830	1.196	1.416	1.427	1.262
Difference (%)		0.665	0.502	0.297	-0.142	-0.441	-0.488	-0.521
PF (MN)	90°	0.470	0.581	0.865	1.246	1.478	1.496	1.301
VF (MN)		0.467	0.578	0.863	1.249	1.486	1.503	1.309
Difference (%)		0.667	0.498	0.153	-0.286	-0.485	-0.488	-0.567
PF (MN)	180°	0.482	0.598	0.877	1.246	1.480	1.517	1.336
VF (MN)		0.479	0.595	0.876	1.250	1.488	1.524	1.343
Difference (%)		0.591	0.463	0.123	-0.340	-0.530	-0.482	-0.526
PF (MN)	270°	0.469	0.581	0.855	1.199	1.408	1.436	1.285
VF (MN)		0.466	0.578	0.853	1.201	1.414	1.444	1.292
Difference (%)		0.680	0.533	0.252	-0.153	-0.456	-0.529	-0.525

Table 75 Standard deviation of mooring line tension of Line A1 under HW condition

	θ_c \ θ_w	0°	30°	60°	90°	120°	150°	180°
PF (MN)	0°	0.080	0.060	0.051	0.089	0.091	0.087	0.083
VF (MN)		0.079	0.061	0.050	0.096	0.095	0.087	0.094
Difference (%)		0.987	-2.632	0.480	-7.486	-4.217	-0.280	-12.620
PF (MN)	90°	0.062	0.048	0.028	0.143	0.144	0.140	0.122
VF (MN)		0.061	0.050	0.029	0.150	0.149	0.138	0.132
Difference (%)		1.363	-2.817	-3.791	-4.773	-3.368	0.827	-8.343
PF (MN)	180°	0.044	0.035	0.023	0.121	0.130	0.162	0.169
VF (MN)		0.045	0.036	0.024	0.130	0.133	0.161	0.177
Difference (%)		-0.428	-2.494	-7.003	-7.192	-2.509	0.664	-4.981
PF (MN)	270°	0.064	0.042	0.030	0.073	0.082	0.104	0.119
VF (MN)		0.063	0.044	0.030	0.079	0.084	0.104	0.129
Difference (%)		1.909	-4.054	-0.038	-8.966	-1.831	-0.117	-8.382

doi:10.6342/NTU202204241

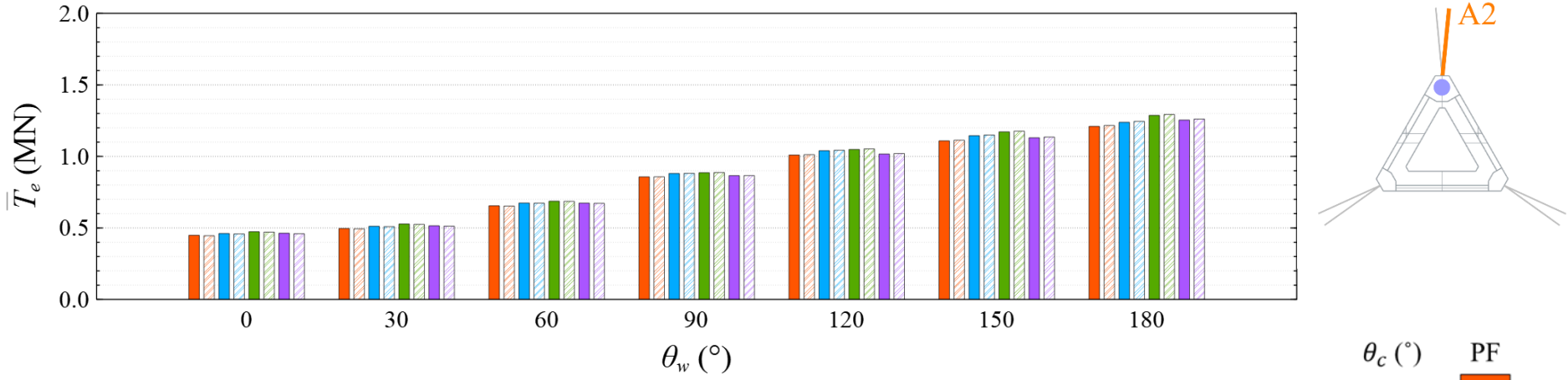

Figure 114 Comparison of mean value of mooring line tension of Line A2 under HW condition

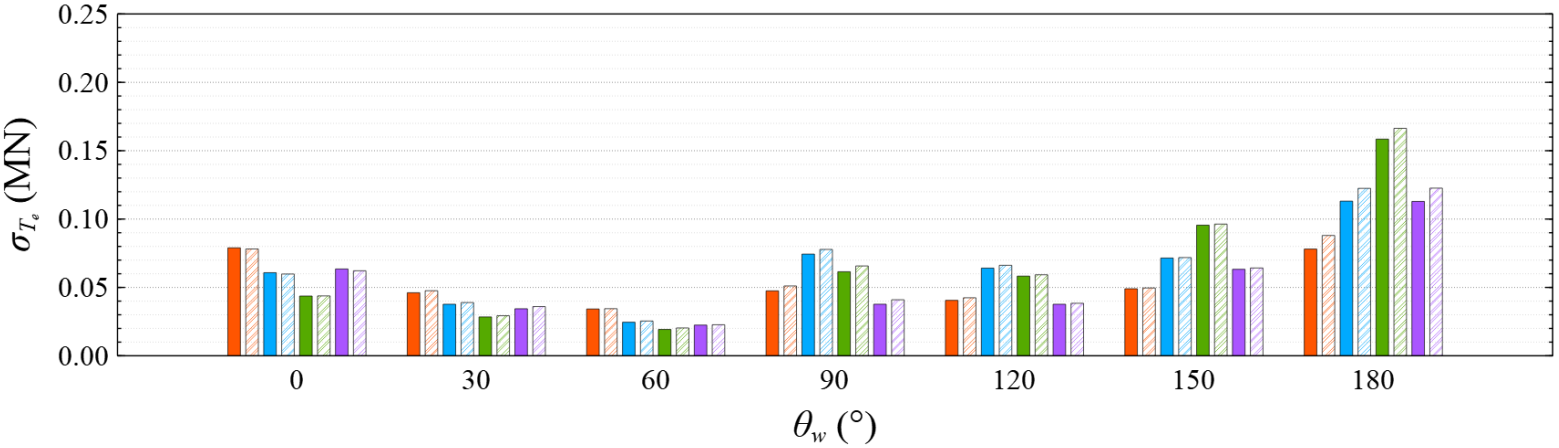

Figure 115 Comparison of standard deviation of mooring line tension of Line A2 under HW condition

doi:10.6342/NTU202204241

Table 76 Mean value of mooring line tension of Line A2 under HW condition

	θ_w / θ_c	0°	30°	60°	90°	120°	150°	180°
PF (MN)	0°	0.449	0.496	0.655	0.857	1.010	1.109	1.210
VF (MN)		0.446	0.494	0.653	0.857	1.013	1.113	1.217
Difference (%)		0.664	0.457	0.287	-0.023	-0.291	-0.391	-0.510
PF (MN)	90°	0.461	0.512	0.674	0.881	1.040	1.145	1.238
VF (MN)		0.458	0.509	0.673	0.882	1.043	1.150	1.245
Difference (%)		0.661	0.443	0.186	-0.120	-0.312	-0.417	-0.506
PF (MN)	180°	0.474	0.528	0.687	0.886	1.049	1.172	1.287
VF (MN)		0.471	0.525	0.686	0.887	1.053	1.177	1.293
Difference (%)		0.582	0.453	0.171	-0.163	-0.369	-0.391	-0.511
PF (MN)	270°	0.463	0.515	0.674	0.866	1.017	1.130	1.254
VF (MN)		0.460	0.513	0.672	0.866	1.020	1.135	1.261
Difference (%)		0.679	0.492	0.253	-0.043	-0.320	-0.435	-0.551

Table 77 Standard deviation of mooring line tension of Line A2 under HW condition

	θ_w / θ_c	0°	30°	60°	90°	120°	150°	180°
PF (MN)	0°	0.079	0.046	0.034	0.047	0.041	0.049	0.078
VF (MN)		0.078	0.048	0.034	0.051	0.042	0.050	0.088
Difference (%)		1.059	-3.164	-0.654	-7.577	-4.609	-1.181	-12.712
PF (MN)	90°	0.061	0.038	0.025	0.074	0.064	0.072	0.113
VF (MN)		0.060	0.039	0.025	0.078	0.066	0.072	0.122
Difference (%)		1.603	-3.232	-3.575	-4.589	-3.198	-0.464	-8.252
PF (MN)	180°	0.044	0.028	0.019	0.061	0.058	0.096	0.158
VF (MN)		0.044	0.029	0.020	0.066	0.059	0.096	0.166
Difference (%)		-0.193	-3.063	-5.566	-6.848	-1.685	-0.831	-4.980
PF (MN)	270°	0.063	0.034	0.022	0.038	0.038	0.063	0.113
VF (MN)		0.062	0.036	0.023	0.041	0.038	0.064	0.123
Difference (%)		2.065	-4.632	-1.128	-8.654	-1.865	-1.516	-8.589

doi:10.6342/NTU202204241

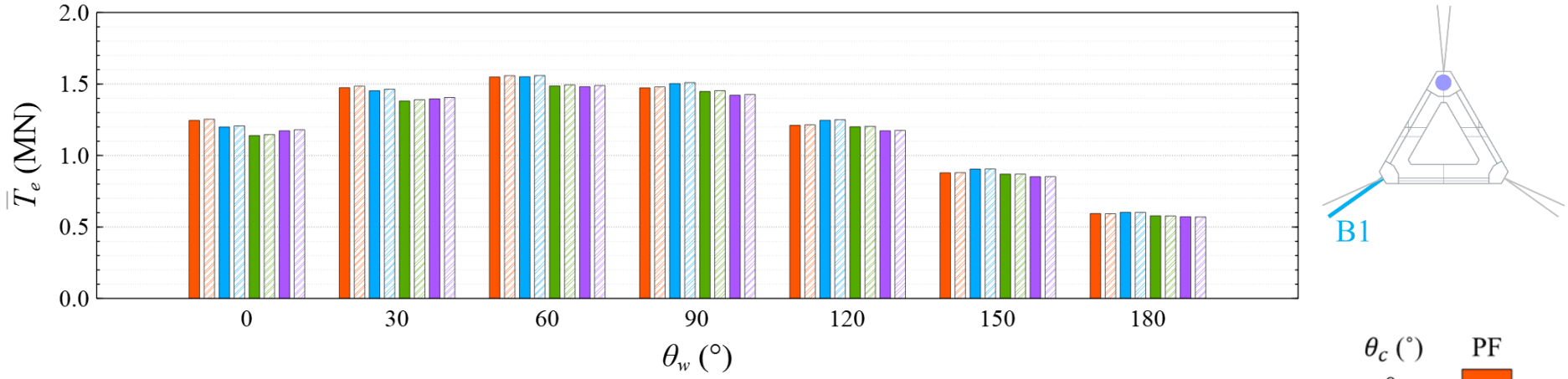

Figure 116 Comparison of mean value of mooring line tension of Line B1 under HW condition

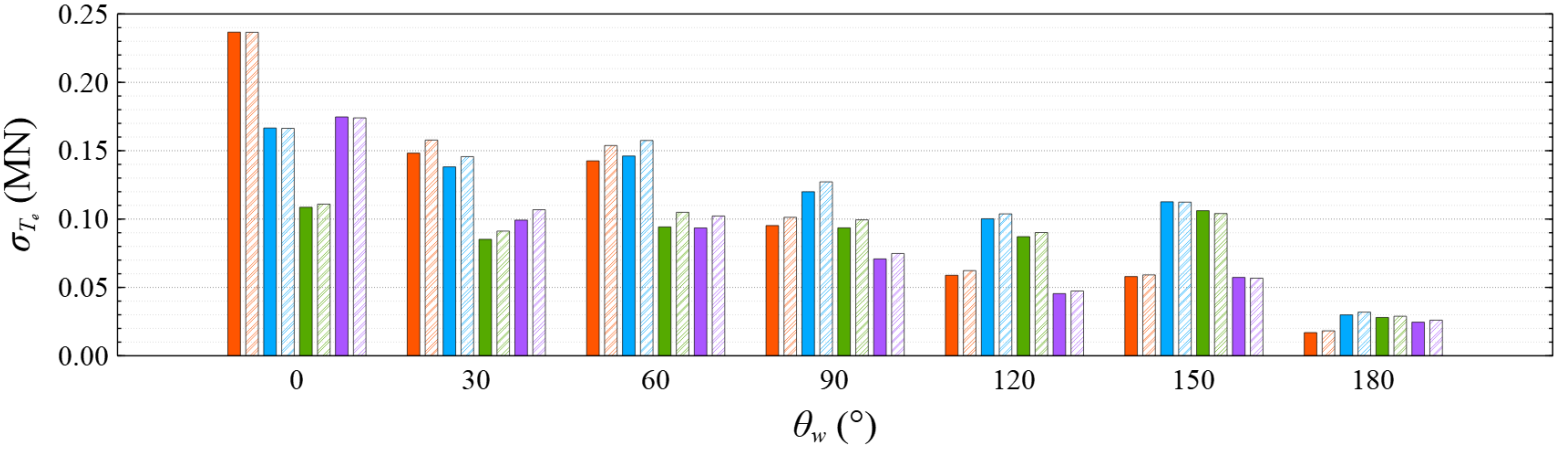

Figure 117 Comparison of standard deviation of mooring line tension of Line B1 under HW condition

doi:10.6342/NTU202204241

Table 78 Mean value of mooring line tension of Line B1 under HW condition

	θ_w / θ_c	0°	30°	60°	90°	120°	150°	180°
PF (MN)	0°	1.246	1.474	1.549	1.473	1.211	0.879	0.594
VF (MN)		1.254	1.485	1.558	1.480	1.215	0.880	0.593
Difference (%)		-0.624	-0.733	-0.580	-0.466	-0.321	-0.105	0.165
PF (MN)	90°	1.200	1.453	1.551	1.503	1.246	0.905	0.602
VF (MN)		1.208	1.463	1.559	1.510	1.251	0.906	0.602
Difference (%)		-0.647	-0.704	-0.523	-0.461	-0.332	-0.093	0.063
PF (MN)	180°	1.140	1.382	1.486	1.448	1.201	0.870	0.578
VF (MN)		1.147	1.390	1.494	1.454	1.204	0.870	0.578
Difference (%)		-0.600	-0.619	-0.493	-0.412	-0.263	-0.020	0.145
PF (MN)	270°	1.173	1.396	1.481	1.421	1.173	0.852	0.572
VF (MN)		1.180	1.406	1.489	1.427	1.175	0.852	0.570
Difference (%)		-0.565	-0.683	-0.514	-0.370	-0.224	-0.041	0.263

Table 79 Standard deviation of mooring line tension of Line B1 under HW condition

	θ_w / θ_c	0°	30°	60°	90°	120°	150°	180°
PF (MN)	0°	0.237	0.148	0.143	0.095	0.059	0.058	0.017
VF (MN)		0.237	0.158	0.154	0.101	0.062	0.059	0.018
Difference (%)		0.042	-6.432	-7.881	-6.330	-5.773	-2.097	-7.586
PF (MN)	90°	0.167	0.138	0.146	0.120	0.100	0.113	0.030
VF (MN)		0.166	0.146	0.157	0.127	0.104	0.112	0.032
Difference (%)		0.141	-5.417	-7.764	-6.012	-3.552	0.242	-6.636
PF (MN)	180°	0.109	0.085	0.094	0.094	0.087	0.106	0.028
VF (MN)		0.111	0.091	0.105	0.099	0.090	0.104	0.029
Difference (%)		-2.100	-7.078	-11.341	-6.250	-3.477	1.977	-3.188
PF (MN)	270°	0.175	0.099	0.094	0.071	0.045	0.057	0.025
VF (MN)		0.174	0.107	0.102	0.075	0.047	0.057	0.026
Difference (%)		0.402	-7.670	-9.327	-5.613	-4.180	0.988	-5.908

doi:10.6342/NTU202204241

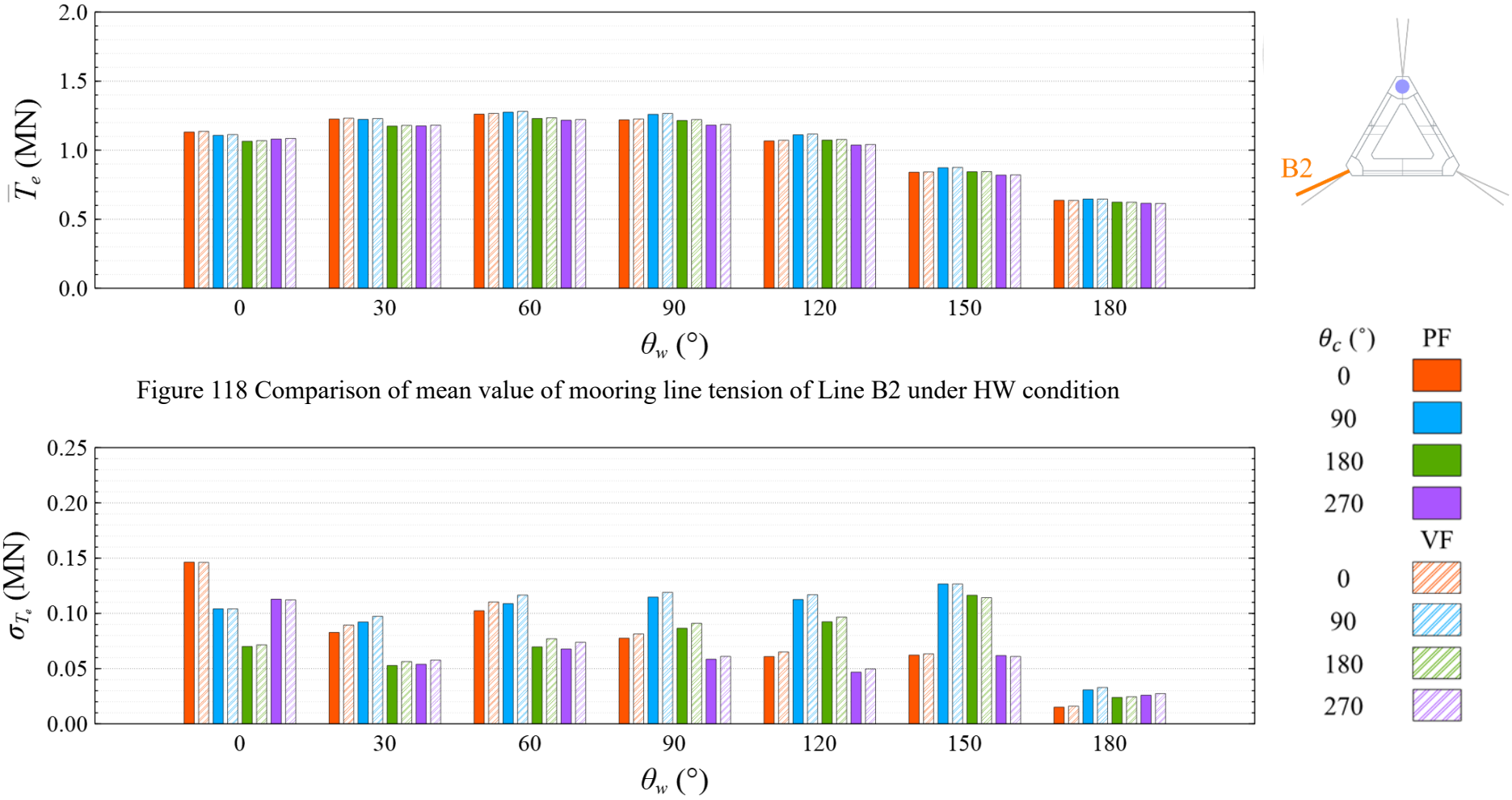

Figure 118 Comparison of mean value of mooring line tension of Line B2 under HW condition

Figure 119 Comparison of standard deviation of mooring line tension of Line B2 under HW condition

doi:10.6342/NTU202204241

Table 80 Mean value of mooring line tension of Line B2 under HW condition

	θ_c \ θ_w	0°	30°	60°	90°	120°	150°	180°
PF (MN)	0°	1.131	1.226	1.261	1.220	1.067	0.841	0.637
VF (MN)		1.137	1.232	1.267	1.226	1.072	0.842	0.637
Difference (%)		-0.463	-0.493	-0.436	-0.480	-0.470	-0.217	0.139
PF (MN)	90°	1.108	1.223	1.275	1.259	1.111	0.873	0.646
VF (MN)		1.113	1.229	1.281	1.266	1.117	0.875	0.646
Difference (%)		-0.505	-0.493	-0.463	-0.529	-0.517	-0.244	0.003
PF (MN)	180°	1.065	1.174	1.229	1.215	1.073	0.844	0.624
VF (MN)		1.070	1.180	1.235	1.222	1.078	0.845	0.623
Difference (%)		-0.442	-0.438	-0.426	-0.532	-0.446	-0.154	0.103
PF (MN)	270°	1.081	1.176	1.217	1.181	1.037	0.820	0.616
VF (MN)		1.085	1.181	1.222	1.187	1.041	0.821	0.615
Difference (%)		-0.414	-0.447	-0.412	-0.444	-0.372	-0.184	0.223

Table 81 Standard deviation of mooring line tension of Line B2 under HW condition

	θ_c \ θ_w	0°	30°	60°	90°	120°	150°	180°
PF (MN)	0°	0.146	0.083	0.102	0.078	0.061	0.062	0.015
VF (MN)		0.146	0.089	0.110	0.081	0.065	0.063	0.016
Difference (%)		0.159	-8.027	-7.729	-4.960	-6.884	-1.754	-6.258
PF (MN)	90°	0.104	0.092	0.109	0.115	0.113	0.127	0.031
VF (MN)		0.104	0.097	0.117	0.119	0.117	0.127	0.033
Difference (%)		-0.004	-5.625	-7.135	-3.787	-3.854	0.001	-7.051
PF (MN)	180°	0.070	0.053	0.070	0.087	0.092	0.116	0.024
VF (MN)		0.072	0.056	0.077	0.091	0.097	0.114	0.025
Difference (%)		-2.175	-6.708	-10.532	-5.192	-4.531	1.924	-2.688
PF (MN)	270°	0.113	0.054	0.068	0.058	0.047	0.062	0.026
VF (MN)		0.112	0.058	0.074	0.061	0.050	0.061	0.027
Difference (%)		0.490	-7.111	-9.019	-4.441	-6.302	1.274	-5.760

doi:10.6342/NTU202204241

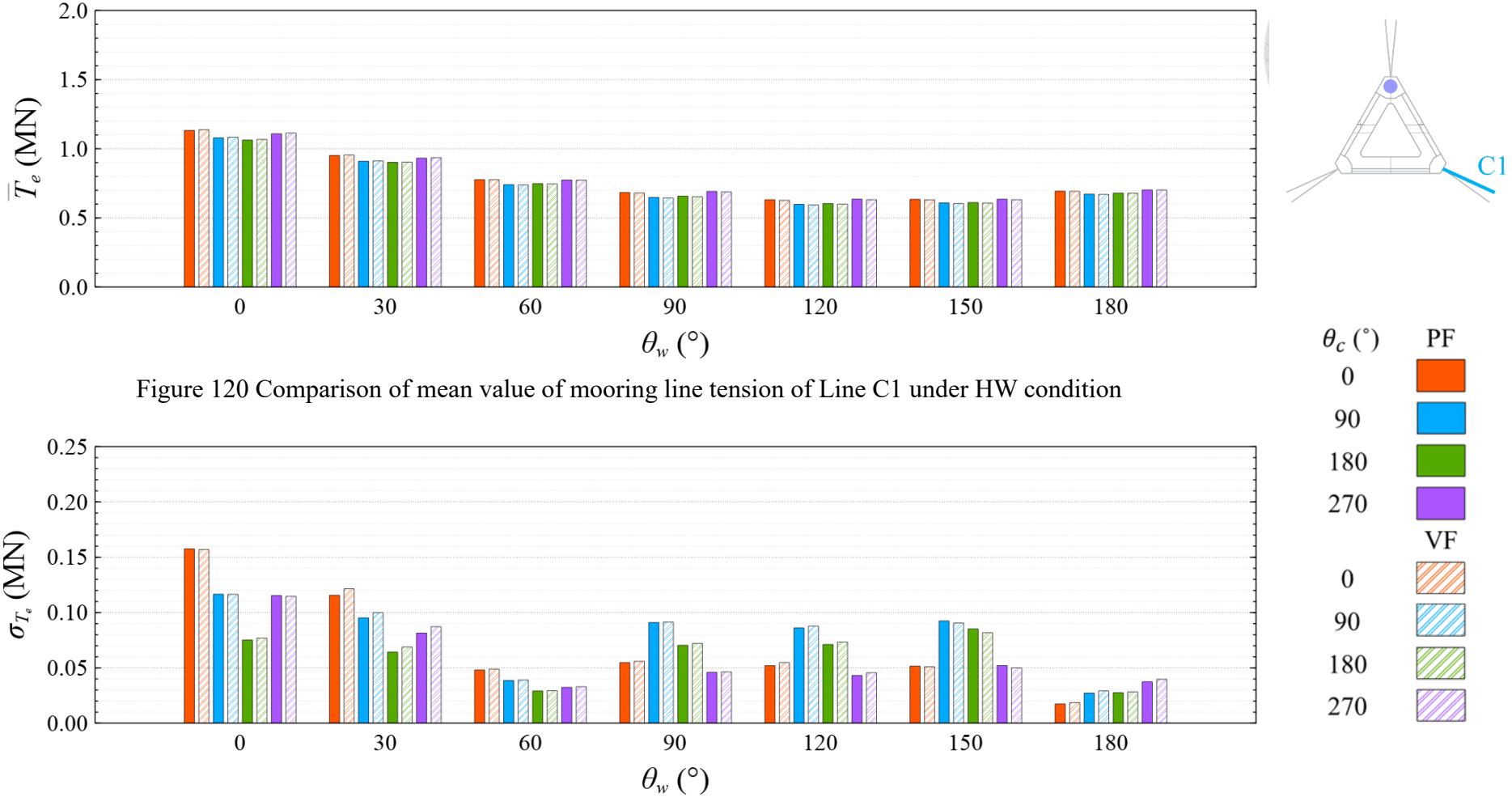

Figure 120 Comparison of mean value of mooring line tension of Line C1 under HW condition

Figure 121 Comparison of standard deviation of mooring line tension of Line C1 under HW condition

doi:10.6342/NTU202204241

Table 82 Mean value of mooring line tension of Line C1 under HW condition

	θ_c \ θ_w	0°	30°	60°	90°	120°	150°	180°
PF (MN)	0°	1.133	0.952	0.777	0.684	0.632	0.635	0.693
VF (MN)		1.138	0.956	0.777	0.681	0.627	0.631	0.692
Difference (%)		-0.470	-0.418	0.024	0.474	0.685	0.566	0.148
PF (MN)	90°	1.080	0.910	0.740	0.649	0.598	0.608	0.672
VF (MN)		1.084	0.912	0.739	0.645	0.594	0.604	0.670
Difference (%)		-0.415	-0.273	0.203	0.573	0.658	0.669	0.238
PF (MN)	180°	1.063	0.902	0.748	0.658	0.604	0.611	0.680
VF (MN)		1.068	0.904	0.746	0.653	0.600	0.607	0.679
Difference (%)		-0.445	-0.220	0.259	0.650	0.665	0.660	0.130
PF (MN)	270°	1.109	0.932	0.774	0.692	0.636	0.635	0.702
VF (MN)		1.114	0.936	0.773	0.688	0.632	0.632	0.702
Difference (%)		-0.502	-0.363	0.098	0.529	0.641	0.572	0.019

Table 83 Standard deviation of mooring line tension of Line C1 under HW condition

	θ_c \ θ_w	0°	30°	60°	90°	120°	150°	180°
PF (MN)	0°	0.158	0.116	0.048	0.055	0.052	0.052	0.017
VF (MN)		0.157	0.122	0.049	0.056	0.055	0.051	0.019
Difference (%)		0.362	-5.035	-1.546	-2.016	-5.546	0.989	-6.446
PF (MN)	90°	0.117	0.095	0.039	0.091	0.086	0.092	0.027
VF (MN)		0.116	0.100	0.039	0.091	0.088	0.091	0.029
Difference (%)		0.112	-4.897	-1.146	-0.361	-1.996	2.031	-7.226
PF (MN)	180°	0.075	0.064	0.029	0.070	0.071	0.085	0.028
VF (MN)		0.077	0.069	0.029	0.072	0.073	0.082	0.028
Difference (%)		-2.296	-7.014	-0.932	-2.405	-3.111	3.972	-2.492
PF (MN)	270°	0.115	0.081	0.032	0.046	0.043	0.052	0.038
VF (MN)		0.115	0.087	0.033	0.046	0.046	0.050	0.040
Difference (%)		0.598	-7.151	-1.825	-0.940	-5.785	3.900	-5.976

doi:10.6342/NTU202204241

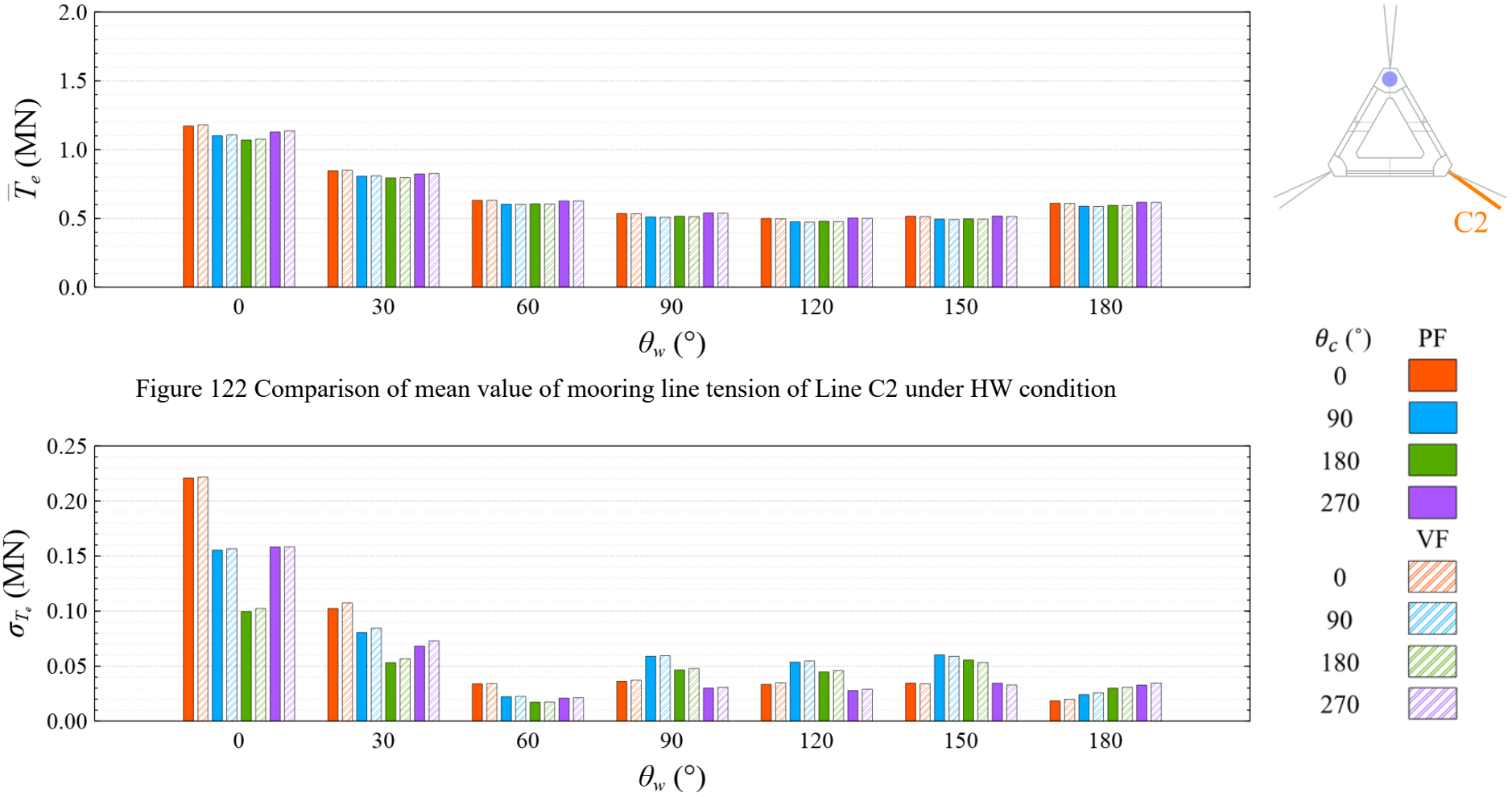

Figure 122 Comparison of mean value of mooring line tension of Line C2 under HW condition

Figure 123 Comparison of standard deviation of mooring line tension of Line C2 under HW condition

doi:10.6342/NTU202204241

Table 84 Mean value of mooring line tension of Line C2 under HW condition

	θ_c \ θ_w	0°	30°	60°	90°	120°	150°	180°
PF (MN)	0°	1.172	0.847	0.632	0.536	0.500	0.516	0.610
VF (MN)		1.180	0.851	0.632	0.534	0.497	0.514	0.609
Difference (%)		-0.654	-0.515	-0.022	0.381	0.528	0.462	0.181
PF (MN)	90°	1.101	0.807	0.603	0.511	0.476	0.495	0.589
VF (MN)		1.107	0.810	0.602	0.509	0.473	0.492	0.587
Difference (%)		-0.609	-0.377	0.130	0.442	0.546	0.551	0.259
PF (MN)	180°	1.070	0.794	0.606	0.516	0.479	0.497	0.595
VF (MN)		1.077	0.796	0.605	0.513	0.477	0.494	0.594
Difference (%)		-0.625	-0.296	0.180	0.499	0.563	0.535	0.164
PF (MN)	270°	1.128	0.823	0.627	0.540	0.503	0.517	0.617
VF (MN)		1.136	0.827	0.627	0.538	0.500	0.515	0.617
Difference (%)		-0.661	-0.460	0.039	0.417	0.519	0.465	0.074

Table 85 Standard deviation of mooring line tension of Line C2 under HW condition

	θ_c \ θ_w	0°	30°	60°	90°	120°	150°	180°
PF (MN)	0°	0.221	0.102	0.034	0.036	0.033	0.035	0.018
VF (MN)		0.222	0.107	0.034	0.037	0.035	0.034	0.020
Difference (%)		-0.422	-4.798	-0.840	-2.891	-4.706	1.516	-7.395
PF (MN)	90°	0.155	0.081	0.022	0.059	0.054	0.060	0.024
VF (MN)		0.157	0.084	0.022	0.059	0.055	0.059	0.026
Difference (%)		-0.764	-4.829	-0.806	-0.814	-2.037	2.211	-6.426
PF (MN)	180°	0.099	0.053	0.017	0.046	0.045	0.056	0.030
VF (MN)		0.102	0.057	0.017	0.048	0.046	0.053	0.031
Difference (%)		-3.011	-6.655	-1.305	-2.998	-2.890	4.148	-2.918
PF (MN)	270°	0.158	0.068	0.021	0.030	0.028	0.034	0.033
VF (MN)		0.158	0.073	0.021	0.031	0.029	0.033	0.035
Difference (%)		-0.090	-7.023	-1.699	-2.430	-4.265	4.437	-5.907

doi:10.6342/NTU202204241

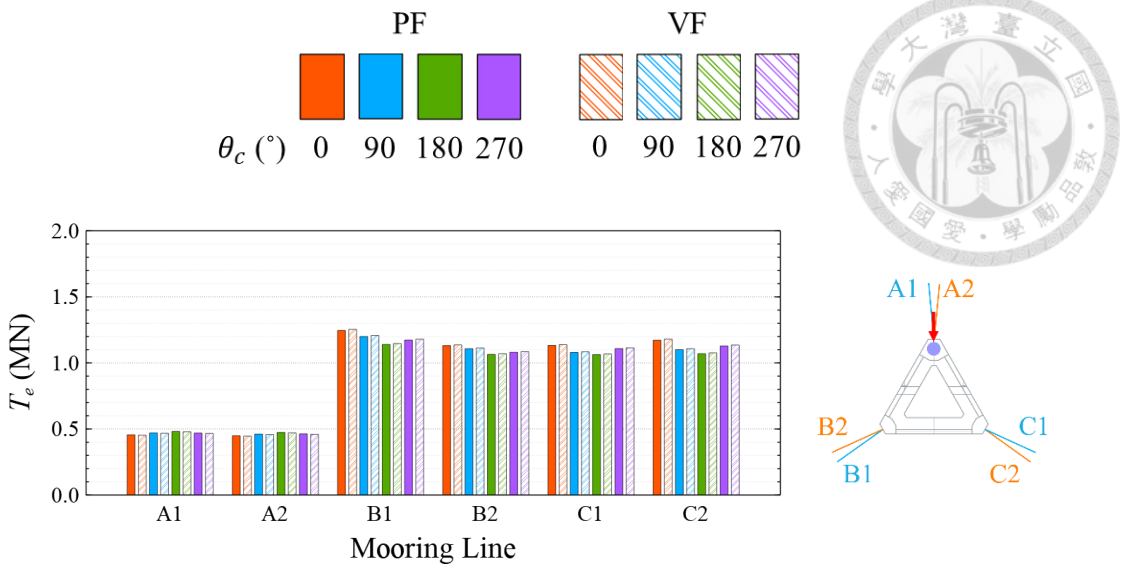

Figure 124 Comparison of mean value of mooring line tension at $\theta_w = 0°$ under HW condition

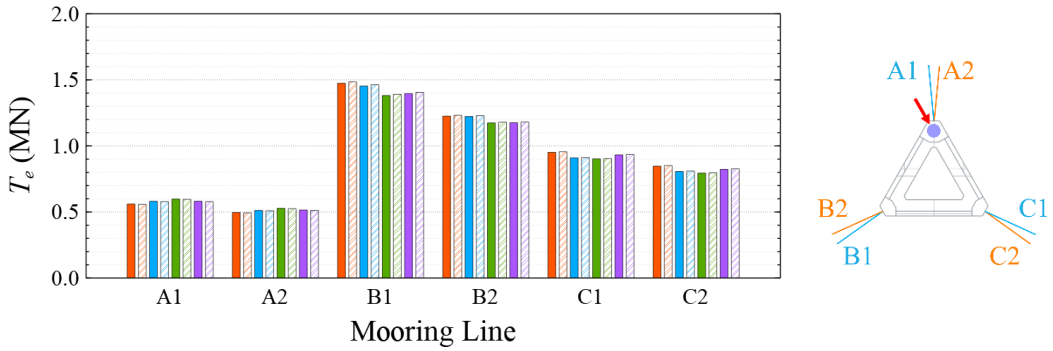

Figure 125 Comparison of mean value of mooring line tension at $\theta_w = 30°$ under HW condition

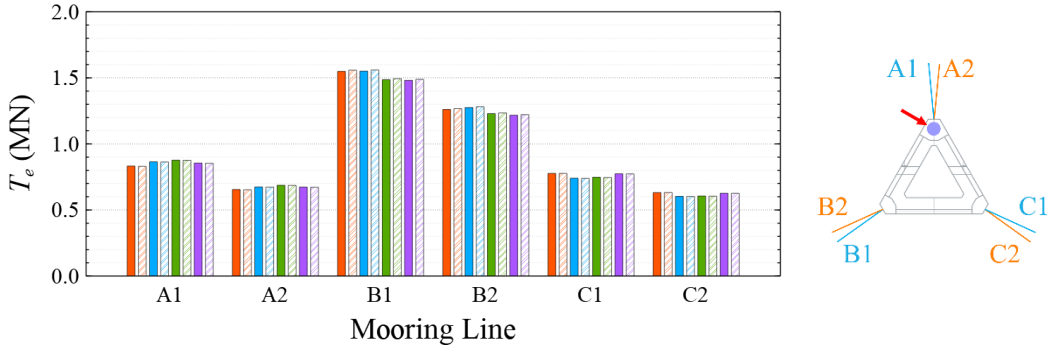

Figure 126 Comparison of mean value of mooring line tension at $\theta_w = 60°$ under HW condition

doi:10.6342/NTU202204241

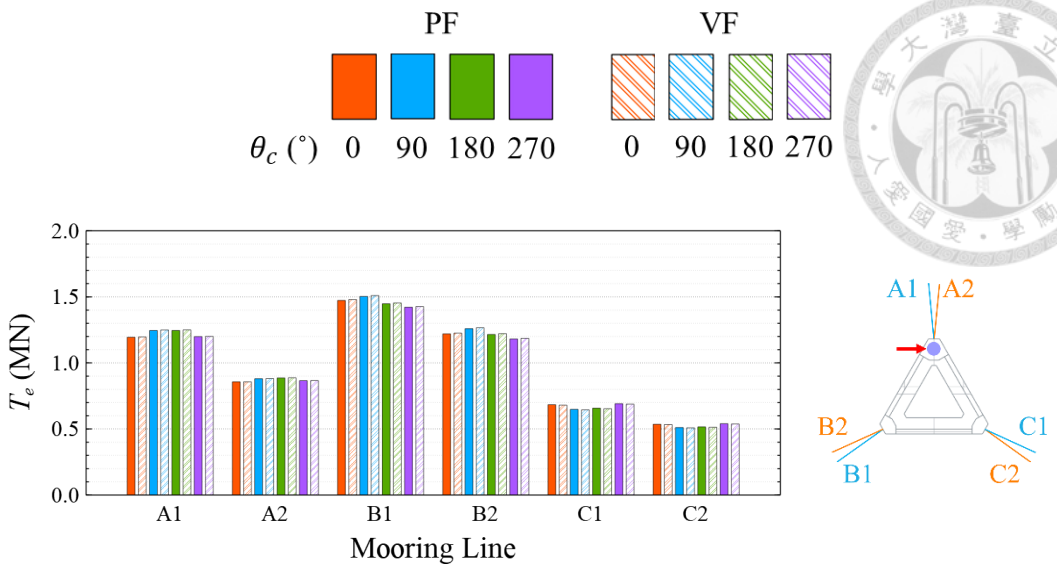

Figure 127 Comparison of mean value of mooring line tension at $\theta_w = 90°$ under HW condition

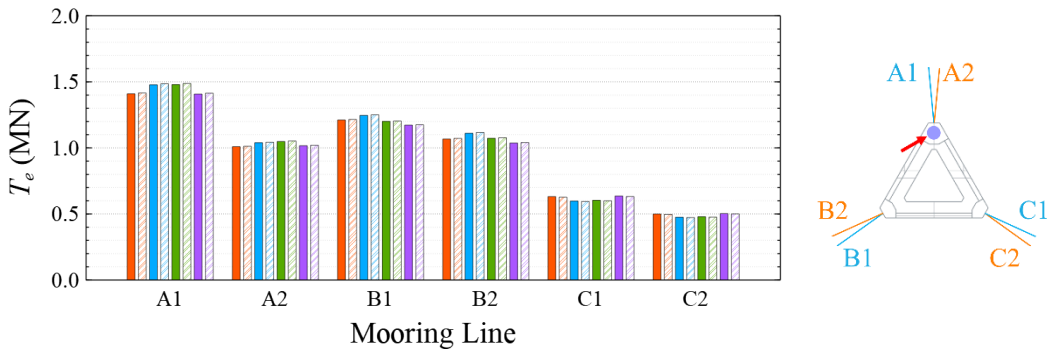

Figure 128 Comparison of mean value of mooring line tension at $\theta_w = 120°$ under HW condition

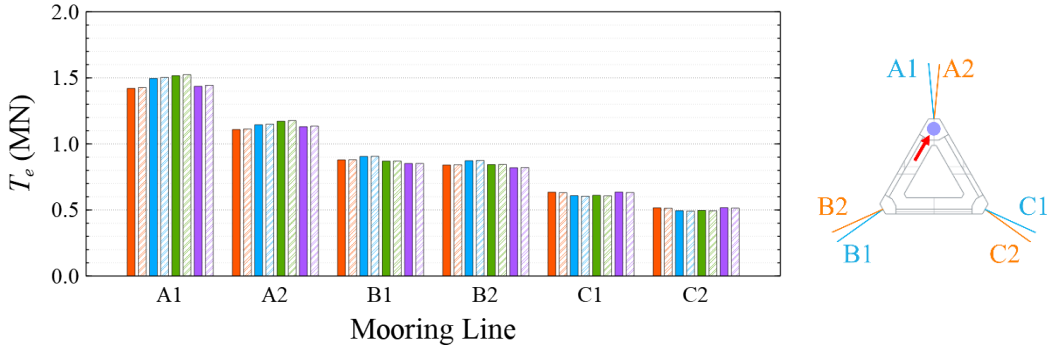

Figure 129 Comparison of mean value of mooring line tension at $\theta_w = 150°$ under HW condition

doi:10.6342/NTU202204241

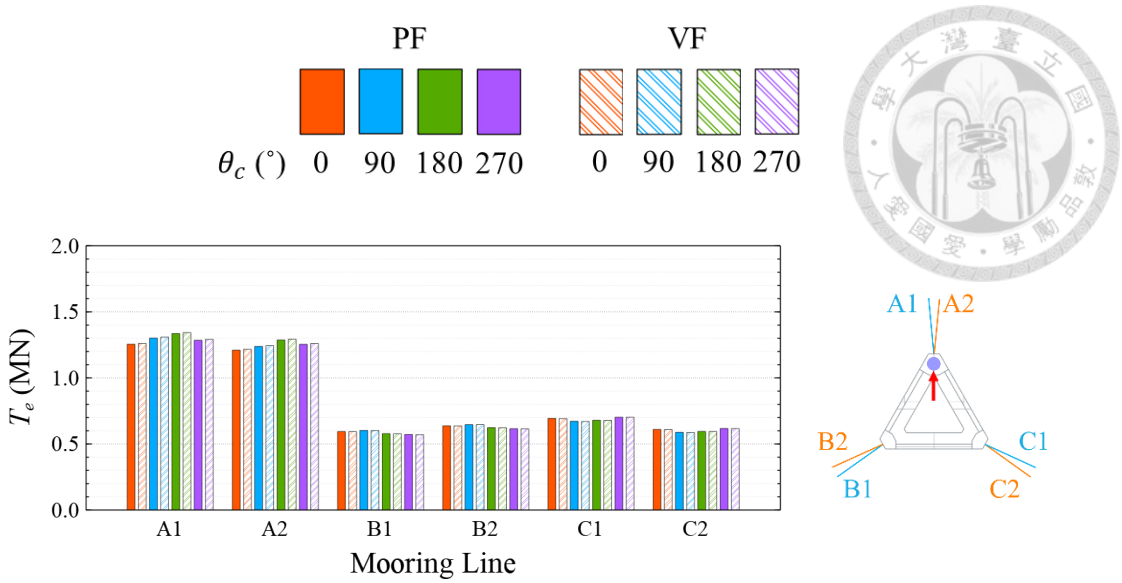

Figure 130 Comparison of mean value of mooring line tension at $\theta_w = 180°$ under HW condition

doi:10.6342/NTU202204241

doi:10.6342/NTU202204241

5 Conclusions

This study aims to predict the normal operating performance of a 15 MW floating wind turbine system equipped with a semi-submersible TaidaFloat platform, an IEA 15-MW offshore wind turbine and a 3×2 mooring design under the metocean conditions of the Hsinchu offshore area in the Taiwan Strait. This study first compares the potential and viscous results of the hydrodynamic properties. This study then compares the mean values and standard deviations of the motion response, generator power and mooring line tension via potential and viscous flow approaches, where the combinations of seven wind directions and four current directions under two wave conditions are considered. The results of this study are summarized below:

1. The viscous effect has a substantial impact on the hydrodynamic properties in the heave, roll and pitch motions than in the surge, sway and yaw motions. The viscous impact on the hydrodynamic properties under the CW condition is larger than those under the HW condition. The potential result of added mass in the heave motion is underestimated by up to 13.035% of the viscous result under the CW condition, while that under the HW condition is underestimated by up to 12.34% in the heave motion. The potential result of damping in the roll motion is underestimated by up to 93.044% of the viscous result, while that under the HW condition is underestimated by up to 86.606%.
2. The mean values of the motion response, generator power and mooring line tension are obviously sensitive to the wind and wave directions but insensitive to the modeling approaches and current directions under both studied wave conditions. The influence of the modeling approaches and current directions mainly shows in the standard deviation rather than in the mean value.

doi:10.6342/NTU202204241

3. Under the CW condition, the offset of the wind turbine system remains under 21 m and the mean pitch angle remains between -5° and 5° at all studied wind directions. All mooring line tensions are lower than one-sixth of the break load. The generator power is relatively high at $\theta_w = 0°$, delivering a mean generator power of up to 14.005 MW. The smallest maximum mean mooring line tension appears at $\theta_w = 0°$ as well, which is up to 1.643 MN. Hence, $\theta_w = 0°$ is the most favorable wind direction for the wind turbine system to operate under the CW condition in the Hsinchu offshore area.
4. Under the HW condition, the offset of the wind turbine system remains under 21 m and the mean pitch angle remains between -5° and 5° at all studied wind directions. All mooring line tensions are lower than one-eighth of the break load. All studied wind directions deliver a mean generator power that approaches the rated power. However, the smallest maximum mean mooring line tension appears at $\theta_w = 0°$, which is up to 1.254 MN. Hence, $\theta_w = 0°$ delivering a mean generator power of up to 14.996 MW, is the most favorable wind direction for the wind turbine system to operate under the HW condition in the Hsinchu offshore area.
5. The most favorable wind direction under the CW and HW condition in this study is suggested to be $\theta_w = 0°$, where the largest mean offset of 4.925 m and 1.954 m, the largest mean pitch of 4.7° and 0.633°, the largest mean generator power of 14.005 MW and 14.996 MW, and the maximum mean mooring line tension of 1.643 MN and 1.254 MN are found under the CW and HW condition, respectively. The wind is most likely coming from the northeast with a probability of 40%, followed by the north-northeast with a probability of 30% in the Taiwan Strait. Therefore, the angle between the leading mooring line of the system, i.e.,

doi:10.6342/NTU202204241

Line A1 and A2 in the study, and the most possible wind direction which is coming from the northeast, is recommended to be 0°.

doi:10.6342/NTU202204241

doi:10.6342/NTU202204241

Reference

[1] Bilgili, M., Yasar, A., and Simsek, E., "Offshore Wind Power Development in Europe and Its Ccomparison with Onshore Counterpart," *Renewable and Sustainable Energy Reviews*, vol. 15, no. 2, pp. 905-915, 2011.

[2] Nikolaos, N., "Deep Water Offshore Wind Technologies," M.S. thesis, Dept. Mechanical Engineering, University of Strathclyde, Glasgow, Scotland, 2004.

[3] Barltrop, N., "Multiple Unit Floating Offshore Wind Farm (MUFOW)," *Wind Engineering*, pp. 183-188, 1993.

[4] Henderson, A. R. and Patel, M. H., "Floating Offshore Wind Energy," presented at the 20th BWEA Conference, London, UK, May, 1998.

[5] Tong, K. C., "Technical and Economic Aspects of a Floating Offshore Wind Farm," *Journal of Wind Engineering and Industrial Aerodynamics*, vol. 74, pp. 399-410, 1998.

[6] Castro-Santos, L. and Diaz-Casas, V., Eds. *Floating Offshore Wind Farms.* Berlin/Heidelberg, Germany: Springer, 2016.

[7] Wang, Y. K., Chai, J. F., Chang, Y. W., Huang, T. Y., and Kuo, Y. S., "Development of Seismic Demand for Chang-Bin Offshore Wind Farm in Taiwan Strait," *Energies*, vol. 9, no. 12, pp. 1036, 2016.

[8] Chang, T. J., Chen, C. L., Tu, Y. L., Yeh, H. T., and Wu, Y. T., "Evaluation of the Climate Change Impact on Wind Resources in Taiwan Strait," *Energy Conversion and Management*, vol. 95, pp. 435-445, 2015.

[9] Lee, Y. J., Ho, C. Y., Huang, Z. Z., and Wang, Y. C., "Improvements on the Output of a Spar-Type Floating Wind Turbine Influenced by Wave-Induced Oscillation," *Journal of Taiwan Society of Naval Architects and Marine Engineers*, vol. 34, no. 2, pp. 55-62, 2015.

[10] Huang, Z. Z., "*Dynamic Response of Floating Offshore Wind Turbine*," M.S. thesis, Dept. Engineering Science and Ocean Engineering, National Taiwan University, Taipei, Taiwan, 2013.

[11] Wang, Y. C., "*Motion Characteristics and Power Evaluation on Floating Offshore Wind Turbine*," M.S. thesis, Dept. Engineering Science and Ocean Engineering, National Taiwan University, Taipei, Taiwan, 2011.

[12] Chen, C. Y., "*Comparative Study on Semi-Submersible Floating Platforms for Offshore Wind in Taiwan Strait*," M.S. thesis, Dept. Engineering Science and Ocean Engineering, National Taiwan University, Taipei, Taiwan, 2020.

[13] Hong, J. J., "*Performance Prediction of a Disk-Type Semi-Submersible Floating Platform in Taiwan Strait*," M.S. thesis, Dept. Engineering Science and Ocean Engineering, National Taiwan University, Taipei, Taiwan, 2022.

[14] Li, B., Liu, K., Yan, G., and Ou, J., "Hydrodynamic Comparison of a Semi-Submersible, TLP, and Spar: Numerical Study in the South China Sea Environment," *Journal of Marine Science and Application*, vol. 10, no. 3, pp. 306-314, 2011.

[15] Jonkman, J., Butterfield, S., Musial, W., and Scott, G., "Definition of a 5-MW Reference Wind Turbine for Offshore System Development," National Renewable Energy Lab, Golden, CO, USA, NREL/TP-500-38060, 2009.

[16] Bak, C., Zahle, F., Bitsche, R., Kim, T., Yde, A., Henriksen, L. C., Hansen, M. H., Blasques, J. P. A. A., Gaunaa, M., and Natarajan, A., "The DTU 10-MW Reference Wind Turbine," Dept. Wind Energy, Technical University of

doi:10.6342/NTU202204241

Denmark, 2013.
[17] Gaertner, E., Rinker, J., Sethuraman, L., Zahle, F., Anderson, B., Barter, G., Abbas, N., Meng, F., Bortolotti, P., Skrzypinski, W., Scott, G., Feil, R., Bredmose, H., Dykes, K., Shields, M., Allen, C., and Viselli, A., "Definition of the IEA Wind 15-Megawatt Offshore Reference Wind Turbine," National Renewable Energy Lab, Golden, CO, USA, NREL/TP-5000-75698, 2020.
[18] Global Wind Energy Council, "Global Wind Report 2022," Brussels, Brussels Hoofdstedelijk Gewest, Belgium, 2022. Accessed: July 1, 2022. [Online]. Available: https://gwec.net/global-wind-report-2022/.
[19] Zheng, C. W., Xiao, Z. N., Peng, Y. H., Li, C. Y., and Du, Z. B., "Rezoning Global Offshore Wind Energy Resources," *Renewable Energy*, vol. 129, pp. 1-11, 2018.
[20] Chang, P. C., Yang, R. Y., and Lai, C. M., "Potential of Offshore Wind Energy and Extreme Wind Speed Forecasting on the West Coast of Taiwan," *Energies*, vol. 8, no. 3, pp. 1685-1700, 2015.
[21] Industrial Technology Research Institute, "Wind Resource Assessment Handbook," Hsinchu, Taiwan, 2011.
[22] Faulkner S., "Offshore wind energy in Taiwan." Open Access Government. https://www.openaccessgovernment.org/taiwan-offshore-wind/129010/ (accessed July 1, 2022).
[23] Dicorato, M., Forte, G., Pisani, M., and Trovato, M., "Guidelines for Assessment of Investment Cost for Offshore Wind Generation," *Renewable Energy*, vol. 36, no. 8, pp. 2043-2051, 2011.
[24] Hsu, I. J., Ivanov, G., Ma, K. T., Huang, Z. Z., Wu, H. T., Huang, Y. T., and Chou, M., "Optimization of Semi-Submersible Hull Design for Floating Offshore Wind Turbines," presented at the 41st International Conference on Ocean, Offshore and Arctic Engineering, Hamburg, Germany, June, 2022.
[25] Huang, W. H., "*Influence of Water Depth Variation on the Mooring Line Design for FOWT in Shallow Waters*," M.S. thesis, Dept. Hydraulic and Ocean Engineering, National Cheng Kung University, Tainan, Taiwan, 2021.
[26] Coupled Analysis of Floating Wind Turbines, DNVGL-RP-0286, DNV, 2019.
[27] Ikhennicheu, M., Lynch, M., Doole, S., Borisade, F., Matha, D., Dominguez, J. L., Vicente, R. D., Habekost, T., Ramirez, L., Potestio, S., Molins, C., and Trubat, P., "Review of the State of the Art of Mooring and Anchoring Designs, Technical Challenges and Identification of Relevant DLCs", INNOSEA, COBRA, DTU, WIND EUROPE, EQUINOR, IREC, UPC, UL DEW, 2020.
[28] Gaertner, E., Rinker, J., Sethuraman, L., Zahle, F., Anderson, B., Barter, G., Abbas, N., Meng, F., Bortolotti, P., Skrzypinski, W., Scott, G., Feil, R., Bredmose, H., Dykes, K., Shields, M., Allen, C., and Viselli, A. "15MW Reference Wind Turbine Repository Developed in Conjunction with IEA Wind." GitHub. https://github.com/IEAWindTask37/IEA-15-240-RWT/. (accessed May 27, 2022).
[29] Haskind, M. D., "The Oscillation of a Ship in Still Water," *Izv. Akad. Nauk SSSR, Otd. Tekh. Nauk*, vol. 1, pp. 23-34, 1946.
[30] Haskind, M. D., "The Hydrodynamic Theory of Ship Oscillations in Rolling and Pitching," *Prikl. Mat. Mekh*, vol. 10, pp. 33-66, 1946.
[31] Wehausen, J. V. and Laitone, E. V., "Surface Waves in Fluid Dynamics III," *Handbuch der Physik*, vol. 9, no. 3, pp. 446-778, 1960.
[32] *Simcenter STAR-CCM+ User Guide, ver. 2206*, Siemens, Berlin, Germany, 2022.

doi:10.6342/NTU202204241

[33] Boussinesq, J., "Essai sur la Théorie des Eaux Courantes," *Mémoires Présentés par Divers Savants à l'Académie des Sciences*, vol. 23, no. 1, pp. 1-680, 1877.
[34] Hirt, C. W. and B. D. Nichols, "Volume of Fluid Method for the Dynamics of Free Surface," *Journal of Computational Physics*, vol. 39, pp. 201-225, 1981.
[35] Goldstein, S., "On the Vortex Theory of Screw Propellers," *Proceedings of the Royal Society of London. Series A, Containing Papers of a Mathematical and Physical Character*, vol. 123, no. 792, pp. 440-465, 1929.
[36] Hansen, M. H., Hansen, A., Larsen, T. J., Øye, S., Sørensen, P., and Fuglsang, P., "Control Design for a Pitch-Regulated, Variable Speed Wind Turbine," Risø National Laboratory, Roskilde, Danmark, RISØ-R-1500(EN), 2005.
[37] *OrcaFlex Documentation Version 11.2d*, Orcina, Cumbria, UK, 2022.
[38] Chuang, T. C., Yang, W. H., and Yang, R. Y., "Experimental and Numerical Study of a Barge-Type FOWT Platform under Wind and Wave Load," *Ocean Engineering*, vol. 230, pp. 109015, 2021.

doi:10.6342/NTU202204241